Core-collapse supernovae and their progenitors

Sergey Lisakov

UNIVERSITÉ CÔTE D'AZUR

ÉCOLE DOCTORALE
SCIENCES FONDAMENTALES ET APPLIQUÉES

THÈSE DE DOCTORAT

Les supernovae par effondrement gravitationnel et leurs progéniteurs

Sergey LISAKOV

Laboratoire Lagrange (UMR 7293)

Présentée en vue de l'obtention du grade de docteur en astrophysique d'Université Côte d'Azur

Dirigée par : Luc Dessart et Thierry Lanz

Soutenue le : 20/11/2018

Devant le jury, composé de :

Mathias Schultheis, Président du jury
Jean-Claude Bouret, Rapporteur
Sylvia Ekström, Rapporteur
Pascal Chardonnet, Examinateur
Luc Dessart, Co-directeur de thèse
Thierry Lanz, Co-directeur de thèse

European Commission
ERASMUS MUNDUS

Les supernovae par effondrement gravitationnel et leurs progéniteurs

Résumé

Les recherches de SNe ont commencé il y a plus de 100 ans. Depuis, il a été possible de collecter beaucoup de données d'observations astronomiques. Les astronomes ont développé une classification détaillée et ont abouti un relatif consensus sur la nature physique de ces événements très différents. Néanmoins, beaucoup de questions restent sans réponse.

En résumé, les supernovae de type II (riche en hydrogène) résultent de l'éjection l'enveloppe des supergéantes rouges (SGR). Les principales sources de connaissance sur ces objets sont l'évolution de leurs luminosité en fonction du temps ('courbes de lumière') et leurs spectres observés à différentes époques. La méthode la plus utilisée pour extraire les informations des données d'observation est la modélisation des courbes de lumières et des spectres des supernovae.

Dans le Chapitre 1, nous présentons successivement l'évolution stellaire, la physique des explosions et l'évolution des éjectas. Nous décrivons aussi les différents types de supernova ; l'état actuel des connaissances sur les CCSNe ainsi que ces limitations. Nous discutons de la théorie de l'évolution stellaire.

Nous décrivons notre approche numérique au Chapitre 2. Elle consiste en trois étapes principales : la modélisation de l'évolution stellaire, l'explosion de l'étoile SGR résultante, et la modélisation de l'évolution des éjectas. Nous présentons la structure modélisée des étoiles SGR.

Dans le Chapitre 3, nous discutons les propriétés observées en photométrie et spectroscopie des CCSNe. Nous extrayons les propriétés statistiques de l'échantillon existant.

En utilisant la technique présentée, nous avons effectué une étude détaillée de SN 2008bk, une supernova bien observée (Chapitre 4). Nous pouvons contraindre les propriétés du progéniteur et des paramètres d'explosion. Notre modélisation nous permet de comparer non seulement les propriétés de base telles que la luminosité, mais aussi à analyser en détail les caractéristiques spectrales, telles que la présence de certaine raies spectrales ainsi que leur morphologie. Nous montrons qu'une étoile de $12M_{\odot}$ sur la séquence principale est un bon candidat au progéniteur de SN 2008bk. Aussi, nous discutons de la forme asymétrique de la raie Hα et concluons qu'elle provient du chevauchement avec la raie forte du Ba II 6496.9 Å.

SN 2008bk, avec quelques dizaines d'autres objets, forme une sous-classe importante de CCSNe — supernovae à faible luminosité. Nous avons consacré une attention particulière à cette classe d'objets, dont l'uniformité et les données d'observation nous permet de tirer des conclusions importantes. Au Chapitre 5, nous étudions l'échantillon de 17 SNe de faible luminosité et analysons la possibilité que ces événements résultent d'explosions de progéniteurs de petite ou de grande masse. Il n'y a pas d'accord solide dans la communauté astronomique sur les progéniteurs possibles des explosions de SNe à faible luminosité. Notre analyse montre que les étoiles massives de masse inférieure ($\sim$12 $M_{\odot}$) sont de bons candidats pour les progéniteurs de cette sous-classe de SNe. De plus, nos simulations d'étoiles de masse élevée (25 et 27 $M_{\odot}$) montrent qu'une explosion ayant une luminosité aussi faible aurait des propriétés d'observation remarquables qui ne sont pas présentes dans les données.

Dans le Chapitre 6, nous étendons notre étude sur toutes les CCSNe, en utilisant des modèles plus énergétiques que dans les Chapitres 4 et 5. Nous fournissons des preuves que ce qui différencie la diversité de SNe II est l'énergie d'explosion plutôt que la masse des éjectas (ou plus précisément la masse de l'enveloppe riche en H de progéniteur).

Mots clés : Évolution stellaire ; Hydrodynamique ; Transfert radiative ; Supernovae.

Core-collapse supernovae and their progenitors

Abstract

Dedicated SN searches started over 100 years ago. Over that time, astronomers have collected large sets of observational data. They have developed detailed classification and achieved general agreement on the nature of these events. Nevertheless, a lot of questions remain unanswered.

In short, most Type II SNe (hydrogen-rich SNe) are terminal explosions of red supergiant (RSG) stars. The main source of knowledge about these objects are the way their luminosity changes with time ('light curves') and how their radiation is distributed in wavelength. One of the widely used methods to extract the information from the observational data is computer modelling. The largest part of our work lays in the numerical simulations.

In Chapter 1 (Introduction), we present succinctly the necessary theory which includes stellar evolution, explosion physics and ejecta evolution. We discuss different types of SNe; the modern knowledge on CCSNe and its problems. We discuss stellar evolution theory. We describe the nucleosynthesis that takes place in the cores of massive stars and gives rise to their final chemical stratification.

We describe our numerical approach in Chapter 2 (Supernova modelling). It includes three major steps: stellar evolution modelling, explosion of the resulting RSG star, and ejecta evolution modelling. We present modelled structure of RSG stars; these models and computational techniques are similar to models used in subsequent chapters. We then discuss our numerical methods of exploding a SN once its degenerate core starts collapsing. We discuss explosive nucleosynthesis and its impact on the progenitor composition, production of unstable isotopes and the basic physics of radioactive decay.

In Chapter 3 (Observational properties), we discuss the photometric and spectral observational properties of core-collapse SNe. We extract statistical properties of the existing sample.

Using the presented technique, we performed a detailed study of the well observed object SN 2008bk (Chapter 4). We are able to constrain its progenitor and explosion properties. Our modelling allows us to compare not only the basic properties such as luminosity, but also to analyze in detail the spectral features, such as line identification and morphology. We show that a $12\,M_\odot$ star on the main sequence is a good candidate for the progenitor of SN 2008bk. Also we discuss the asymmetric shape of the Hα line and conclude that it stems from the overlap with the strong Ba II 6496.9 Å line.

SN 2008bk, together with about 20 objects, form a subclass of low-luminosity CCSNe Type II. We devoted a particular attention to this class of objects, whose uniformity and observational data allows us to draw important conclusions. In Chapter 5 (Low-luminosity Type II-P SNe), we study the sample of 17 low-luminosity SNe and analyze the possibility that these events are the result of explosions of low- and high-mass progenitors. There is no solid agreement in the astronomical community on the possible progenitors of the low-luminosity explosions of Type II SNe. Our analysis shows that lower-mass massive stars ($\sim 12\,M_\odot$) are good candidates for the progenitors of this subclass of SNe. Moreover, our simulations of high-mass stars (25 and $27\,M_\odot$) show that such low brightness of the explosion of such a massive object would have notable observational properties which are not present in the data.

In Chapter 6 (Kinetic energy variation), we extend our study further on the whole class of hydrogen-rich core-collapse SN, using more energetic models than in Chapters 4 and 5. We provide evidences that what differentiates the diversity of SNe II is the explosion energy rather than the ejecta mass (or H-rich envelope mass of the progenitor).

Keywords: Stellar evolution; Hydrodynamics; Radiative transfer; Supernovae.

Contents

Chapter 1

Introduction

1.1 Historical background

One hundred years ago our conception of the Universe was remarkably different from now. The estimated size of the Milky Way spanned from 5 to 300 thousand light years, the location of the Solar System inside the Milky Way remained an open question, and there was no agreement whether observed spiral nebulae (which today are known to be galaxies) belong to the Milky Way or not. Devoted to these controversies, the Great Debate between Harlow Shapley and Doust Curtis took place in 1920 (Shapley & Curtis, 1921). Objects, which today are known as 'novae' and 'supernovae', were prominent actors in this dispute. However, at that time all new stellar-like bright objects, that gradually faded in months, were called 'novae'. Tradition to give this name to such objects was established in the 16th century by Tycho Brahe in his work *'De nova et nullius aevi memoria prius visa stella'*[1] on the famous object SN 1572, a SN in our galaxy visible to the naked eye. At that time, of course, it was not called 'supernova'.

Prior to 1917 only two 'novae stars' had been discovered in spirals — S Andromedae in 1885 and Z Centauri in 1895, whereas dozens of 'novae' had been registered in the Milky Way[2]. Discovery of a 'new star' in NGC 6946 by Ritchey (1917) motivated many observatories to start a search for such objects in old plate material. As a result, Shapley (1917) reported a list of eleven 'temporary stars' in spiral nebulae — today we know that only three of these were novae and eight were SNe (van den Bergh, 1988). Curtis (1917) adopted mean values $\overline{m}_{\max} \approx 5$ for Galactic 'novae' and $\overline{m}_{\max} \approx 15$ for the 'novae' in spirals. Therefore, 'novae' in spirals were on average ∼10 mag fainter than other 'novae'. This could be explained in two ways: either 'novae' in spirals are generally 10^4 times fainter, or 'novae' in spirals are in average 100 times further away than other 'novae'. Shapley doubted Curtis' idea that spirals are galaxies comparable in size with our own[3]. If one adopts this 'comparable galaxy' theory, then distance to the spirals, estimated through their angular diameter, would be immense. Shapley noted among the points of agreement between him and Curtis: 'If our galaxy approaches the larger order of dimensions, a serious difficulty at once arises for the theory that spirals are galaxies of stars comparable in size with our own: it would be necessary to ascribe impossibly great magnitudes to the new stars that have appeared in the spiral nebulae'. Curtis suggested at maximum ∼10 times smaller

[1] Concerning the new and previously unseen star (from Latin).

[2] Today S Andromedae and Z Centauri are classified as SNe — SN 1885A and SN 1895B respectively.

[3] This, however, was not a cornerstone in Shapley's theory. Unlike Curtis, he was correct in placing Solar System far out of the center of the Milky Way and in his suggestion that size of our galaxy is much larger than it was previously estimated. Shapley and Curtis estimations — 300 and 30 thousand light years correspondingly — were almost equally erroneous in comparison to the modern value of 100 thousand light years.

dimensions of the Milky Way. With such a reduced scale of the Universe it was easier to accept still impressively great magnitudes of 'novae' in spirals.

Few years after the Great Debate, a relation between recessional velocity and distance to spirals was established. In 1927, Georges Lemaître published *'A homogeneous Universe of constant mass and growing radius accounting for the radial velocity of extragalactic nebulae'*[4] in the *Annals of the Scientific Society of Brussels* (Lemaître, 1927). In this work he found dynamic solutions to Einstein's general relativity equations. These solutions indicated that there is a linear relation between the recessional velocity of a galaxy and its distance. It seems that Lemaître was the first to estimate the value of the parameter, linking the recessional velocity V and galaxy distance D. Today this parameter is known as the Hubble constant H_0: $V = H_0 \times D$.

Using redshift measurements of Vesto Slipher from Stromberg (1925) and distance estimations from Hubble (1926) for 42 galaxies, he obtained a value of 625 km s^{-1} Mpc^{-1}. In cited work, Hubble used a statistical expression for distance in parsecs $\log(D) = 4.04 + 0.2\,m$, where m is the total apparent magnitude. Lemaître noted, however, that contemporary uncertainties in distances to galaxies are too high to show this linear relation between velocity and distance. His value of H_0 is quite different from the modern $H_0 = 67.8 \pm 0.77$ km s^{-1} Mpc^{-1} (Planck Collaboration, 2014), but close to the value of 500 km s^{-1} Mpc^{-1} obtained by Hubble two years later (1929), where he used Cepheid variable stars to find distances to galaxies. The main reason of their significant error was the incorrect determination of distances to galaxies. To determine distances, Hubble used period-luminosity relation for the Cepheid variables for nearby galaxies and the brightest resolved stars as the most luminous individual locators for distant galaxies. In 1952 it was shown that there are two types of Cepheid variables with different period-luminosity relations (Baade, 1952), and Allan Sandage summarized problems of both approaches (Sandage, 1958).

Once the distances to the hosts of 'novae' stars have been determined, it became possible to estimate their absolute magnitudes. It turned out that some 'novae' are orders of magnitude brighter than others, and astronomers realised that 'novae' should be divided into two subclasses. This division occurred in 1934, when Fritz Zwicky and Walter Baade suggested the term 'super-novae' for exceptionally bright 'novae'[5].

Today we consider that a classical nova is an event with the peak absolute magnitude $M_V \approx -8$ mag, fading within months. A mechanism of novae is thought to be a thermonuclear runaway at the surface of a white dwarf (WD) due to the accretion of matter from a large companion star.

In 1938 Baade noticed that SNe constitute a homogeneous class of objects. He found that the mean absolute magnitude at maximum light for 18 SNe is -14.3 mag with a dispersion of $\sim$1.1 mag.

Since then SNe have been considered as good distance indicators in the Universe (Baade, 1938), and 70 years later Saul Perlmutter, Brian P. Schmidt and Adam G. Riess were awarded the Noble Prize for the discovery of dark energy and the accelerating expansion of the Universe through observations of the SNe. Interestingly, both groups, led by S. Perlmutter and B. Schmidt, expected to find deceleration of the expansion of the Universe (Riess et al., 1998; Perlmutter et al., 1999).

[4] The original French title: 'Un Univers homogène de masse constante et de rayon croissant rendant compte de la vitesse radiale des nébuleuses extragalactiques.'

[5] Though appeared first in 1933 in publication of Lundmark (Osterbrock, 2001), according to Zwicky (1940) it has been in use since 1931 in seminars and courses in Caltech by Zwicky and Baade.

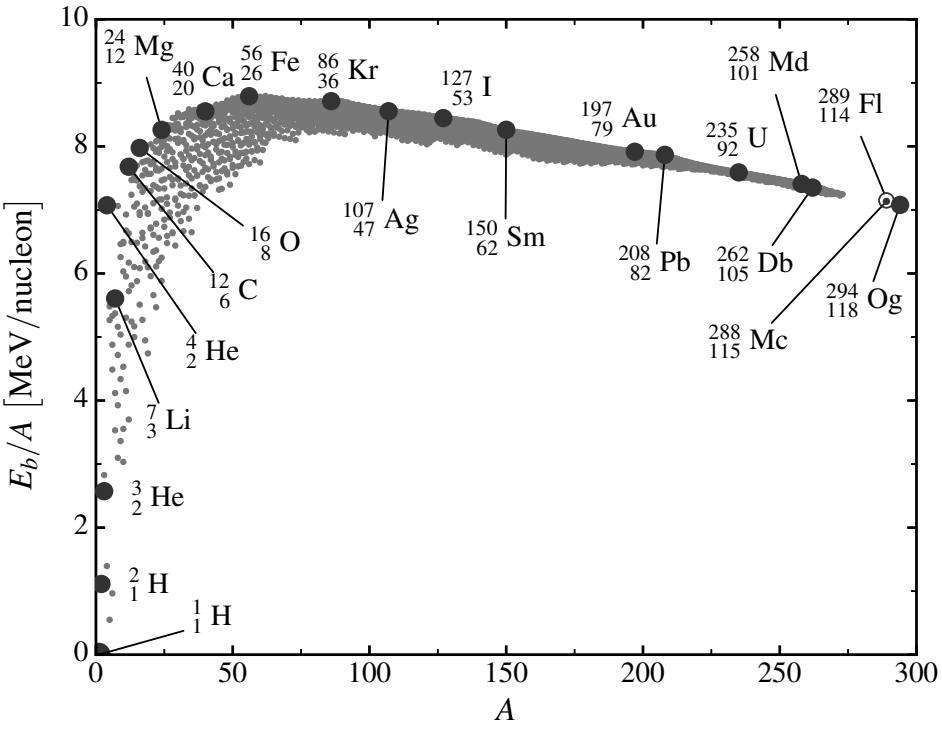

Figure 1.1 – The binding energy $E_b = \left(Zm_p + (A-Z)m_n - m_{\text{nucleus}}\right) \times c^2$ per nucleon as a function of mass number. The most stable of all nuclei is $^{56}_{26}$Fe. For all nuclei to the left of $^{56}_{26}$Fe, nuclear fusion releases energy. For the reminder, nuclear fission does. This is the reason why the stars do not burn elements further than the elements of iron peak. The gap at $A \sim 270$ is due to the incompleteness of the database used to plot the figure; a few recently discovered elements (such as $^{288}_{115}$Mc, $^{289}_{114}$Fl, $^{294}_{118}$Og) have been added to extend the relation. The range of E_b/A for the given A stems from the isotopes (including unstable ones) with the same A.

1.2 Stellar evolution theory

The way stars evolve and explode is crucial for understanding SNe. To explain and to model observed SNe, we need to specify the initial parameters for our simulations. In this section, we review the current knowledge on stellar evolution.

The diversity of core-collapse SNe stems from the many different evolutionary paths of their progenitors. The main parameter controlling stellar evolution is the initial mass. Primarily, H in stellar cores converts to He. If a star is sufficiently massive, heavier elements (C, O, Ne, N, Mg, Si, Fe) are subsequently produced in nuclear synthesis reactions. All stars of interest to core-collapse SNe are massive enough to form either an O-Ne-Mg core (Poelarends et al., 2008) or a Fe core (Woosley et al., 2002).

Figure 1.1 shows the binding energy per nucleon vs. mass number A. The atomic data come from Meija et al. (2016). Figure 1.1 shows that the most energetic release occurs when ^{1}H converts to ^{4}He. The most stable element made during stellar evolution is ^{56}Fe, further fusion does not occur.

Massive single stars ($\gtrsim 8\,M_\odot$) would eventually experience collapse of the core. With the increase in the mass of the star, the stellar wind mass loss rate also increases. SN progenitors could possess several solar masses of H-rich envelope or could be left out without H-rich and even He-rich layers. Final radius and mass depend on variety of parameters, including mass loss, binarity, metallicity, rotation, etc. Final radii lie in the range from hundreds to a thousand of solar

radii, and final masses could be in the range from ~7 to ~15 $M_\odot$ (see, e.g., Fig. 16 in Woosley et al., 2002).

In addition, stellar evolution in a close binary system could be substantially different from the evolution of a single star (Podsiadlowski, 1992). Hence, the progenitors could differ a lot in mass, radius, and composition, which would impact the resulting SN and its remnant. That is why we discuss stellar evolution in some detail. The understanding of stellar evolution is necessary to explain the observational properties of SNe.

1.2.1 The spectral types of stars and Hertzsprung–Russell diagram

A simplified spectral taxonomy lists spectral types of stars as follows: O B A F G K M L T. In this sequence, the effective temperature decreases from type O (40 000 K and above) to type T (1300 K and below). According to the Planck's law of black-body radiation, the spectral energy distribution for the hottest stars peaks in the blue or ultra-violet (UV) part of the spectrum, and for the coolest stars in the infra-red (IR) part of the spectrum.

It was found that stars of the same spectral type (hence the same effective temperature) show a range of luminosities. The expression for stellar luminosity (total radiant energy coming out) is:

$$L = 4\pi R_\star^2 \sigma T_{\rm eff}^4, \tag{1.1}$$

where $R_\star$ is the hydrostatic radius, or R where $\tau_{\rm radial} = 2/3$, and $\sigma \approx 5.67 \times 10^{-5}$ erg cm^{-2} s^{-1} K^{-4} is a Stefan–Boltzmann constant.

It was probably Hertzsprung (1905) who first termed 'dwarf' and 'giant' to describe the stars of different luminosity. Today we call 'supergiants' the stars with an absolute optical magnitude brighter than about −3 mag (or $L > 1.3 \times 10^3\, L_\odot$), populating the upper part of the Hertzsprung–Russell (H–R) diagram. If the color is blue, they referred to as blue supergiants (BSG). Red stars of such luminosity are called red supergiants (RSG). It will be explained below which stars and at which evolutionary stages become RSG.

1.2.2 CNO cycle

It is well known that the source of energy for the stars on the main sequence (MS), such as the Sun today, is the 'burning' of H, i.e. nuclear fusion reactions where H is being converted to He (Arnett, 1996). Typically, a star spends roughly 90% of its life on the MS (irrespective of mass). In stars below ~1.3 $M_\odot$ with central temperatures on the MS from $\sim 4 \times 10^6$ to $\sim 17 \times 10^6$ K it happens mainly in proton–proton chain (p–p chain), and in more massive stars, where the central temperature $\gtrsim 17 \times 10^6$ K, the CNO cycle becomes a more effective way to burn H into He. Both p–p and the CNO cycle serve to convert $^1_1$H to $^4_2$He through intermediate reactions.

The energy production rates of p–p chain and CNO cycle show highly different dependence on the temperature. p–p energy production rate is

$$\epsilon_{pp} \approx \epsilon^0_{\rm PPI} \rho X_H^2 \left(\frac{T}{T_0}\right)^{4.6}, \tag{1.2}$$

where $\epsilon^0_{\rm PPI} = 0.068$ erg g^{-1} s^{-1}, $T_0 \approx 10^7$ K, $X_{\rm H}$ is the mass fraction of all isotopes of H, and CNO cycle production rate near $T_6 = 25$ ($T_6 = T/10^6$ K) is

$$\epsilon_{\rm CNO} \approx \epsilon^0_{\rm CNO} \rho X_{\rm H} X_{\rm CNO} f_{\rm N} \left(\frac{T_6}{25}\right)^{16.7}, \tag{1.3}$$

where $X_{\rm CNO}$ is the mass fraction of all isotopes of C, N, O; $\epsilon^0_{\rm CNO} = 2.2 \times 10^4$ erg g^{-1} s^{-1} and $f_{\rm N}$ is the screening factor for $^{14}{\rm N}(p,\gamma)^{15}{\rm O}$ (Arnett, 1996).

In other words, in low-mass stars p–p chain dominates, whereas for stars with M $>$ 1.3 M$_\odot$ the CNO cycle is more productive. This difference plays an important role in the structure of stellar interiors. The CNO cycle was proposed by Bethe (1939). C, N and O are consumed and then regenerated in the cycle.

When the temperature and the density become high enough, He nuclei will be able to overcome the Coulomb repulsion, so the $^{12}_{6}$C production in the so-called 3–α process will begin.

1.2.3 The triple-alpha process

In the triple-alpha process He is being converted to C:

$$\begin{aligned} {}^4_2{\rm He} + {}^4_2{\rm He} &\rightleftharpoons {}^8_4{\rm Be} \\ {}^8_4{\rm Be} + {}^4_2{\rm He} &\rightarrow {}^{12}_6{\rm C} \end{aligned} \tag{1.4}$$

In the first step, an unstable Be is produced, which will rapidly decay back into two He nuclei if not immediately struck by another α-particle. The energy production rate in the triple-alpha process beyond $T = 10^8$ K is:

$$\epsilon_{3\alpha} \approx \epsilon_1 \rho^2 X_\alpha \left(\frac{T_8}{2}\right)^{18.5}, \tag{1.5}$$

where $\epsilon_1 = 23.1$ erg g^{-1} s^{-1} (Arnett, 1996).

1.2.4 Carbon, neon and oxygen burning

During the triple-alpha process μ continues to rise, therefore the core continues to shrink due to equation of state ($P = \frac{\rho k T}{\mu m_{\rm H}}$). In the core of massive stars, the pressure is dominated by radiation hence this has a weaker effect compared to lower mass stars. Core also contracts at C ignition because it cools efficiently through neutrinos. Neutrino losses are a critical aspect of the evolution of massive stars once they finish He burning (Woosley et al., 2002). A neutrino loss term is roughly proportional to T^9 for advanced burning stages (Clayton, 1968). The temperature sensitivity of neutrino losses and the need of higher temperatures in order to burn fuels with larger charge barriers lead to a rapid acceleration of the stellar evolution during C, Ne, O, and Si burning, the latter typically taking only about a day (see, e.g., Table 1 in Woosley et al., 2002).

After a sufficient amount of C is generated, O and Ne are produced in the nuclear reactions:

$$\begin{aligned} {}^{12}_6{\rm C} + {}^4_2{\rm He} &\rightarrow {}^{16}_8{\rm O} + \gamma \\ {}^{16}_8{\rm O} + {}^4_2{\rm He} &\rightarrow {}^{20}_{10}{\rm Ne} + \gamma \end{aligned} \tag{1.6}$$

If the star is massive enough, the core temperature reaches 6×10^8 K and the Coulomb repulsion cannot prevent the following reactions anymore:

$${}^{12}_6{\rm C} + {}^{12}_6{\rm C} \rightarrow \begin{cases} {}^{16}_8{\rm O} + 2\,{}^4_2{\rm He} & \text{(endothermic)} \\ {}^{20}_{10}{\rm Ne} + {}^4_2{\rm He} & \\ {}^{23}_{11}{\rm Na} + p^+ & \\ {}^{23}_{12}{\rm Mg} + n & \text{(endothermic)} \\ {}^{24}_{12}{\rm Mg} + \gamma & \end{cases} \tag{1.7}$$

C burning for the stars with initial mass of 20 $M_\odot$ lasts ~300 years (see Table 2.1 for burning time of H and He for our set of models). After all C is consumed in the core, Ne burning starts ($T \gtrsim 1.2 \times 10^9$ K). Ne is consumed and O and Mg are accumulated in the core.

When the temperature reaches $\gtrsim 1.5 \times 10^9$ K, O burning starts:

$$ {}^{16}_{8}\mathrm{O} + {}^{16}_{8}\mathrm{O} \rightarrow \begin{cases} {}^{24}_{12}\mathrm{Mg} + 2\,{}^{4}_{2}\mathrm{He} & \text{(endothermic)} \\ {}^{28}_{14}\mathrm{Si} + {}^{4}_{2}\mathrm{He} \\ {}^{31}_{15}\mathrm{P} + p^+ \\ {}^{31}_{16}\mathrm{S} + n \\ {}^{32}_{16}\mathrm{S} + \gamma \end{cases} \tag{1.8} $$

In reactions marked endothermic, energy is absorbed. Other reactions from Equations 1.7 and 1.8 are exothermic, i.e. energy is released. O burning for a 20 $M_\odot$ star takes around one year (see Table 1 in Woosley et al., 2002).

1.2.5 Si burning

After the C, Ne and O burning processes the inner core of the star consists mainly of Si and S. When the central temperature reaches ~3×10^9 K, Si burning starts:

$$ \begin{aligned} {}^{28}_{14}\mathrm{Si} + {}^{4}_{2}\mathrm{He} &\rightleftharpoons {}^{32}_{16}\mathrm{S} + \gamma \\ {}^{32}_{16}\mathrm{S} + {}^{4}_{2}\mathrm{He} &\rightleftharpoons {}^{36}_{18}\mathrm{Ar} + \gamma \\ {}^{36}_{18}\mathrm{Ar} + {}^{4}_{2}\mathrm{He} &\rightleftharpoons {}^{40}_{20}\mathrm{Ca} + \gamma \\ {}^{40}_{20}\mathrm{Ca} + {}^{4}_{2}\mathrm{He} &\rightleftharpoons {}^{44}_{22}\mathrm{Ti} + \gamma \\ {}^{44}_{22}\mathrm{Ti} + {}^{4}_{2}\mathrm{He} &\rightleftharpoons {}^{48}_{24}\mathrm{Cr} + \gamma \\ {}^{48}_{24}\mathrm{Cr} + {}^{4}_{2}\mathrm{He} &\rightleftharpoons {}^{52}_{26}\mathrm{Fe} + \gamma \\ {}^{52}_{26}\mathrm{Fe} + {}^{4}_{2}\mathrm{He} &\rightleftharpoons {}^{56}_{28}\mathrm{Ni} + \gamma \end{aligned} \tag{1.9} $$

Si burning produces a host of nuclei centered near the ${}^{56}_{26}\mathrm{Fe}$ peak of the binding energy per nucleon (see Figure 1.1). Any further reactions which produce nuclei heavier than ${}^{56}_{26}\mathrm{Fe}$ are endothermic, i.e. absorb energy rather than release it.

1.2.6 Photodisintegration and core collapse

After the formation of the Fe core, further burning of elements would only absorb energy. In the result of nuclear reactions, starting from H burning which happens in a timescale of billions of years and finishing with Si burning (Equation 1.9) which is completed in a few days (depending on stellar mass), there are no more nuclear fuel in deep hot stellar regions, where temperature is above the threshold for combustion at least for H. The star by the end of its life has an 'onion-like' structure, i.e. iron core, then Si-rich, O-rich, C-rich, He-rich and H-rich layers (see, e.g., Fig. 31 from Paxton et al., 2011). Shell burning still occurs. With such high temperatures which are in the center of the star during the Si-burning an important process of photodisintegration commences. Photons have enough energy to destroy heavy nuclei (this is the reason for reverse arrows in Equation 1.9). Without it, Si-burning would not be possible because of lack of He nuclei. Particularly important photodisintegration processes are:

$$ \begin{aligned} {}^{56}_{26}\mathrm{Fe} + \gamma &\rightarrow 13\,{}^{4}_{2}\mathrm{He} + 4n \\ {}^{4}_{2}\mathrm{He} + \gamma &\rightarrow 2p^+ + 2n \end{aligned} \tag{1.10} $$

The core is primarily supported by electron degeneracy pressure. The internal conditions become extreme: $T_c \sim 8 \times 10^9$ K and $\rho_c \sim 10^{10}$ g cm^{-3} for a 15 $M_\odot$ star. Free electrons are captured by heavy nuclei and by the protons that were produced through photodisintegration, e.g.,

$$p^+ + e^- \rightarrow n + \nu_e \tag{1.11}$$

Neutrino luminosity L_ν dominates the photon luminosity $L_{\rm photons}$ after C burning. At the stage before core collapse, neutrino luminosity of the star could be 6–7 orders of magnitudes higher than the photon luminosity (Arnett, 1996; Woosley et al., 2002). Also, because time left before collapse is small, there is no longer any energy transport through the star. Captured electrons do not anymore contribute to the core pressure through degeneracy pressure. They are suddenly gone and the core begins to collapse on a dynamical timescale extremely rapidly — up to $0.25c$. Former iron core had a dimensions similar to that of the Earth, and it is collapsed to the size of tens of kilometers within about 100 ms.

As the density reaches $\rho_{\rm trap} \approx 10^{12}$ g cm^{-3}, neutrinos become trapped in the core. When the central density reaches $\sim 2 \times 10^{14}$ g cm^{-3}, neutrons begin to experience a repulsive strong force due to the Pauli principle. The core bounces and send shock waves outward into the infalling material from the outer core. The core bounce with the formation of a shock wave is the starting point of a sequence of events that ultimately triggers a supernova explosion.

In numerical simulations, the shock wave is not strong enough to stop the collapse and to explode the outer shells of the star (e.g., Burrows et al. 1995; Janka & Mueller 1996). The shock uses up its energy mostly by the dissociation of heavy nuclei into nucleons, there are also huge losses through neutrino radiation. The shock is weakened so much that it finally stalls and turns into a standing accretion shock at a radius between 100 and 200 km.

The compact remnant forms at core bounce. After that it rapidly grows in mass by the accretion of infalling stellar material. This proto-NS will evolve to a NS or may eventually collapse to a black hole (BH). Neutrinos are trapped in the formed NS because their mean free paths in the dense matter are significantly shorter than the radius of the NS. It takes 1–10 seconds for the trapped neutrinos to diffuse out (Burrows, 1990). On their way to the neutrinosphere, the neutrinos convert their initially high degeneracy energy to thermal energy of the stellar medium (Burrows & Lattimer, 1986). The further cooling of the hot interior of the proto-NS then proceeds by neutrino-pair production and diffusive loss of neutrinos of all three lepton flavors. After several tens of seconds the neutrino luminosity drops significantly, because there is not much thermal energy left in the NS (Burrows, 1988). During the explosion phase (< 1 s), it is the neutrinos from accreted matter onto the NS surface that boost the L_ν, not those in the NS, which take longer to come out.

In the explosion scenario by the ‘delayed neutrino-heating mechanism’, the stalled shock wave can be revived by the neutrinos streaming off the neutrinosphere. These neutrinos carry most of the energy set free in the gravitational collapse of the stellar core (Burrows, 1990) and deposit some of their energy in the layers between the proto-NS surface and the stalled shock front mainly by charged-current ν_e and $\overline{\nu}_e$ captures on free nucleons (Bethe & Wilson, 1985):

$$\begin{aligned} \nu_e + n &\rightarrow e^- + p \\ \overline{\nu}_e + p &\rightarrow e^+ + n \end{aligned} \tag{1.12}$$

This neutrino heating increases the pressure behind the shock and the heated layers begin to expand, creating between shock front and NS surface a region of low density but rather high temperature, the so-called ‘hot bubble’ (Colgate, 1989). The persistent energy input by neutrinos keeps the pressure high in this region and drives the shock outwards again, eventually leading to a supernova explosion. This may take a few 100 ms and requires that during this time interval a

few percent of the radiated neutrino energy (or 10–20% of the energy of electron neutrinos and antineutrinos) are converted to thermal energy of nucleons, leptons, and photons. The canonical explosion energy of a supernova is 1–2 percent of the total gravitational binding energy lost by the nascent NS in neutrinos (Janka et al., 2007).

Gravitational collapse is often listed among the most intriguing scientific puzzles of our time. Not every aspect of it is understood today, but generally it is believed that the simplified explanation of the process, presented above in this section, is a satisfactory yet not complete picture of what is really happening. A great luck was an explosion of SN 1987A in Large Magellanic Cloud, when neutrinos have been registered in three separate neutrino detectors on the Earth (Kamiokande II, IMB and Baksan, total 25 neutrinos in ~12 seconds. These neutrinos correspond to the long term cooling of the proto-NS, not the neutrinos that could have acted to generate the explosion). These 25 registered neutrinos in 12 seconds served as a confirmation of some basic aspects of understanding of gravitational core-collapse.

1.3 Supernovae

All SNe appear as a previously unseen stellar-like object, in most cases associated with a host galaxy. After discovery of a SN, it usually gradually fades out with a time-scale of a year, although not all SNe have their peak bolometric luminosity at shock breakout. Also, we usually refer to maximum as the time of optical maximum, because this is the filter normally used to observe them. The range of the bolometric luminosities is from $\sim 10^{41}$ erg s^{-1} to $\sim 10^{44}$ erg s^{-1}, sometimes brighter than the Milky Way galaxy.

SNe either explode in the thermonuclear runaway of a compact WD (see Section 1.3.2) or they end their life in the collapse of the degenerate core of a massive star (see Section 1.3.3). Whatever the mechanism of the explosion is, the typical kinetic energy of SN ejecta at infinity is of the order of 10^{51} erg (e.g., Blinnikov et al., 2000; Maoz et al., 2014).

We discussed the origin of the term 'supernova' in the historical introduction. Given the present understanding of the SNe physical nature, the word 'supernova', used to describe these events, could be quite deceiving from one point of view: it is the end of the star life that we witness, not the beginning. However, a SN explosion of either type ejects large amount of heavy elements. One can hardly imagine how different would be the Universe without SNe: the distribution of the heavy elements in the interstellar space is crucial for everything, including the life on the Earth. Any planet or star in the Universe, as well as any person on the Earth, consists partially of the matter that is ejected in the explosions of SNe.

Milky Way, our galaxy, consists of $\sim 10^{10}$ stars. Stars with initial mass between ~8 and $\sim 30\,M_\odot$ end their life with a collapse of the core. The luminosity function (Kroupa, 2001) predicts ~0.3% of stars in the Galaxy to populate this range of masses. WDs generally start their way to the thermonuclear explosion after the evolution of the $0.5 - 8\,M_\odot$ and they need a companion star to accrete the matter from or a companion WD to coalesce with. The most recent[6] observed SN in our galaxy happened to explode in 1604 and is known as a 'Kepler supernova'. Studies of the remnant in the Modern Age determined that it was an explosion of an accreting WD. Even pessimistic rates of SN explosions allows us to expect one visible from the Earth in the near future in the Milky Way.

Conselice et al. (2016) estimate that there are $2^{+0.7}_{-0.6} \times 10^{12}$ galaxies in the Universe. This

[6] The youngest known SN Ia remnant is G1.9+0.3, exploded in the 19th century, but unobserved due to the large extinction along the Galactic plane (Chakraborti et al., 2016).

number, however, largely depends on the adopted number of small galaxies of very little mass. Such galaxies are very numerous but contribute nothing to the SN rates due to small number of massive stars.

Milky Way hosts several SNe each century (e.g., The et al. 2000). Making an assumption that there are $\sim 10^{11}$ galaxies in the Universe similar to Milky Way, one obtains a rate of $\sim 10^{10}$ SNe per year in the Universe, which is of the order of 100 SNe per second. During the time while the author of this manuscript performed his PhD study, around 10 billion SNe exploded, which is a number of stars in a decent galaxy[7].

Nowadays, most of the SNe are discovered by specialized projects, that widely use varying degree of automation to survey the whole sky or its part. Such surveys are the Lick Observatory Supernova Search (LOSS, Li et al. 2000), the Panoramic Survey Telescope & Rapid Response System (Pan-STARRS, Kaiser et al. 2002), the Texas Supernova Search (Quimby, 2006), the Sloan Digital Sky Survey (SDSS) Supernova Survey (Frieman et al., 2008), the Catalina Real-Time Transient Survey (CRTS, Drake et al. 2009), the CHilean Automatic Supernova sEarch (CHASE, Pignata et al. 2009), the Palomar Transient Factory (PTF, Law et al. 2009), the Gaia transient survey (Hodgkin et al., 2013), the La Silla-QUEST (LSQ) Low Redshift Supernova Survey (Baltay et al., 2013), the Mobile Astronomical System of TElescope Robots (MASTER, Lipunov et al. 2010; Gorbovskoy et al. 2013), the Optical Gravitational Lensing Experiment-IV (OGLE-IV, Wyrzykowski et al. 2014), the All-Sky Automated Survey for SuperNovae (ASAS-SN[8]; Shappee et al. 2014), and numerous others. For example, ASAS-SN surveys the entire visible night sky on a rapid cadence to find the bright SNe, and thus provides a very complete census of nearby SNe.

1.3.1 SN classification

In 1941 Rudolph Minkowski analyzed the spectra of SNe, dividing them into two main types (Minkowski, 1941). To the Type I he attributed the SNe which had no H lines in their spectra and the entire spectrum consisted from broad maxima and minima which were not possible to explain (interpretation of Type I SNe spectra has been done later by Pskovskii, 1969). Type II SNe, on the contrary, showed presence of H in their spectra. Over time, a more detailed classification appeared (Figure 1.2)[9]. Type I SNe were divided into three subtypes: Ia, Ib and Ic, based on the presence of Si and He lines in the spectra. Today it is known that the SN Ia phenomenon arises from either a thermonuclear explosion of a WD or a merger of two WDs, and the energy source for SNe II and SNe Ib/c is core collapse of a massive star at the final stage of its evolution (e.g., Hoyle & Fowler 1960). Thus, SN Ia explosions differ in their origin from the rest of SNe. The SNe classification was being developed step by step alongside with the increasing knowledge of these objects. In 1979, two subclasses of Type II SNe were proposed by Barbon et al., Type II-P (plateau) and II-L (linear), based on the B-band light curve morphology. In 1993, a peculiar SN 1993J exploded in the spiral galaxy M81. It initially displayed strong H emission lines as other Type II SNe, but within a month the H lines disappeared. Spectral evolution changed to that of a Type Ib. A new subclass IIb was added to the classification to cover this type of objects. The possibility of the transition from Type II to Type Ib contains an important indication that these events are related in some way. We will discuss it in the next section.

[7] In other words, an average PhD student needs a galaxy to explode to accomplish his task.

[8] http://www.astronomy.ohio-state.edu/~assassin/

[9] It was noticed that the majority of the doctoral students try to build their own SN classification scheme by the time of defence (author of this manuscript is no exception). Serving a meritorious purpose of not copying the work of the others, it proves once again that a perfect scheme of the SN classification is an unreachable goal due to the state of the classification.

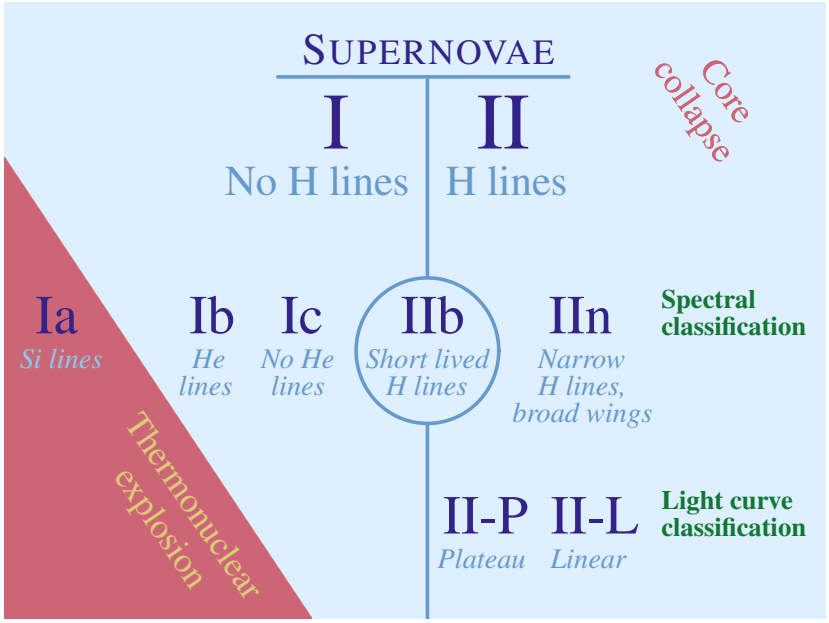

Figure 1.2 – A simplified SN classification scheme. Note that Type IIn SNe may be distinct (e.g., pair instability pulsations rather than core collapse).

To show the SNe diversity, in Figure 1.3 we present V-band light curves and in Figure 1.4 we present a spectral montage for representatives of SN types. It worth noticing that a large fraction of SNe are attributed to different types in different studies. It can be partially explained by the fact that CCSNe form a continuum of observational properties. Below, we will discuss in turn all main SN types.

1.3.2 Thermonuclear Type Ia SNe

Though this type of SNe is not directly connected with the topic of the present dissertation, we will succinctly discuss the main observational and physical properties of Type Ia SNe. The observational properties of Type Ia SNe are presented in Figures 1.3 and 1.4, compared to other SNe types. The typical absolute V-band magnitude at maximum is $M_V \approx -19$ mag (e.g., Hicken et al. 2009). The subsequent V-band LC is powered by the radioactive decay of ^{56}Ni. The absolute V-band magnitude of -19 mag corresponds to the bolometric luminosity of 4×10^{43} erg s^{-1}, which is 10^9 times greater than the Sun.

SNe Ia do not show any presence of H in their spectra, except for possible contamination from superposed circumstellar matter (CSM, so-called SNe Ia-CSM or SNe Ian, Hamuy et al. 2003). The lines are broad due to the high ejecta velocity. SNe Ia are characterized by a deep absorption trough around 6150 Å produced by blueshifted absorption associated with Si II 6347 Å, 6371 Å lines (collectively called 6355 Å, Filippenko 1997). This feature is highlighted in Figure 1.4.

One of the most important distinguishing features of SNe Ia is a homogeneity of their LCs after maximum. When enough observational data have been collected, it became obvious that SNe Ia can be accurately used as 'standard candles' to measure the distances in the Universe. However, in reality their light curves, though very similar, differ between each other. Moreover, some objects show '1991bg'-like behavior, which are typically ~2 mag fainter and decline faster than standard SNe Ia. Others, like SN Ia 1991T, have greater maximum brightness and slower decline rates. Rarer members are in the subclass of peculiar SN Type Iax with the range of V-band peak absolute magnitudes $-14.2 \geq M_{V,\,\mathrm{peak}} \geq -18.9$ mag.

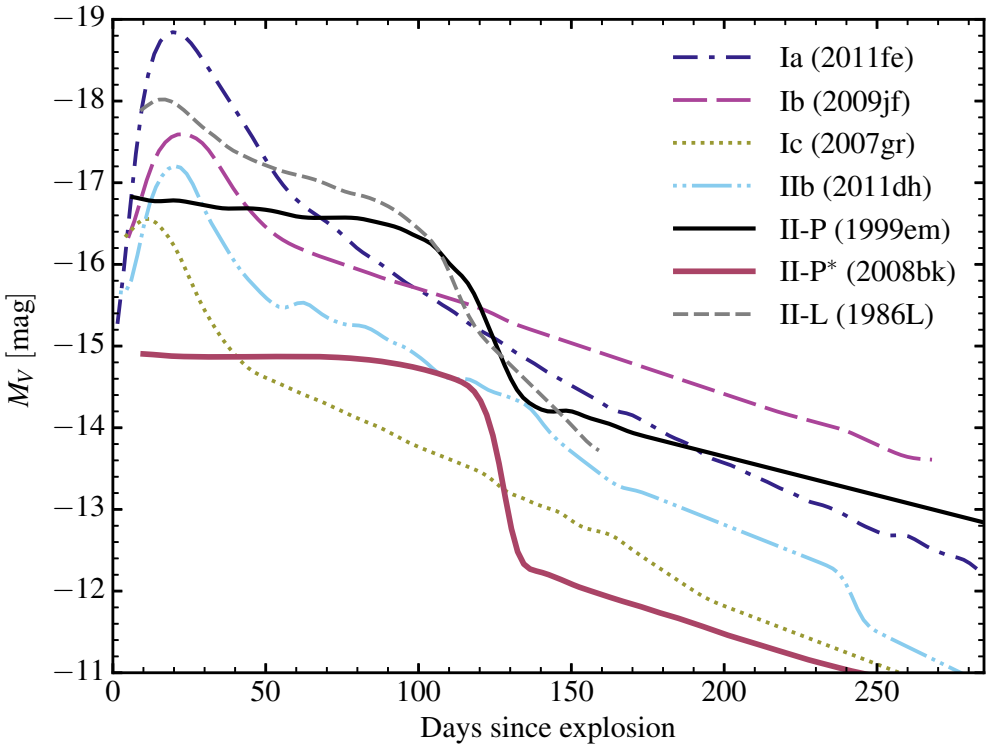

Figure 1.3 – Comparison of V-band light curves for different types of SNe. The 'II-P*' label corresponds to low-luminosity SNe II-P.

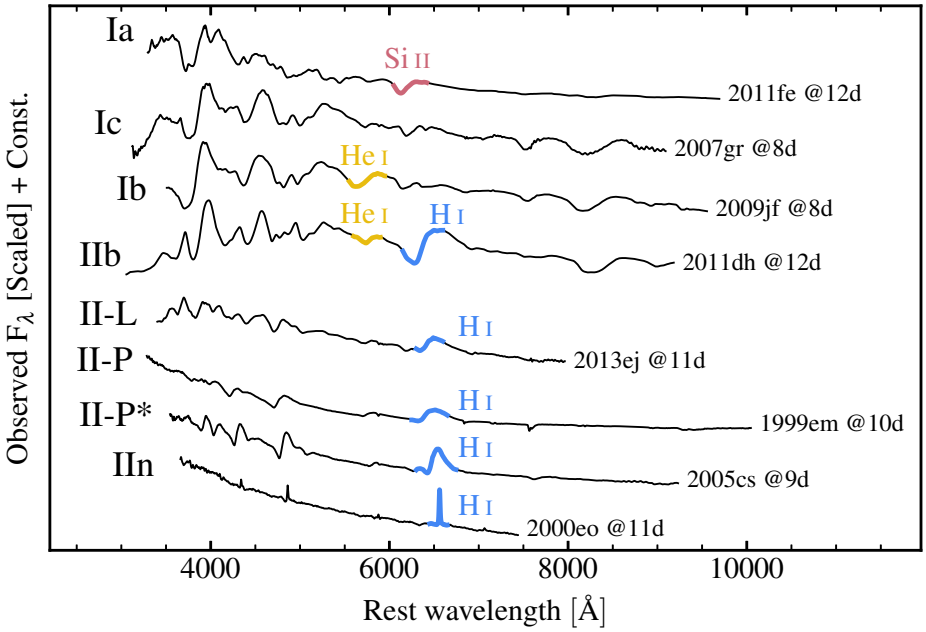

Figure 1.4 – Spectral montage of different SNe types at around one-two weeks since explosion. Some distinctive lines are highlighted with color. For SNe Ic, the distinctive feature is an absence of H, He and Si lines, so nothing is highlighted. The line with the absorption maximum near 5735 Å for SN Ic is the Na line. II-P* refers to low luminosity Type II-P SN. See Figure A.2 for evolved spectra at around 40 days since explosion.

And still, SNe Ia nowadays are known to be the 'standardizable candles' (peculiar 1991bg and 1991T-like objects are excluded for cosmological analysis). There are a lot of standardization techniques, and all of them are mainly based on the fact that the higher SN Ia luminosity, the slower its decline rate after the maximum in the LC (stretch correction; Rust 1974; Pskovskii 1977, 1984). Later it was shown that their absolute brightness depends also on the color (color correction; Hamuy et al. 1996; Tripp 1998). These and other more recent studies allowed to perform robust measurements to discover the accelerating expansion of the Universe. For the history of development of SNe Ia standardization techniques see Pruzhinskaya & Lisakov (2016).

As for the physical processes leading to the SN Ia event, it was proposed that they result from thermonuclear explosions of CO WD after exceeding the Chandrasekhar limit (Hoyle & Fowler, 1960). WD is a typical remnant after the evolution of the star with initial mass in the range approximately from 0.5 to 8 $M_\odot$. A characteristic size of the WD is similar to the size of the Earth ($R \sim 10^9$ cm). The mass of the remnant is not high enough to start further nuclear burning of the elements, and hydrostatic equilibrium is preserved by electron degeneracy pressure. It was shown that a limit on the mass of the WD, known today as a Chandrasekhar limit, exists (Anderson 1929; Stoner 1930; Chandrasekhar 1931):

$$M_{\rm Ch} \approx \frac{5.83\,M_\odot}{\mu_e^2} = 1.46\,M_\odot \left(\frac{2}{\mu_e}\right)^2, \tag{1.13}$$

where μ_e is a number of electrons per nucleon. For the elements heavier than He, $\mu_e \geq 2$.

A single-degenerate scenario (e.g., accretion from companion star onto a WD) was proposed by Whelan & Iben (1973) and double-degenerate scenario (coalescence of two WDs) was discussed by Iben & Tutukov (1984). It is an uncovered CO core of the star, left after the loss of H- and He-rich envelopes. There are a few SNe Ia that show strong evidence for the SD scenario, possibly with a RSG companion. Photoionization and subsequent recombination of CSM has been observed in relatively normal SNe Ia (Patat et al., 2007; Blondin et al., 2009; Simon et al., 2009), and CSM has been detected in the spectra of at least 20% of SNe Ia in spiral galaxies (Sternberg et al., 2011) and has been linked to SN Ia explosion properties (Foley et al., 2012). 'Super-Chandrasekhar' mass SNe Ia that are thought to contain $> 1.4\ M_\odot$ of SN ejecta are likely formed from the DD scenario (e.g., Howell et al., 2006; Yamanaka et al., 2009; Scalzo et al., 2010; Silverman et al., 2011; Taubenberger et al., 2011).

1.3.3 Core-collapse SNe

1.3.3.1 Mass loss

Neutrinos deposit a comparable amount of energy into ejecta into most of the CCSNe, but the observational properties differ a lot. The main reason for the difference is a chemical composition of the progenitor star just before the collapse of the core and its spatial distribution.

Mass loss is a process by which the gravitationally bound stellar material becomes unbound, so the stellar mass is reduced by losing the outer shells. Early-type stars have high mass-loss rates, which substantially affects their evolution (Vink et al., 2000). Stars that would eventually explode as CCSNe, i.e. stars with initial mass $M_{\rm i} > 8\ M_\odot$, normally belong to spectral class O or B during their evolution on the main sequence.

During the first ~90% of lifetime massive stars evolve slowly, converting H into He. The radius of the star is relatively small and the outer layers have high binding energy. Mass loss rates ($\frac{dM}{dt} \equiv \dot{M}$) for supergiants with masses from 10 to 30 $M_\odot$ and effective temperatures $30\,000 \leq T_{\rm eff} \leq 50\,000$ K, calculated by Vink et al. (2000), lie in the range from 10^{-8} to

10^{-5} $M_\odot$/yr. Once the H is exhausted in the core, stellar evolution becomes much more rapid. Star will typically experience a series of contractions and expansions, but the overall trend is that the radius of the star increases significantly, so the outer envelope becomes less bound to the star. Normally, the largest fraction of the mass is lost after the main sequence. Mass loss of RSG is important for the evolution of massive stars, but is not fully explained. An important parametrization for estimating $\dot{M}$ as a function of basic stellar characteristics (i.e. $M, L, T_{\rm eff}$) is the empirical law built by de Jager et al. (1988). Mauron & Josselin (2011) confirmed the de Jager prescription at solar metallicity and suggest to apply a $(Z/Z_\odot)^{0.7}$ dependence (but see Figure 1 from Meynet et al. 2015, which shows large discrepancies between the simulated mass-loss rates and those deduced from spectroscopy by different authors. This suggests that the RSG mass loss rates can cover 2–3 orders of magnitude for a given stellar luminosity. This makes the calibration of $\dot{M}$ vs. L highly uncertain).

RSG are H-rich stars known as progenitors of H-rich Type II SNe. Mass loss becomes generally more important for more massive stars, and H-deficient Wolf-Rayet stars are the best candidates for progenitors of SNe Ib/c. The most popular prescriptions for their mass loss rates are given by Nugis & Lamers (2000). These rates, however, have difficulties in explaining the luminosity distribution of WR stars of WC and WO types and the SN Ic progenitor properties. WR stars have high mass loss rates ($\dot{M} \gtrsim 10^{-5}$ $M_\odot$/yr) and their evolution is heavily dependent on mass loss (Yoon, 2017).

The relation between the initial and final masses of the star is not linear and depends on many factors, such as metallicity and rotational velocity. Moreover, starting from the initial mass of ~20 $M_\odot$, the final mass decreases, since the stellar wind becomes very efficient for high-mass stars. For instance, 40 $M_\odot$ star would normally evolve to a less massive SN progenitor than a 15 $M_\odot$ star, but these progenitors would be very different: 40 $M_\odot$ star ends its life as exposed massive CO core without H- and He-rich layers, whereas the 15 $M_\odot$ star evolves to a H-rich progenitor with compact and relatively light CO core. Hence it is considered that the SNe of different types stem from progenitors of different masses. Initially massive stars explode as SN Ic, intermediate-mass stars explode as SN Ib, and low-mass stars explode as SN II. In Chapter 5 we will compare progenitors simulations of 12, 25 and 27 $M_\odot$ in details to emphasize this point.

Type II-L, II-P and IIb SNe are also thought to be dependent on the initial mass of their progenitors. The long V-band plateau of SNe II-P is explained by the massive H-rich envelope, and Type II SNe that show a fast declining V-band LC likely arise from RSG progenitors that have a lower H-rich envelope mass (Bartunov & Blinnikov, 1992; Moriya et al., 2016). One can summarize the present knowledge of the progenitors for different types of SNe in the Table 1.1.

1.3.3.2 Red supergiants

Once a star has undergone the evolutionary stages described above, the pre-explosion progenitor is formed. It could be a star with a final radius from ~1 to ~1000 $R_\odot$, with or without H- and He-rich layers. The most common types of core-collapse SNe are II-P/L (~60% of all CCSNe, Smartt et al. 2009), which arise from the explosions of very extended (R from ~200 to ~1000 $R_\odot$) red supergiant (RSG) stars. These progenitors are sometimes identified in the pre-explosion photometric observations.

When the progenitor is identified in the archival images, it is possible to measure its color and to deduce the temperature (correcting for the reddening). Then, using the distance measurements to the host galaxy, one can derive the absolute luminosity of the pre-SN star. These estimates are generally robust enough, though Davies et al. (2018) argue that the higher reddening in higher mass RSG stars introduces a strong bias in the inference of the progenitor mass (causing an underestimate). Finally, based on theoretical stellar evolutionary tracks, one can estimate the

Table 1.1 – A summary of the present knowledge on the progenitors of different types of SNe. Only single star evolution scenarios are considered except for II-pec SNe, which are believed to stem mainly from binary systems. WD stands for a white dwarf, LBV stands for a luminous blue variable, BSG stands for a blue supergiant star, YSG stands for a yellow supergiant star, WR stands for a Wolf-Rayet star, WN stands for a WR star that shows H lines in the spectra, WO stands for a WR star with strong O VI emission lines.

SN type	M_{init} [$M_\odot$]	M_{fin} [$M_\odot$]	R_{fin} [$R_\odot$]	Final class	Reference[1]
Ia	1–8	0.5–1.44	$\lesssim$0.01	WD	P13
Ib (single)	30–40	10–20	$\lesssim$10	WR (WN)	P13
Ic (single)	40–100	5–10	$\lesssim$10	WR, LBV	P13
IIb	25–35	5–15	$\lesssim$10	Y(B)SG	P13
II-pec	—	—	~50	BSG	P13
II-L	15–30	7–20	~500	RSG	P13
II-P	8–20	7–18	$\gtrsim$500	RSG	P13, S09
IIn	—	—	—	RSG in CSM	S14
PISN	$\gtrsim$140	—	—	WO, LBV	K17, G17

[1] G17: Gilmer et al. (2017), K17: Kozyreva et al. (2017), P13: Piro & Nakar (2013), S09: Smartt et al. (2009), S14: Smith (2014).

initial and final mass of the progenitor. These latter properties are subject to higher uncertainties, since mass loss rate, rotation speed, metallicity, mixing parameters are unknown; even the presence of a companion stars could not be established. The estimates of the initial mass based on the determined pre-SN L and $T_{\rm eff}$ are quite homogeneous throughout the literature. However, robust identification of progenitor is rare.

We list the identified progenitors for CCSNe in Table 1.2. Most of the progenitors for SN II are found to be RSG. Sometimes, YSGs are identified as SN II progenitors (e.g., Maund et al. 2011).

The analysis of explosion sites of SNe 2008cn, 2009kr and 2009md (Maund et al., 2015) suggests that these identifications are most likely mistaken due to low-resolution pre-explosion images, when it is difficult to distinguish between a single star and a compact cluster. This also might be a problem for a large fraction of other progenitor identifications.

Almost all SNe except for Type Ia (thermonuclear runaway) are core-collapse SNe[10]. There are also some rare events and proposed SNe models, such as pair-instability (which are for the most are not core collapse and do not stem from the progenitors with degenerate core), magnetar-powered, jet-driven SNe. They will be discussed in Section 1.3.4.

The energy source for core-collapse SNe is different from thermonuclear SNe. As the name suggests, the source of energy is the collapse of the core. The core ends its life through a collapse after the evolution of a star more massive than ~8 $M_\odot$. Initial mass function predicts about 3 out of 1000 stars to be more massive than 8 $M_\odot$ (Kroupa, 2001). A typical core-collapse SN releases 10^{53} erg as neutrinos, of which about 1% is deposited in the ejected material and appears as kinetic energy. Less than 0.01% of the total energy is released as photons.

[10] Explosion physics for SNe IIn may be distinct, e.g., pair instability (Woosley et al., 2007a).

Table 1.2 – Direct SN progenitor detections to date (adopted from Van Dyk, 2017). SNe, progenitors of which are confirmed to vanish, are marked with †. Strikethrough text corresponds to the SNe which progenitors were identified, but were later found not to be.

SN	Type	Reference
1961V †	IIn?	Bertola (1964); Zwicky (1964)
1978K	IIn	Ryder et al. (1993)
1987A †	II-P (pec)	White & Malin (1987); Gilmozzi et al. (1987); Sonneborn et al. (1987)
1993J †	IIb	Aldering et al. (1994); Cohen et al. (1995)
1996al	II-L?	Benetti et al. (2016)
1997bs †	IIn?	Van Dyk et al. (2000)
1999ev	II-P?	Van Dyk et al. (2003a); Maund & Smartt (2005); Maund et al. (2014b)
2003gd †	II-P	Van Dyk et al. (2003b); Smartt et al. (2004)
2004A †	II-P	Hendry et al. (2006a)
2004et †	II-P	Li et al. (2005); Crockett et al. (2011)
2005cs †	II-P	Maund et al. (2005); Li et al. (2006)
2005gl †	IIn	Gal-Yam et al. (2007); Gal-Yam & Leonard (2009)
2006my †	II-P	Maund et al. (2014b); Li et al. (2007); Leonard et al. (2008)
~~2006ov~~	II-P	Li et al. (2007); Crockett et al. (2011)
2008ax †	IIb	Crockett et al. (2008)
2008bk †	II-P	Mattila et al. (2008); Van Dyk et al. (2012a); Maund et al. (2014a)
2008cn †	II-P	Elias-Rosa et al. (2009); Maund et al. (2015)
2009hd	II-L?	Elias-Rosa et al. (2011)
2009ib	II-P	Takáts et al. (2015)
2009ip	IIn?	Smith et al. (2010); Foley et al. (2011)
~~2009kr~~	II-L?	Fraser et al. (2010); Elias-Rosa et al. (2010); Maund et al. (2015)
~~2009md~~	II-P	Fraser et al. (2011); Maund et al. (2015)
2011dh †	IIb	Maund et al. (2011); Van Dyk et al. (2011)
2012A	II-P	Prieto et al. (2012); Tomasella et al. (2013)
2012aw †	II-P	Van Dyk et al. (2012b); Fraser et al. (2012)
2012ec	II-P	Maund et al. (2013)
2013df	IIb	Van Dyk et al. (2014)
2013ej †	II-L?	Fraser et al. (2014)
iPTF13bvn †	Ib	Cao et al. (2013)
2014C	Ib/IIn	Milisavljevic et al. (2015)
ASASSN-14ha	II-P	Van Dyk (2017)
2015bh	IIn	Elias-Rosa et al. (2016); Thöne et al. (2017)
2016bkv	IIn?	Van Dyk (2017)
2016gkg	IIb	Tartaglia et al. (2017); Kilpatrick et al. (2017)

1.3.3.3 Type II-P/L SNe

SNe II arise from stars with initial masses from approximately 8 to 30 $M_{\odot}$, which die as a RSG star (Woosley & Weaver, 1995; Heger et al., 2003; Limongi & Chieffi, 2003; Eldridge & Tout, 2004; Hirschi et al., 2004). Historically, Type II SNe were divided into Type II-P (plateau) and Type II-L (linear) subtypes based on their light curve behavior (Barbon et al., 1979). During a long time it was unclear whether these subtypes represented two physically different populations or if there is a smooth transition between them. Recently, large samples of SNe II by Anderson et al. (2014a) and Sanders et al. (2015) revealed a continuity in light curve slopes of Type II SNe. SNe from progenitors that kept a sufficient amount of hydrogen in the envelope, produce a 'plateau' in the V-band light curve (LC) for 3–4 months after explosion and show the prominent H I lines in their spectra. The plateau duration is controlled by the mass of the hydrogen-rich (H-rich) envelope, the energy of explosion, ^{56}Ni mass and the final radius of the progenitor (e.g., Grassberg et al., 1971; Falk & Arnett, 1977; Litvinova & Nadezhin, 1983; Swartz et al., 1991; Popov, 1993).

1.3.3.4 Type IIb SNe

Some SNe initially show H lines in their spectra but it vanishes after a few weeks (see e.g., Filippenko, 1997). A well observed example is SN 1993J. A number of groups concluded that the progenitor of SN 1993J had low-mass H envelope (Nomoto et al., 1993; Podsiadlowski et al., 1993; Utrobin, 1994; Bartunov et al., 1994; Woosley et al., 1994).

1.3.3.5 Type Ibc SNe

Some SNe does not show H lines at all. If they are He-rich, they are classified as Type Ib SNe, otherwise Type Ic SNe. In fact, it is often difficult to distinguish between these two types and they are often referred to as SNe Ibc or Ib/c (e.g., Filippenko, 1997).

Type Ib/c SNe along with SNe IIb are sometimes called 'stripped-envelope' SNe. As derived from observations and modelling, mass of H-rich envelope decreases in a following sequence of SNe types: II-P – II-L – IIb – Ib – Ic (e.g., Nomoto et al. 1995). In view of mass loss (Section 1.3.3.1), this suggests that the progenitors of SNe of different types has lost different mass of outer H-rich layers. One important possibility of this difference is an initial mass of the progenitor star, second is binarity.

1.3.4 Other rare SNe types and proposed models

Some SNe do not fit into the presented classification. Below we discuss the diversity of rare types of SNe and possible scenarios of their origins.

1.3.4.1 SNe Type Ibn

Some SNe, such as SN 2006jc, show prominent He lines, similar to Type Ib SNe, although with narrow emission lines, similar to Type IIn SNe. These CSM-interacting stripped-envelope SNe are now referred to as SNe Ibn (Pastorello et al., 2008).

1.3.4.2 SNe Type IIc

In simulations of Dessart et al. (2012), some models show H at early times (produced by non-LTE effects alone, see Dessart et al. 2011), followed by the absence of He I lines as in Type Ic

SNe. Such objects, which could be referred to as Type IIc SNe, have never been identified with confidence (but see Branch et al. 2006 for a possible identification of Hα in the Type Ic SN 1994I).

However, Type Ib/c SNe are rarely captured at a few days since explosions, so the absence of the observed Type IIc SNe may just be a bias of observational campaigns. In view of simulations from Dessart et al. (2012), a Type IIc classification could be explained as stemming from a progenitor with both H and He, the former being underabundant but easily seen, and the latter arbitrarily abundant but quickly invisible in the absence of non-thermal excitation (Dessart et al., 2011).

1.3.4.3 Peculiar Type II SNe

Some H-rich SNe, such as 1987A (Catchpole et al., 1987; Menzies et al., 1987), may stem from BSG progenitors rather than from RSG progenitors, do not show II-L or II-P like luminosity evolution and referred to as 'peculiar' or Type II-pec (e.g., Langer 1991). It is now generally believed that this kind of behavior for SN 1987A and other representatives of Type II-pec can be explained by the interaction of members in close binary systems (e.g., Podsiadlowski 1992; Menon & Heger 2017). In fact, almost all massive stars are members of binary (or multiple) systems (Sana et al., 2012), and this can partially help to explain the diversity of all SNe explosions.

1.3.4.4 SN impostors

There is a class of objects that sometimes has been classified as genuine SN, but their observational properties point to the fact that the 'progenitor' may still be alive (e.g., 1961V). For such objects, the late-time decline rate is slower than ^{56}Co decay and the expansion rate is small ($\sim$1000 km s^{-1}). These events are labeled as 'SN impostors' and thought to stem from the luminous outbursts of extragalactic LBV stars that may mimic the behavior of a real, although very faint, SN. SN impostors may eventually undergo a terminal explosion as may have occurred for the very peculiar SN 2009ip (Drake et al., 2010).

1.3.4.5 Super-luminous SNe

SNe with absolute magnitude brighter than ~ -21 mag, i.e. 10–100 times brighter than standard SNe, sometimes are called super-luminous SNe (SLSNe). They are sometimes divided into H-poor SLSN-I, H-rich SLSN-II, and radioactively powered SLSN-R (Gal-Yam, 2012)[11]. Up to mid-2017, few dozens of SLSNe have been observed (e.g., Yu et al. 2017 study LCs of 31 SLSNe). The energy sources of SLSNe are not clearly understood.

For the SLSN-R type, the observations indicate that unusually large amount of ^{56}Ni — several solar masses — is expelled. The energy source for such objects could be a collapse of the iron core as in usual CCSNe but with greater energy release (e.g., Moriya et al. 2010), or the pair-instability mechanism (see next section).

For SLSN-II explosion mechanism, two main options are: (1) powerful outward shock wave in the very large progenitor and (2) interaction between the expanding ejecta and massive CSM generated by the progenitor.

SLSN-I explosions are generally of Type Ic, because they also do not show He lines in the spectra. However, SNe Ic luminosity is dominated by ^{56}Ni decay, so there is a correlation between the amount of ejected ^{56}Ni and peak luminosity. No such correlation is observed for SLSN-I. Type Ic SNe arise from progenitors with radii of $< 10^{11}$ cm, whereas it has been shown

[11] This classification is not flawless since relies on a model of the explosion.

that the energy radiated by SLSNe-I must have been deposited at large initial radii of $\sim 10^{15}$ cm (Quimby et al., 2011). These properties may be explained through various options, including interaction with expanding shells of H-free material (Chevalier & Irwin, 2011), perhaps ejected by the pulsational pair instability (e.g., Woosley 2010), or re-emission of energy injected by an internal engine, such as magnetar spin-down (Woosley, 2010; Kasen & Bildsten, 2010) or a 'collapsar'-like accreting BH (e.g., Quimby et al. 2007; Pastorello et al. 2010; Chomiuk et al. 2011; Leloudas et al. 2012).

1.3.4.6 Pair-instability SNe

For very massive stars with O-core mass of ~ 50 $M_\odot$ and more, high temperatures in the core are reached at relatively low densities. Barkat et al. (1967) and Rakavy & Shaviv (1967) proposed a pair-instability supernova (PISN) mechanism for very massive stars. Stars that are sufficiently massive for the production of $e^- e^+$ pairs from γ-ray annihilation would successively go through an implosion, a thermonuclear runaway, and an explosion without forming a remnant (for very massive stars, there are various scenarios. Only a certain mass range should lead to PISN). Some studies suggested that some of SLSNe could be attributed to PISNe, e.g. SNe 2006gy and 2007bi (Smith et al., 2007; Gal-Yam et al., 2009). However, this is no longer widely supported. For instance, recent modelling of such explosion suggests that PISNe are yet to be discovered (Dessart et al., 2013a; Jerkstrand et al., 2017).

1.3.4.7 GRB-associated Type Ic-BL SNe

SNe explosions are sometimes associated with gamma-ray bursts (GRB). GRBs are isotropically distributed in the sky, short ($\sim$seconds) intense flashes of electromagnetic radiation with typical photon energies ~ 100 keV. GRBs are believed to result from some small amount of matter accelerated in a collimated beam to ultra-relativistic speeds. The total kinetic energy of a typical GRB corrected for the beaming is $\sim 10^{51}$ erg, i.e. of the same order of magnitude as for SNe.

After the GRB, the optical emission of the object (so-called 'afterglow') will develop. Afterglow emerges because of the interaction between the relativistic material with surrounding medium. Unfortunately, γ-ray telescopes cannot localize the direction to the source better than within an error box of tens of square degrees, and it is not possible to immediately start a follow-up in the optical with big telescopes. First, the localization from other surveys is needed. But when observed, the afterglow is a long-lasting rapidly declining emission in optical, γ-rays and radio. Sometimes, in several weeks to month the bump in R-band is visible. It is usually interpreted as the underlying SN emission (e.g., Piran 2004). After correcting for the afterglow, observers obtain SNe light curves. For today, around $\sim$40 SN-GRB pairs have been observed (Cano et al., 2017). For such SNe, a typical marker is the broad lines in the spectra, indicating high velocities of expansion. SNe of this type are subclassified as Type Ic-BL (broad line) SNe. However, this designation stems from the observational properties only, and SN could be attributed to this type whether it is associated with GRB or not. A label of 'hypernova' is sometimes used to refer to GRB-SNe (Woosley & Bloom, 2006).

The models of GRB central engines must not only explain the total energy release, but also the mechanism of matter collimation. The most successful models are the millisecond magnetar model, where the energy source for GRBs is the rotation of a highly magnetized NS with an initial period of about one millisecond (e.g., Wheeler et al. 2000; Lyutikov & Blackman 2001), and collapsars (e.g., Woosley 1993; MacFadyen & Woosley 1999). Generally it is agreed that our understanding of the physics of GRBs needs further work.

1.4 The need to better understand the diversity of CCSNe

The physics that drive the diversity of SNe is not clearly understood. For instance, recent studies of large SNe II samples have not shown two separate populations for SNe II-P and II-L. Instead, a smooth transition between these two types has been revealed (Anderson et al. 2014a; Sanders et al. 2015, see Chapter 3 for details; we also address this question in Chapters 4 and 5). With this work, we make our contribution to the problem of CCSNe diversity origins.

Chapter 2

Supernova modelling

2.1 1-D stellar evolution with MESA

Modules for Experiments in Stellar Astrophysics (MESA) is a suite of open source, robust, efficient, thread-safe libraries for a wide range of applications in computational stellar astrophysics (Paxton et al., 2011, 2013, 2015, 2018). MESA Star module is a one-dimensional stellar evolution module of MESA allowing to perform numerical simulations with wide range of input parameters, solving the fully coupled structure and composition equations simultaneously.

In contrast to codes in the radiative transfer community, the different codes in stellar evolution (e.g., KEPLER, GENEC) have much more in common, since they solve more or less the same equations. Differences are fewer, like nuclear networks or possibility to model binary stars.

2.1.1 13–25 $M_\odot$ model grid

In this section, we present a suite of models computed with MESA from the main sequence until core collapse. Main sequence temperatures, mass loss rates, amount of lost mass on different stages of evolution, and other properties for our set of models are presented in Table 2.1.

The diagram of Hertzsprung–Russell for seven models with initial mass in the range from 13 to 25 $M_\odot$ is shown in Figure 2.1. Lower-mass model shows typical stages of evolution. H burning occurs between the points 1 and 2 and lasts roughly 90% of the time for any model (~14 Myr for 13 $M_\odot$ model). The evolution between points 2 and 3 corresponds to the overall contraction of

Table 2.1 – Summary of the progenitor properties for our set of MESA models. 'MS' subscript or superscript corresponds to properties of the MS evolution. E.g., $T_\star^{\rm MS}$ is an effective temperature roughly in the middle of the MS; $dM_{\rm MS}$ is a mass, lost during the MS; $\dot{M}_{\rm MS}$ is a mean mass loss rate during the MS. '>MS' subscript corresponds to properties after the MS evolution. Other properties correspond to the time at the onset of core collapse. Numbers in parentheses correspond to powers of ten.

Model	Z	$T_\star^{\rm MS}$ [K]	$dM_{\rm MS}$ [$M_\odot$]	$\dot{M}_{\rm MS}$ [$M_\odot$/yr]	$dM_{>\rm MS}$ [$M_\odot$]	$\dot{M}_{>\rm MS}$ [$M_\odot$/yr]	$T_\star$ [K]	$L_\star$ [$L_\odot$]	$R_\star$ [$R_\odot$]	$M_\star$ [$M_\odot$]	He-core [$M_\odot$]	Burning time [10^6 yr] H	He
13 $M_\odot$	0.02	26 964	0.55	4.0(−8)	1.3	7.9(−7)	3965	58 020	511	11.1	3.5	13.7	1.64
15 $M_\odot$	0.02	28 772	0.70	6.2(−8)	2.4	1.9(−6)	3873	83 978	644	11.9	4.4	11.3	1.24
17 $M_\odot$	0.02	30 294	0.91	9.4(−8)	1.9	1.7(−6)	3912	108 157	717	14.2	5.1	9.6	1.09
19 $M_\odot$	0.02	31 612	1.20	1.4(−7)	4.2	4.6(−6)	3852	127 645	803	13.6	5.8	8.5	0.89
21 $M_\odot$	0.02	32 734	1.56	2.0(−7)	11	1.3(−5)	3873	188 282	965	8.6	6.8	7.6	0.85
23 $M_\odot$	0.02	33 717	2.02	2.9(−7)	13	1.7(−5)	4527	222 996	769	8.1	7.9	7.0	0.73
25 $M_\odot$	0.02	34 569	2.08	3.2(−7)	14	2.0(−5)	5186	251 153	622	8.6	8.5	6.5	0.67

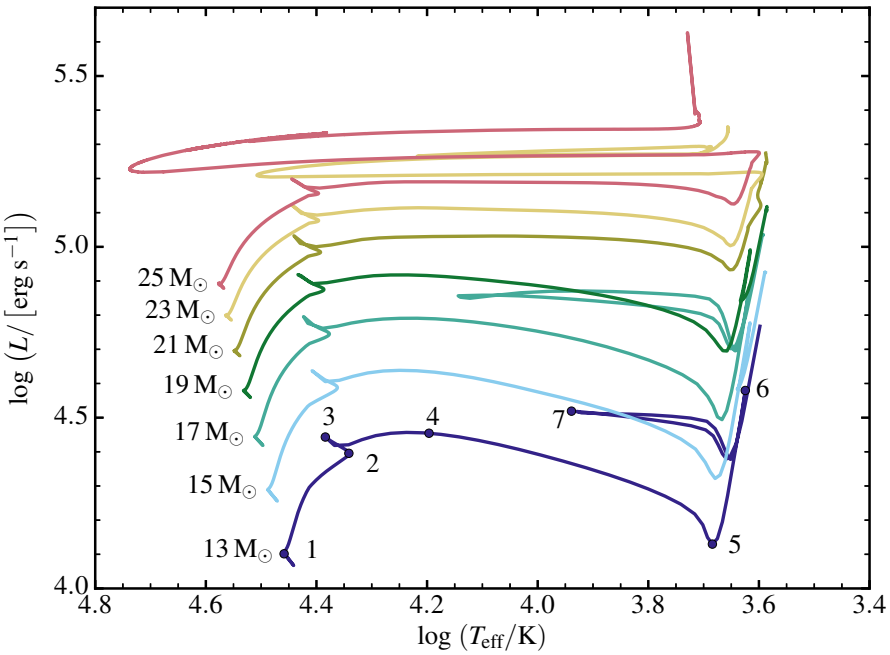

Figure 2.1 – Hertzsprung–Russell diagram for 13–25 $M_\odot$ model grid. The line corresponding to the evolution of 13 $M_\odot$ model is marked with numbers, corresponding stages of the evolution are described in text.

the star. The pressure and the temperature in the He core and the H-rich layer around it increases. At point 3, H ignites in the shell around the He core. At point 4, the Schönberg–Chandrasekhar limit is reached and the core begins to contract rapidly, causing the evolution to proceed on much faster Kelvin–Helmholtz timescale. The envelope of the star expands owing to the release of the gravitational energy. The effective temperature of the envelope decreases and the star moves right to the red part of the diagram. This evolution stage is known as the subgiant branch (SGB).

It takes only 45 kyr for 13 $M_\odot$ model to evolve from point 4 to point 5. The core continues to contract, and the density and temperature of the H-burning shell increase, and the energy production rate increases rapidly, causing the stellar envelope expansion once again. The expanding envelope absorbs enough energy for a time to cause the luminosity to decrease before recovering (point 5).

Evolution from point 5 ($R \approx 165$ $R_\odot$ for 13 $M_\odot$ model) to point 6 ($R \approx 365$ $R_\odot$) is the RSG phase (60 kyr for 13 $M_\odot$ model). Point 6 in Figure 2.1 corresponds to the moment when the triple-alpha process starts in the core (see Section 1.2.3), making the star move along the so-called horizontal branch. Blueward part of the horizontal branch (from point 6 to point 7) is the period when the He is converted to the C in the core of the star. The turning point (7) corresponds to the time when the mean molecular weight increases to the point when the core begins to contract. At this time, the envelope expands and cools. Shortly after the point (7), the He is exhausted in the core and the CO core is formed. The core contracts akin the rapid evolution across the SGB following the extinction of core H burning.

The density structure of the set of evolved models is shown in Figure 2.2. Bumps in the curves reflect the ‘onion-like’ structure at the onset of core collapse for all models. The least dense part, below 10^{-5} g cm^{-3}, corresponds to the extended outer H-rich layer. For 13–19 $M_\odot$ models, the mass of H-rich layer is 7–8 $M_\odot$, though their He core masses differ significantly

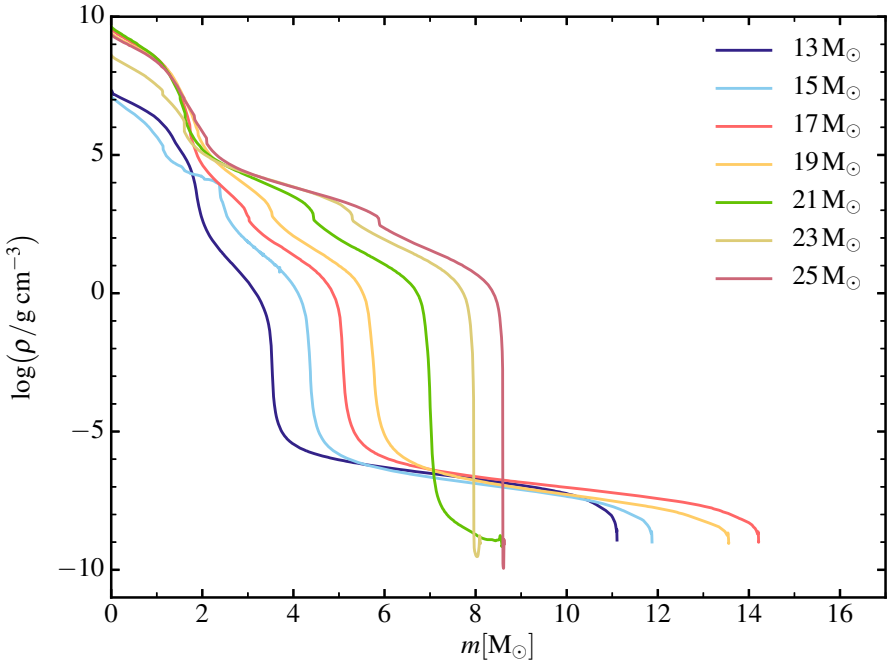

Figure 2.2 – Density structure of the set of models from 13 to 25 $\mathrm{M}_\odot$ by the time near the collapse of the core.

(from 3.5 to 6 $\mathrm{M}_\odot$). This is an important point to keep in mind when only H-rich envelope mass can be constrained. More massive models, 21, 23 and 25 $\mathrm{M}_\odot$, have little or no H-rich envelope.

The radius evolution for 13 $\mathrm{M}_\odot$ model is shown in Figure 2.3. Top panel of the figure shows how the stellar radius changes with time on the H–R diagram. Initial $R_\star$ at zero-age main sequence (ZAMS) is 5 $\mathrm{R}_\odot$ and final radius is 514 $\mathrm{R}_\odot$. After He burning via triple-alpha process starts at 365 $\mathrm{R}_\odot$, the star moves along the horizontal branch. Its radius decreases to 80 $\mathrm{R}_\odot$ as the star gets hotter again.

In Section 1.2, we discussed qualitatively the burning time of different elements. Here, we show results of our modelling in Table 2.1, which are in good agreement with model results from Woosley et al. (2002).

Chemical composition for the 12–25 $\mathrm{M}_\odot$ models is shown in Figure 2.4. The figure demonstrates a cumulative mass fraction for eight species (^{1}H, ^{4}He, ^{12}C, ^{16}O, ^{20}Ne, ^{24}Mg, ^{28}Si, ^{32}S) and the iron core (^{54}Fe, ^{56}Fe, ^{56}Ni and ^{56}Cr). A lot of information can be extracted from the plot. It is visible, for instance, that the size of an iron core varies only slightly with mass. Oxygen-rich layer is constantly growing, from ~0.3 $\mathrm{M}_\odot$ (12 $\mathrm{M}_\odot$ progenitor) to ~4 $\mathrm{M}_\odot$ (25 $\mathrm{M}_\odot$ progenitor). Oxygen mass fraction in the ‘oxygen core’ is around 60%, the rest is the contribution from C, Ne, Mg, Si and S. He core also demonstrates stable mass increase, from 2.6 $\mathrm{M}_\odot$ in the low-mass progenitor to almost 10 $\mathrm{M}_\odot$ in the high-mass progenitor.

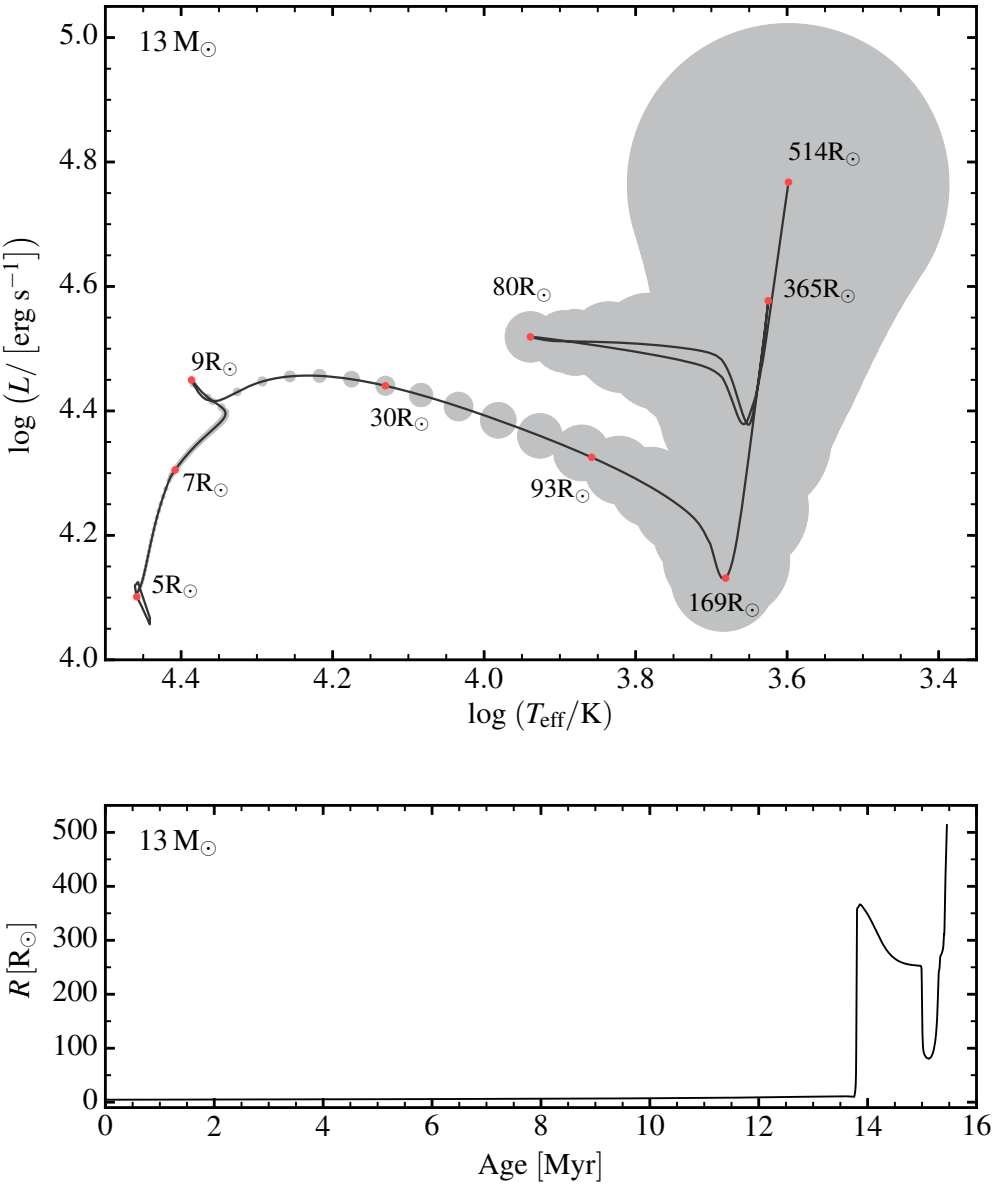

Figure 2.3 – Top: radius versus time evolution of the 13 $M_\odot$ model, shown in the Hertzsprung-Russell diagram. Marker size (gray color) is at any time proportional to the radius of the star at the moment. Bottom: radius versus time evolution. Slow, roughly constant increase in radius (5 to 10 $R_\odot$) from ZAMS to 13.7 Myr (~90% of the lifetime) corresponds to the H burning. Then, evolution of the star occurs on much faster timescale.

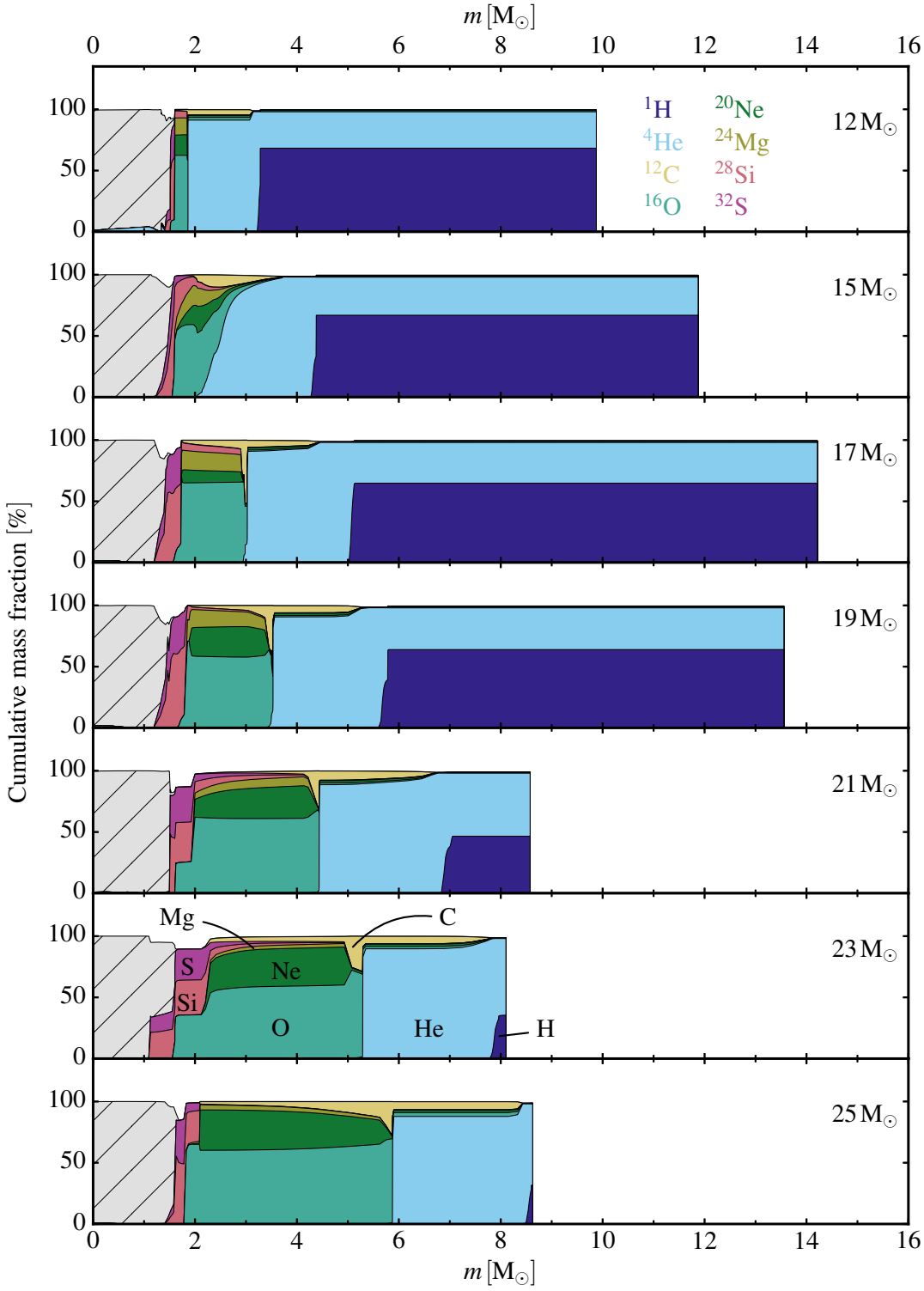

Figure 2.4 – Chemical composition of several models at the time just before the collapse of the core. Hatched light-gray area is used to highlight several species at once: ^{54}Fe, ^{56}Fe, ^{56}Ni, and ^{56}Cr. It corresponds to what is called an 'iron core'. See text for discussion.

2.2 Massive star explosions

2.2.1 Introduction

As discussed above, stellar explosions, leading to a CCSN, stem from the sudden release of energy associated with the collapse of the degenerate core. The development of an explosion includes core collapse, 'bounce', shock emergence, shock propagation through the envelope, shock breakout, and explosion. Each component may be treated differently, which produces a wide range of simulation results. The main feature of the explosion is that a shock crosses the envelope and unbinds it. Nucleosynthesis, fallback and mixing are secondary matters. Paxton et al. (2015) compare results the codes `V1D` (Section 2.2.2) and `MESA` (Section 2.1) produce in propagation of the shock, the properties of the shocked material, and the magnitude of energy conservation errors.

Popular numerical tools for explosion of a massive star in the astronomical community are, for example, the following codes:

- `FLASH` (public hydrodynamical code with explosive nucleosynthesis, Fryxell et al. 2000; Dubey et al. 2009),
- `V1D` (see Section 2.2.2),
- `Super Nu` (multi-group LTE radiative transfer code, Wollaeger et al. 2013; Wollaeger & van Rossum 2014),
- `MCRH` (radiation hydrodynamics code, Noebauer et al. 2012; Noebauer & Sim 2015),
- `SNEC` (The SuperNova Explosion Code, a public spherically-symmetric Lagrangian radiation-hydrodynamics code, Morozova et al. 2015),
- `STELLA` (1-D spherically symmetrical multi-group radiation hydrodynamics code which treats non-equilibrium radiative transfer according to chemical composition and inner structure of a pre-supernova star, Blinnikov et al. 1998, 2006),
- `HERACLES` (3-D hydrodynamical code used to simulate astrophysical fluid flows, González et al. 2007),
- `P-HOTB` (Prometheus-Hot Bubble, 1-D hydrodynamical code, Janka & Mueller 1996; Kifonidis et al. 2003),
- `MESA` (see Section 2.1),
- `KEPLER` (the code is able to model both hydrodynamic evolution phases and the supernova explosion, Weaver et al. 1978; Rauscher et al. 2002; Woosley & Heger 2007).

Most of these codes 'explode' a star by depositing the thermal energy or moving a piston at a some location close to the outer edge of an iron core. This location is within the Si-rich shell, near the base of the O-rich shell (Woosley & Janka, 2005).

In Sukhbold et al. (2016), an innovative treatment of the explosion mechanism is implemented. Two sorts of calculations (both 1-D) of the explosion are carried out for each mass. Iron-core collapse and bounce, neutrino transport, and the propagation of the outgoing shock are followed in one simulation until sufficiently late that the final mass cut and explosion energy have been well determined. This calculation, which includes a high density equation of state and neutrino

transport that captures the essential effects of neutrinos, also gives an estimate of nucleosynthesis, especially for ^{56}Ni. The second calculation tracks the results of the first in a study of detailed nucleosynthesis and radiation transport that gives the bolometric light curve. Pre-SN models in these simulations were exploded with KEPLER and P-HOTB.

2.2.2 Numerical simulations with V1D

The MESA simulations are usually stopped when the maximum infall core velocity reached 1000 km s^{-1}. At that time, we remap the MESA model into V1D (Livne, 1993; Dessart et al., 2010a,b). The model was resampled onto a grid with a mass resolution δm of $10^{-4} - 10^{-3}$ M$_\odot$ at the base, increasing to 10^{-2} M$_\odot$ at and beyond 2 M$_\odot$. Within a few percent of the stellar surface, the mass resolution is progressively increased to have a surface resolution of $10^{-6} - 10^{-5}$ M$_\odot$. At the progenitor surface, we go down to a density of 10^{-12} g cm^{-3} but ideally one should use an even lower value in order to have optically thin shells at the outer boundary where the shock breaks out.

The explosion is in all cases triggered by moving a piston at $\sim 10\,000$ km s^{-1} at the inner boundary, which we place at the location where the entropy rises outward from the center to 4 k$_B$ baryon^{-1} (see, e.g., Ugliano et al. 2012). This location is typically in the outer part of the Si-rich shell, just below the O-rich shell, and located around 1.55 M$_\odot$ in models presented in current work.

The explosion models are done iteratively until we obtained an ejecta with the desired ^{56}Ni mass. Iteration is needed because the ^{56}Ni mass is sensitive to the piston properties (location, speed) and to the magnitude of fallback. The asymptotic ejecta energy also depends on fallback.

In most of our simulations, we enforce a chemical mixing using a boxcar algorithm (see Dessart et al. 2012 for discussion) that affects all species. In Section 4.3.2, we also explore the impact of mixing only ^{56}Ni (and substituting it with H to keep the mass fraction normalized to unity at each depth).

2.2.2.1 Explosive nucleosynthesis

Explosive nuclear burning is often treated in the CCSN simulations (see, e.g., Ugliano et al. 2012; Ertl et al. 2016; Sukhbold et al. 2016; Kozyreva et al. 2017; Janka et al. 2017). In our work, we also calculate explosive nucleosynthesis. In Figure 2.5 we show the chemical stratification and velocity versus mass at $t = 0$ s and at $t = 2$ s after explosion in model m12mlt3du2p5a[12]. In the Si-rich shell, the shock changes the composition to produce some ^{56}Ni and intermediate-mass elements (largely independent of the initial composition).

This means that the heavy elements ($A > 28$) are made primarily by the shock, while below they come primarily from the nuclear burning prior to explosion (the material in the O-rich shell and further out in mass space).

2.2.2.2 Fallback

Fallback is an important component of SN explosions and is often treated in CCSNe simulations (see, e.g., Kasen & Woosley, 2009; Ugliano et al., 2012; Ertl et al., 2016; Sukhbold et al., 2016). As discussed in Section 2.2.2.1 and, e.g., in Kasen & Woosley (2009), the fallback amount (along with the piston location) is an important factor for the final ejection of ^{56}Ni, which is primarily produced in the explosive nuclear burning.

[12] The model is discussed in Chapter 4 (name X) and Chapter 5 (name m12). See Table 4.1 for details on progenitor properties and Table 4.2 for details on ejecta properties.

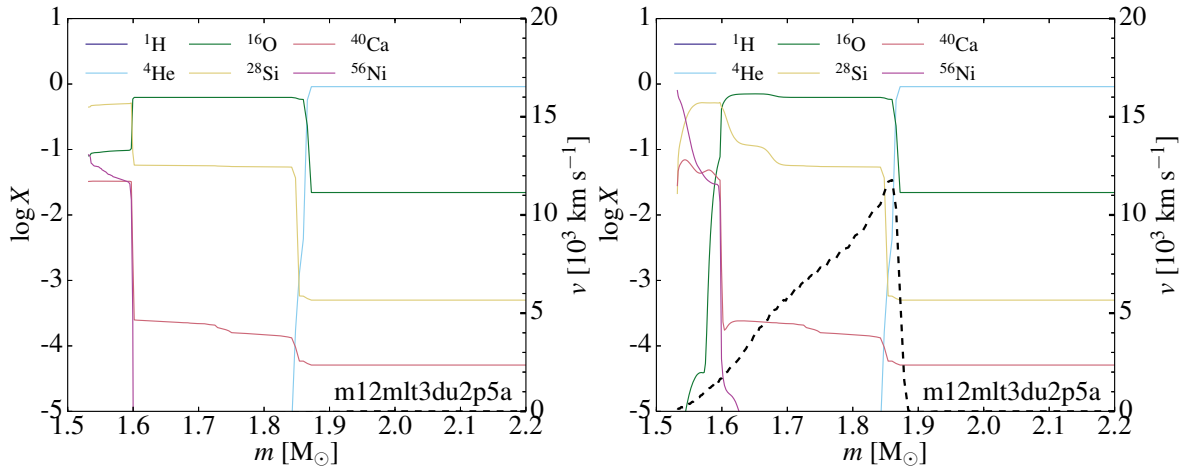

Figure 2.5 – Chemical stratification versus mass at moments $t = 0$ (left panel) and 2 seconds since the piston was triggered (right panel). Dashed line shows the velocity distribution (right axis).

Because the explosion energy is low in our models aimed to match SN 2008bk (see Chapter 4), some fallback of the order of 0.01 M$_\odot$ may occur.

Fallback is an important issue for our models m25 and m27 (discussed in Chapter 5). Explosion energy is relatively low (4.2×10^{50} erg for both models), and the mass on the onset of core collapse is rather high (15.6 and 12.8 M$_\odot$). As a result, no ^{56}Ni is expelled, which is an interesting result (see Section 5.5 for discussion).

2.2.2.3 Mixing

Another important constituent of the SN explosion physics is mixing, discussed in details in, e.g., Kifonidis et al. (2000, 2003, 2006); Wongwathanarat et al. (2015). For mixing, we use two approaches that are crude representations of the process of mixing as simulated in core-collapse SNe (Fryxell et al., 1991; Wongwathanarat et al., 2015). In the first approach, we step through each ejecta mass shell m_i and mix all mass shells within the range $[m_i, m_i + \delta m]$ with $\delta m = 0.4$ M$_\odot$ — this is the usual way we proceed (Dessart et al., 2012). The advantage is that it is straightforward to implement. This mixing is carried out during the `V1D` simulation, at 10 000 s after the explosion was triggered (and thus about one day before shock breakout). This mixing is both macroscopic (material is shuffled in mass/velocity space) and microscopic (each 1-D/spherical mass shell on the `CMFGEN` grid is homogeneous).

In the second approach only ^{56}Ni is mixed; all other species are essentially left as in the original `MESA` model except for hydrogen. In practice, after mixing ^{56}Ni, regions where the sum of mass fractions is below unity, hydrogen is added, while in regions where the sum of mass fractions is above unity (typically by 1%), all species' mass fractions are scaled so that the total is unity. Both approaches are compared in Section 4.5.3.

2.3 SN radiation modelling: approaches and codes

Present work involves sophisticated numerical simulations of almost the entire life of the star from the main sequence until core collapse and the explosion as a SN. A little percent of studies published in the literature cover the whole chain of events leading to the SN explosion. A lot of studies are dedicated to the stellar evolution alone and do not include calculations of the

ejecta evolution in case of SN explosion. Other studies, on the contrary, start simulations with progenitor models, obtained without stellar evolution, and calculate only ejecta properties and its evolution. The reason why most of the studies do not combine stellar evolution modelling with an explosion and ejecta evolution modelling is that the physics of stellar evolution and of ejecta evolution is very different. One code cannot provide such a vast field of application. The basic point is that different equations are solved. Stellar evolution modelling does not have to treat shocks, which are essential in hydrodynamics of explosions. Similarly, nuclear burning is key for producing a massive star model at death but it is not critical to model the explosion.

In the present work, the approach is to start a simulation with the 1-D stellar evolution with MESA from the main sequence till the core collapse. As a result, we obtain pre-supernova models with different mass, radius, chemical composition, density and temperature distribution. All these parameters are important input data for the explosion, which is performed with V1D code. Starting at post-explosion time of ~ 11 days, when the ejecta reach homologous expansion, we perform the radiative-transfer modelling using the non-Local-Thermodynamic-Equilibrium time-dependent radiative transfer code CMFGEN.

One way to study the impact of the certain input parameter on the resulting ejecta is to explode different pre-supernova models with the same kinetic energy. Note that different pre-supernova models can be obtained from the identical main sequence progenitors, evolved with different prescriptions (e.g., mass loss). The other way is to explode identical pre-SN models with different kinetic energy or to apply different mixing to these explosions. Both ways are used in the present work.

A number of codes is used in the community to calculate the radiative transfer in the expanding ejecta of SN explosion.

2.3.1 STELLA

STELLA (Blinnikov et al., 1998, 2006) is a package of one-dimensional spherically symmetrical multi-group radiation hydrodynamics code which treats non-equilibrium radiative transfer according to chemical composition and inner structure of a pre-supernova star. The code has been used for light curve modelling of different types of SNe: Ia (Blinnikov et al., 2006); Ib/c (Folatelli et al., 2006; Tauris et al., 2013); IIb (Blinnikov et al., 1998); IIn (Chugai et al., 2004); II-P (Baklanov et al., 2005; Tominaga et al., 2009); II-L (Moriya et al., 2016); GRB-associated Type Ic-BL SN (Volnova et al., 2017).

The supernova outburst geometry assumed to be simple as in the empirical method, but the consideration of chemical abundances and distribution of chemical elements inside a pre-supernova star allows to calculate radiative transfer during the explosion and to build physically consistent light curve.

STELLA does not treat nuclear burning so the composition is a mix of the progenitor composition plus some ad hoc prescription for ^{56}Ni production. For SNe Ia, STELLA starts from an existing explosion model (i.e., an ejecta).

STELLA solves the radiative transfer problem using a multi-group approach and treats the gas in LTE with a Saha solver. It computes the emergent radiation at 100–1000 energies, from which multi-band light curves can be extracted. The behavior of the photosphere is computed from the evolution of the ejecta (expansion, ionization, temperature, composition, etc.) Spectra are calculated for every specific time since the explosion allows one to model the multicolor light curves and photospheric velocities of the SN expanding envelope. The calculations take into account the chemical distribution of the elements in the envelope before the explosion, the interaction between the inner layers and the compact core. Modelling with STELLA also makes

it possible to investigate a line-of-sight extinction of the circumburst medium by comparing modelled and observed light curves in various photometric filters.

The results from the STELLA code were found to be in a good agreement with those from other well-known hydro-dynamic codes SEDONA and ARTIS (e.g., Woosley et al., 2007b; Kromer & Sim, 2009; Sim et al., 2010; Kozyreva et al., 2017). A public version of STELLA is included in the latest release of MESA (Paxton et al., 2018) to allow SNe modelling.

2.3.2 SEDONA

The SEDONA (Kasen et al., 2006) code uses a Monte Carlo approach to the multidimensional time-dependent radiative transfer problem in expanding SN atmospheres. Given an arbitrary 3-dimensional ejecta structure (i.e., the density, composition and velocity structure of freely expanding SN material) SEDONA self-consistently calculates the emergent broadband light curves, spectral time-series (in both optical and γ-rays) and polarization spectra from various viewing angles. No free parameters need to be adjusted in the transfer calculations, providing a direct link between multidimensional hydrodynamical explosion models and observations. SEDONA has been used, for example, for modelling of PISNe alongside with STELLA (Kozyreva et al., 2017).

2.3.3 ARTIS

The ARTIS code is a radiative transfer code (Kromer & Sim, 2009), which has been developed for application to SN Ia explosion models. The code is based on a Monte Carlo indivisible packet scheme described by Lucy (2002, 2003, 2005). It uses the same approach as the SEDONA code.

The code is designed to simulate time-dependent, three-dimensional radiation transport in supernova ejecta during the phase of homologous expansion. The optical display of SNe Ia is powered by the energy released in the radioactive decay of isotopes synthesized during the explosion, predominantly ^{56}Ni and its daughter nucleus ^{56}Co. Therefore, the code starts from an initial distribution of ^{56}Ni in the ejecta and then the subsequent radioactive decays are followed. These decays initially give rise to γ-ray photons which, at least for early epochs when the ejecta are optically thick, are rapidly down-scattered and absorbed by photoelectric processes. This heats the ejecta. The subsequent re-emission of ultraviolet, optical and infrared emission by the ejecta is then simulated to obtain spectra and light curves. An important point is that SEDONA, ARTIS, or STELLA do not solve the kinetic equations (also called statistical equilibrium equations).

The code does not assume local thermodynamic equilibrium (LTE) but includes an approximate non-LTE (NLTE) treatment of ionization and a detailed approach to line scattering and fluorescence. ARTIS is capable of building synthetic spectra (using a reasonably large atomic line list $\sim 8 \times 10^6$ lines) and light curves.

2.3.4 PHOENIX

PHOENIX (Hauschildt et al., 1997; Baron & Hauschildt, 1998; Hauschildt & Baron, 1999; Hauschildt et al., 2001) is a general-purpose stellar and planetary atmosphere code. It can calculate atmospheres and spectra of stars all across the HR-diagram including main sequence stars, giants, white dwarfs, stars with winds, τ-Tauri stars, novae, supernovae, brown dwarfs and extrasolar giant planets. One important point to note is that PHOENIX is similar to CMFGEN in that it solves simultaneously the kinetic equations and the radiative transfer.

Using PHOENIX, Knop et al. (2007) modelled the spectral evolution of SN 2003Z, which we included in our sample of low-luminosity SNe II (see Chapter 5).

2.3.5 CMFGEN

In our work, most of the results discussed in detail are produced with the CMFGEN code (Hillier & Miller, 1998; Dessart & Hillier, 2005a, 2008; Hillier & Dessart, 2012; Dessart et al., 2013b). CMFGEN is a non-local-thermodynamic-equilibrium time-dependent radiative-transfer code. The CMFGEN code was initially designed to model the spectra of stars with stellar winds. It groups levels with similar excitation energies and levels together. Departure coefficients within this group are assumed to be identical. Only the departure coefficient of the 'super level' needs to be solved in order to fully specify the populations of the levels within a super level.

Technique When the ejecta reach homologous expansion after explosion with V1D (see Section 2.2), we remap each model into CMFGEN to compute the subsequent evolution of the gas and the radiation until nebular times. The code computes the gas and radiation properties by solving iteratively the statistical equilibrium equations, the gas-energy equation, and the first two moments of the radiative transfer equation. Time-dependent terms are included in all equations. Non-thermal processes and thermal heating associated with radioactive decay are included. For each converged model, the code produces a spectrum with a sub-Å resolution that covers from the far-UV to the far-IR and from which one can extract the bolometric luminosity and various photometric magnitudes. It is thus the same tool that produces multi-band light curves and spectra. We can directly compare the multi-band light curves computed by CMFGEN with the observed ones, constraining the reddening from the color and spectral information.

Numerical setup All time sequences with CMFGEN are started at ~ 11 d. The entire progenitor H-rich envelope is in homologous expansion by then, but not the slow moving He-core material. So, by enforcing homologous expansion, we modify slightly the velocity of the He-core material, i.e. in regions moving with $<$700–800 km s^{-1} (see Figure 4.3). Homology requires that we reset the time to R/V, which causes a shift to an earlier time by ~ 0.5 d. This new time differs from the time elapsed since explosive nucleosynthesis took place, making the ^{56}Ni and ^{56}Co masses incompatible. In practice, the ^{56}Co mass is overestimated by $\sim 10\%$, so the effect is minor. For consistency, we quote for each model an initial ^{56}Ni mass inferred from the ejecta ^{56}Co mass at nebular times.

The CMFGEN simulations use 100 grid points, which are placed to adequately resolve the variations in optical depth. This is an asset over a radiation hydrodynamics code like V1D, which uses a grid tied to the Lagrangian mass. With this choice, our CMFGEN simulations resolve well the (moving) recombination fronts associated with H and He (see Dessart & Hillier 2010).

The numerical setup is comparable to that of Dessart et al. (2013b). We use the same model atoms, with updates to the atomic data (in particular for Fe and Co) as described in Dessart et al. (2014). We treat the following ions: H I, He I–II, C I–IV, N I–III, O I–V, Ne I–III, Na I, Mg I–III, Si I–IV, S I–IV, Ar I–III, K I, Ca I–IV, Sc I–III, Ti II–III, Cr II–IV, Fe I–VI, Co II–VI, and Ni II–VI. See summary of the complete model atom used in our radiative-transfer calculations in Table 2.2.

We include only the radioactive decay from ^{56}Ni and ^{56}Co — no other unstable isotope is considered in the present calculations.

2.4 Radioactive decay power from unstable istopes

SN LCs are different at early times, but become similar after $\sim$150 days since explosion (see Figure 1.3). At that time, LC is powered primarily by the two-step radioactive decay ^{56}Ni$\rightarrow^{56}$Co$\rightarrow^{56}$Fe:

Table 2.2 – Summary of the model atom used in our radiative-transfer calculations. The source of the atomic datasets is given in text. N_f refers to the number of full levels, N_s to the number of super levels, and N_{trans} to the corresponding number of bound-bound transitions. The last column refers to the upper level of a given ion included in our treatment. At the bottom of the table, we give the total number of full levels treated, and the corresponding number of transitions explicitly included.

Species	N_f	N_s	N_{trans}	Upper Level
H I	30	20	435	$n \leq 30$
He I	51	40	374	$n \leq 11$
He II	30	13	435	$n \leq 30$
C I	26	14	120	$n \leq 2s2p^3\ ^3P_0$
C II	26	14	87	$n \leq 2s2s4d^2D_{5/2}$
C III	112	62	891	$n \leq 2s8f^1F^o$
C IV	64	59	1446	$n \leq 30$
N I	104	44	855	$n \leq 5f^2F^o$
N II	41	23	144	$n \leq 2p^3d^1P_1$
O I	51	19	214	$n \leq 2s^22p^3\ ^4S\ 4f\ ^3F_3$
O II	111	30	1157	$n \leq 2s^22p^2\ ^3P\ 4d^2D_{5/2}$
O III	86	50	646	$n \leq 2p^4f^1D$
O IV	72	53	835	$n \leq 2p^2p^3p^2P$
O V	78	41	523	$n \leq 2s5f^1F^o_3$
Na I	71	22	1614	$n \leq 30w2W$
Mg II	65	22	1452	$n \leq 30w2W$
Si II	59	31	354	$n \leq 3s^2\ ^1S\ 7g^2G_{7/2}$
Si III	61	33	310	$n \leq 3s5g^1G^e_4$
Si IV	48	37	405	$n \leq 10f^2F^o$
S II	324	56	8208	$n \leq 3s3p^3\ ^5S\ 4p^6P$
S III	98	48	837	$n \leq 3s3p^2\ ^2D\ 3d\ ^3P$
S IV	67	27	396	$n \leq 3s3p\ ^3P\ 4p^2D_{5/2}$
Ca II	77	21	1736	$n \leq 3p^630w2W$
Ti II	152	37	3134	$n \leq 3d^2\ ^3F\ 5p^4D_{7/2}$
Ti III	206	33	4735	$n \leq 3d^6f^3H^o_6$
Fe II	115	50	1437	$n \leq 3d^6\ ^1G1\ 4sd^2G_{7/2}$
Fe III	477	61	6496	$n \leq 3d^5\ ^4F\ 5s^5F^e_1$
Fe IV	294	51	8068	$n \leq 3d^4\ ^5D\ 4d^4G_{5/2}$
Fe V	191	47	3977	$n \leq 3d^3\ ^4F\ 4d^5F^e_3$
Fe VI	433	44	14103	$n \leq 3p5\ ^2P\ 3d^4\ ^1S\ ^2P^c_{3/2}$
Fe VII	153	29	1753	$n \leq 3p5\ ^2P\ 3d^3\ b^2D\ \ ^1P_1$
Co II	144	34	2088	$n \leq 3d^6\ ^5D\ 4s4p\ ^7D^o_1$
Co III	361	37	10937	$n \leq 3d^6\ ^5D\ 5p^4P_{3/2}$
Co IV	314	37	8684	$n \leq 3d^5\ ^2P\ 4p\ ^3P_1$
Co V	387	32	13605	$n \leq 3d^4\ ^3F\ 4d^2H_{9/2}$
Co VI	323	23	9608	$n \leq 3d^3\ ^2D\ 4d\ ^1S_0$
Co VII	319	31	9096	$n \leq 3p5\ ^2P\ d^4\ ^3F\ ^2D_{3/2}$
Ni V	183	46	3065	$n \leq 3d^5\ ^2D3\ 4p\ ^3F_3$
Ni VI	314	37	9569	$n \leq 3d^4\ ^5D\ 4d^4F_{9/2}$
Ni VII	308	37	9225	$n \leq 3d^3\ ^2D\ 4d\ ^3P_2$
Sc I	72	26	734	$n \leq 3d4s(^3D)5s\ ^2D_{5/2}$
Sc II	85	38	979	$n \leq 3p^63d4f\ ^1P_1$
Sc III	45	33	235	$n \leq 7h\ ^2H_{11/2}$
Ba II	100	38	2514	$n \leq 3s30w\ ^2W$

$$
\begin{aligned}
{}^{56}\mathrm{Ni} &\rightarrow {}^{56}\mathrm{Co} + \gamma + \nu_e \\
{}^{56}\mathrm{Co} &\rightarrow \begin{cases} {}^{56}\mathrm{Fe} + \gamma + \nu_e & (81\%) \\ {}^{56}\mathrm{Fe} + e^{+} + \gamma + \nu_e & (19\%) \end{cases}
\end{aligned}
\tag{2.1}
$$

In ^{56}Ni decay, total energy emitted via gamma photons $Q_\gamma = 1.75$ MeV, total energy of neutrinos $Q_{\nu_e} = 0.41$ MeV. In ^{56}Co decay, total energy emitted via gamma photons $Q_\gamma = 3.61$ MeV, total kinetic energy of positrons $Q_{\mathrm{kin}} = 0.12$ MeV, and total energy of neutrinos $Q_{\nu_e} = 0.84$ MeV. The half-life $T_{1/2}$ of ^{56}Ni is 6.1 days and half-life of ^{56}Co is 77.12 days, and lifetime $\tau_{\mathrm{Ni}} = T_{1/2}/\log(2) = 8.8$ days; $\tau_{\mathrm{Co}} = 111.3$ days.

The number of ^{56}Ni, ^{56}Co, ^{56}Fe nuclides, applied to the ^{56}Ni decay chain, is controlled by the following set of differential equations (Nadyozhin, 1994):

$$
\begin{aligned}
\frac{dN_{\mathrm{Ni}}}{dt} &= -\frac{N_{\mathrm{Ni}}}{\tau_{\mathrm{Ni}}} \\
\frac{dN_{\mathrm{Co}}}{dt} &= \frac{N_{\mathrm{Ni}}}{\tau_{\mathrm{Ni}}} - \frac{N_{\mathrm{Co}}}{\tau_{\mathrm{Co}}} \\
\frac{dN_{\mathrm{Fe}}}{dt} &= \frac{N_{\mathrm{Co}}}{\tau_{\mathrm{Co}}}
\end{aligned}
\tag{2.2}
$$

with the initial conditions $N_{\mathrm{Ni}} = N_{\mathrm{Ni}_0}$, $N_{\mathrm{Co}} = N_{\mathrm{Fe}} = 0$ at $t = 0$. These equations and initial conditions apply to the ^{56}Ni decay chain. In nature, there is some ^{56}Fe initially. Solution of Equation 2.2 gives the following equations for number of nuclides of ^{56}Ni, ^{56}Co, ^{56}Fe as a function of time:

$$
\begin{aligned}
N_{\mathrm{Ni}} &= N_{\mathrm{Ni}_0} e^{(-t/\tau_{Ni})} \\
N_{\mathrm{Co}} &= N_{\mathrm{Ni}_0} \frac{\tau_{\mathrm{Co}}}{\tau_{\mathrm{Co}} - \tau_{\mathrm{Ni}}} \left(e^{(-t/\tau_{Co})} - e^{(-t/\tau_{Ni})} \right) \\
N_{\mathrm{Fe}} &= N_{\mathrm{Ni}_0} \left(1 + \frac{\tau_{\mathrm{Ni}}}{\tau_{\mathrm{Co}} - \tau_{\mathrm{Ni}}} e^{(-t/\tau_{Ni})} - \frac{\tau_{\mathrm{Co}}}{\tau_{\mathrm{Co}} - \tau_{\mathrm{Ni}}} e^{(-t/\tau_{Co})} \right)
\end{aligned}
\tag{2.3}
$$

The total energy production rate of this decay chain is given by:

$$
\epsilon = \left(6.45 \times 10^{43} e^{(-t/\tau_{Ni})} + 1.45 \times 10^{43} e^{(-t/\tau_{Co})} \right) \frac{M_{\mathrm{Ni}}}{M_\odot} \ \mathrm{erg\ s^{-1}} \ (t \text{ in days}) \tag{2.4}
$$

The illustration of Equations 2.3 and 2.4 is presented in Figure 2.6.

^{56}Ni is not the only radioactive isotope produced in the explosion nucleosynthesis, but the most abundant and the most important in therms of influence on the LC during the typical time of observations of SN (~1–2 years). First three to four years after the explosion ^{56}Co and ^{57}Co dominate the energy balance. Modelling predicts that radioactive ^{22}Na, ^{44}Ti, ^{57}Ni and ^{60}Co are also produced in the explosion (e.g, Pinto et al. 1988; Woosley et al. 1989; Timmes et al. 1996). For close SN remnants such as Cas A and SN 1987A, it might be possible to detect some of these decays, especially ^{44}Ti. For SN 1987A, the detection is reported (Jerkstrand et al., 2011; Grebenev et al., 2012).

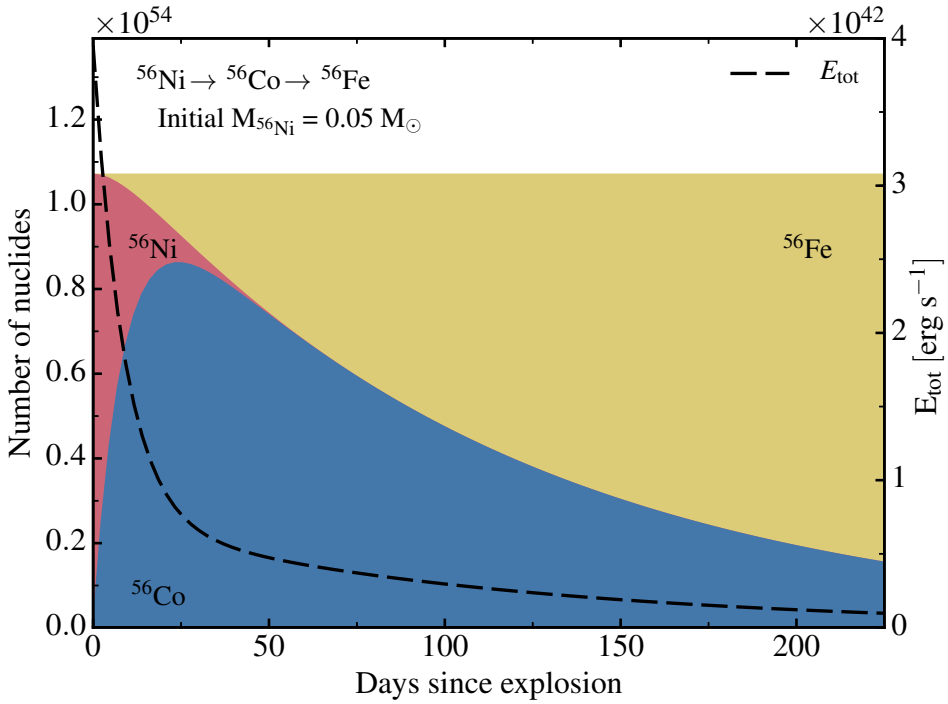

Figure 2.6 – Illustration of ^{56}Ni→^{56}Co→^{56}Fe two-step decay chain. Initial mass of ^{56}Ni is set to 0.05 $M_\odot$, which is a typical amount for Type II-P SNe. The number of ^{56}Ni nuclides, corresponding to this mass, is $N_{^{56}Ni} \approx 1.07 \times 10^{54}$. Cumulative fractions of different nuclides are shown with color. The total number of nuclides ($N_{^{56}Ni} + N_{^{56}Co} + N_{^{56}Fe}$) is constant in the decay process, so there is a horizontal line at $\sim 1.07 \times 10^{54}$ nuclides. It is visible that number of ^{56}Co nuclides increases up to 24 days since the start of decay. Evolution of the total energy production is shown with the dashed black line (the right vertical axis). Starting from about the same time, the energy, released in ^{56}Ni→^{56}Co decay becomes negligible in comparison to that of ^{56}Co→^{56}Fe decay, so the slope of total energy production becomes less steep, since the half-life time for ^{56}Co is longer.

Chapter 3

Observational properties

In present chapter, we describe the observational properties of CCSNe. We also extract the physical properties of the ejecta from the observational data and deduce possible pre-SN and main sequence parameters. In Section 3.1, we discuss observational properties of Type II-P SNe. In Section 3.2, we discuss Type II-L SNe. In Section 3.3, we discuss so-called 'stripped-envelope' SNe, i.e. IIb, Ib and Ic. The data sources are presented in Appendix A. In some cases, we revise the literature values for distance modulus and/or reddening. We discuss photometric and spectral properties for SNe of types II-P, II-L and Ib/c. In Section 3.1 we focus on the subclass of low-luminosity Type II-P SNe.

3.1 Type II-P SNe

According to Graur et al. (2017), the fraction of SN II-P/L in the LOSS volume-limited sample of CC SNe completed out to 60 Mpc is 57.1% in galaxies with stellar masses $> 10^{10}$ $M_{\odot}$.

An absolute magnitude during the 'plateau' phase may vary over a wide range for Type II SNe. Over the last ~20 years a number of faint Type II SNe has been observed. Spectroscopic and photometric observational data for most of these objects and its extensive analysis have been presented in Pastorello et al. (2004) and Spiro et al. (2014). These works emphasize the distinctive features of subluminous Type II SNe such as low expansion rate (approximately in the range from 1300 to 2500 km s^{-1} at the phase of 50 days since explosion), narrow lines in the spectra, small amount of ^{56}Ni produced in the explosion (10^{-3} to 2×10^{-2} $M_{\odot}$, which is 1–2 orders of magnitude less than in standard Type II-P SNe), low-luminosity (pseudo-bolometric luminosity L_{BVRI} ranges from 3.5×10^{40} to 2.8×10^{41} erg s^{-1}) and low kinetic energy of explosion (~0.1×10^{50} to ~0.5×10^{50} erg). The typical plateau duration of low-luminosity SNe II-P is ~110–120 days, which is the same as standard-energy SNe II-P (see Figure 3.1). According to Pastorello et al. (2004), the rate of low-luminosity Type II-P SNe could be 4–5% of all Type II SNe. Due to selection effects, only few low-luminosity SNe events have been observed.

Low-luminosity Type II-P SNe are a very uniform class of CCSNe in terms of the low scatter in main properties, such as the plateau duration, kinetic energy of explosion and spectral evolution.

Two possible explanations of the origin of low-luminosity Type II-P SNe have been proposed in the literature. The first suggests the moderate mass of the progenitor star at the pre-SN stage, since lower-mass massive stars would produce very weak explosion and very little ^{56}Ni. Direct identification of the progenitors of low-luminosity SNe 2005cs and 2008bk in pre-explosion images supports the hypothesis that such events stem from moderate mass progenitors (see Maund et al., 2005; Li et al., 2006 for SN 2005cs; Mattila et al., 2008; Van Dyk et al., 2012a; Maund

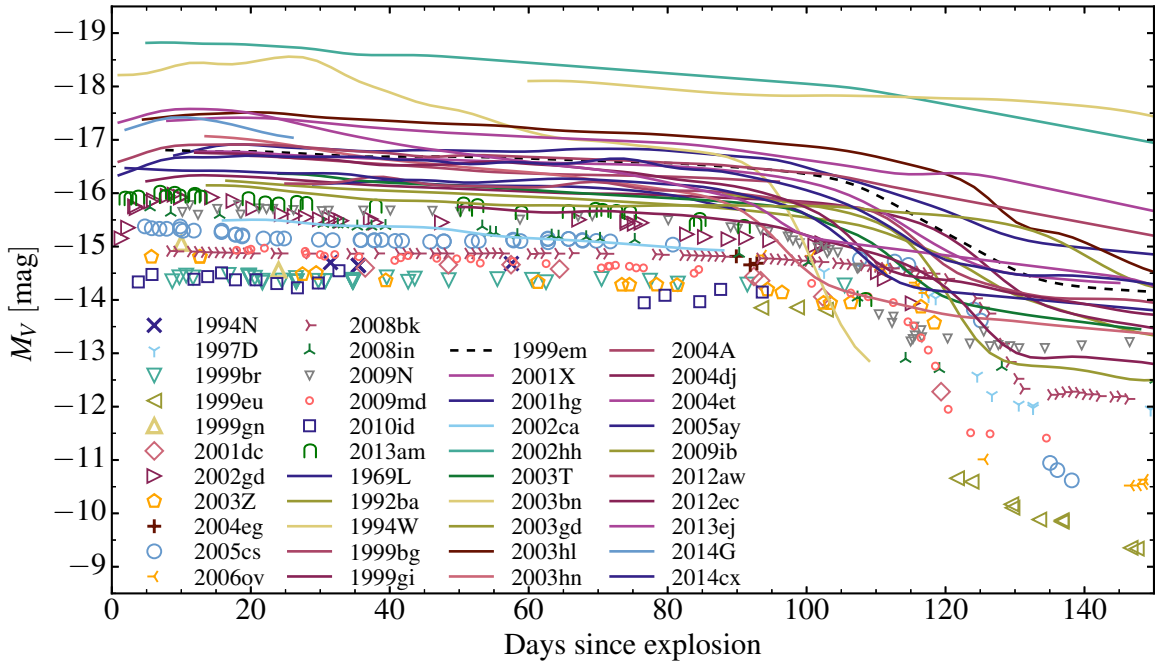

Figure 3.1 – Absolute V-band light curves for Type II-P SNe. Low-luminosity sample is shown with markers, standard SNe are shown with lines. The data are corrected for the reddening. Obviously, there is a continuum of absolute magnitudes in V-band. All low-luminosity SNe show a 'plateau'-like LC, with the same duration as standard SN II-P 1999em, but with a range of brightness. Non of the known low-luminosity SNe is a fast decliner.

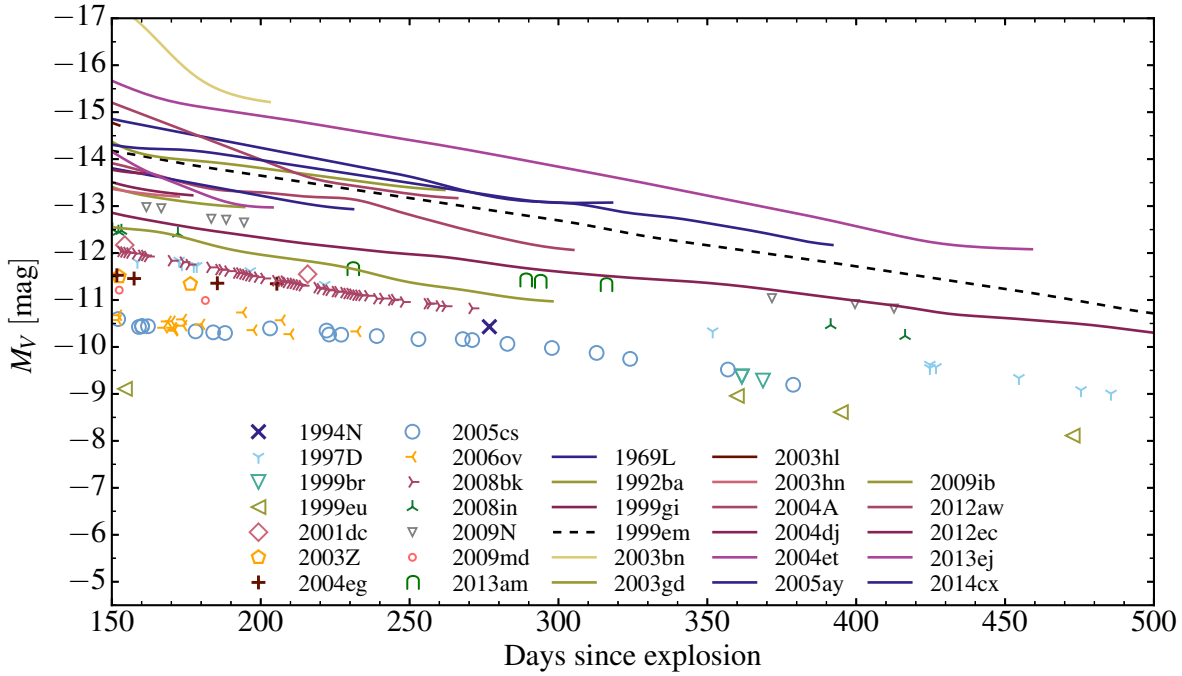

Figure 3.2 – Same as Figure 3.1, but for the nebular phase — from 150 to 500 days since explosion.

et al., 2014a for SN 2008bk). The second explanation suggests high-mass progenitors with a large fallback (Turatto et al., 1998; Zampieri et al., 2003), which is therefore in contradiction with estimates from pre-explosion images when available.

The progenitor of SN 2005cs has been identified. It was a RSG star of spectral type K3–M4 with an initial mass $M_{\rm i}$ of $10 \pm 3\,{\rm M}_{\odot}$ (Li et al., 2006) and RSG with $M_{\rm i} = 9^{+3}_{-2}\,{\rm M}_{\odot}$ (Maund et al., 2005). The mass of the SN 2008bk progenitor is estimated to be 8–8.5 $\rm M_{\odot}$ (Van Dyk et al., 2012a) and $M_{\rm i} = 12.9^{+1.6}_{-1.4}\,{\rm M}_{\odot}$ (Maund et al., 2014a). The progenitor candidate for SN 2009md was found in the archival *Hubble Space Telescope* data, and the pre-SN mass of the RSG progenitor is estimated to be $8.5^{+6.5}_{-1.5}\,{\rm M}_{\odot}$ (Fraser et al., 2011), though Maund et al. (2015) suggest that the disappearance of the progenitor cannot be confirmed.

The large part of the analysis of low-luminosity Type II-P SNe we present below has already been done in Pastorello et al. (2004); Spiro et al. (2014). However, here we study a slightly broader sample and we also extract statistical properties of the sample. In Appendix A we present sources of the observational data and Table A.1 gives a summary of distance moduli, visual extinction A_V, explosion dates, recessional velocities for our sample of low-luminosity SNe II. In some cases we revised distances, reddening or recessional velocity compared to Pastorello et al. (2004); Spiro et al. (2014). We discuss each case explicitly in Appendix A.

3.1.1 Light curves

We present V-band LCs for Type II-P SNe in Figure 3.1 (0–150 days since explosion) and in Figure 3.2 (130–350 days since explosion). From Figure 3.1 one can see that all the objects from the low-luminosity sample follow the same photometric evolution. During the first 110–120 days the luminosity is roughly constant, which forms the 'plateau' in the light curve. It corresponds to the photospheric phase, when the ejecta is optically thick. SNe from our sample show a range of brightness during the photospheric phase, but they have a similar plateau shape — there are no fast decliners.

After the end of the plateau there is a fast transition to the nebular phase with the steep drop in the luminosity by 2.5–4.5 mag during the 10–20 days. The luminosity of the nebular phase is controlled primarily by the amount of ^{56}Ni ejected in the explosion in the absence of additional power sources like interaction with CSM or magnetar energy injection. The scatter of the data points at the nebular phase is higher than during the photospheric phase. We will discuss the origin of this effect later in the section.

The plateau length does not depend on the V-band brightness during the photospheric phase. The whole range of luminosities is populated. Absolute magnitudes (corrected for the reddening) in V-band during the plateau phase for most SNe from our sample lie between -14 and -15.5 mag (Figure 3.1), i.e. the luminosity of these SNe varies by no more than a factor of three (although one could say that the division between low-luminosity and standard-luminosity II-P is subjective). A standard SN II-P has $M_V \sim -16.7$ mag during the plateau phase (Anderson et al., 2014a).

There is no sharp boundary where one can distinguish between 'low-luminosity' (or faint, or subluminous) SNe II-P and 'standard' SNe II-P. We present SNe 1992ba, 1999bg, 1999gi, 2001hg and 2003gd in Figure 3.1 to show that there is a continuum in SNe V-band magnitudes. This might indicate that there is a continuous range in progenitor and explosion properties rather than distinct classes.

We show the nebular phase LCs (130–350 days since explosion) in Figure 3.2. Late time light curves allow to estimate the amount of ^{56}Ni produced in the explosion. For the standard Type II-P SN 1999em, Utrobin et al. (2007) suggest 0.036 $\rm M_{\odot}$ of ^{56}Ni and Bersten et al. (2011) suggest 0.056 $\rm M_{\odot}$, while for the least luminous from our sample SN 1999eu mass of ^{56}Ni is only

Table 3.1 – Mean magnitudes in V-band for some observational properties for our sample of low-luminosity SNe II-P and for large sample of hydrogen-rich Type II SNe (Anderson et al., 2014a). $M_{\rm max}$ is the magnitude at the initial peak if observed, otherwise first photometric point; $M_{\rm end}$ is the magnitude at the end of the plateau phase; $M_{\rm tail}$ is the magnitude at the beginning of the nebular phase. See text for more detailed description.

	Low-luminosity SNe II-P V-band [mag]	SNe II V-band [mag]
$\overline{M}_{\rm max}$	-15.29 ($\sigma = 0.53$, 7 SNe)	-16.74 ($\sigma = 1.01$, 68 SNe)
$\overline{M}_{\rm end}$	-14.53 ($\sigma = 0.50$, 13 SNe)	-16.03 ($\sigma = 0.81$, 69 SNe)
$\overline{M}_{\rm tail}$	-11.65 ($\sigma = 0.81$, 11 SNe)	-13.68 ($\sigma = 0.83$, 30 SNe)

about 0.001 $M_\odot$ (Spiro et al., 2014). Note, however, that these estimates depend on the inferred bolometric luminosity, which depends on the bolometric correction (we normally observe the optical only), the adopted reddening, and the adopted distance. Uncertainties of several 10% are expected.

Anderson et al. (2014a) studied V-band light curves for a sample of 116 Type II SNe. To provide some quantitative comparison with this work, we show the mean values and the standard deviation σ for the $M_{\rm max}$, $M_{\rm end}$ and $M_{\rm tail}$ in Table 3.1, using the same definitions of these values as in their work (see their Fig. 1). $M_{\rm max}$ is the magnitude at the initial peak if observed, otherwise first photometric point. $M_{\rm end}$ is defined as an absolute magnitude in V-band measured 30 days before $t_{\rm PT}$, where $t_{\rm PT}$ is the mid point of the transition from the plateau phase to the radioactive tail. $M_{\rm tail}$ is the absolute magnitude in V-band measured 30 days after $t_{\rm PT}$. Note that the work of Anderson et al. (2014a) contains 5 SNe from our sample.

3.1.2 Color evolution

We present the color evolution ($V - I$) for Type II-P SNe in Figures 3.3 and 3.4. There is little scatter during the photospheric phase, but then there is a large scatter as the SNe enter the nebular phase. All the SNe from our sample evolve in a very similar way. At early times the photospheric temperature of the ejecta is high (the spectral energy distribution peaks in the far-ultraviolet). As the ejecta expands and cools, the peak of the spectral energy distribution shifts to the red (Filippenko, 1997). At the end of the plateau phase, approximately 110–120 days after explosion, the ejecta becomes transparent and the value of $V - I$ is significantly greater. If one includes SNe with luminosities between those of SNe 2002gd and 1999em, such as 2002ca, 1992ba, 1999bg, 2003gd, 1999gi, 2001hg, 2005ay, 2012ec, it does not increase the dispersion of data points.

The dispersion of the observational data rises rapidly after the end of the photospheric phase. As we showed in Section 4.5.3, the level of ^{56}Ni mixing has a strong impact on the nebular phase color. The scatter of the data at nebular times probably depends on the 3D structure of the material left by the explosion. The structure depends on the chemical segregation, clumping, and macroscopic mixing (e.g., Wongwathanarat et al., 2015). It appears that the scatter in optical colors in the late time spectra is driven by differences in the strength of the Hα, Ca II 7300 Å, and the Ca II NIR triplet. For example, the flux in the I-band is primarily controlled by the Ca II NIR triplet.

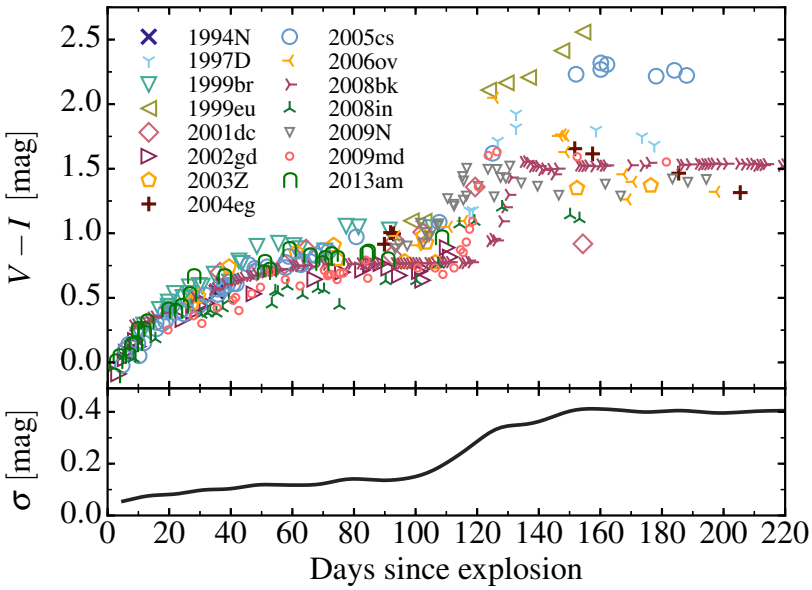

Figure 3.3 – Color evolution of our sample of low-luminosity SNe. We chose $V - I$ since most SNe from our sample have observational data in these bands simultaneously. At the bottom panel we show the value of standard deviation σ for the low-luminosity sample, i.e. without SN 1999em. The scatter of the data is small during the plateau phase (first 110–120 days) and is much higher thereafter.

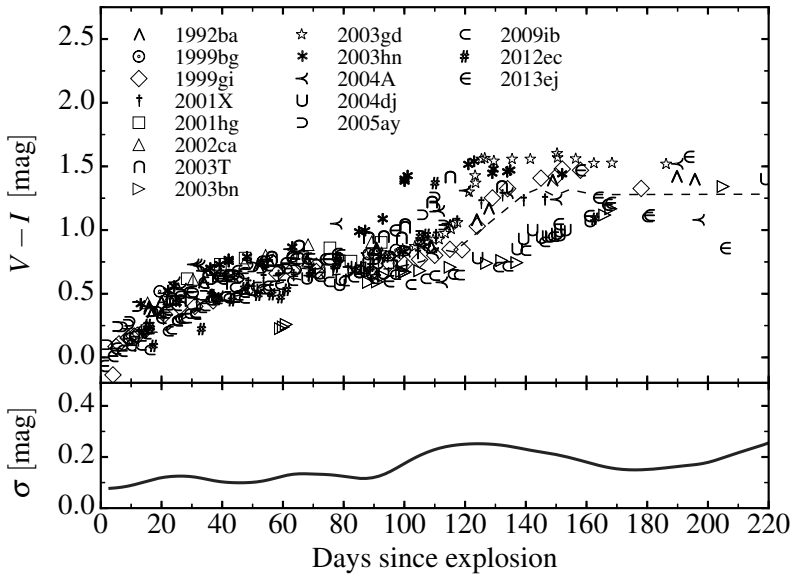

Figure 3.4 – Same as Figure 3.3, but for standard II-P SNe sample. Scatter of data points do not increase as much as for the low-luminosity sample at the beginning of the nebular phase.

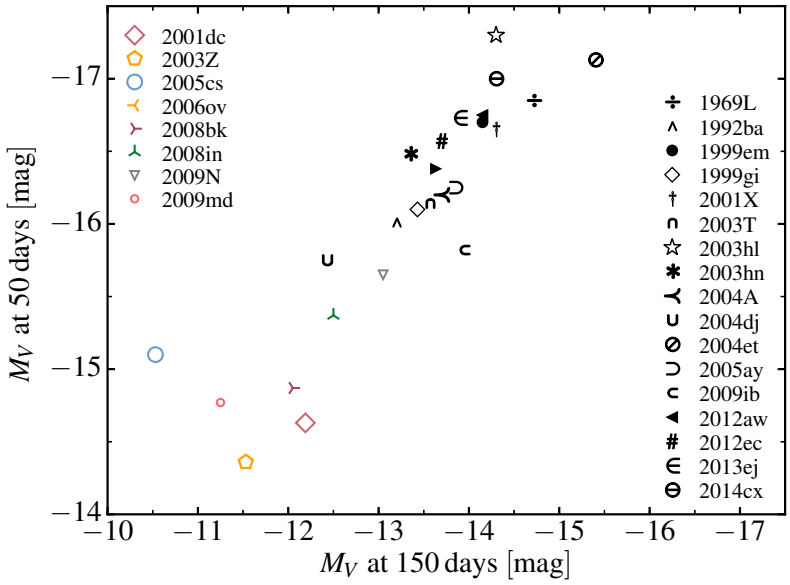

Figure 3.5 – Relation between plateau phase brightness (M_V at 50 days since explosion) and nebular phase brightness (M_V at 150 days since explosion) for low, moderate and standard luminosity SNe. Our low-luminosity sample is shown in color and other SNe are shown in black. Brighter at the plateau phase SNe tend to eject more ^{56}Ni. SN 2009ib near the center of the plot is a somewhat peculiar object with an unusually long photospheric phase (Takáts et al., 2015).

3.1.3 M_V at plateau – M_V at nebular phase relation

In Figure 3.5, we compare the plateau and nebular phase luminosities. The relation, although the data scatter is significant, is well visible in the figure. It indirectly connects the explosion energy and the mass of ejected ^{56}Ni. More energetic explosions tend to produce more ^{56}Ni. This makes sense since strong explosions have a stronger shock and have a more efficient explosive nucleosynthesis (Müller et al., 2017).

3.1.4 M_V at plateau – expansion rate relation

In Figure 3.6 we show $V_{\rm abs}$ in Fe II 5169 Å, derived from the position of the absorption maximum of the line. This gives a measure of the expansion rate. This measure is quite homogeneous and remarkably lower than for the standard archetypal Type II-P SN 1999em.

Hamuy & Pinto (2002) noticed that in their sample of 17 Type II SNe objects with brighter plateaus have higher envelope expansion velocities (see their Fig. 1). We show the absolute magnitude versus expansion rate measured by the position of the maximum absorption for the bound-bound transitions at Fe II 5169 Å (both at 50 days since explosion, which is roughly the middle of the plateau) in the Figure 3.7. Thirteen objects from our sample have both photometric and spectroscopic observations close to 50 days; values have been interpolated to the value at 50 days if enough information is available.

It is difficult to find a strict relation between the luminosity and the expansion rate for our sample alone. It could be a result of rather high uncertainties in the distances, redshifts and reddening due to host galaxies. However, when our sample is plotted alongside with other moderate luminosity and standard SNe II-P and the data from Hamuy (2003), it is visible that all the objects in the plot follow the same relation, though the scatter for low-luminosity SNe

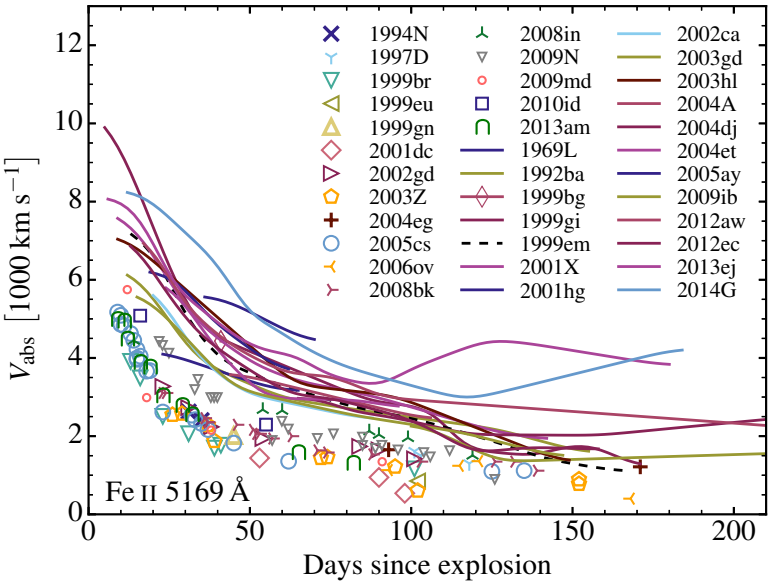

Figure 3.6 – Doppler velocity at maximum absorption in Fe II 5169 Å for our sample of low-luminosity SNe II-P and other, more energetic, Type II-P SNe, including 1999em, 1992ba, 2001hg and 2003gd. Relative to SN 1999em, low-luminosity SNe II-P have systematically lower expansion rates. This suggests they not only have a low luminosity but also a low ejecta kinetic energy.

is a bit higher. Fits to data from Hamuy (2003) and to all SNe listed in legend in Figure 3.6 show different slopes. These fits take into account errors along the vertical axis (uncertainties in distance moduli and V-band photometry errors). The main outlier is SN 2010id, for which the observations in the V-band seem problematic (see Appendix A.1.14).

3.1.5 Spectral evolution

In Figure 3.8, we show the spectral evolution for our set of SNe. All of them follow the same pattern and show very similar spectral features. One advantage of low-luminosity SNe over standard SNe is that spectral lines are narrower due to the smaller expansion rates, therefore there is less overlap and it is easier to distinguish between different lines. This analysis will be presented in Section 5.3.2. A spectral comparison of a low-luminosity SN 1999br and Standard Type II SN 2013ej is shown in Figure 3.10.

Dessart & Hillier (2005a) discussed the optical-depth effect at the origin of the blue-shifted emission peaks of P-Cygni profiles in SNe II (see also Anderson et al. 2014b for a summary of the alternative explanations). This blue shift is observed in all Type II SN spectra irrespective of V-band decline rate (Anderson et al., 2014b). In Hα, the peak blue shift is greatest at early times, decreases through the photospheric phase, and vanishes as the SN becomes nebular. The spectra for our sample of low-luminosity SNe show the same behavior.

The evolution of the spectral morphology of standard Type II-P SNe has been discussed numerous times, both from observational data and tailored models (see, e.g., Leonard et al. 2002b; Dessart & Hillier 2011). This evolution is the same for low-luminosity SNe II-P. At very early times ($\lesssim$5 days since explosion), the spectra have a color temperature greater than 10^4 K, are very blue, and show weak lines of H I, He I–II, and from neutral (and more rarely once ionized) species of C, N, or O. Metal lines (in particular from Ti II, Fe II), which eventually cause

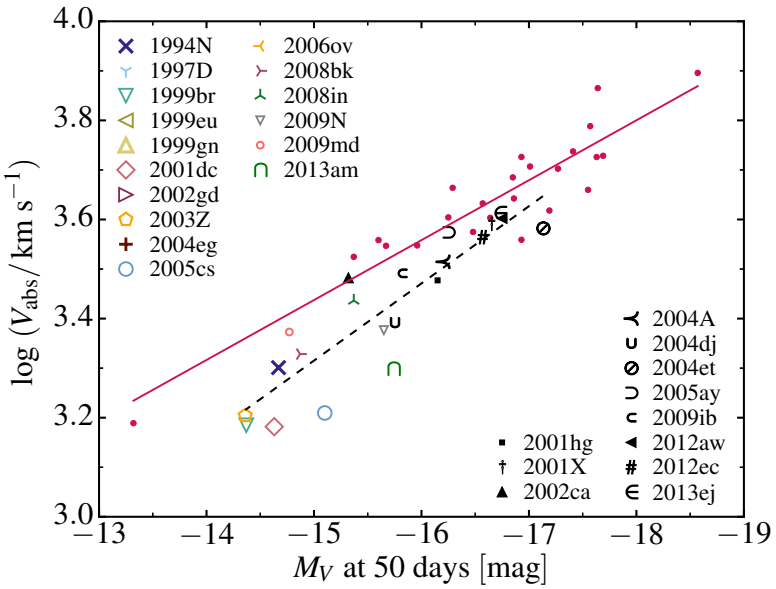

Figure 3.7 – Variation of the Doppler velocity at maximum absorption in Fe II 5169 Å with the intrinsic V-band brightness 50 d after explosion for low-luminosity SNe II-P (colored symbols; we exclude SN 2010id since its photometry seems anomalous, see Appendix A.1.14) and standard-luminosity SNe II-P (black symbols). When necessary, photometric/velocity measurements have been interpolated to a post-explosion epoch of 50 d. Small red filled circles correspond to the Type II SN sample from Hamuy (2003), not described in this text, and the solid red line is a fit to these data points. The dashed black line is a fit to all the SNe listed in the legend. The fitted lines are of the form $\log V_{abs} = a + bM_V$, where V_{abs} is in km s^{-1}. For the low-luminosity sample, we find $a = 0.88$ and $b = -0.16$, and for the sample from Hamuy (2003), we find $a = 1.62$ and $b = -0.12$.

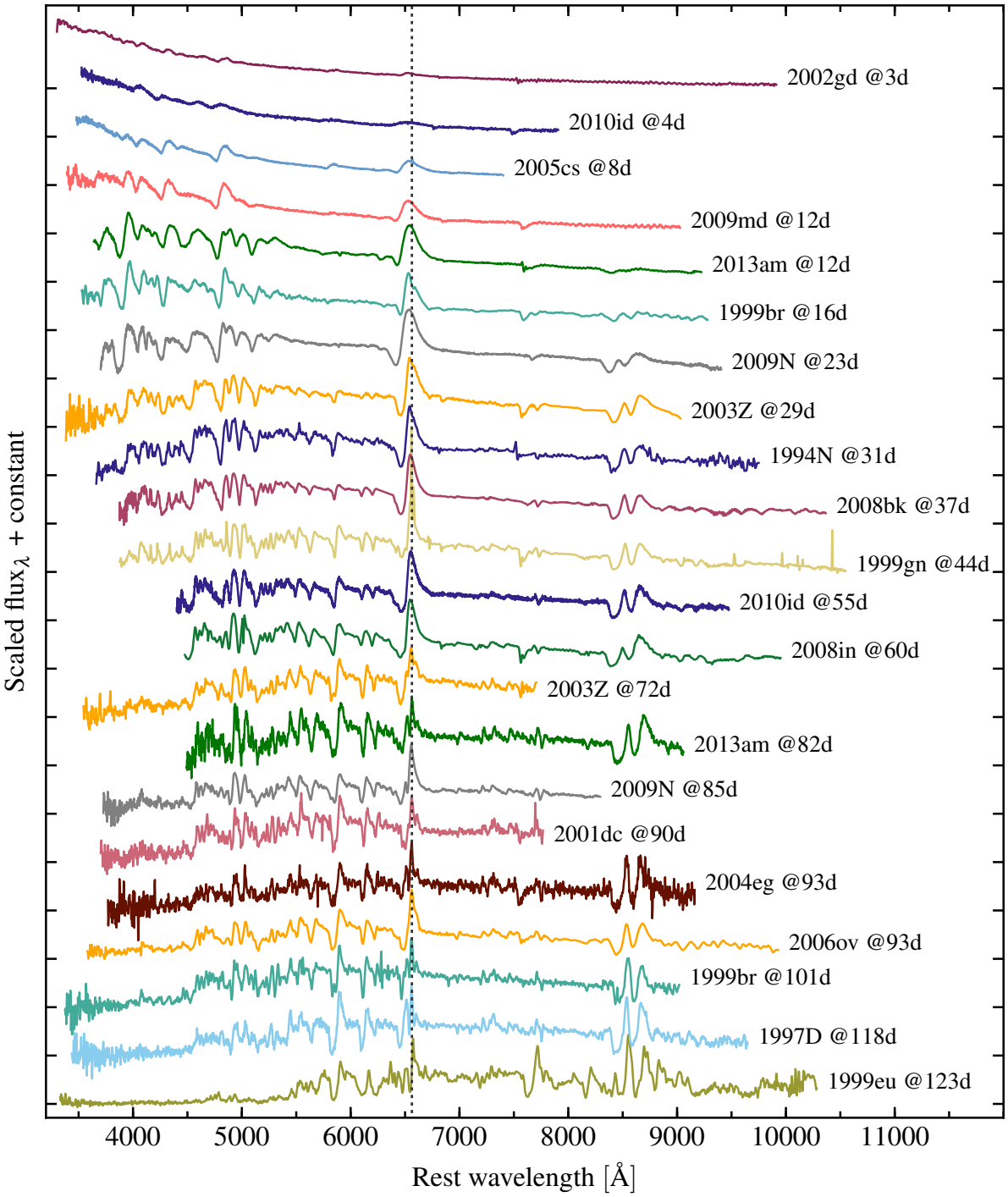

Figure 3.8 – Montage of spectra (corrected for redshift and reddening) showing the evolution of low-luminosity SNe II-P during the photospheric phase. Each of the 17 SNe in our sample is shown at least at one epoch. The ordinate ticks mark the zero flux level for each spectrum. The spectral evolution for these events is very generic, forming a smooth sequence towards redder optical colors and narrower spectral lines. The vertical line locates the Hα rest wavelength and helps identifying any skewness in the line profile. For each spectrum, we indicate the phase with respect to the inferred time of explosion.

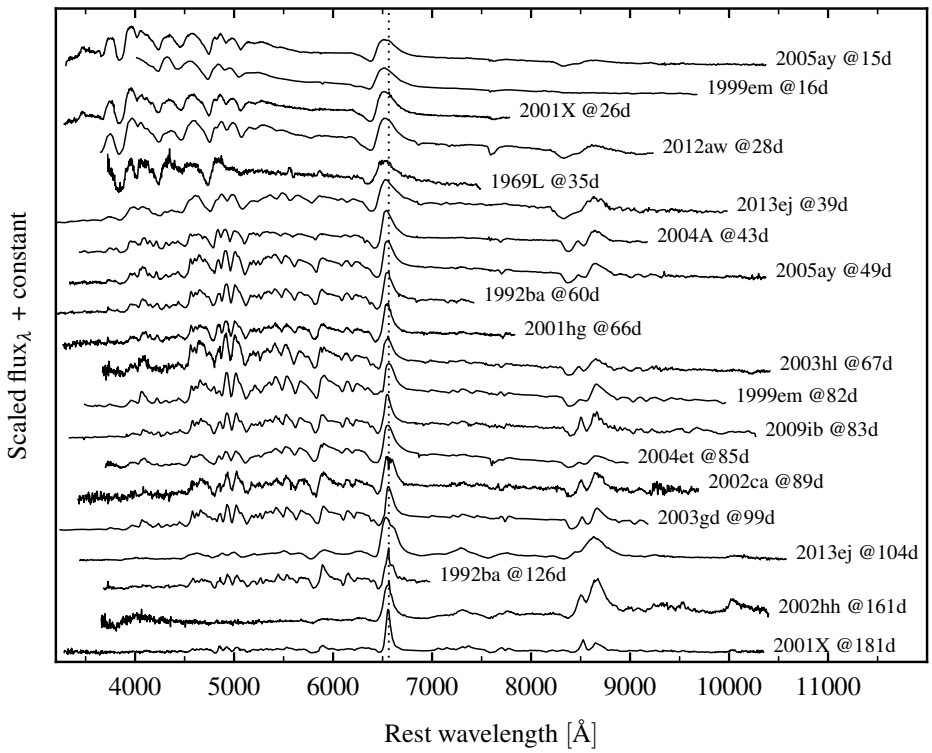

Figure 3.9 – Same as Figure 3.8, but for standard SNe II-P. Note the wider line profiles for standard II-P throughout the evolution.

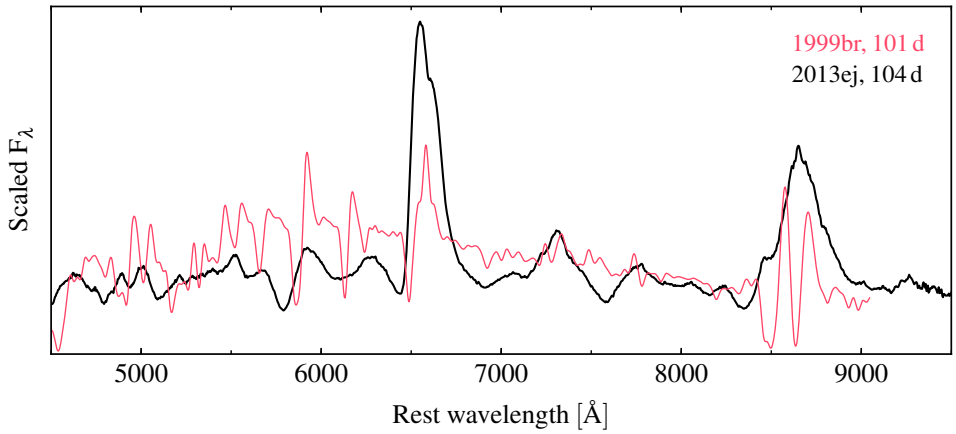

Figure 3.10 – A spectral comparison between low-luminosity Type II SN 1999br and Type II SN 2013ej at the same phase of ∼100 d since explosion. In the spectra of 1999br lines are markedly narrower, allowing more thorough analysis of the spectral features and thus qualitatively and quantitatively more adequate comparison to our models. Both spectra have been smoothed to reduce the noise level.

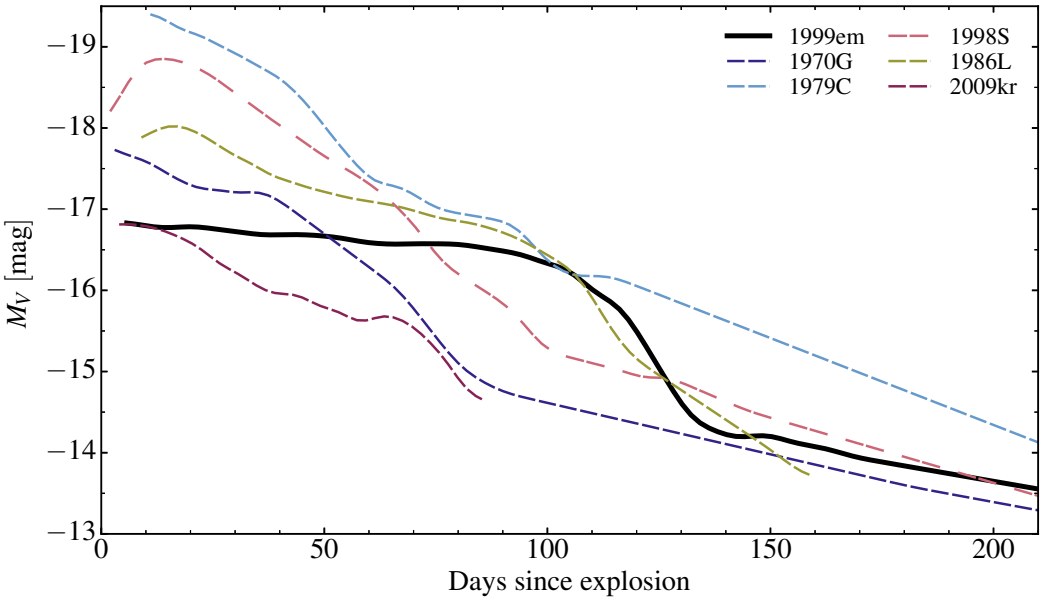

Figure 3.11 – Absolute V-band light curves for Type II-L SNe. The data are corrected for the reddening. Dashed lines correspond to SNe II-L. SN II-P 1999em is plotted with solid line.

line blanketing, start to develop as the photospheric layers recombine, which takes place after about two weeks. This is accompanied by the strengthening of the NIR Ca II triplet at about 8500 Å, Na I D, lines of Sc II and Ba II. Many of these lines remain strong until the nebular phase, in part because they are tied to low lying levels which can be more easily excited (thermally or non-thermally).

The Hα profile becomes structured at the end of the plateau phase in low-luminosity SNe II-P (Pastorello et al. 2004; Roy et al. 2011; Spiro et al. 2014). Standard Type II SNe rarely show a complex Hα profile because their higher expansion rates cause a stronger Doppler broadening and line overlap[13].

3.2 Type II-L

As we discussed in Chapter 1, it has been recently shown that SNe of types II-P and II-L constitute a continuous range of observational properties. The faster brightness decline of II-L SNe may stem from the smaller amount of H-rich envelope in these objects (e.g., Bartunov & Blinnikov, 1992; Moriya et al., 2016).

In Figure 3.11, we show V-band light curves for Type II-L SNe. The decline rate for SNe II-L from maximum (which occurs usually at 10–15 d since explosion) to 50 d since explosion is in the range from 0.8 to 1.8 mag, i.e. 0.020–0.045 mag per day (compare to 0.1 mag for Type II-P SN 1999em, i.e. 0.0025 mag per day).

Type II-L SNe tend to be brighter at maximum light than SNe II-P, although brightest II-P SNe can reach $M_V \approx -19$ mag. Note that the maximum magnitude is not known for all SNe since the LC continuously fades after discovery. The explosion time is also rarely well constrained.

In Figure 3.12, we show the spectral evolution for Type II-L SNe. Lines are somewhat wider that for Type II-P SNe and the prominence of H lines is somewhat reduced (see Figure 3.9).

[13] This feature is discussed and modelled in Chapter 4, see Figure 4.14 for the difference of Hα profile for low-luminosity and standard Type II-P SNe.

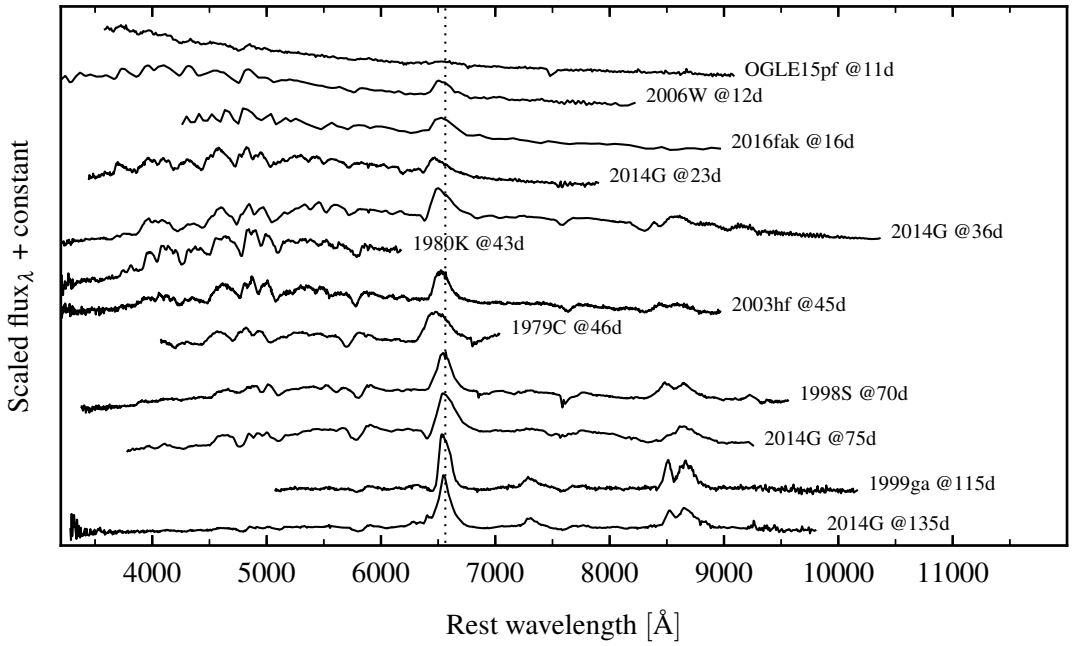

Figure 3.12 – Spectral montage for Type II-L SNe. Note the similarity with II-P spectra (see Figure 3.9). For II-L SNe, lines are wider and Hα height is reduced compared to II-P SNe. Late spectra, dominated Ca II near-IR triplet and Hα, are of great similarity for SNe II-L and II-P.

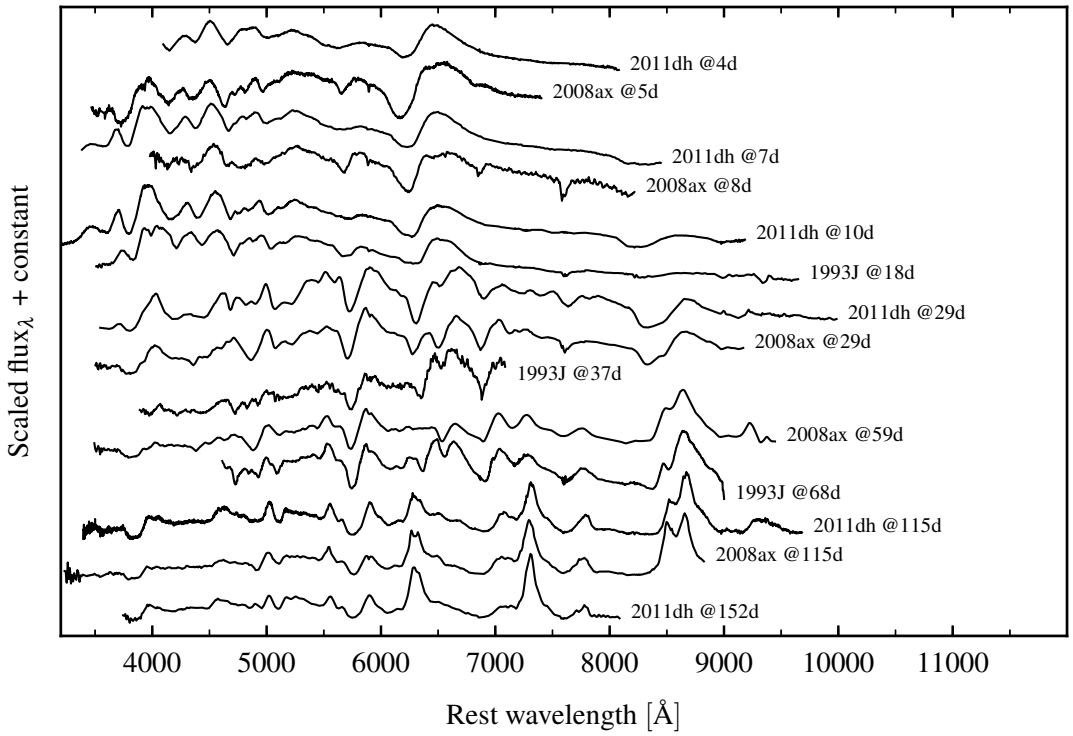

Figure 3.13 – Spectral montage for 3 Type IIb SNe — 1993J, 2008ax and 2011dh. Early spectra are similar to those of II-L SNe (see Figure 3.12). With time, however, Hα line vanishes from the spectra. It happens typically around bolometric maximum, but with notorious exceptions, like SN 1993J (Matheson et al., 2000).

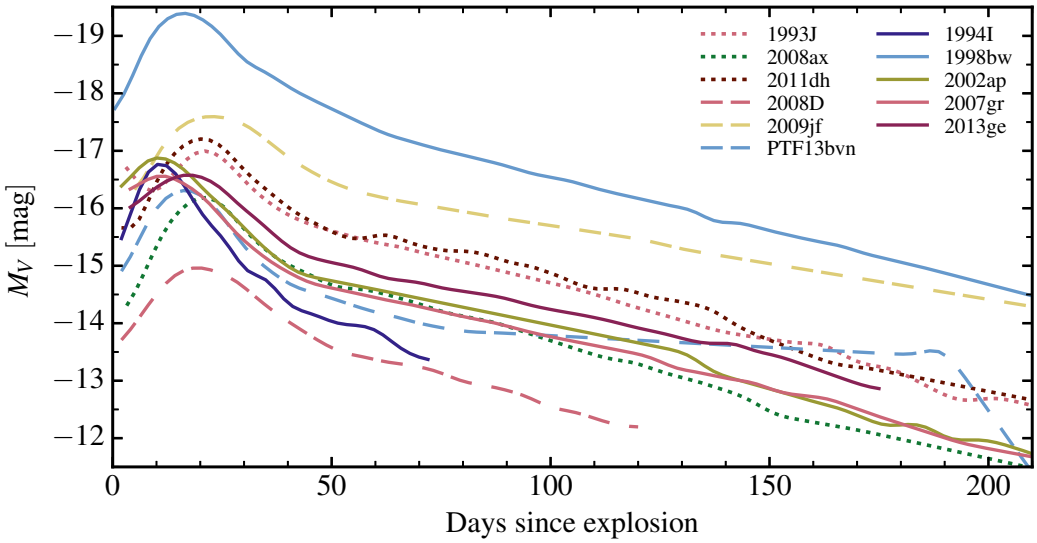

Figure 3.14 – Absolute V-band LCs for stripped-envelope CCSNe. The data are corrected for the reddening. Dotted lines correspond to IIb, dashed to Ib and solid — to Ic SNe. SN 1998bw has been associated with GRB 980425.

3.3 Stripped-envelope SNe

Stripped-envelope supernovae (SE-SNe, Clocchiatti & Wheeler 1997) are a subset of CCSNe where the progenitor star has lost much of its outer layers of H and in some cases He. Type IIb SNe show evidence of H I lines in their spectra during few weeks, however, later H I lines vanish from the spectra (see Figure 3.13). Type Ib SNe are classified as H-poor and He-rich, and Type Ic SNe as H-poor and He-poor (see, e.g., Filippenko 1997). This suggests placing SNe in a sequence of increasing mass loss from the progenitor star: II-P – II-L – IIb – Ib – Ic (e.g., Nomoto et al. 1995). Binarity is also thought to be essential for the production of SNe IIb/Ib/Ic by Roche lobe overflow.

It is often difficult to distinguish between SNe Ib and Ic, and these objects are often referred to as Ib/c or Ibc SNe. Characteristic feature of SNe Ibc is almost symmetrical bell-shaped LC from explosion to 40–50 d after with the maximum light roughly in the middle of the period. After 40–50 d since explosion the decline rate of the brightness changes normally to the smaller one, around −0.02 mag per day, whereas decline rate from maximum to 40–50 d is around −0.05 mag per day for most of SE-SNe. From this point of view, LCs of Type IIb SNe are indistinguishable from Ibc light curves (see Figure 3.14). The LC is powered by ^{56}Ni, like in SNe Ia, but the amount of ^{56}Ni is much lower (about 0.1 $M_\odot$ for CCSNe).

In Figure 3.15, we show the spectral evolution for Type Ib/Ic SNe. Note SN 1998bw with very broad lines (20 d spectrum). This SN is associated with GRB 980425. Compared to spectral evolution of other CCSNe (Figures 3.8, 3.9, 3.12, 3.13), SNe Type Ib/Ic show wider lines and complete absence of H lines. More detailed discussion on photometric and spectral evolution of SE-SNe can be found in, e.g., Dessart et al. (2011); Modjaz et al. (2014).

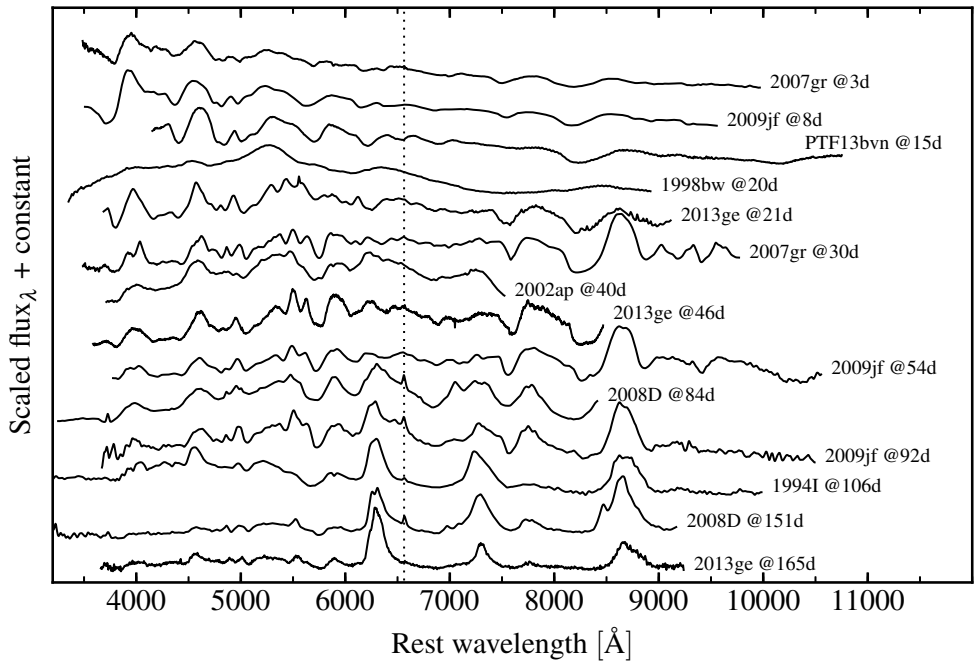

Figure 3.15 – Spectral montage for Type Ib and Ic SNe. SN 1998bw with extremely broad lines is a SN of Type Ic-BL (sometimes called hypernova). This SN is associated with gamma-ray burst GRB 980425 and may be an example of collapsar (see Section 1.3.4.5).

Chapter 4

SN 2008bk — a low-luminosity Type II-P supernova

SN 2008bk is a well observed low-luminosity Type II event visually associated with a low-mass red-supergiant progenitor. To model SN 2008bk, we evolve a 12 $M_\odot$ star from the main sequence until core collapse, when it has a total mass of 9.88 $M_\odot$, a He-core mass of 3.22 $M_\odot$, and a radius of 502 $R_\odot$. We then artificially trigger an explosion that produces 8.29 $M_\odot$ of ejecta with a total energy of 2.5×10^{50} erg and $\sim 0.009\,M_\odot$ of ^{56}Ni. We model the subsequent evolution of the ejecta with non-Local-Thermodynamic-Equilibrium time-dependent radiative transfer. Although somewhat too luminous and energetic, this model reproduces satisfactorily the multi-band light curves and multi-epoch spectra of SN 2008bk, confirming the suitability of a low-mass massive star progenitor. As in other low-luminosity SNe II, the structured Hα profile at the end of the plateau phase is probably caused by Ba II 6496.9 Å rather than asphericity. We discuss the sensitivity of our results to changes in progenitor radius and mass, as well as chemical mixing. A 15% increase in progenitor radius causes a 15% increase in luminosity and a 0.2 mag V-band brightening of the plateau but leaves its length unaffected. An increase in ejecta mass by 10% lengthens the plateau by ~ 10 d. Chemical mixing introduces slight changes to the bolometric light curve, limited to the end of the plateau, but has a large impact on colors and spectra at nebular times.

4.1 Introduction

Massive stars with an initial mass greater than $\sim 8\,M_\odot$ are expected to end their lives with the gravitational collapse of their degenerate core. If a successful explosion follows, an H-rich progenitor leads to a Type II SN, the most frequently observed type of core-collapse SNe (Smith et al., 2011). These SNe are characterised by the presence of strong hydrogen Balmer lines in their optical spectra. Their high-brightness phase, which also coincides with the photospheric phase, lasts about one hundred days. Early simulations of such Type II SNe (Grassberg et al. 1971, Falk & Arnett 1977) suggest a progenitor star with a massive and extended H-rich envelope, as typically found in red-supergiant (RSG) stars. The physics underlying the evolution of a SN II-Plateau (II-P) has been extensively discussed by, for example, Falk & Arnett (1977) or more recently Utrobin (2007). The association between Type II-P SNe and RSG stars has also been more directly made through the identification of the progenitor star on pre-explosion images (see Smartt, 2009 for a review).

Type II SNe exhibit a broad range in R-band absolute magnitude, spanning about 5 mag during the photospheric phase and the nebular phase (Hamuy, 2003). The latter suggests a

range of $\gtrsim 10$ in the mass of ^{56}Ni ejected. The ejecta expansion rate inferred from P-Cygni profile widths halfway through the plateau also spans a range from 1000 to 8000 km s^{-1} (Hamuy, 2003), suggestive of a large scatter in the ratio of ejecta kinetic energy $E_{\rm kin}$ and ejecta mass $M_{\rm e}$. More recent surveys document this diversity further (Anderson et al., 2014a; Faran et al., 2014a,c; Sanders et al., 2015; Galbany et al., 2016), and also emphasize, for example, the range in photospheric phase durations, the V-band decline rate after maximum, how various radiative properties correlate.

The existence of low-luminosity (i.e., intrinsically faint) SNe II was well established in the 90s. SN 1997D was one of the first Type II to exhibit abnormally narrow P-Cygni profiles (of the order of 1000 km s^{-1}) and a low optical brightness during the photospheric phase (always fainter than -14.65 mag in the V-band; Turatto et al. 1998), both suggestive of a low energy explosion in an extended H-rich star. The sample of low-luminosity Type II SNe now includes a handful of objects (Pastorello et al., 2004; Spiro et al., 2014), with an absolute V-band magnitude that covers from -14 to -15.5 mag around 50 d after explosion, thus 2–3 mag fainter than the prototypical Type II-P SN 1999em (Leonard et al., 2002a). The fraction of low-luminosity SNe could be $\sim 5\%$ of all Type II SNe (Pastorello et al., 2004).

Numerous radiation-hydrodynamic simulations of low-luminosity Type II SNe have been carried out. Constraints on the progenitor star and the ejecta (explosion energy, ^{56}Ni mass) are obtained through iteration until a good match to the bolometric light curve and the photospheric velocity evolution. Utrobin et al. (2007) modelled the low-luminosity SN 2003Z and obtained an ejecta mass of 14 $M_\odot$, an ejecta kinetic energy of 2.45×10^{50} erg, 0.006 $M_\odot$ of ^{56}Ni, and a progenitor radius of 230 $R_\odot$. Spiro et al. (2014) used a similar approach and proposed progenitor masses in the range 10–15 $M_\odot$ for the whole sample of low-luminosity SNe II. These results suggest that low-luminosity Type II SNe are intrinsically under-energetic and synthesize little ^{56}Ni. Other studies have argued that these low-luminosity Type II SNe are the result of weak explosions in higher mass RSG stars. In this context, the low ^{56}Ni mass arises from the significant fallback of material onto the proto-NS, associated potentially with the subsequent formation of a BH.

Turatto et al. (1998) propose this scenario with a 26 $M_\odot$ progenitor star for SN 1997D (Benetti et al., 2001), and argue against the possibility of a lower mass progenitor. Later work by Zampieri et al. (2003), using a semi-analytic modelling of the light curve, give support to the association with higher mass progenitors, in which the explosion is followed by fallback. The situation is therefore unsettled. For SN 1997D, Zampieri (2007) proposes a 14 $M_\odot$ progenitor, which disagrees with Turatto et al. (1998). For the low-luminosity SNe II-P 2005cs and 2008bk, a progenitor detection exists and suggests a low/moderate mass massive star (in the range 9–13 $M_\odot$ on ZAMS; Maund et al. 2005; Li et al. 2006; Mattila et al. 2008; Van Dyk et al. 2012a; Maund et al. 2014a).

Even when an ejecta mass is inferred from light-curve modelling, estimating the corresponding progenitor mass on the main sequence is subject to error because of the uncertain mass loss history. Furthermore, the light curve modelling above is primarily sensitive to the H-rich ejecta mass, not the total ejecta mass. The helium core mass can only be estimated by modelling nebular phase spectra and the helium core dynamics (Dessart et al., 2010b; Dessart & Hillier, 2011; Maguire et al., 2012; Jerkstrand et al., 2012; Dessart et al., 2013b).

In this work, we model the low-luminosity SN 2008bk because it is the best observed SN of this class of event, with a good photometric monitoring in the optical that started about a week after explosion (Pignata, 2013). Based on pre-explosion images and evidence of the disappearance of a source on post-explosion images, inferences have been made to constrain the nature of the progenitor star and its mass. The consensus is that it is a RSG star, although its

inferred ZAMS mass differs somewhat between studies, with 8–8.5 $M_\odot$ (Mattila et al. 2008; Van Dyk et al. 2012a; see also Van Dyk 2013) and 11.1–14.5 $M_\odot$ (Maund et al., 2014a). In contrast, there has been little analysis of the SN spectroscopic and photometric data. A preliminary analysis is presented in Pignata (2013), who proposes an ejecta with $E_{\rm kin} = 2.5{\times}10^{50}$ erg, a total mass of 12 $M_\odot$, and a ^{56}Ni mass of 0.009 $M_\odot$, together with a progenitor radius of 550 $R_\odot$, Maguire et al. (2012) present an analysis of a nebular-phase spectrum at 547 d after explosion and propose a progenitor star with a main-sequence mass of 12 $M_\odot$.

The simulations presented here are based on models of the progenitor evolution from the main-sequence until core collapse, together with the subsequent simulation of the piston-driven explosion including explosive nucleosynthesis. The bulk of the work lies, however, in the non-Local-Thermodynamic-Equilibrium (nLTE) time-dependent radiative-transfer modelling of the photometric and spectroscopic evolution of SN 2008bk. Since a low/moderate mass progenitor has been proposed by all former studies on SN 2008bk, we limit our investigation to a progenitor star of 12 $M_\odot$ on the main sequence. In a forthcoming study, we will investigate the properties of the whole sample of low-luminosity Type II SNe, and consider progenitors from both low and high mass RSG stars.

In the next section, we summarise the source of observational data for SN 2008bk. In Section 4.3, we present our numerical approach for the modelling of the pre-SN evolution with `MESA` (Paxton et al., 2011, 2013, 2015), the explosion with `V1D` (Livne, 1993; Dessart et al., 2010a,b), and the modelling of the SN radiation from 10 d after explosion until nebular times with `CMFGEN` (Hillier & Miller, 1998; Dessart & Hillier, 2005a, 2008; Hillier & Dessart, 2012; Dessart et al., 2013b). Our best match model to the photometric and spectroscopic observations of SN 2008bk is presented in Section 4.4. In Section 4.5, we discuss the sensitivity of our results to changes in progenitor/ejecta radius (Section 4.5.1), progenitor mass (Section 4.5.2), and chemical mixing (Section 4.5.3). We conclude in Section 4.6.

4.2 Observational data

The optical and near-IR photometry that we use for SN 2008bk comes from Pignata (2013). For the spectroscopic data, we limit our analysis to the optical range, and use observations from Pignata as well as the spectropolarimetric observations of Leonard et al. (2012a, see also Leonard et al., in prep.). The spectropolarimetric data is, however, not accurately calibrated in flux (no flux standard was used during the observing night) so the corresponding spectra are used mostly to compare the morphology of line profiles (in practice, we distort the observed spectrum so that it has the same overall shape as the model at the same epoch; see Section 4.4).

Following the earlier estimate of a low reddening towards SN 2008bk (Pignata, 2013), we adopt an $E(B-V) = 0.02$ mag. This is within 0.01 mag of the value reported by Schlegel et al. (1998) for the line-of-sight towards NGC 7793, the galaxy host of SN 2008bk. This suggests the source of extinction to SN 2008bk is exclusively galactic. Our reference model X (see below) gives a satisfactory agreement to the spectral and color evolution of SN 2008bk but it overestimates its plateau brightness. This discrepancy is reduced with a larger reddening although an $E(B-V)$ value greater than ~ 0.1 mag causes a mismatch in color.

We adopt the Cepheid-based distance modulus of 27.68±0.05 mag (internal error) ± 0.08 mag (systematic error) inferred by Pietrzyński et al. (2010). Finally, we adopt a recession velocity of 283 km s^{-1} for SN 2008bk, as inferred from nearby H II regions (Pignata, private comm.).

By drawing an analogy between the light curves of SN 2008bk and SN 2005cs, Pignata (2013) proposes an explosion date of MJD 54548.0± 2. Our best match model yields an improved

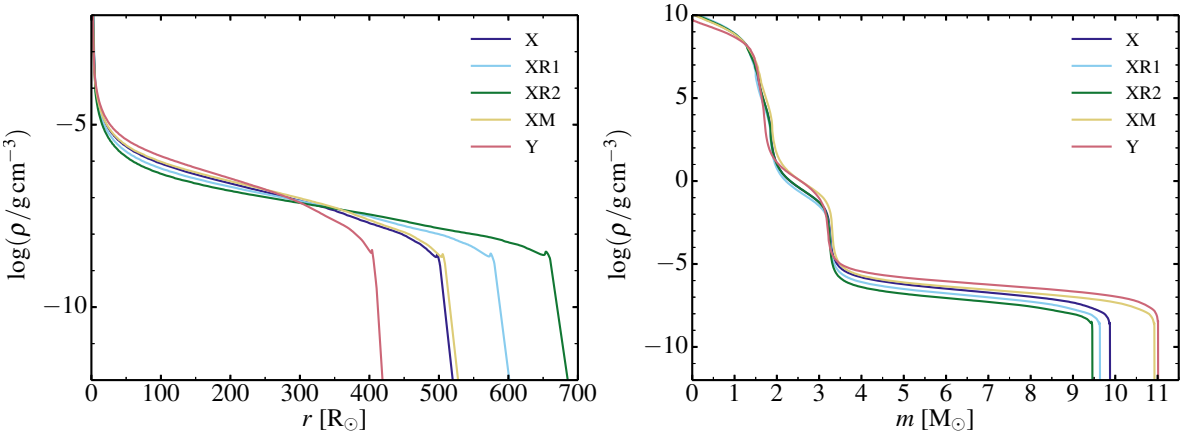

Figure 4.1 – Density structure versus radius (left) and mass (right) for our set of pre-SN models.

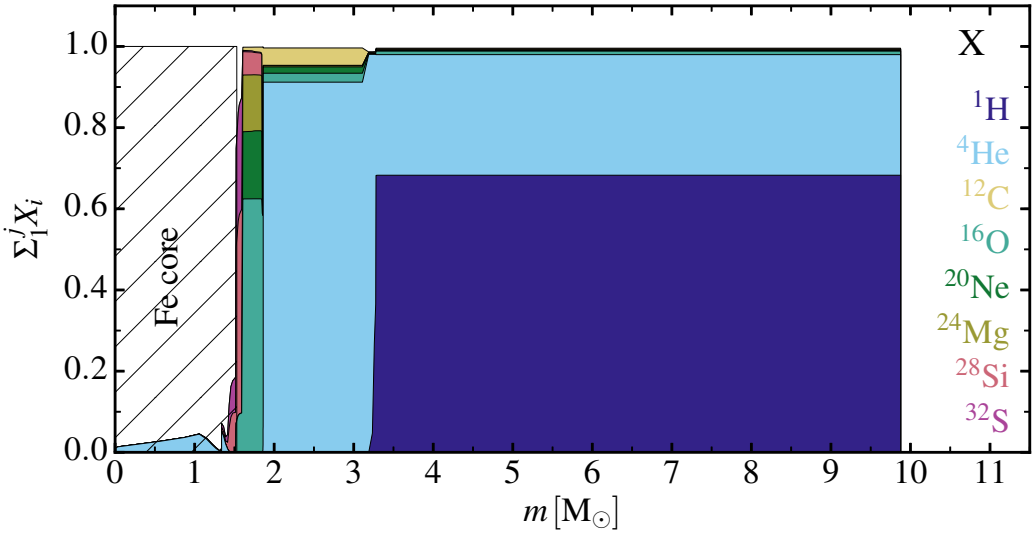

Figure 4.2 – Composition profile versus mass for model X. We show the cumulative mass fraction to better highlight the dominance of H and He in such a low-mass massive-star model. The Si-rich and the O-rich shells occupy a very narrow mass range.

agreement with observations if we adopt instead MJD 54546.0, which is within the uncertainty of Pignata's choice.

4.3 Numerical setup

4.3.1 Pre-SN evolution

Using in all cases an initial mass of 12 $M_\odot$, we evolved several models from the main sequence to the gravitational collapse of the iron core using `MESA` version 7623 (Paxton et al., 2011, 2013, 2015). We used the default massive star parameters of `MESA` (those given in `inlist_massive_defaults`), except for the adjustments discussed below.

Models X, XR1, XR2, and XM were evolved at a metallicity of 0.02. Convection is followed according to the Ledoux criterion, with a mixing length parameter $\alpha_{\rm MLT}$ that varies between models, a semi-convection efficiency parameter $\alpha_{\rm sc} = 0.1$, and an exponential overshoot with

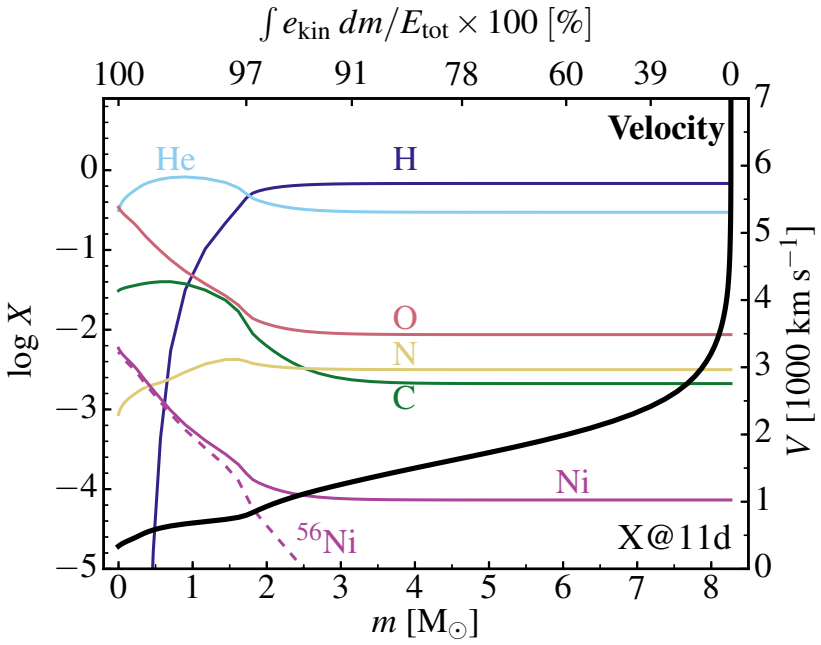

Figure 4.3 – Variation of the mass fraction for H, He, C, N, O, and Ni (the dashed line gives the contribution from the ^{56}Ni) with interior mass and velocity (thick line; see right axis) for model X at 11 d. We have applied some chemical mixing for all species (see Section 4.3.2 for details). The top axis shows the depth variation of the fractional inward-integrated kinetic energy. About 50% of the total ejecta kinetic energy is contained in the outer 1 $M_\odot$ of the ejecta, and only a few per cent in the former He core (below 1000 km s^{-1}).

parameter $f = 0.004$. The mixing length parameter $\alpha_{\rm MLT}$ was adjusted to modulate the stellar radius at the time of death. In Dessart et al. (2013b), it is found that to reconcile the color evolution of SNe II-P with observations, more compact RSG progenitors were needed. In MESA, this can be achieved by employing for $\alpha_{\rm MLT}$ a value larger than standard (the 'standard' used by default in MESA is 1.6) — by enhancing the efficiency of convection within the MLT formalism we allow the star to carry the core radiative flux through a denser/smaller envelope. Models X, XR1, and XR2 use a value of $\alpha_{\rm MLT}$ of 3, 2.5, and 2, respectively. For these three models, we enhanced the mass loss rate from the 'Dutch' recipe by a factor of 2.5. This choice is to compensate for the lower mass loss rates that result from the higher effective temperatures of our more compact RSG models and also to reduce the final star mass to $\lesssim 10\,M_\odot$ (originally motivated by the low progenitor masses of 8–8.5 $M_\odot$ inferred by Mattila et al. 2008 and Van Dyk et al. 2012a). In model XM, we use $\alpha_{\rm MLT} = 3$, but enhance the mass loss by a factor of 1.5 instead of 2.5 in order to obtain a higher mass model at death.

Model X is our best match model to the observations of SN 2008bk so these other models are computed to explore the sensitivity of our results to a number of evolution parameters. In a 12 $M_\odot$ star, most of the mass loss occurs during the RSG phase. Hence, the modulations in the mass loss rate impact primarily the H-rich envelope mass and leave the He-core largely unaffected. As discussed later, 10% changes in H-rich envelope mass or progenitor radius can visibly impact the resulting SN radiation, although in different ways.

Model Y was computed as part of a separate effort (with MESA version 4723) and so uses slightly different parameters from the above set. It was evolved at a metallicity of 0.0162 with the 'Dutch' mass-loss recipe, with an enhancement factor of 1.4. Convection is followed according to the Ledoux criterion, with a mixing length parameter $\alpha_{\rm MLT} = 3$, a semi-convection efficiency

Table 4.1 – Summary of the progenitor properties at the onset of iron core collapse. All models start on the main sequence with a mass of 12 $M_\odot$ and a metallicity Z. Model X is our best-match model to the observations of SN 2008bk. Other models are used to discuss the sensitivity of our results to variations in progenitor radius (XR1 and XR2), progenitor mass (XM), or ^{56}Ni mixing (YN1, YN2, and YN3). For the iron core, we report the location where the electron fraction rises outward to 0.499, for the CO core where the oxygen mass fraction rises inward to 0.1, and the He core where the hydrogen mass fraction drops inward to 0.001 — the exact criterion for these masses is unimportant.

Model	Z	$R_\star$ [$R_\odot$]	$M_\star$ [$M_\odot$]	$T_\star$ [K]	$L_\star$ [$L_\odot$]	Fe core [$M_\odot$]	CO core [$M_\odot$]	He core [$M_\odot$]
X	0.02	502	9.88	3906	52733	1.53	1.86	3.22
XR1	0.02	581	9.63	3644	53436	1.50	1.85	3.20
XR2	0.02	661	9.45	3390	51770	1.60	1.85	3.19
XM	0.02	510	10.92	3943	56408	1.50	1.89	3.27
Y	0.0162	405	11.01	4195	45715	1.38	1.73	3.15

parameter $\alpha_{sc} = 0.1$, and an exponential overshoot with parameter $f = 0.008$. Model Y is included here to discuss the effect of mixing (see next section) on the SN ejecta and radiation.

These various incarnations of a 12 $M_\odot$ star yield similar stellar properties at the time of core collapse. All models produce RSG stars at death with surface radii of 405–661 $R_\odot$, total masses of 9.46–11.01 $M_\odot$, and He-core masses of 3.13–3.26 $M_\odot$. The progenitor density structure at collapse shows the typical RSG profile, with a high-density highly bound He core and a low-density extended massive H-rich envelope (Figure 4.1). In such a low-mass massive star, there is only $\sim 0.2\,M_\odot$ between the outer edge of the iron core and the inner edge of the He-rich shell. The H-rich shell is about 7 $M_\odot$, hence about 7 times more massive than the He-rich shell.

4.3.2 Piston-driven explosions

We presented the numerical setup of the explosion with the `V1D` code in Section 2.2.2. Three levels of mixing are enforced in the present simulations, increasing from model YN1 to YN2 and YN3. These simulations and additional information on the mixed composition profiles are presented in Section 4.5.3.

The ejecta properties of our model set are given in Table 4.2. We also show the composition profile for model X in mass and velocity space in Figure 4.3.

4.3.3 Radiative-transfer modelling

The numerical `CMFGEN` setup is described in Section 2.3.5. In one instance, we recompute the model X at one time step with the addition of Ba II in order to test the impact of that ion on the spectrum at the end of the photospheric phase Section (4.4.3).

We show the bolometric light curve for all models in Figure 4.4. The maximum 'plateau' luminosity is in the range $\sim 10^{41.5} - 10^{42.0}$ erg s^{-1}, and the plateau duration is in the range $\sim$ 120–140 d. Each model will be discussed in turn in the following sections, starting with a detailed presentation of model X, our best-match model to the observations of SN 2008bk. A summary of the results is presented in Table 4.3.

Table 4.2 – Summary of the ejecta properties. The column $^{56}Ni_0$ gives the original total mass of ^{56}Ni. The mass of the H-rich envelope is $M_\star - M_{\text{He-core}}$ and covers the range ~ 6.3–$7.9\,M_\odot$ in the progenitor star. When applying mixing, H may be mixed into shells that were originally H deficient so the total mass of H-rich shells (i.e., with $X_H > 0.1$) may shift to a larger value in the corresponding ejecta — this does not apply to models YN1, YN2, and YN3 in which we mix only ^{56}Ni. Numbers in parentheses correspond to powers of ten. See Section 4.3 for discussion.

Model	Ejecta [$M_\odot$]	H-rich [$M_\odot$]	H [$M_\odot$]	He [$M_\odot$]	O [$M_\odot$]	$^{56}Ni_0$ [$M_\odot$]	E_{kin} [10^{50} erg]
X	8.29	6.66	4.54	3.24	0.22	8.57(−3)	2.5
XR1	8.08	6.43	4.38	3.17	0.19	8.19(−3)	2.6
XR2	7.90	6.26	4.25	3.13	0.22	9.00(−3)	2.7
XM	9.26	7.65	5.20	3.54	0.23	7.20(−3)	2.7
YN1	9.45	7.86	5.41	3.74	0.09	1.00(−2)	2.5
YN2	9.45	7.86	5.41	3.74	0.09	1.00(−2)	2.5
YN3	9.45	7.86	5.41	3.74	0.09	1.00(−2)	2.5

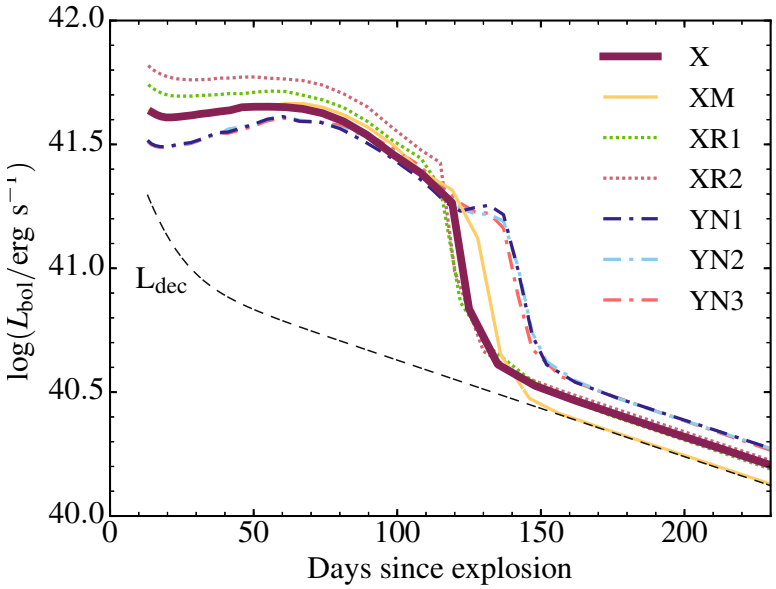

Figure 4.4 – Bolometric light curves computed with CMFGEN for our set of models. Model X is our best-match model to the observations of SN 2008bk. Our sample includes models that differ only slightly from model X, either in the pre-SN evolution or in the explosion properties, in order to test the sensitivity of our results to changes in $R_\star$ (models X, XR1, and XR2), changes in H-rich envelope mass (model X and XM), and changes in ^{56}Ni mixing (models YN1, YN2, YN3) — see Table 4.2 for details. The dashed line corresponds to the instantaneous decay power from an initial mass of $0.0072\,M_\odot$ of ^{56}Ni.

Table 4.3 – Sample of results for our set of simulations. Model X is the closest match to the observations of SN 2008bk, while other models are used to test the sensitivity of our results to changes in progenitor and explosion characteristics (see also Tables 4.1, 4.2). Here, we give the approximate duration Δt_P of the 'plateau' phase (we set its end when the bolometric luminosity or V-band magnitude suddenly drops), and then the bolometric luminosity, the absolute V-band magnitude, the $(U-V)$ color, the photospheric velocity (the electron-scattering opacity is used), and the velocity at maximum absorption in Hα at 15 and 50 d after explosion. Numbers in parentheses correspond to powers of ten.

Model	Δt_P [d]	L_{bol} [erg s^{-1}]		M_V [mag]		$U-V$ [mag]		V_{phot} [km s^{-1}]		V_{abs} (Hα) [km s^{-1}]	
		(15 d)	(50 d)	(15 d)	(50 d)	(15 d)	(50 d)	(15 d)	(50 d)	(15 d)	(50 d)
X	120	4.36(41)	4.46(41)	–15.46	–15.50	–0.01	2.11	4833	2334	5362	4208
XR1	115	5.32(41)	5.13(41)	–15.60	–15.67	–0.33	1.96	4854	2468	5344	4251
XR2	115	6.33(41)	5.92(41)	–15.70	–15.84	–0.56	1.79	4685	2612	4887	3979
X	120	4.36(41)	4.46(41)	–15.46	–15.50	–0.01	2.11	4833	2334	5362	4208
XM	120	4.23(41)	4.53(41)	–15.43	–15.51	–0.01	2.10	4731	2323	5126	4101
YN1	140	3.16(41)	3.81(41)	–15.16	–15.30	0.41	2.29	4534	2177	5057	4197
YN2	140	3.15(41)	3.81(41)	–15.16	–15.30	0.41	2.31	4530	2182	5072	4200
YN3	140	3.13(41)	3.75(41)	–15.16	–15.27	0.44	2.49	4519	2194	5042	4555

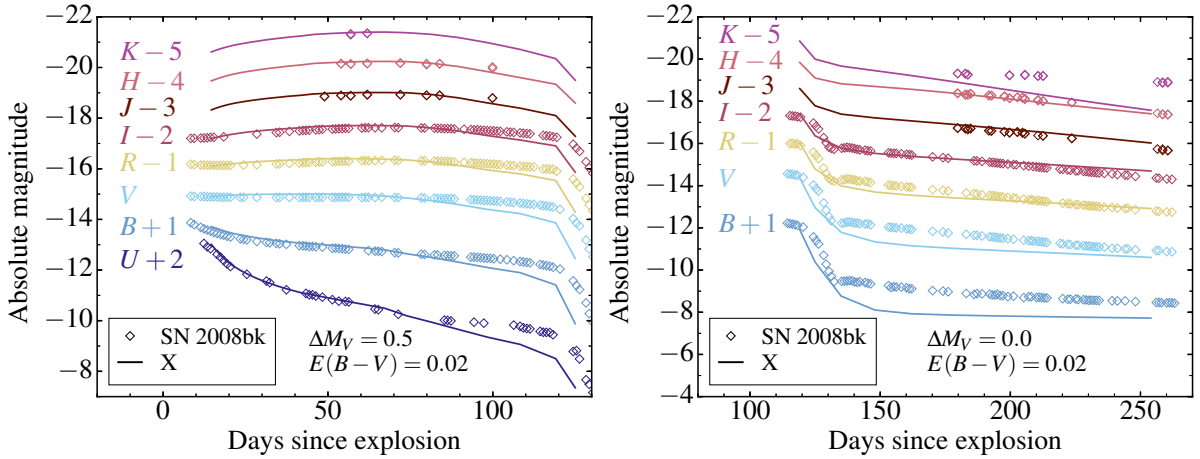

Figure 4.5 – Comparison of optical and near-IR light curves for SN 2008bk (corrected for reddening and distance) and model X during the plateau phase. At early times model X is somewhat overluminous and we have adjusted all magnitudes by $\Delta M_V = M_{V,obs} - M_{V,model} = 0.5$ mag to facilitate the comparison with SN 2008bk. During the nebular phase the luminosity is set primarily by the original ^{56}Ni mass, and no adjustment was necessary (see Section 4.2 and discussion in Section 4.4.2).

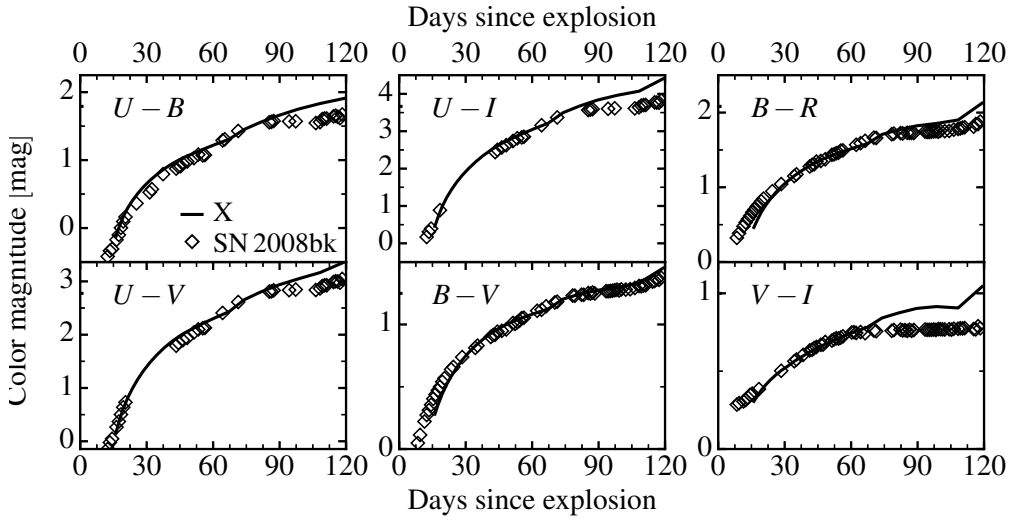

Figure 4.6 – Color evolution for our best-match model X and the de-reddened observations of SN 2008bk. See Section 4.2 for details on the observational data.

4.4 Properties of our best-match model to the observations of SN 2008bk

Model X stems from a 12 $M_\odot$ main-sequence star evolved at solar metallicity and dying with a pre-SN radius of 502 $R_\odot$. The resulting SN ejecta is 8.29 $M_\odot$, with a kinetic energy of $2.5{\times}10^{50}$ erg and 0.0086 $M_\odot$ of ^{56}Ni. These parameters do not yield a perfect match to observations of SN 2008bk and therefore do not correspond exactly to the progenitor and the ejecta of SN 2008bk, but they produce a reasonable match to the observations. In this section, we present the photometric and spectroscopic properties of model X. We also discuss the possible origin of the discrepancies and how they may be reduced to provide a better match.

4.4.1 Ejecta temperature and ionization

In Figure 4.7 we show $T \times R$ evolution as a function of time and ejecta velocity. According to the first law of thermodynamics, for a system expanding in a quasi-static process the change in internal energy of the system is:

$$dE = \delta Q - PdV, \tag{4.1}$$

where δQ is the infinitesimal increment of heat supplied to the system. We consider the T evoultion for an optically thick shell deep in the ejecta, where there is no ^{56}Ni. Only expansion affects the T evolution, therefore $\delta Q = 0$.

The work done by the system on the environment is the product of pressure and volume change (PdV). The plasma is radiation dominated, so $P_{\rm rad} \gg P_{\rm gas}$ and $E_{\rm rad} \gg E_{\rm gas}$. In that case,

$$P = P_{\rm rad} = \frac{aT^{4/3}}{3}, \tag{4.2}$$

$$E = aVT^4. \tag{4.3}$$

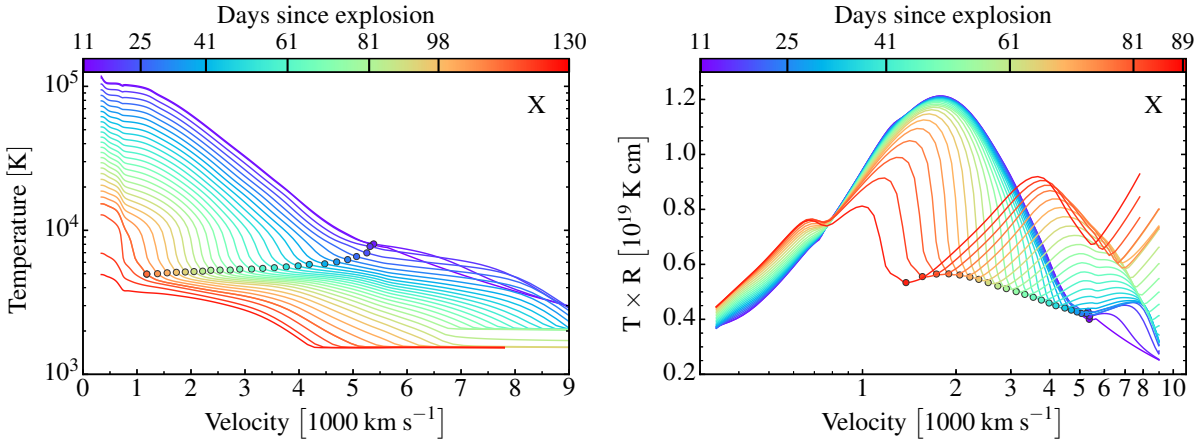

Figure 4.7 – Left panel: temperature distribution as a function of ejecta velocity and time. A color coding is used to differentiate the epochs. We overplot with a dot the corresponding location of the photosphere. From left to right, the two steep drops in the temperature curve at the last time in the sequence (red curve) correspond to the He I and H I recombination fronts. Right panel: same as the left panel, but now for the quantity R × T, which should be a constant of time for an adiabatically expanding ejecta (we use a logarithmic abscissa scale for better visibility). Deviations from the initial curve stem from energy gain due to radioactive decay at depth (below 1000 km s^{-1}) and from energy losses (radiation leakage) in the photosphere region and above.

Substituting P and E from 4.2 to 4.1, one obtains:

$$d\left(aVT^4\right) = -\frac{a}{3}T^4 dV, \tag{4.4}$$

$$aT^4 dV + aV dT^4 = -\frac{a}{3}T^4 dV, \tag{4.5}$$

$$\frac{4T^3 dT}{T^4} = \frac{-\frac{4}{3}dV}{V}, \tag{4.6}$$

$$\frac{dT}{T} = -\frac{dV}{3V} \tag{4.7}$$

Therefore $T \propto V^{-1/3}$, i.e. $T \propto R^{-1}$, and $T \times R =$ const in regions that evolve adiabatically. Hence $T \times R$ is not constant in regions rich in ^{56}Ni or at/beyond the photosphere. In Figure 4.8 we show electron density evolution as a function of time and ejecta velocity. In the right panel, the quantity $n_e \times R^3$ is used as a constant of time under fixed ionization.

4.4.2 Photometric properties

Figure 4.5 compares the optical ($UBVRI$) and near-IR (JHK) light curves of model X with the observations of SN 2008bk. A global magnitude offset (equivalent to a shift in distance modulus) has been applied because model X is somewhat too bright during the photospheric phase (the offset is of 0.5 mag, equivalent to a $\lesssim 60\%$ overestimate in luminosity), and somewhat too faint during the nebular phase.

The overestimate of the plateau brightness suggests that model X is somewhat too energetic and/or its progenitor radius is somewhat too large (Section 4.5.1). The Cepheid-based distance to the galaxy hosting SN 2008bk is unlikely to be a sizeable source of error, but the adopted reddening may be underestimated. If we adopt a reddening $E(B-V) = 0.1$ mag, the match to the color evolution is somewhat degraded but the absolute offset is then reduced from 0.5 to

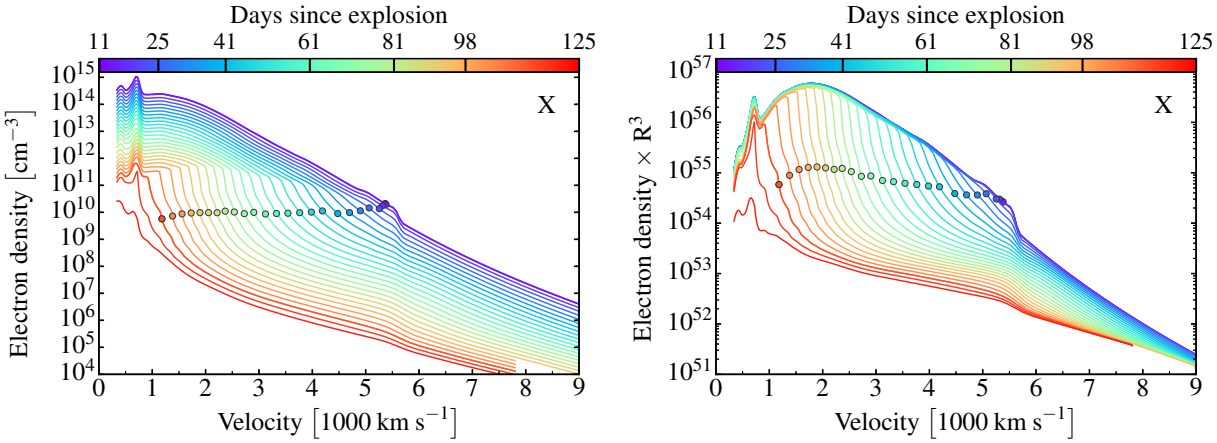

Figure 4.8 – Left: same as Figure 4.7, but now for electron density n_e. Note the steady decrease of the electron density with time t, following a general $1/t^3$ evolution, but steepening at late times and at intermediate velocities as hydrogen recombines in those regions. Right: same as the left panel, but now for the quantity $R^3 \times n_e$, a quantity that is a constant of time under fixed ionization. While the curves overlap at early times, several dips develop at later times, associated with the recombination of hydrogen (one recombination front) as well as of helium (two recombination fronts in theory).

0.2 mag. At nebular times, model X is under-luminous in the B and V bands, but it matches satisfactorily the redder bands $RIJH$ — most of the flux falls in the range 5000–10000 Å at nebular times. As we discuss in Section 4.5.3, the mixing has a large impact on the SN optical colors at nebular times. However, given the reasonable match to the filter bands where most of the flux falls (within the range 5000–10000 Å), the 0.0086 $M_\odot$ mass of ^{56}Ni in model X is satisfactory (given the adopted distance/reddening).

Leaving the color mismatch aside, Figure 4.5 shows that the multi-band light curve of model X matches adequately the multi-band light curve evolution from the U-band to the near-IR. The match to the steep drop in the U band suggests the small progenitor radius of 502 $R_\odot$ is roughly adequate, something that arises in the MESA simulation of the progenitor star from the adoption of an enhanced mixing-length parameter for convection (Dessart et al., 2013b). As we discuss in Section 4.5.1, a change of 10–20% in progenitor radius has a visible impact on the color evolution.

During the photospheric phase, the SN radiation is comparable to a blackbody modified by the effect of scattering, atmospheric extension, and line-blanketing, and it is mostly influenced by the global parameters of the progenitor star and explosion, namely $M_\star$, $R_\star$, and $E_{\rm kin}$. These aspects seem to be properly captured here. However, at nebular times (right panel of Figure 4.5), the spectrum is less directly connected to $M_\star$, $R_\star$, and $E_{\rm kin}$. Instead, it becomes primarily influenced by heating from radioactive decay and cooling from line emission. The spectrum is then more directly sensitive to chemical composition and mixing. It is therefore not surprising that model X can match better the photospheric phase than the nebular phase of SN 2008bk (see Section 4.5.3 for discussion).

The color evolution of model X during the photospheric phase is also in good agreement with the observations of SN 2008bk (Figure 4.6). In Type II SNe, the color evolution is monotonic and follows the progressive decrease of the photospheric temperature (Figure 4.9; see also Table 4.4), from the high temperature conditions at shock breakout until the recombination phase when the photospheric temperature is set by the recombination temperature of hydrogen. This phase starts in model X at 20–30 d and is associated with a flattening of the evolution of $T_{\rm phot}$, which levels

off at ~ 5500 K — $R_{\rm phot}$ is then of the order of 10^{15} cm. This is in contrast to ^{56}Ni powered SNe (e.g., SNe Ia, Ib, and Ic), in which decay heating leads to a non-monotonic evolution of the color during the photospheric phase. A $\lesssim 0.1$ mag color offset appears at the end of the high-brightness phase (the model is too red), in particular for $(V - I)$ — this is also visible in Figure 4.5. This small offset may be related to the adopted mixing between the He-core and the H-rich envelope (which is treated crudely in our approach), an overestimate of line blanketing (perhaps connected to a problem with the atomic data, e.g., with Fe I; see next section), or a problem with the data reduction of the I-band photometry (Pignata, priv. communication).

Compared to models of standard SNe II-P computed in the past with the same approach, model X is underluminous, with a typical bolometric luminosity of $\sim 1.1{\times}10^8$ L$_\odot$. For comparison, the $1.2{\times}10^{51}$ erg s15 model of Dessart & Hillier (2011) had a plateau luminosity of $\sim 6{\times}10^8$ L$_\odot$ and the more compact progenitor model MLT3 of Dessart et al. (2013b) had a plateau luminosity of $\sim 4{\times}10^8$ L$_\odot$. Both had the same photospheric temperature of ~ 5500 K at the recombination epoch. Instead, model X differs from these more energetic explosions by a much reduced photospheric radius. Model X has a radius of 10^{15} cm, a factor of 2–3 times smaller than models s15 and MLT3.

Another interesting feature, shared by models X and the higher energy variants s15 and MLT3, is that at 50 d after explosion, the photosphere has not receded by more than 1 M$_\odot$ below the progenitor surface (see also, e.g., Falk & Arnett 1977). This implies that when intrinsically polarised continuum radiation is observed soon after explosion in a SN II-P (Leonard et al., 2012b), the outermost ejecta layers have to be asymmetric.

The photospheric phase (i.e., when the ejecta Rosseland-mean or electron-scattering optical depth exceeds 2/3), or the high-brightness phase, correspond to epochs when the spectrum forms in the H-rich ejecta layers (see, e.g., Kasen & Woosley 2009, Dessart & Hillier 2011). Both the optical depth and the brightness plummet when the photosphere recedes into the layers rich in helium and intermediate-mass elements (regions that were formally part of the highly-bound compact He core), at velocities below ~ 1000 km s^{-1} in model X (see details in Table 4.4 and illustrations in Figures. 4.9, 4.10).

4.4.3 Spectroscopic properties

Figure 4.11 shows a comparison of the spectroscopic observations of SN 2008bk with model X at multiple epochs during the photospheric phase. The nebular phase will be discussed in Section 4.5.3 and in a separate study. Here, we have corrected the model for reddening, redshift, and distance to directly compare to the observations. As before for the multi-band light curves at early times, we apply a global scaling of the model that corresponds to a magnitude offset of ~ 0.5 mag (the model is 70% too luminous for our adopted distance and reddening — see discussion in the previous section).

While the photometric observations of SN 2008bk started within a week of explosion, the spectroscopic monitoring started only three weeks after explosion. The SN has entered the recombination phase (see Figure 4.9), the spectral energy distribution is already quite red, and we see clear signs of line blanketing (Fe II and Ti II) in the optical. This is made more obvious by comparing the synthetic spectrum (black) with the continuum flux from the model (blue; the continuum flux is computed, in a post-processing step, by including only the bound-free and free-free processes in the formal solution of the radiative transfer equation). Line blanketing suppresses strongly the flux shortward of 5000 Å, although one clearly sees that the continuum flux is not strong below the Balmer edge, as expected for a cool photosphere (Table 4.4 and Figure 4.4). Similarly, He I lines have already vanished and Na I D (rather than He I 5875 Å) is

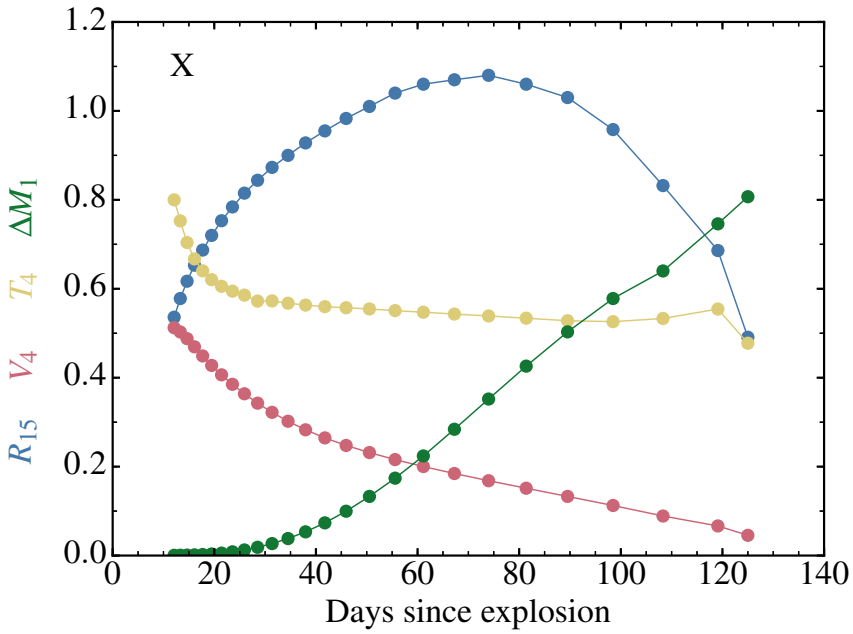

Figure 4.9 – Evolution of the properties at the photosphere of our best-match model X. We show the evolution of the photospheric radius R_{15} ($R_{15} = R_{\rm phot}/10^{15}$ cm), the photospheric velocity V_4 ($V_4 = V_{\rm phot}/10^4$ km s^{-1}), the photospheric temperature T_4 ($T_4 = T_{\rm phot}/10^4$ K), and the mass above the photosphere ΔM_1 ($\Delta M_1 = \Delta M_{\rm phot}/10\,{\rm M}_\odot$) until 140 d after explosion. The dots correspond to the actual times at which the radiation-transfer simulations were performed.

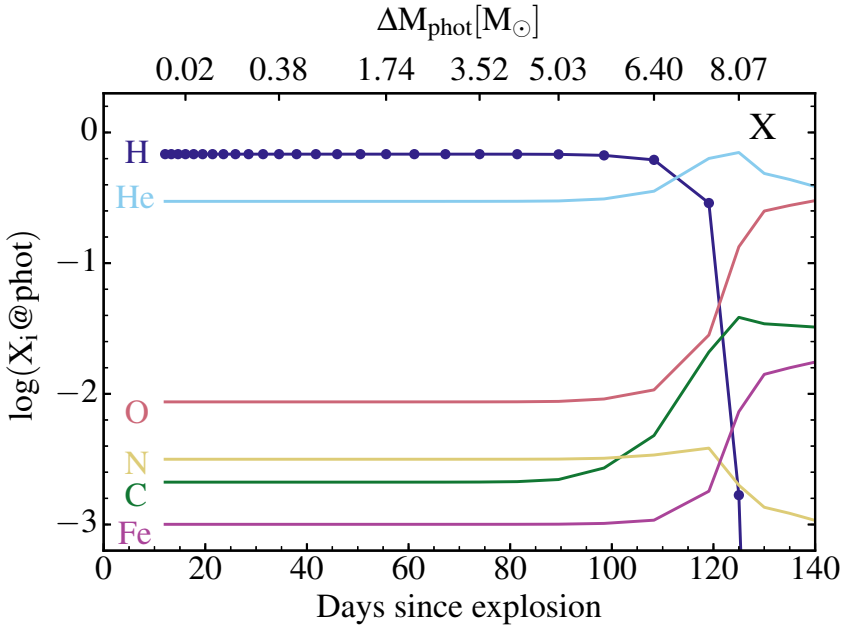

Figure 4.10 – Evolution of the composition at the photosphere for a few species.

Table 4.4 – Evolution during the photospheric phase of the total ejecta electron-scattering optical depth, and of the radius, velocity, temperature, and overlying mass at the electron-scattering photosphere (using the Rosseland-mean opacity would shift the photosphere slightly outwards in radius/velocity space). We also include the (observer's frame) bolometric luminosity. Numbers in parentheses correspond to powers of ten.

Age	$\tau_{\rm base,\,es}$	$R_{\rm phot}$	$V_{\rm phot}$	$T_{\rm phot}$	$\Delta M_{\rm phot}$	$L_{\rm bol}$
[d]		[cm]	[km s^{-1}]	[K]	[M$_\odot$]	[10^8 L$_\odot$]
12.10	26324	5.36(14)	5124	8000	5.66(−3)	1.25
13.31	21746	5.78(14)	5028	7526	7.45(−3)	1.18
14.64	17968	6.17(14)	4878	7040	1.06(−2)	1.15
16.10	14841	6.53(14)	4694	6671	1.55(−2)	1.12
17.71	12231	6.87(14)	4489	6403	2.33(−2)	1.10
19.48	10067	7.20(14)	4276	6203	3.56(−2)	1.09
21.43	8274	7.53(14)	4064	6055	5.48(−2)	1.09
23.57	6803	7.84(14)	3851	5946	8.42(−2)	1.09
25.93	5584	8.15(14)	3638	5856	1.26(−1)	1.09
28.52	4568	8.44(14)	3427	5723	1.86(−1)	1.09
31.37	3711	8.73(14)	3221	5726	2.69(−1)	1.10
34.51	2973	9.00(14)	3020	5675	3.82(−1)	1.10
37.96	2335	9.28(14)	2828	5633	5.33(−1)	1.12
41.76	1818	9.55(14)	2646	5597	7.35(−1)	1.13
45.94	1416	9.83(14)	2476	5573	9.97(−1)	1.16
50.53	1100	1.01(15)	2316	5546	1.33	1.16
55.58	857	1.04(15)	2158	5508	1.74	1.16
61.14	671	1.06(15)	2002	5472	2.24	1.16
67.25	521	1.07(15)	1845	5431	2.84	1.13
73.98	395	1.08(15)	1683	5388	3.52	1.09
81.38	288	1.06(15)	1514	5338	4.26	1.01
89.52	195	1.03(15)	1330	5281	5.03	0.885
98.47	114	9.58(14)	1126	5260	5.78	0.737
108.30	45	8.32(14)	889	5332	6.40	0.619
119.10	4	6.86(14)	666	5544	7.46	0.470
125.00	1	4.91(14)	455	4775	8.07	0.173

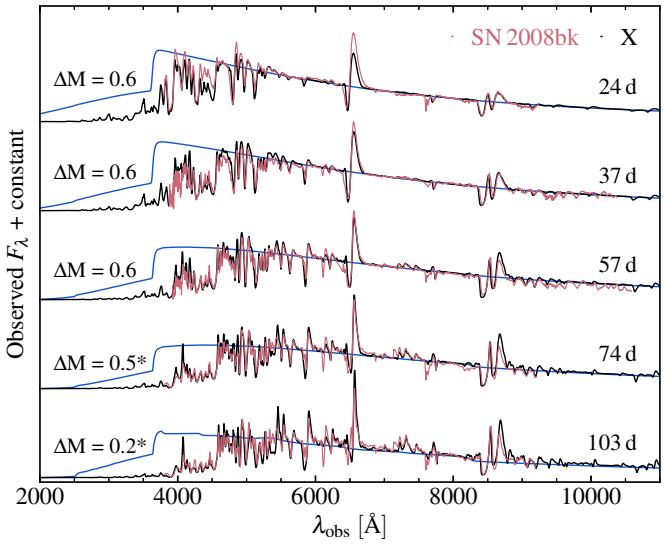

Figure 4.11 – Comparison of synthetic spectra for our best-match model X (black: full spectrum; blue: continuum only) with the observations of SN 2008bk at multiple epoch during the photospheric phase. The model spectra have been reddened, red-shifted, and distance-scaled (see Section 4.2). To facilitate the comparison of spectral features, a global flux shift has been applied to each spectrum (see the corresponding magnitude offset $\Delta M_V = M_{V,\mathrm{obs}} - M_{V,\mathrm{model}}$). In addition, when this label has a star superscript, a scaling of the relative flux distribution has been applied to match the model flux (see Section 4.2 for discussion). The poor match to the 6150 Å feature is caused by the neglect of Ba II lines in these spectral calculations (but see Section 4.4.4). See text for discussion.

already present in the first spectrum. We see H I Balmer lines (and in particular Hα) together with Ca II H&K, the Ca II near-IR triplet, O I 7773.4 Å, and a trace of Si II 6355 Å.

The spectrum evolves slowly through the photospheric phase. Line blanketing strengthens as the photospheric temperature progressively drops and the line profiles become increasingly narrow as the photosphere recedes into deeper/slower ejecta layers (Table 4.4). The photospheric velocity of model X is $\gtrsim 2000$ km s^{-1} halfway through the plateau phase, about 10–20% too large for SN 2008bk, but 50% lower than for a standard SN II-P like SN 1999em (Dessart & Hillier, 2006; Utrobin, 2007; Pignata, 2013; Bersten et al., 2011; Dessart et al., 2013b). As we approach the end of the plateau, the ionization level at the photosphere decreases so ions with a lower ionization potential start contributing. We see the strengthening of lines from Fe I and Sc II, as well as from Fe II in the red part of the optical.

Figure 4.12 illustrates the evolution of the velocity at maximum absorption in strong optical lines of H I, Fe II, Sc II, Na I, and O I. We see that the line that matches best the evolution of the photosphere (shown in black) is O I 7773.4 Å. Fe II 5169 Å, which is often used for estimating V_{phot}, tends to overestimate it in the second half of the plateau, while it underestimates it at early times (see discussion in Dessart & Hillier 2005b). Compared to SN 2008bk, the expansion rate of the model X ejecta is too large by 10–20%. The overestimate of the velocity at maximum absorption by model X is in the same sense as for the luminosity; our model X is slightly over-energetic for its mass and radius.

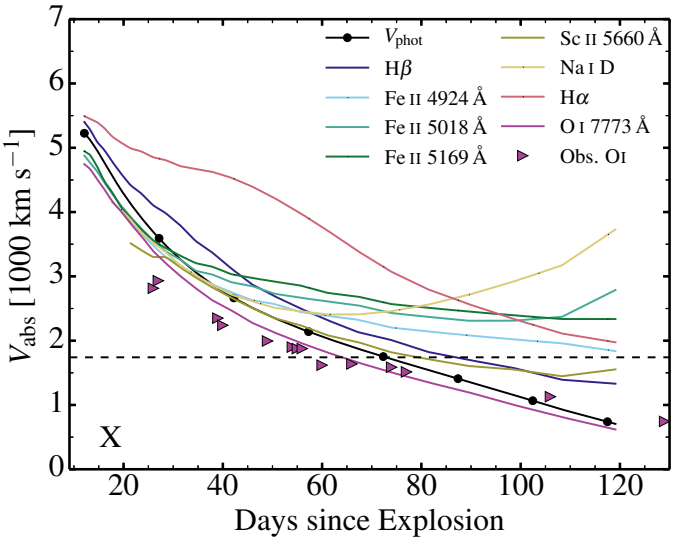

Figure 4.12 – Evolution of the velocity at maximum absorption for the bound-bound transitions at Hβ, Fe II 4924, Fe II 5018, Fe II 5169, Sc II 5660, Na I D, Hα, and O I 7773 Å. The dashed line corresponds to the quantity $V_{\rm m} \equiv \sqrt{2E_{\rm kin}/M_{\rm e}} = 1741$ km s^{-1}, and the line with dots corresponds to the photospheric velocity (calculated using the Rosseland-mean opacity). The filled triangles correspond to the observed velocity at maximum absorption for O I 7773 Å in SN 2008bk.

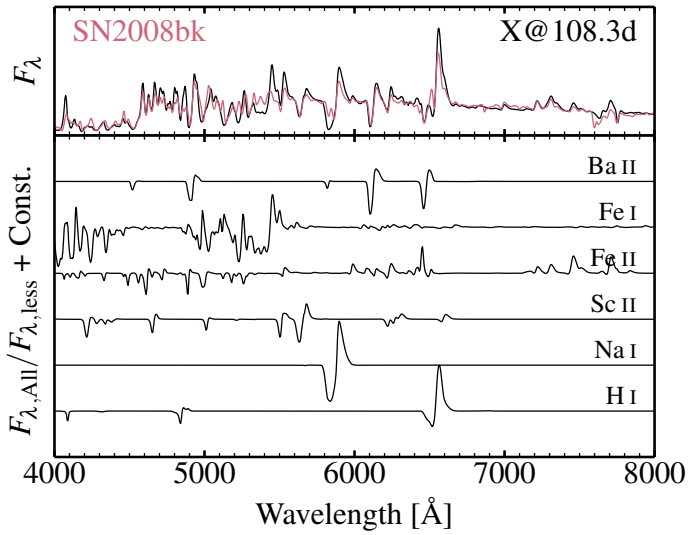

Figure 4.13 – Comparison between the observations of SN 2008bk taken on the 1st of July 2008 (corresponding to an inferred post-explosion time of 103.0 d) and a calculation for model X at 108.3 d that includes Ba II. In low-luminosity SNe II-P like 2008bk, the structure in Hα at the end of the plateau phase is caused by overlap with Ba II 6496.9 Å (not perfectly fitted here), a conclusion that is reinforced by the good match to the isolated Ba II 6141.7 Å line (compare with Figure 4.11 for the prediction with the model that does not include Ba II).

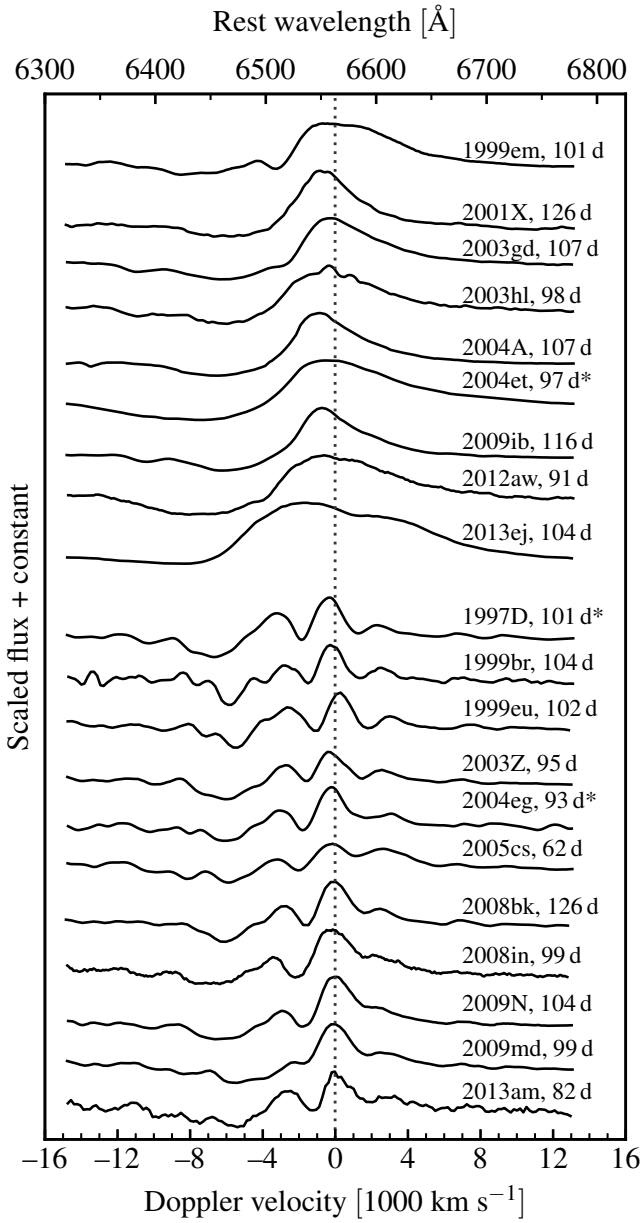

Figure 4.14 – Spectral montage of the Hα region for low-luminosity and standard SNe II-P, low-luminosity SNe are plotted in the bottom part of the figure (from 1997D to 2013am) and standard SNe (from 1999em to 2013ej) are plotted at a top. An epoch around 100 days since explosion is chosen, since the complex structure in the Hα profile is better seen at that time. If no data is available at this epoch, we use the closest observation. Low-luminosity demonstrate more complex structure of the line profile, though some of standard SNe II-P also show similar, less prominent, features in the Hα profile. The top axis shows the rest wavelength. Spectra marked with an asterisk have been smoothed to reduce the noise level.

4.4.4 Ba II lines and the structure seen in Hα

The spectral morphology is markedly different from standard SNe II; line profiles are narrower and suffer much less overlap with neighbouring features. At the end of the photospheric phase the Hα profile in SN 2008bk shows a complex structure, which is absent in model X (Figure 4.11). This may be a signature of asphericity in the inner ejecta, which our 1-D approach cannot capture. But a simpler alternative is the contamination from Ba II lines. This seems likely since we strongly underestimate the strength of the feature at 6150 Å, which may stem primarily from Ba II 6141.7 Å. Ba was not included in any time sequence here because it is an s-process element not treated in our MESA simulations.

Most low-luminosity SNe II-P exhibit a structured Hα profile at the end of the photospheric phase, while standard SNe II-P tend not to (see Figure 4.14). To investigate whether Ba II is at the origin of this complex structure, we recomputed model X at one time step with Ba II included. Because we did not have Ba in the time-dependent CMFGEN model, we used Sc II to set the Ba II departure coefficients at the previous time step. We also initialise the Ba abundance in the H-rich envelope and in the inner ejecta to the same values as those obtained in the detailed KEPLER model s15iso presented in Dessart & Hillier (2011) — our adopted Ba mass fraction in the H-rich envelope is 1.32×10^{-8}. As shown in Figure 4.13, with the inclusion of Ba II in the model atom, we now reproduce the observed feature at 6150 Å, and we also obtain a much more structured Hα line profile, although the model profile does not match exactly the observations. We also predict a weaker Ba II line overlapping with Na I D: this line has a double dip in the observations but the model shows just one broad absorption, perhaps because the model overestimates the range of velocities over which Na I D forms. The expansion rate in model X is slightly larger than needed for SN 2008bk (see also Figure 4.12), so the broader lines of the model tend to overestimate line overlap and erase the structure in the Hα region.

We surmise that the complex appearance of the Hα region at the end of the photospheric phase in low-luminosity SNe II is due to Ba II 6496.9 Å. In standard SNe II the higher expansion rate at the base of the H-rich envelope causes the contributions of Ba II 6496.9 Å and Hα to merge into a single spectral feature. In addition to the influence of Ba II, interaction with the progenitor RSG wind (ignored in our model) may influence at such late times the Hα and Hβ line profile morphology through the formation of a high-velocity absorption notch (Chugai et al., 2007). It is however unclear whether the effect would apply for our model X since its low mass RSG progenitor should have a low wind mass loss rate.

4.4.5 Additional remarks

Leaving aside the discrepancies associated with the neglect of Ba II, Figure 4.11 shows that model X reproduces closely the observed spectra of SN 2008bk — no tuning is done to the composition either initially (we just adopt the composition of the MESA model evolved at solar metallicity) or in the course of the CMFGEN time sequence. Our model seems to overestimate the absorption at 5400 Å associated with Fe I lines (see appendix), perhaps because of problems with the atomic data (the strength of Fe II lines seems adequate). The features around 9000 Å–1 μm seen in the observations of SN 2008bk at 35 and 55 d are not predicted by our models — these are perhaps observational artefacts (e.g., second order contamination when using a dichroic).

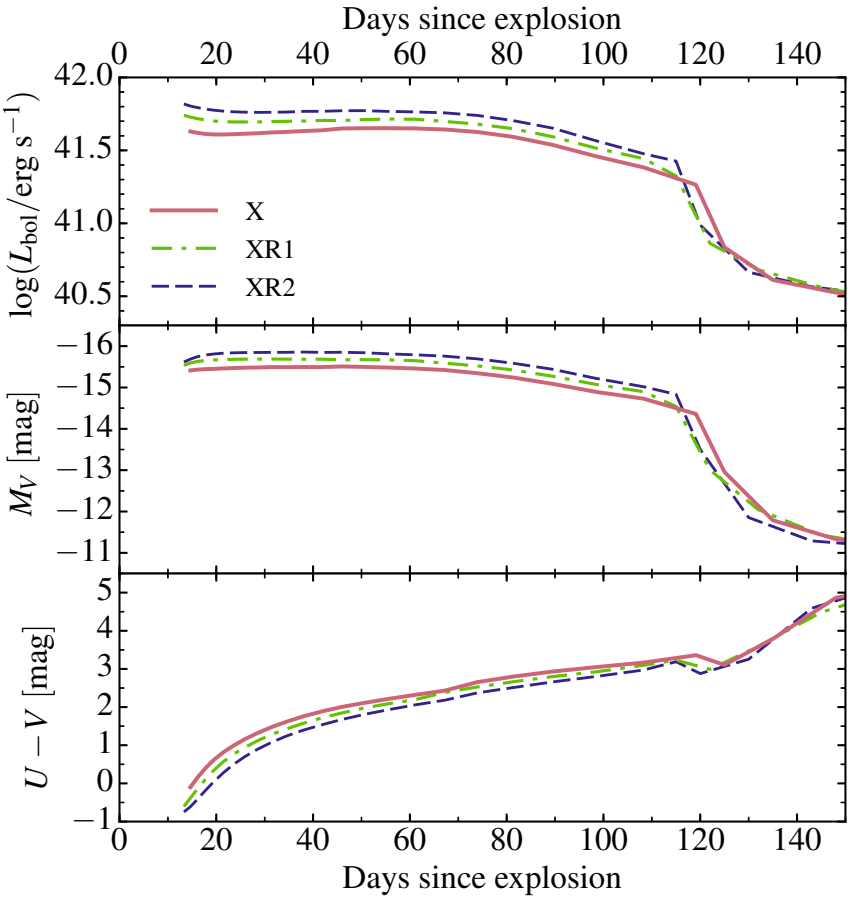

Figure 4.15 – Bolometric luminosity (top), V-band magnitude (middle) and $(U - V)$ color (bottom) for models X, XR1, and XR2, which differs primarily in the surface radius of their RSG progenitor star.

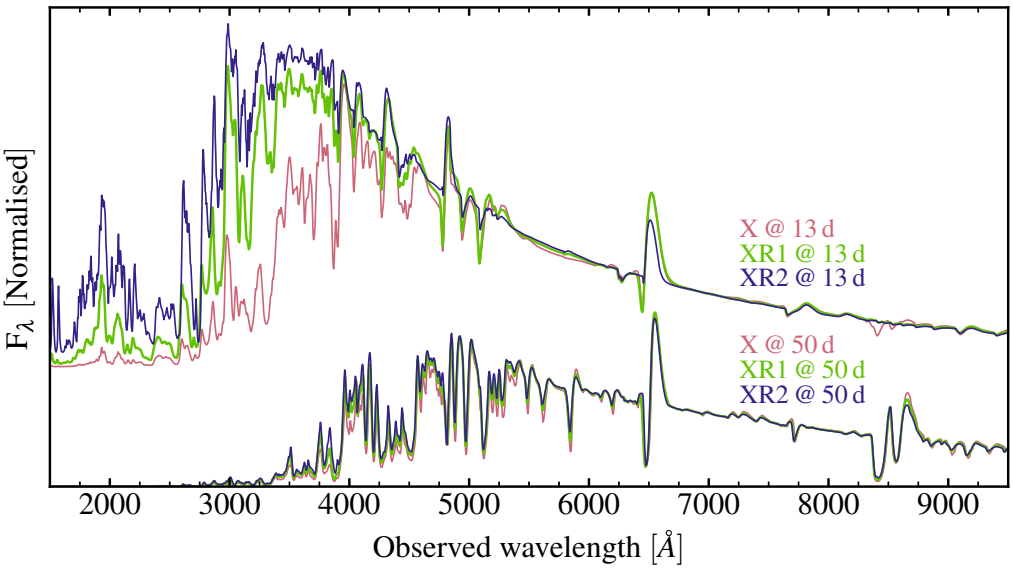

Figure 4.16 – Comparison between synthetic spectra (normalized at 9800 Å) of models X, XR1, and XR2 at the onset of the recombination phase (13.3 d; top) and half-way through the plateau phase (50.5 d; bottom). A change in progenitor radius visibly impacts the spectral appearance early on, but the impact is subtle at late times.

4.5 Sensitivity to progenitor and explosion properties

In this section, we study the impact of slight changes in the progenitor radius, chemical mixing, and ejecta mass on the resulting photometric and spectroscopic predictions. In the process, we build physical error bars for the properties of the progenitor and explosion associated with SN 2008bk.

4.5.1 Radius

To test the influence of a change in progenitor radius, we use the same approach as in Dessart et al. (2013b). In practice, we vary the efficiency of convection within the MLT formalism in MESA, by tuning the parameter $\alpha_{\rm MLT}$ from 3 (model X), to 2.5 (model XR1), and 2.0 (model XR2). As $\alpha_{\rm MLT}$ decreases, the RSG star model at death increases in radius, from 502 (X), to 581 (XR1), and 661 $R_\odot$ (XR2). The main effect of a change in the RSG progenitor radius is to mitigate the cooling of the ejecta as it expands. The larger the progenitor star, the weaker the cooling of the ejecta. Here, to isolate the influence of a change in $R_\star$, models X, XR1, and XR2 are exploded to produce ejecta with about the same kinetic energy at infinity ($\approx 2.6\times10^{50}$ erg) and about the same ^{56}Ni mass (0.008–0.009 $M_\odot$) — see Table 4.2 for details.

Figure 4.15 shows the bolometric luminosity, the absolute V-band and the $(U-V)$ light curve for models X, XR1, and XR2. A larger progenitor radius yields a larger bolometric luminosity, a greater V-band brightness, and a bluer color throughout the photospheric phase. It does not affect the length of the plateau phase. For the bolometric luminosity, the offset is roughly constant during the photospheric phase and corresponds to an increase of 15% (for an increase of 16% in $R_\star$) between models X and XR1, and an increase of 15% (for an increase of 14% in $R_\star$) between models XR1 and XR2. The offset of about 0.2 mag in V-band magnitude between X and XR1, and between XR1 and XR2, is also roughly constant past 30 d after explosion — the offset is reduced at earlier times in part because of the different colors of the model early on. The color is systematically bluer for the more extended progenitor star, and the more so at earlier times. The offset in $(U-V)$ is about 0.2 mag between each model for most of the photospheric phase, but it decreases near the end. Consequently, changes in progenitor radii may introduce a scatter in the intrinsic color of SNe II-P.

Figure 4.16 compares the synthetic spectra for models X, XR1, and XR2 at 13.3 d and 50.5 d after explosion. We normalize the models at 9800 Å to better reveal the relative variation in flux across the UV and optical. The color shift discussed above is visible in the spectra at early times. The bluer spectrum of model XR2 at a given post-explosion epoch is suggestive of a higher photospheric temperature and ionization. For example, the Ca II near-IR triplet is hardly visible in model XR2 at 13.3 d, but readily visible as a weak absorption feature in model X in which the transition to the recombination phase is more advanced. As apparent, a change of only 15% in the progenitor radius causes a significant difference in colors at early times (this offset may be missed without the correct explosion time since a larger progenitor radius merely shifts the color to later in time). The spectral offset between models X, XR1, and XR2 is however smaller than obtained between the models MLT1 and MLT3 of Dessart et al. (2013b), which resulted from the explosion of RSG stars with a much larger difference in surface radius (1100 and 500 $R_\odot$, respectively). Modulations in intrinsic color may stem from diversity in progenitor radii, although in observations, such variations can also originate from reddening.

Model X is brighter than SN 2008bk by 0.5 mag during the photospheric phase. Given the results for models XR1 and XR2, a reduction in radius by 15% would make it fainter by 0.2 mag — this could arise from the adoption of a lower metallicity, like for model Y. But a greater reduction would be needed to cancel the present offset and this would likely impact the color.

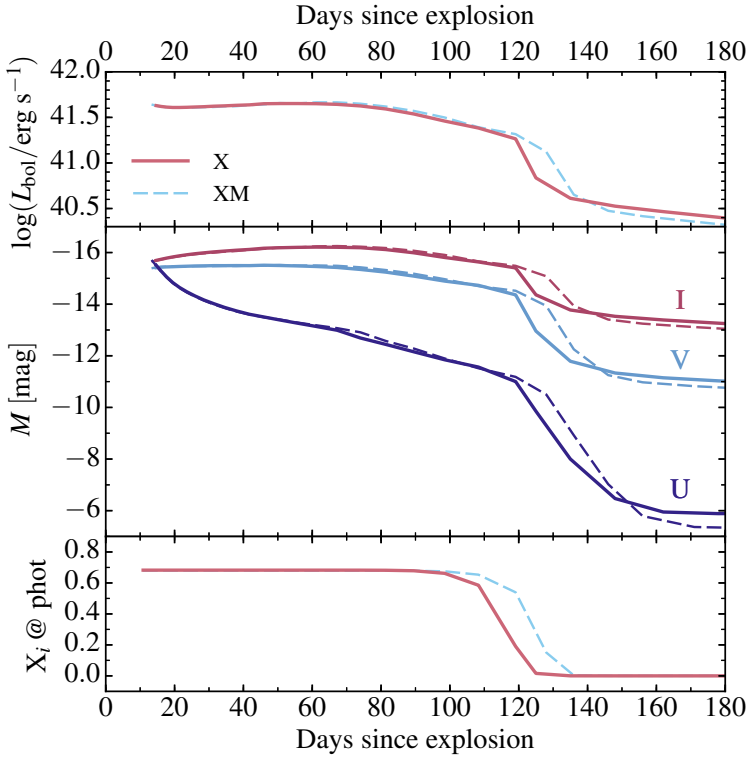

Figure 4.17 – Comparison between models X and XM showing the bolometric light curve (top), the *UVI* light curves (middle), and the H mass fraction at the photosphere during the first 180 d after the explosion.

However, the color of model X matches that of SN 2008bk, and confirms the need for a rather compact RSG progenitor star, as advocated by Dessart et al. (2013b) for SNe II-P in general (see also González-Gaitán et al. 2015). To reconcile model X with the observations (brightness and expansion rate inferred from line profile widths) would likely require a lower ejecta kinetic energy (or an increase in ejecta mass). A 10–20% increase in the distance to SN 2008bk would reduce the offset, just like an increase in reddening from 0.02 to 0.1 mag.

4.5.2 Mass

In this section, we discuss the impact of a different ejecta mass on the resulting SN radiation. We compare our best-match model X with model XM, which starts on the main sequence with the same initial conditions (mass, metallicity, etc.) but evolved with a smaller mass loss rate (see Section 4.3). This influences primarily the RSG phase and the impact is limited to the H-rich envelope mass, which is 1 $M_\odot$ greater in model XM — both models have the same He-core mass. The corresponding SN ejecta reflect this difference (see Table 4.1). In practice, the explosion models X and XM differ slightly in explosion energy so that the E_{kin}/M_e is about the same for both.

Figure 4.17 shows the resulting bolometric light curve, the *UVI* light curves, and the variation of the H mass fraction at the photosphere. The light curves are essentially identical for models X and XM, except for the longer duration of the high-brightness phase in model XM. Here, an offset in ejecta mass of 1 $M_\odot$ (which is tied to a difference in the progenitor H-envelope mass) extends the photospheric phase by ~ 10 d[14]. The bottom panel of Figure 4.17 emphasizes how

the high-brightness phase coincides with the epochs during which the photosphere is located within the layers that were formerly part of the low-density H-rich progenitor envelope.

As the photosphere moves into the layers that were formerly in the highly-bound high-density He core, the luminosity plummets. In our model X, when the optical depth at the base of the H-rich layers drops to 1, the total electron-scattering optical depth across the deeper layers (from the former He core) is only 10 and it drops to 1 within a week. This whole transition occurs during the fall off from the plateau. The light curve transition can be modulated by mixing of H and He. However, the properties of the highly bound slow-moving He-core material are hard to constrain from the light curve since the corresponding ejecta regions have a low/moderate optical depth at the end of the plateau phase.

4.5.3 Mixing

We now discuss mixing in order to test how our implementation affects our results. We use two approaches, discussed in Section 2.2.2.3. The first approach is used in models X, XR1, XR2, XM; the second in models YN1, YN2, YN3. For three latter models, there is a spike in the H mass fraction in the innermost shells because the ^{56}Ni mass fraction was close to unity in those layers prior to mixing (Figure 4.18). Models YN1, YN2, YN3 differ in the values of δm used. We have used δm = 0.5, 1.0, and 1.5 $M_\odot$. We show the composition for a selection of species in the top row of Figure 4.18.

This exercise is instructive because our various models all derive from a 12 $M_\odot$ main sequence star, with similar H-rich envelope and He-core properties. Yet, these different levels of mixing produce drastic variations at nebular times, as we discuss now.

The middle-left panel of Figure 4.18 shows the bolometric luminosity for models X and YN1/YN2/YN3. During the photospheric phase, the early-time luminosity is higher in model X because of the large progenitor radius (502 compared to 405 $R_\odot$) and the higher ratio $E_{\rm kin}/M_{\rm e}$. The lower ejecta mass of model X (8.29 compared to 9.45 $M_\odot$) produces a shorter plateau length by 20 d (all four models have the same ejecta kinetic energy of 2.5×10^{50} erg). Interestingly, the three models YN1/YN2/YN3 show a similar bump at the end of the plateau phase, despite their different levels of ^{56}Ni mixing. Model X, which has a similar level of ^{56}Ni mixing as model YN1, does not show a bump. This bump is controlled by the mixing of other species, and in particular how H and He are mixed in velocity/mass space at the He-core edge (see, e.g., Utrobin 2007). In model X, all species are mixed and this tends to soften the changes in composition in the inner ejecta, which the photosphere probes at the end of the plateau phase. H is important here because it is the main electron donor so that different levels of H mixing can modulate the evolution of the optical depth at the end of the plateau phase (and modulate the recession of the photosphere and the variation in luminosity).

The middle-right panel of Figure 4.18 shows the evolution of the $(U - V)$ color for the four models. The more extended model X is bluer during the photospheric phase, but redder at nebular epochs. Model YN3 with the strongest mixing is the redder of all four models during the photospheric phase — the extra heating does not compensate for the increased opacity from metals, but it is the bluer of all models at nebular times. The drastic change is seen when the models transition to the nebular phase. Model X becomes exceedingly red, while models YN1, YN2, and YN3 remain systematically bluer, the more so the larger the mixing of ^{56}Ni.

The broad-band fluxes of Type II SNe do not depend on the temperature in the same way at nebular times as during the photospheric phase, when the escaping radiation has roughly the

[14] We do not show a spectral comparison because both models are essentially identical at all epochs apart from the timing of the transition to the nebular phase.

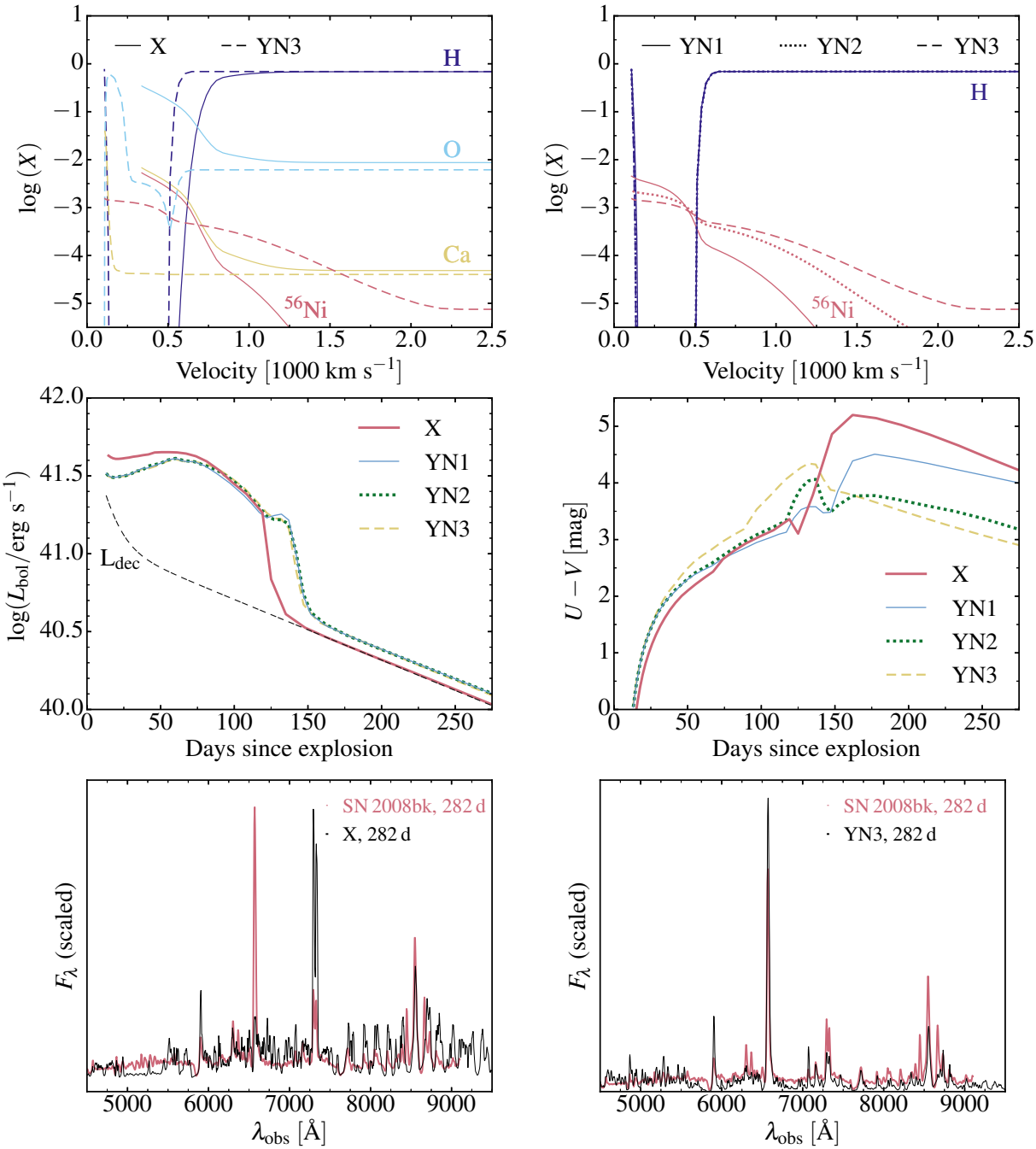

Figure 4.18 – Top row: Composition profile for models X and YN3 (left), and for models YN1, YN2, and YN3 (right) versus velocity (only the inner 2500 km s^{-1} are shown to emphasize the properties of the inner ejecta regions where the effect of mixing is strong). Middle row: Comparison of the bolometric luminosity (the dashed line gives the instantaneous decay power from an initial ^{56}Ni mass of 0.00857 $M_\odot$) and $(U - V)$ color for models X, YN1, YN2, and YN3. The longer photospheric phase for models YN1, YN2, and YN3 is consistent with their progenitor having a $\sim 1\,M_\odot$ larger H-rich envelope mass. Bottom row: Comparison of model X (left) and model YN3 (right) with the observations of SN 2008bk at 282 d after explosion. Model X underestimates the strength of Hα but overestimates the strength of the Ca II doublet at 7300 Å. In contrast, the strongly mixed model YN3 matches quite well Ca II 7300 Å and overestimates somewhat the strength of Hα.

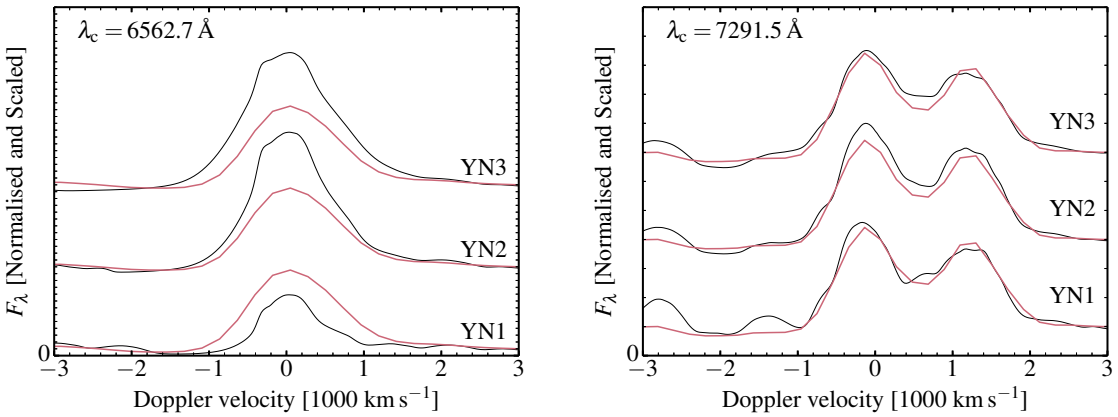

Figure 4.19 – Comparison between the observations of SN 2008bk at 282 d after explosion (red) with the models YN1, YN2, and YN3 (black) at the same epoch and for the spectral regions around Hα (left) and the Ca II doublet (the x-axis is centered on the rest wavelength of the blue component, at 7291.5 Å). In all cases, we normalize all spectra at the red-most wavelength and shift vertically for better visibility.

properties of a blackbody. At nebular times, the SN radiates the energy deposited by radioactive decay through strong emission lines, many of which being forbidden. Here, temperature and ionization of the gas control which lines cool the ejecta. Then, depending on the location of these transitions in wavelength space, one can produce different colors, even if the bolometric luminosity (which is set by the amount of decay energy absorbed by the gas) is the same between models.

In the bottom row of Figure 4.18, we show a comparison of model X (left) and model YN3 (right) with the observations of SN 2008bk at 282 d after explosion (the models and observations have been normalized at 6310 Å to better reveal the relative offsets in flux). Model X follows roughly the observed spectral energy distribution, but it underestimates the flux in the 5000 Å region and overestimates it in the red part of the optical. Model X has cooler and more recombined H-rich shells (e.g., with dominance of Fe I) than model YN3 (with dominance of Fe II). More importantly, it strongly overestimates the Ca II 7300 Å doublet and underestimates the strength of Hα. In contrast, model YN3, which has the same amount of ^{56}Ni and a similar core composition as model X, has a completely different nebular spectrum. Model YN3 matches well the Ca II 7300 Å doublet and the Ca II 8500 Å triplet and overestimates the strength of Hα by about a factor of two (model YN1, characterised by a weaker ^{56}Ni mixing, slightly underestimates the strength of Hα). The half-width-at-half-maximum is ~ 500 km s^{-1} for Hα (this velocity corresponds to the innermost H-rich layers in the ejecta) and is about 350 km s^{-1} for the Ca II 7300 Å doublet (this velocity corresponds to the He-rich ejecta regions). In both cases, the line forms over a range of velocities. For Hα, model YN3 strongly overestimates the extent of the absorption trough — model YN1 with a weaker ^{56}Ni mixing has a narrower trough that matches closer the observations (Figure 4.19). The different levels of mixing affect the Hα widths, but not Ca II 7300 Å — the ^{56}Ni mixing affects more the ionization of H I than that of Ca II in the outer ejecta.

This short exploration on mixing highlights the complications it introduces even for ejecta that have the same overall composition, mass, and energetics. How the different elements are distributed at both the microscopic and macroscopic level is a fundamental aspect of the problem (Fryxell et al., 1991; Jerkstrand et al., 2012; Wongwathanarat et al., 2015), and it depends both

on the composition prior to explosion as well on the impact of the explosion on this distribution. We will come back to the issue of mixing for nebular phase spectra in a future study.

4.6 Conclusions

We have presented the results of numerical simulations that aim at understanding the properties of the ejecta/radiation associated with SN 2008bk, as well as the progenitor star at its origin. We have focused on a single mass of 12 $M_\odot$ for the progenitor, and have evolved this model with MESA at solar metallicity but with different parameterisations for mass loss and convection in order to produce RSG stars at death that cover a range of final masses and surface radii. These models were then exploded with the radiation hydrodynamics code V1D to produce ejecta with various explosion energies and ^{56}Ni mass. Finally, starting at a post-explosion time of 10 d, we have evolved these ejecta with the nLTE radiative transfer code CMFGEN, building multi-band light curves and multi-epoch spectra that can be directly compared to observations.

Our model X, which closely matches SN 2008bk, corresponds to a star with an initial mass of 12 $M_\odot$, a final mass of 9.88 $M_\odot$, an H-rich envelope mass of 6.7 $M_\odot$ a final surface radius of 502 $R_\odot$. The associated ejecta has a mass of 8.29 $M_\odot$, a kinetic energy of 2.5×10^{50} erg and 0.0086 $M_\odot$ of ^{56}Ni. Provided we introduce a 0.5 mag offset, model X follows closely the multi-band optical and near-IR light curves of SN 2008bk, including the color evolution (e.g., the sharp drop in the U band and the near-constant evolution of the $V-$band magnitude) and the plateau duration. Model X reproduces well the spectral evolution of SN 2008bk (provided we renormalize the spectra to cancel the 0.5 mag offset in brightness), the progressive reddening of the spectra as the photospheric temperature drops and line blanketing strengthens, the reduction in line widths as the photosphere recedes to deeper/slower ejecta layers. The early color evolution and reddening of the spectra is best matched with an explosion date of MJD 54546.0. We find that model X yields lines that are 10–20% too broad — it typically overestimates the expansion rate by 10–20%. Our model X is therefore somewhat too energetic for SN 2008bk. A lower explosion energy could reduce the offset in line widths and brightness. The offset in luminosity could be reduced by invoking a larger reddening (perhaps up to $E(B-V) = 0.1$ mag) to SN 2008bk. The uncertainty in the Cepheid-based distance to the host of SN 2008bk is probably small. Given all the uncertainties involved, these offsets are reasonably small to suggest that model X is a sensible representation of SN 2008bk.

Our model of SN 2008bk is a low-energy counterpart of the models for 'standard' SNe II-P like 1999em. The mechanisms that control their evolution are the same for both — in our approach we merely reduce the energy injection to produce a model for SN 2008bk rather than one for SN 1999em. However, the lower expansion rate in SN 2008bk allows a much better inspection of the line profile fits. Interestingly, in low-luminosity SNe II, the Hα line systematically develops a complex structure at the end of the plateau phase. This structure is most likely not a signature of asymmetry, but instead caused by overlap with the strong Ba II 6496.9 Å line. This conclusion is reinforced by the good match obtained to the isolated line of Ba II 6141.7 Å in SN 2008bk.

We have performed additional models to gauge the sensitivity of our results to changes in progenitor/explosion parameters. A 15% increase in the progenitor surface radius leads to a $\sim$ 15% increase in plateau luminosity and a 0.2 mag brightening of the V-band magnitude, but does not affect the length of the photospheric phase. An increase in ejecta mass of 1 $M_\odot$ hardly affects the results for model X, except for the lengthening of the photospheric phase by 10.0 d.

In our simplistic approach, chemical mixing has little impact on the SN radiation throughout most of the plateau phase. Early on, increased mixing causes extra line blanketing and produces redder optical colors. In our models where only ^{56}Ni is mixed outwards (but no mixing is applied

to H and He), the light curve develops a 15-d long ledge before dropping from the plateau. Mixing of H with He smoothes that transition, most likely because it allows a much smoother evolution of the electron-scattering optical depth, which controls the release of radiative energy stored in the ejecta (and the rate of recession of the photosphere). However, the most drastic impact of mixing in our models is seen at the nebular times. Depending on how we perform the mixing, we can completely quench Hα, boost Ca II 7300 Å, or mitigate the temperature and ionization state of the gas to alter the SN colors. Because of all these complications, we defer the modelling of the nebular-phase spectra of SN 2008bk.

4.7 Line identifications for model X at early and late times in the photospheric phase

Here we show contributions of the individual ions to the model spectra (Figures 4.20 and 4.21). More figures for the model X are given in the Appendix B. Note that model labels ‘m12’ and ‘X’ correspond to the same model.

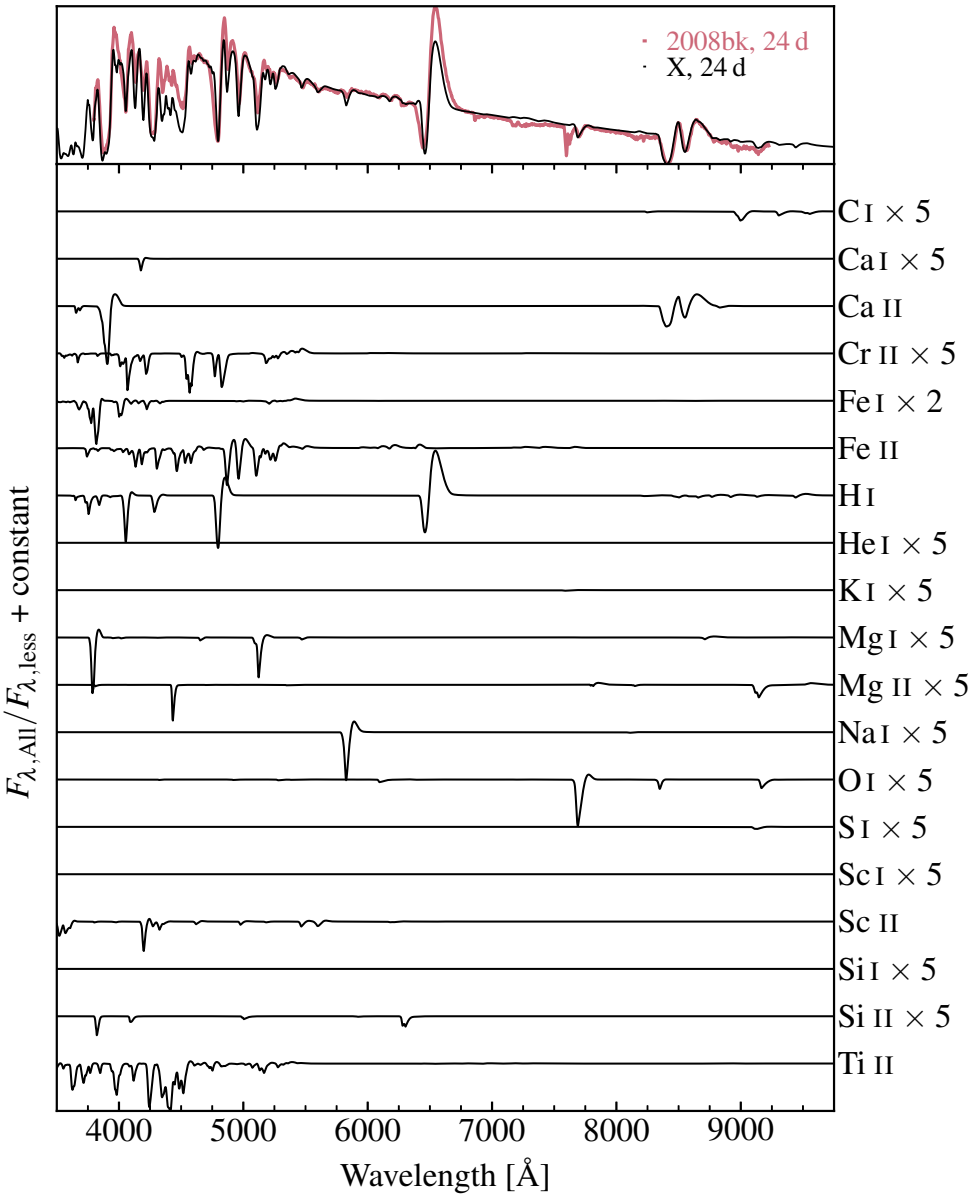

Figure 4.20 – The top panel compares model X at 24 d with the observations (dereddened, deredshifted and normalized at 7100 Å) of SN 2008bk on 13th of April 2008 (which is about 24 d after our adopted time of explosion of MJD 54546.0). The bottom panel stacks the quantity $F_{\lambda,\mathrm{All}}/F_{\lambda,\mathrm{less}}$, where $F_{\lambda,\mathrm{All}}$ is the total synthetic spectrum and $F_{\lambda,\mathrm{less}}$ is the spectrum computed with the bound-bound transitions of one atom/ion omitted (see label). For marked species, we apply some scaling factor (2 to 5, see label) to reveal the weak line features.

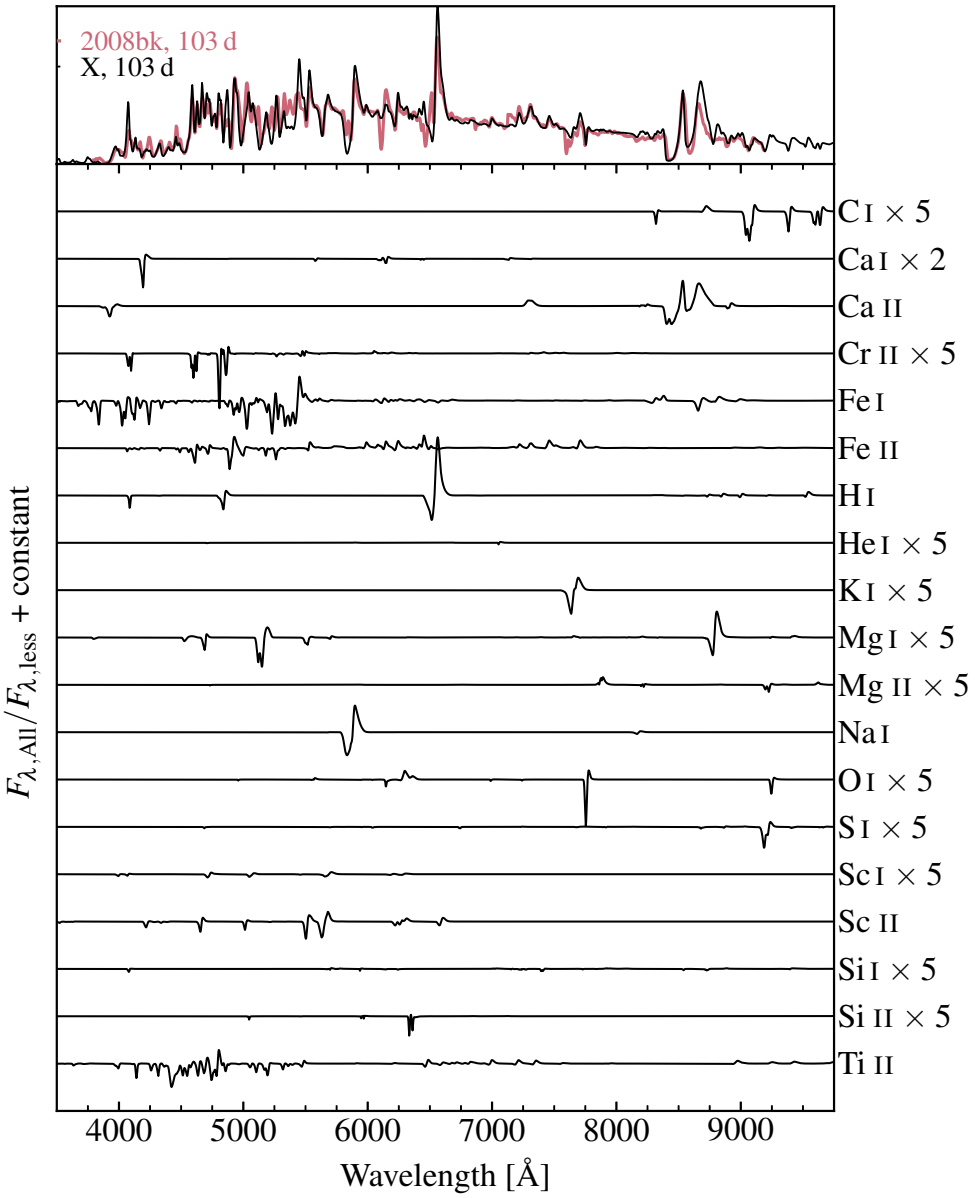

Figure 4.21 – Same as Figure 4.20, but now for model X at 103.0 d after explosion and the observations of SN 2008bk on the first of July 2008 (which corresponds to 103 d after our adopted time of explosion of MJD 54546.0; data from VLT/FORS spectropolarimetry program; Leonard et al. in prep). Because the observed flux was not well calibrated, we distort the global shape of the observed spectrum to match that of the model, which is fine here since the purpose is to inspect how line features compare between model and observations.

Chapter 5

Low-luminosity Type II-P SNe

The progenitors of low-luminosity SNe II-P are believed to be RSG stars, but there is much disparity in the literature concerning their mass at core collapse and therefore on the main sequence. In this chapter, we model the SN radiation arising from the low-energy explosion of RSG stars of 12, 25, and 27 $M_\odot$ on the main sequence and formed through single star evolution. Despite the narrow range in ejecta kinetic energy ($2.5-4.2\times10^{50}$ erg) in our model set, the SN observables from our three models are significantly distinct, reflecting the differences in progenitor structure (e.g., surface radius, H-rich envelope mass, He-core mass). Our higher mass RSG stars give rise to Type II SNe that tend to have bluer colors at early times, a shorter photospheric phase, and a faster declining V-band LC more typical of Type II-linear SNe, in conflict with the LC plateau observed for low-luminosity SNe II. The complete fallback of the CO core in the low-energy explosions of our high mass RSG stars prevents the ejection of any ^{56}Ni (nor any core O or Si), in contrast to low-luminosity SNe II-P, which eject at least 0.001 $M_\odot$ of ^{56}Ni. In contrast to observations, Type II SN models from higher mass RSGs tend to show an Hα absorption that remains broad at late times (due to a larger velocity at the base of the H-rich envelope). In agreement with the analyses of pre-explosion photometry, we conclude that low-luminosity SNe II-P likely arise from low-mass rather than high-mass RSG stars. These results are published in Lisakov et al. (2018).

5.1 Modelling

The numerical approach followed in this work is identical to the one presented in Dessart et al. (2013b). It consists of simulations for the progenitor star from main sequence to core collapse with `MESA` (Paxton et al., 2011, 2013, 2015), its subsequent explosion with the radiation-hydrodynamics code `V1D` (Livne, 1993; Dessart et al., 2010a,b), and the evolution until late times with the time-dependent radiative-transfer code `CMFGEN` (Hillier & Miller, 1998; Dessart & Hillier, 2005a, 2008; Hillier & Dessart, 2012; Dessart et al., 2013b). We briefly review each step in the forthcoming sections.

By modelling the observed SN II-P LCs and spectra, we aim to constrain the ejecta and progenitor properties. Doppler-broadened spectral lines can be used to infer the expansion rate. The Type II SN plateau duration correlates with the progenitor radius and H-rich envelope mass, as well as the explosion energy (Arnett, 1980; Litvinova & Nadezhin, 1983, 1985; Popov, 1993; Young et al., 2004; Kasen & Woosley, 2009; Dessart et al., 2013b). The SN color evolution correlates with the progenitor radius (Dessart et al., 2013b). In this paper, we investigate how the different properties of low- and high-mass RSG stars impact the SN II-P observables. For example, the He-core mass increases with main sequence mass (Woosley et al., 2002). This then

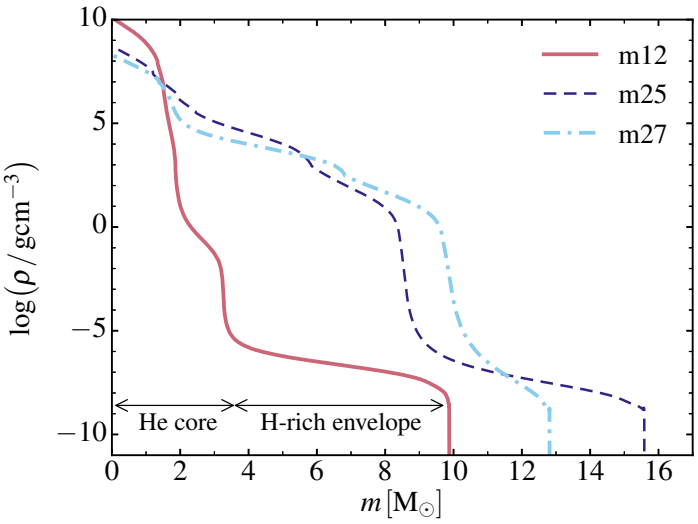

Figure 5.1 – Density versus Lagrangian mass for our set of pre-SN models, evolved with MESA. The extended H-rich envelope is the external region with $\rho < 10^{-5}$ g cm^{-3} and the region below is the He core (these two regions are indicated for model m12). The other large density jump that appears deeper in the star corresponds to the transition to the CO core.

impacts the stellar luminosity, which affects both the envelope mass (through the effect of mass loss) and the envelope radius (through the constraint of radiative diffusion).

5.1.1 Pre-SN evolution with MESA

Using MESA, we evolve three massive star models with an initial mass of 12, 25 and 27 $M_\odot$ (named m12, m25 and m27) from the main sequence until core collapse. We do not consider binary star evolution, which can alter the relation between the mass on the zero-age-main-sequence and the mass of the SN progenitor at the time of explosion. We use the same parameters as in Lisakov et al. (2017), hereafter L17. Model m12 is the same as model X from L17. For the new models m25 and m27, we use $Z = 0.0162$ rather than 0.02. Models m12, m25 and m27 end their lives with final masses of 9.9, 15.6 and 12.8 $M_\odot$, and surface radii of 502, 872 and 643 $R_\odot$. A summary of model properties is given in Table 5.2. We adopt the same prescriptions for the convection, mass loss, core overshooting etc. in all models. While the processes controlling massive star evolution are not accurately known or described, the trends that emerge from our study should be robust. Our progenitor models are in good agreement with those of Woosley et al. (2002).

Figure 5.1 shows the density profile for the three models at the onset of core collapse. In this figure, the extended H-rich envelope corresponds to the region with $\rho < 10^{-5}$ g cm^{-3}, which is exterior to the He core (its outer edge coincides with the large density jump at the base of the H-rich envelope). We take the location where the H mass fraction suddenly drops from its surface value (the whole convective envelope is homogeneous) as the interface between H-rich envelope and He core. With this definition, the H-rich envelope mass is 6.6–7.0 $M_\odot$ for the m12 and m25 models, but it is only 3 $M_\odot$ in the m27 model due to the greater mass lost during the RSG phase. In single stars, the H-rich envelope mass depends on the adopted wind mass loss rate, which is uncertain, but the trend is robust. In particular, while models m12 and m25 have a similar H-rich envelope mass, they have a very different He core mass of about 3.3 and 8.6 $M_\odot$. The core/envelope mass ratio in model m12 (3.3/6.6) is reversed in model m27 (9.8/3.0). This

Table 5.1 – Mean velocities for the whole ejecta or for the H-rich ejecta only, and velocity at the base of the H-rich layer for our models m12, m25, and m27. See text for details.

	$\overline{V}_{\rm ej}$ [km s^{-1}]	$\overline{V}_{\rm H}$ [km s^{-1}]	$V_{\rm H,min}$ [km s^{-1}]
m12	1550	1800	800
m25	1900	2200	1320
m27	2200	3150	2200

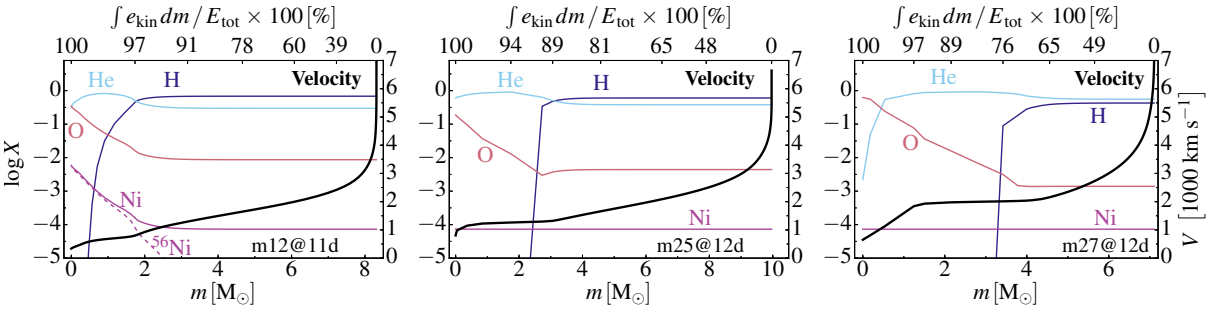

Figure 5.2 – Variation of the mass fraction for H, He, O, and Ni (the dotted line corresponds to ^{56}Ni in model m12; left panel) with ejecta lagrangian mass for models m12, m25, and m27. We overplot the velocity (thick line; right axis) and indicate the depth variation of the fractional inward-integrated kinetic energy (top axis). See Section 5.1.1 for discussion.

reversal in core/envelope mass ratio is fundamental for understanding the difference in SN properties resulting from the explosion of low- and high-mass RSG stars.

5.1.2 Piston-driven explosion with `V1D`

At the onset of core collapse, the `MESA` models are exploded with the radiation hydrodynamics code `V1D` by moving a piston at $\sim 10\,000$ km s^{-1}. The mass cut for the piston location is where the progenitor entropy rises outward from the center to 4 $k_{\rm B}$ baryon^{-1} (see, e.g., Ugliano et al. 2012). This location is at a lagrangian mass coordinate of 1.51, 1.93, and 1.78 M$_\odot$ in models m12, m25, and m27.

To produce our models of low-luminosity SNe II-P, the piston is kept at 10 000 km s^{-1} until the deposited energy exceeds the binding energy of the material above the piston by an amount $E_{\rm kin}$, where $E_{\rm kin}$ is the ejecta kinetic energy at infinity. The binding energy of the material above the piston mass cut is 1.14, 7.47, and 5.18×10^{50} erg in models m12, m25, and m27, while we aim to produce an ejecta with $E_{\rm kin} \sim 2 \times 10^{50}$ erg (which is the $E_{\rm kin}$ inferred for the prototypical low-luminosity SN 2008bk; Pignata 2013; L17). This value of $E_{\rm kin}$ is therefore of the order or smaller than the binding energy above the piston. To prevent the hydrodynamical simulation from going on hold because of a Courant-time limitation, we set a minimum piston velocity of 100 km s^{-1} (rather than zero) in these simulations. This prevents the growth of a hot and dense shell with negative velocities above the inner boundary. We consider as fallback material any material moving slower than 150–200 km s^{-1} at 10^6 s after the piston trigger. With this assumption, our weak explosions produce significant fallback material in the inner layers, much more than in standard SNe II-P where the ejecta kinetic energy exceeds the binding energy of the material to expel (see., e.g., Dessart et al. 2010a). In models m12, m25, and m27, the fallback mass (i.e., envelope material moving within a factor of 1.5–2 of the asymptotic piston velocity) is 0.08, 3.69, and 4.0 M$_\odot$. In m12, this means that most of the Si-rich layer falls back, while

in models m25 and m27, it is the entire CO core that falls back, leading to the formation of a 5–6 $M_\odot$ BH. In models with fallback, it is not straightforward to predict the kinetic energy of the ejected material. Here, our ejecta have a kinetic energy of 2.5, 4.2, and 4.2×10^{50} erg in models m12, m25, and m27. While about 0.009 $M_\odot$ of ^{56}Ni is expelled in model m12, the strong fallback in models m25 and m27 prevents any ejection of ^{56}Ni. We have not tried to prevent this by additionally enhancing the mixing (we use the same mixing in models m12, m25, and m27; see L17 for details). Lacking a decay power source, the ejecta of models m25 and m27 produce a negligible luminosity at nebular times. Hence, most of our discussion will be focused on the photospheric phase, when the photosphere is located in the H-rich layers of the progenitor star.

We show the composition profile for the ejecta for our models in mass and velocity space in Figure 5.2. For model m12, about 50% of the total ejecta kinetic energy is contained in the outer 2 $M_\odot$ of the ejecta, and only a few percent in the former He core (below 2000 km s^{-1}). For models m25 and m27, the former He core contains $\sim$9% and $\sim$25% of the total ejecta kinetic energy, respectively. The mass-weighted mean velocity of the whole ejecta ($\overline{V}_{\rm ej}$) and of the H-rich material ($\overline{V}_{\rm H}$) are given in Table 5.1, together with the velocity at the junction between H-poor/H-rich layers (corresponding to the former core/envelope transition; $V_{\rm H,min}$). This value correlates with the minimum width of Hα in the Type II SN spectrum (Dessart et al., 2010b).

Because of variations in $E_{\rm kin}$ and/or $M_{\rm ej}$ and differences in the chemical/mass stratification, the $\overline{V}_{\rm H}$ and $V_{\rm H,min}$ vary significantly between models. These variations will have a clear impact on the resulting SN observables, which are discussed in Sections 5.2 and 5.3. The value $V_{\rm H,min}$ is, however, uncertain because it is not clear how much and how deep H will be mixed inwards. Wongwathanarat et al. (2015) have demonstrated that in a standard energy explosion of a 15 $M_\odot$ progenitor, H may be mixed all the way to the innermost layers. No simulation has provided reliable constraints for H mixing in a low energy explosion of a higher mass star, in which the He core mass is much larger (and may exceed the H-rich envelope mass) and in which strong fallback occurs. We note that strong inward mixing of H is not guaranteed. Type IIb SNe are a notorious example since they show broad Hα typically for 1–2 weeks. Hα is absent in the nebular-phase spectra of SN 2011dh (Jerkstrand et al., 2015). H mixing is perhaps facilitated in progenitors with a small He core mass and a massive H-rich envelope, hence lower mass stars on the main sequence.

It is interesting to compare our model set to the simulations of Sukhbold et al. (2016), in particular those produced using a light bulb mimicking a neutrino-driven explosion, nicknamed `P-HOTB`. Model m12 properties correspond closely to the 9–12 $M_\odot$ models of Sukhbold et al. (2016) exploded with the Z9.6 engine, which systematically yield low energy explosions, a low/moderate ^{56}Ni mass, and a NS remnant. The 25 $M_\odot$ progenitor models of Sukhbold et al. (2016) all explode with a 10^{51} erg ejecta kinetic energy with a large ^{56}Ni mass, in contrast with our model m25. However, the model 27.3 of Sukhbold et al. (2016), exploded with `P-HOTB` using the W18 calibration yields an ejecta devoid of ^{56}Ni, with a kinetic energy of 4.1×10^{50} erg, and leaves behind a BH of 6.24 $M_\odot$. These properties are similar to those of model m27. Hence, our models based on piston-driven explosions have counterparts in the more physically consistent explosion models of Sukhbold et al. (2016), although the latter depend significantly on the way the explosion engine is calibrated (engines N20 and W18 can yield drastically different outcomes for the same progenitor).

5.1.3 Radiative-transfer modelling with `CMFGEN`

At a post-explosion time of $\sim$11 d, the ejecta are close to being in homologous expansion. We then remap the `V1D` ejecta structure and composition into the radiative-transfer non-Local-

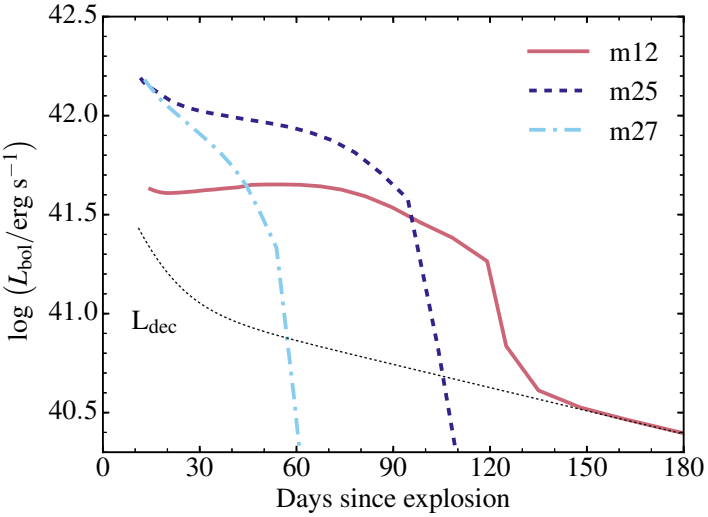

Figure 5.3 – CMFGEN bolometric light curves for models m12, m25, and m27. In this sequence, the light curve evolves from a II-P to a II-L morphology, with a greater luminosity at earlier times and an earlier transition to the nebular phase.

Table 5.2 – Summary of progenitor and ejecta properties for our models m12, m25, and m27. The left half of the table gives the initial mass M_i and pre-SN properties (M_f, $R_\star$, T_{eff}, $L_\star$, H-rich envelope mass, He-core mass, binding energy above the piston mass cut). The right half gives some properties of the corresponding ejecta, i.e., the ejecta mass, the remnant mass, the total yields for H, He, O, the amount of ^{56}Ni synthesized in the explosion and the asymptotic ejecta kinetic energy.

Model	M_i	M_f	$R_\star$	T_{eff}	$L_\star$	H-rich	He-core	E_b	M_{ej}	M_{remn}	H	He	O	^{56}Ni	E_{kin}
	[M$_\odot$]	[M$_\odot$]	[R$_\odot$]	[K]	[L$_\odot$]	[M$_\odot$]	[M$_\odot$]	[B]	[M$_\odot$]	[M$_\odot$]	[M$_\odot$]	[M$_\odot$]	[M$_\odot$]	[M$_\odot$]	[B]
m12	12	9.9	502	3906	52733	6.6	3.3	0.11	8.29	1.59	4.54	3.24	0.22	0.0086	0.25
m25	25	15.6	872	4299	233050	7.0	8.6	0.75	9.98	5.62	4.34	5.17	0.13	0	0.42
m27	27	12.8	643	5227	276761	3.0	9.8	0.52	7.02	5.78	1.37	4.72	0.4	0	0.42

Thermodynamic-Equilibrium (nLTE) time-dependent radiative transfer code CMFGEN and model the subsequent evolution of the gas and the radiation until nebular times. The code computes the gas and radiation properties by solving iteratively the statistical equilibrium equations, the gas-energy equation and the first two moments of the radiative transfer equation — time-dependent terms are accounted for in all equations. Our numerical setup (numerical grid, atomic data, model atoms) is identical to L17. We present the results of the radiative-transfer modelling in the next section.

SN 2008bk follows closely the average brightness, expansion rate, and color during the photospheric and nebular phases of our sample of low-luminosity SNe II-P (Figs. 3.1, 3.2, 3.3, 3.5, 3.6, 3.8). SN 2008bk can therefore be used as a template for this class of events when confronting models to observations of low-luminosity SNe II-P.

Table 5.3 – Sample of results for our set of simulations. $\Delta t_{\tau>1}$ gives the post-explosion time when the ejecta turns optically thin to electron scattering. We then quote the values at 15 and 50 d after explosion of the bolometric luminosity, the V-band magnitude, the $U-V$ color, the photospheric velocity, and the Doppler velocity at maximum absorption in Hα. Numbers in parentheses correspond to powers of ten.

Model	$\Delta t_{\tau>1}$ [d]	$L_{\rm bol}$ [erg s^{-1}]		M_V [mag]		$U-V$ [mag]		$V_{\rm phot}$ [km s^{-1}]		V(Hα) [km s^{-1}]	
		(15d)	(50d)	(15d)	(50d)	(15d)	(50d)	(15d)	(50d)	(15d)	(50d)
m12	131	0.45(42)	4.8(41)	–15.49	–15.61	–0.06	2.01	4833	2401	5290	3910
m25	112	1.38(42)	9.3(41)	–16.22	–16.50	–0.87	1.46	5065	3371	5724	4213
m27	64	1.37(42)	3.0(41)	–16.38	–15.28	–0.72	2.95	6251	2498	6706	6062

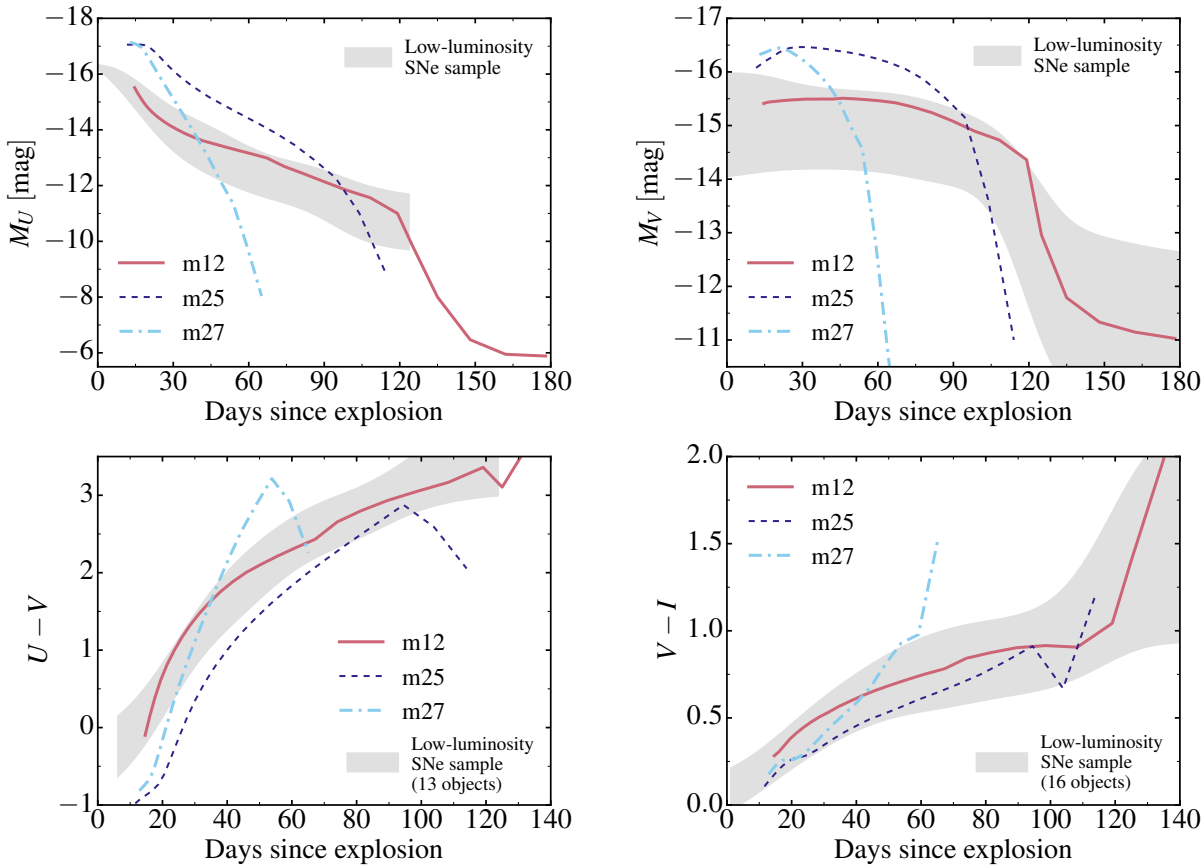

Figure 5.4 – Evolution of the CMFGEN U and V absolute magnitudes, as well as $U-V$ and $V-I$ colors for models m12, m25, and m27. We shade the region where the observed low-luminosity SNe II-P reside (see Chapter 3). Model m12 produces the closest match to the data.

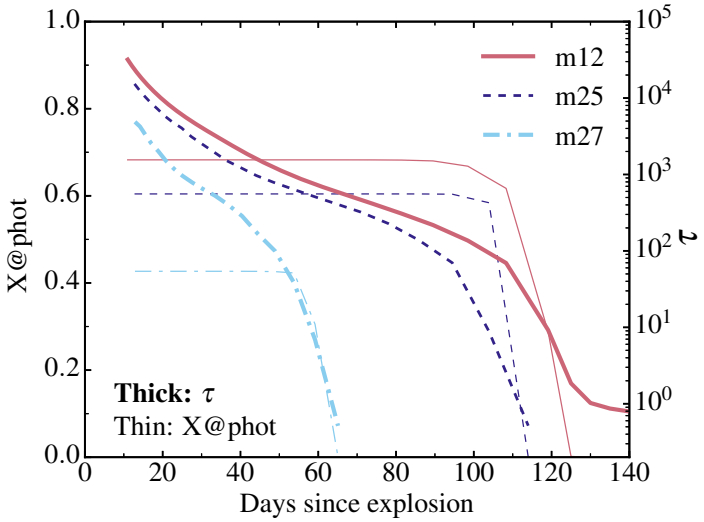

Figure 5.5 – Evolution of the hydrogen mass fraction at the photosphere (thin lines) and the total ejecta electron-scattering optical depth τ (thick lines) obtained by CMFGEN for models m12, m25, and m27.

5.2 Bolometric and multi-band light curves

5.2.1 Results from simulations

Figure 5.3 shows the CMFGEN bolometric light curves for models m12, m25, and m27. In this order, the morphology of the bolometric light curve goes from a plateau to a fast declining one. The faster the decline rate, the greater the early-time luminosity, and also the earlier the transition to the nebular phase. These properties are a consequence of the progenitor structure. Here, the II-P/II-L morphology is largely a result of the high/low H-rich envelope mass in the progenitor (Bartunov & Blinnikov, 1992). The association of a faster-declining light curve with a higher brightness at early times and a shorter photospheric phase duration is a consequence of the greater $E_{\rm kin}/M_{\rm ej}$ in model m27 compared to model m12. This correlation is observed in the large sample of Type II SNe of Anderson et al. (2014a).

Figure 5.4 shows the evolution of the U and V bands absolute magnitudes as well as the $U-V$ and $V-I$ colors for the models m12, m25, and m27. The morphology of the bolometric light curve discussed above is partly reflected by these curves but not exactly because of the different color evolution. The larger radius in models m25 and m27 (870 and 640 $\mathrm{R}_\odot$) cause bluer optical colors than in model m12 (500 $\mathrm{R}_\odot$). However, the higher $E_{\rm kin}/M_{\rm ej}$ cause a faster drop of the brightness in all optical bands for the two higher mass models. The effect is exacerbated in model m27 because of the low H-rich envelope mass in the progenitor. This produces a faster declining U-band light curve in higher mass models (they start bluer but fade faster bolometrically). In model m25, the rise time to the brighter V-band maximum is longer than in model m12 because of the bigger radius, as obtained in Dessart & Hillier (2011) and Dessart et al. (2013b).

The V-band LC for model m12 shows a long plateau of ~ 120 d, which corresponds closely to the duration of the photospheric phase (i.e., when the ejecta electron-scattering optical depth is greater than 2/3). For higher mass models, the LC first rises to a maximum at $\gtrsim 20$ d and then declines rapidly without showing a plateau. The duration of the photospheric phase for models m12, m25 and m27 is 131, 112, and 64 d. In the presence of ^{56}Ni, the photospheric phase in models m25 and m27 would have been longer, although physically, the strong fallback in such

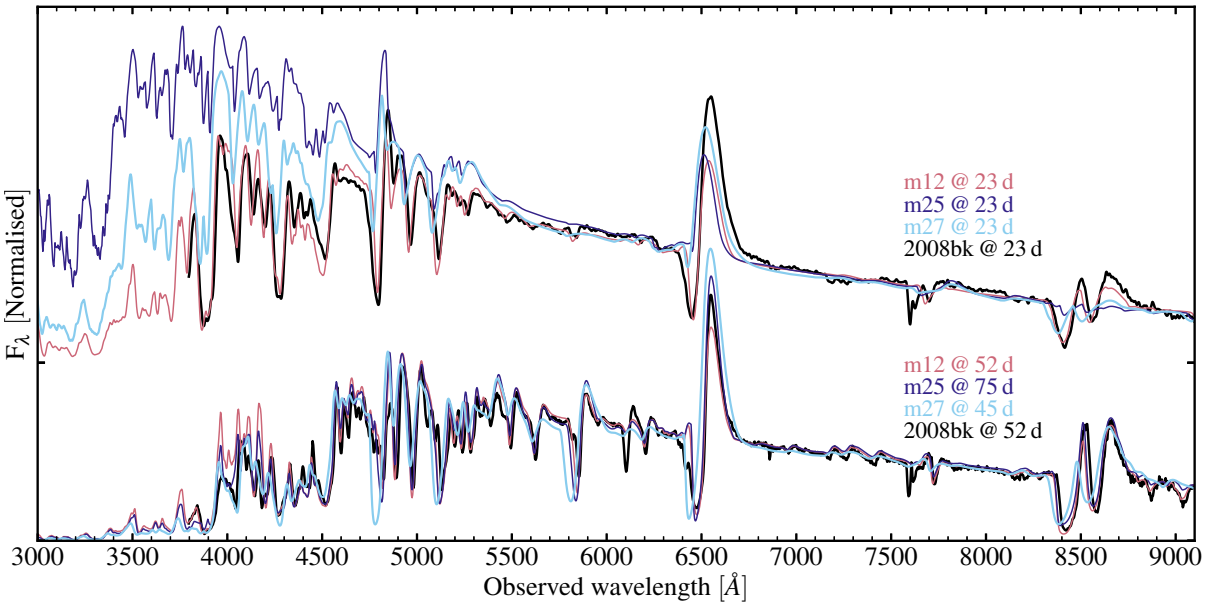

Figure 5.6 – Spectral comparison of models m12, m25, and m27 at 23 d after explosion and when their $U-V$ color is ~ 2 mag (which corresponds to different post-explosion times, as indicated by the labels; see also Figure 5.4). The ordinate ticks mark the zero flux level for each spectrum. We overplot the corresponding spectrum of SN 2008bk (corrected for extinction and redshift). Fluxes are normalized at 7100 Å. While it is hard to distinguish the models at the recombination epoch (ignoring the offset in line widths, the high mass models agree with SN 2008bk as well as model m12), the spectra for high mass models are strongly discrepant at early times. The broad absorption at 7600 Å is caused by atmospheric absorption.

ejecta likely inhibits the escape of ^{56}Ni. The stark contrast between models at nebular times is thus a reflection of the difference in ^{56}Ni mass between m12 ($0.009\,M_\odot$) and m25/m27 (zero).

Figure 5.5 illustrates how the total ejecta electron-scattering optical-depth τ and the H mass fraction at the photosphere evolve with time. The photosphere remains in the H-rich layers until τ drops to a few tens, after which it decreases faster. In an homologous ejecta, τ evolves as $1/t^2$ if the ionization is fixed. When the material recombines (at early times and also at the end of the plateau), τ drops much faster (see also Dessart & Hillier 2011). In model m12, τ follows a steady $1/t^2$ evolution at nebular times because the ionization changes little (we are in a steady state and the luminosity follows the ^{56}Co decay rate). In models m25 and m27, the absence of ^{56}Ni in the ejecta makes τ (or the ionization) and the luminosity plummet.

5.2.2 Comparison to observations

In Figure 5.4, the shaded area in each panel contains the scatter of data points for the observed SNe II-P. Model m12 fits best the observed distribution, while model m25 gives a poor match, and model m27 does not fit the observations at all. The disagreement comes from separate properties of the m25/m27 models.

While all observed low-luminosity SNe II-P exhibit a 120-d long plateau in their V-band light curve, this property is best matched by model m12 (Figure 3.1). Model m25 shows roughly a V-band plateau (but shorter). Model m27 has an even shorter high-brightness phase and a more pronounced declining V-band light curve (model m27 shows a 0.7 mag drop in V-band magnitude between 20 and 40 d after explosion, which is similar to the 0.6 mag drop that is observed in the Type II-L SN 1979C; de Vaucouleurs et al. 1981). The lack of fast decliners

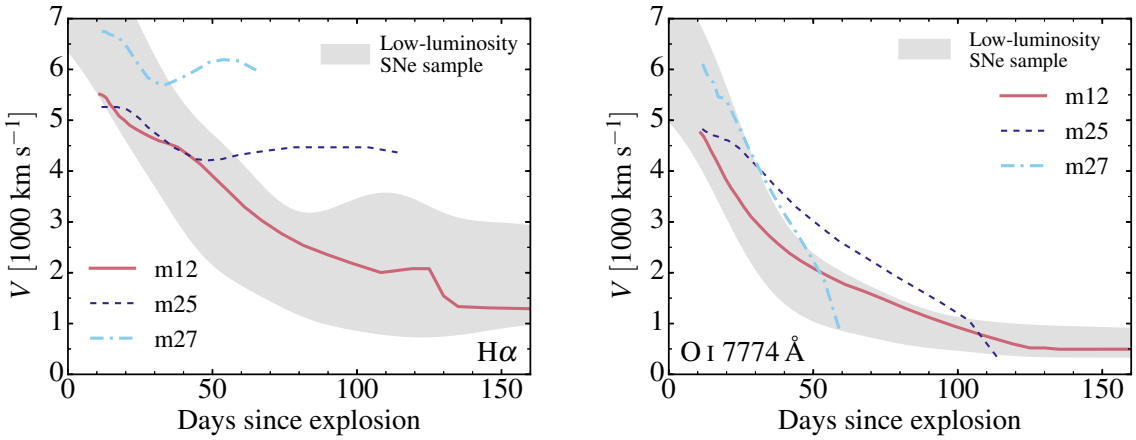

Figure 5.7 – Velocity at absorption maximum in Hα (left) and O I 7774 Å (right) for models m12, m25 and m27 compared to the observations. The Doppler velocity at maximum absorption in O I 7774 Å is a good tracer of the photospheric velocity (L17), while Hα provides constraints on the H-rich envelope mass and kinematics.

in the observed low-luminosity SNe II-P suggests that the progenitors have massive and dense H-rich envelopes, which excludes a high mass progenitor like m27.

At nebular times, the ^{56}Ni-deficient models m25/m27 do not match any low-luminosity SN II-P, which eject at least 0.001 $M_\odot$ of ^{56}Ni (Pastorello et al., 2004; Spiro et al., 2014). Mixing in 1-D piston-driven explosions is a parameter so it could be artificially enhanced in our high mass models to attempt to eject a small amount of ^{56}Ni. However, this would be highly contrived. In model m12, the low production of ^{56}Ni is a natural consequence of the weak SN shock and the progenitor density structure (i.e., little mass at high density). A low ^{56}Ni mass production in a low-mass RSG is therefore expected (Kitaura et al., 2006). Although not compelling evidence, the absence of low-luminosity SNe II-P that eject no ^{56}Ni is suggestive that a low-mass progenitor is more suited for these events.

At early times, the high mass models m25 and m27 also exhibit bluer colors than the observed sample of low-luminosity SNe II-P. The effect is more striking when comparing blue and red filters in the optical, e.g., $U - V$ rather than $V - I$, because the peak of the spectral energy distribution is around 6000 Å. The bluer colors of high mass progenitors stem primarily from their larger progenitor radius, which arises from their larger He-core luminosity. Although the early-time brightness can be reduced by lowering the explosion energy (or by reducing the progenitor mass loss to produce a more massive H-rich envelope), high-mass models will tend to be bluer and decline faster than both the lower-mass counterparts and the observations.

5.3 Spectra

5.3.1 Results from simulations

Figure 5.6 shows a spectral comparison for models m12, m25, and m27 at 23 d after explosion and when $U - V \approx 2$ mag (which corresponds to post-explosion times of about 50 – 70 d after explosion).

At early times, the color difference discussed above is reflected in the different spectral energy distribution. As we step from model m12, m27, to m25, the optical spectrum is bluer, shows weaker signs of line blanketing, and has broader lines. This directly reflects the trend in

progenitor radius, which impacts the cooling from expansion. The spectral signatures are broader (with more line overlap) in model m27, something that arises from the similar $E_{\rm kin}/M_{\rm ej}$ amongst models but the much lower H-rich envelope progenitor mass in model m27.

In model m12, the Hα and Hβ line widths and strengths are somewhat underestimated, while the width and strength of Ca II, Na I, Sc II, or Fe II lines are well matched. One possible origin for the mismatch of the Balmer lines is an inadequate treatment of the outermost layers of the progenitor. In model X we impose a very steep surface scale height of 0.01 $R_\star$ that results in a steep drop in the ejecta density at 5500 km s^{-1}. A more extended progenitor atmosphere would have produced a more gradual and continuous decrease in density at large velocities, perhaps resolving this conflict. The complexity of RSG atmospheres compromises an adequate description of these layers in our pre-explosion model. However, the fair agreement for all lines suggests the ejecta kinetic energy is adequate (L17).

At later times during the photospheric phase (when $U - V \approx 2$ mag), the spectral properties are very similar between our three models. The difference is primarily from the width of the lines, which is somewhat greater in models m25 and m27 because of the greater $E_{\rm kin}/M_{\rm H\text{-}env}$ relative to model m12. The broader lines in model m27 cause greater line overlap, in particular in the blue part of the optical where line blanketing is strongest in Type II SNe. The effect is present in Hα, but also in metal lines like O I 7774 Å (Figure 5.7; the Doppler velocity at maximum absorption in this line matches closely the photospheric velocity during the high-brightness phase; L17). The comparison at this late epoch should be considered with caution. Models m25 and m27 have an ejecta optical depth of about 200, but this is about 1000 for model m12. Combined with the higher velocities, this implies lower photospheric densities in the higher mass models.

Overall, the synthetic spectra for our three models m12, m25, and m27, are very similar when compared at the same $U - V$ color. When considered with respect to the time of explosion, the offset between spectra is much greater because of the impact of differences in progenitor radius, mean expansion rate etc., which strongly affect the photometric (brightness and color) evolution.

The evolution of the Hα line width can be used to distinguish the models. Because of the different H-rich envelope to He-core mass ratio in the models m12, m25, and m27, the velocity at the base of the H-rich envelope is very different (despite the similar ejecta kinetic energy; Table 5.1; see also Dessart et al. 2010b). Although mixing was applied to all models, the big He-core in models m25 and m27 prevents much mixing of H deep inside the He core. As a result, the Hα line remains broad at late times. This is in contrast to the m12 model in which most lines progressively narrow as time progresses.

5.3.2 Comparison to observations and spectral line identifications

In Chapter 4, we demonstrated that model m12 (named model X in Chapter 4) gave a good match to the spectral evolution of SN 2008bk, which is a prototype for the sample of low-luminosity SNe II-P. The distinct spectral evolution of models m25 and m27 relative to model m12 implies that these high mass models fail to match the spectral evolution of SN 2008bk, and by extension that of the whole sample of low-luminosity SNe II-P (see Figure 3.8). The mismatch at early times is tied to the different color evolution (which impacts the spectral index and ionization; Figure 5.6). The evolution of the Doppler velocity at maximum absorption in Hα also shows a late plateau at a high value of 4000–6000 km s^{-1} in models m25 and m27, while the observations show a reduction of this Doppler velocity to very low values of $\sim$ 1000 km s^{-1}, as obtained in model m12 (Figure 5.7). Hence, we find that high mass models show numerous photometric and spectroscopic discrepancies with respect to observed low-luminosity SNe II-P, while the low mass model m12 fares better.

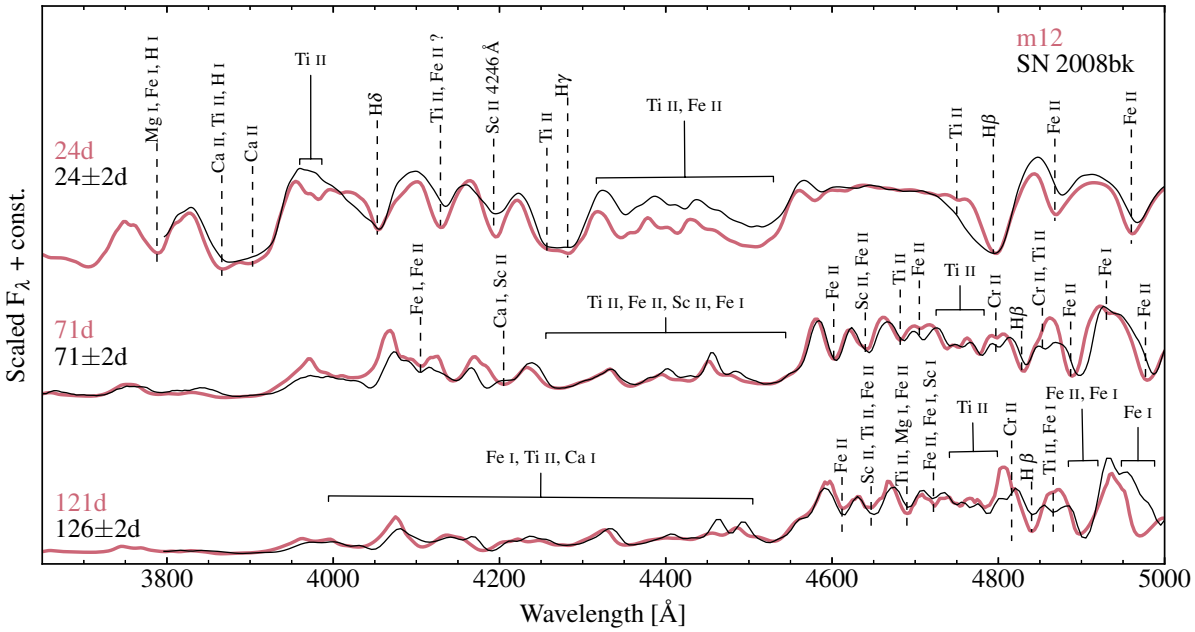

Figure 5.8 – A comparison between low-luminosity SN 2008bk and our model m12. Spectra of SN 2008bk are corrected for the redshift and the reddening. The ordinate ticks mark the zero flux level for each spectrum. Dashed lines point to the position of the absorption maximum of the corresponding ion for model m12. Lines are identified from the synthetic spectra computed without the bound-bound transitions of a given ion.

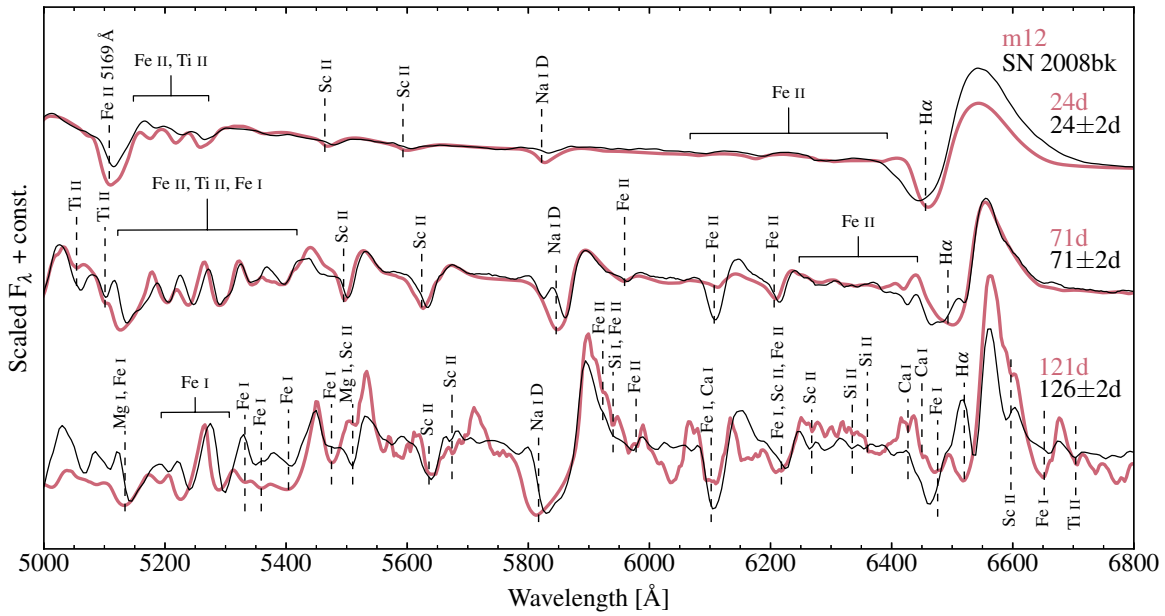

Figure 5.9 – Same as Figure 5.8, but showing the 5000–6800 Å region. Region from 6250 Å to 6350 Å is formed by complex and rich contributions from Fe I, Fe II, Sc II, Si II, O I, Sc I, and Si I. We show in the plot only those lines that can be identified with certainty. Ba II, which is omitted in the spectral model, is responsible for the feature at 6100 Å and contributes to the complicated structure in the Hα region (see L17 for details).

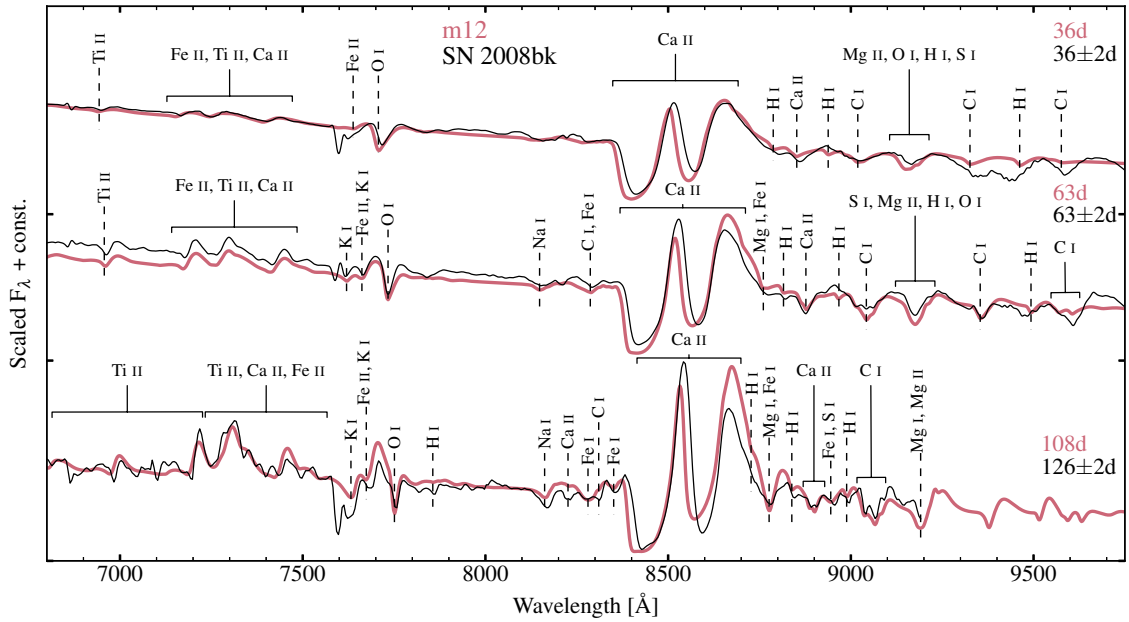

Figure 5.10 – Same as Figure 5.8, but showing the 6800–9750 Å region. The dip at ~ 7600 Å is caused by atmospheric absorption.

The lower expansion rate of low-luminosity SN II-P ejecta reduces the amount of line overlap and facilitates line identifications. In the remainder of this section, we discuss in more detail the spectral lines seen in our model m12 and the high quality observations of SN 2008bk.

Figures 5.8, 5.9 and 5.10 show a spectral comparison for model m12 and SN 2008bk in three consecutive spectral ranges spanning the optical from 3500 to 9750 Å, and covering the early photospheric phase, the plateau phase, and the beginning of the nebular phase. Lines that we could identify are labelled in these figures. We find that all lines observed are predicted by model m12, with just a few exceptions. First, as reported in L17, some features in the red part of the optical in SN 2008bk are absent in model m12 — this may be an instrumental artifact or an improper correction for atmospheric absorption. As discussed in L17, our simulations do not have Ba II by default. Ba is an s-process element and is not treated in `MESA`. In L17, assuming a solar abundance for Ba, we were able to explain a few lines blueward of Hα as stemming from Ba II (most notably 6141.7 and 6496.9 Å). A striking feature not predicted by model m12 is the double-dip in Na I D. This double dip fits within the Na I D P-Cygni trough in model m12. It may be caused by Ba II 5853.7 Å, although our model with Ba II in L17 predicts that line to be quite weak. This feature requires further study.

5.4 Comparison to other work

Our results for the V-band magnitude and the photospheric velocity at 50 d after explosion in model m12 (–15.61 mag, 2401 km s^{-1}) are in rough agreement with those of Kasen & Woosley (2009) for their model `M15_E0.3_Z1` of comparable ejecta energy and mass (–15.96 mag and 3125 km s^{-1}). The plateau duration of 120 d in model m12 is, however, unmatched by any of the low energy models in Kasen & Woosley (2009), which are all longer than 150 d. This likely arises from the large ^{56}Ni mass in their simulations, which exceeds 0.1 $M_\odot$ in all cases. The ^{56}Ni mass distribution of their model set is 1–2 orders of magnitude larger than the value inferred for low-luminosity SNe II-P.

Table 5.4 – Summary of the inferred properties for low-luminosity SNe II-P ejecta and progenitors. $M_{\rm init}$ is the initial mass of the progenitor star at the main sequence. $M_{\rm fin}$ and $R_{\rm fin}$ correspond the properties at the time of explosion.

SN	$M_{\rm init}$ [$M_\odot$]	$M_{\rm fin}$ [$M_\odot$]	$M_{\rm ej}$ [$M_\odot$]	$R_{\rm fin}$ [$R_\odot$]	$M\left(^{56}{\rm Ni}\right)$ [$M_\odot$]	$E_{\rm kin}$ [10^{50} erg]	Reference
1997D	10±2	—	6±1	85±60	0.002	1.0±0.3	Chugai & Utrobin 2000
	—	26	24	$\lesssim$300	0.0025±0.0015	4.0	Turatto et al. 1998
	—	—	17	130	0.008	9.0	Zampieri et al. 2003
1999br	—	—	14	108	0.002	6.0	Zampieri et al. 2003
2003Z	14.15±0.95	12.95±0.35	11.3	260	0.005±0.003	1.6	Pumo et al. 2017
	15.9±1.5	—	14±1.2	229±39	0.0063±0.0006	2.45±0.18	Utrobin et al. 2007
2005cs	—	—	10.5±2.5	100	0.003	3.0	Pastorello et al. 2009
	18.2±1	17.3±1	—	600±140	0.0082±0.0016	4.1±0.3	Utrobin & Chugai 2008
2008bk	12	9.88	8.29	502	0.0086	2.5	L17
	12.15±0.75	11.65±0.35	10.0	503	0.007±0.001	1.8	Pumo et al. 2017
2008in	20	—	16±4	—	0.025±0.01	8.6±2.5	Gurugubelli et al. 2011
	$\leq$ 20	—	16.7	126	0.015	5.4	Roy et al. 2011
	—	15.5±2.2	13.6±1.9	570±100	0.015±0.005	5.05±3.4	Utrobin & Chugai 2013
2009N	—	13.25±0.25	11.5	287	0.02±0.004	4.8	Takáts et al. 2014
2009md	12.15±0.75	11.65±0.35	10.0	287	0.004±0.001	1.7	Pumo et al. 2017
	—	$8.5^{+6.5}_{-1.5}$	—	500	0.0054±0.003	—	Fraser et al. 2011

Our models m25 and m27 do not eject any ^{56}Ni because of the strong fallback in those progenitors. In contrast, the models of Kasen & Woosley (2009) eject a significant amount of ^{56}Ni even in the low energy explosions of high mass progenitors (e.g., 0.34 $M_\odot$ in their model `M25_E0.6_Z1`). The reason for this difference is unclear. In the simulations of Dessart et al. (2010b), most of the CO core falls back if the progenitor mass is $\gtrsim 20\,M_\odot$ and the ejecta kinetic energy at infinity is 3×10^{50} erg. The smaller the piston power, the greater is the fallback. So, the large ^{56}Ni mass obtained in Kasen & Woosley (2009), which is well above the inferred value for SNe II-P, may result partly from overestimating its power.

In Table 5.4 we present the ejecta/progenitor properties inferred from radiation-hydrodynamics modelling and/or pre-explosion photometry of low-luminosity SNe II-P. As discussed in the introduction, there is a large scatter in progenitor masses (but also surface radii etc.). In this work, we have studied the whole sample of low-luminosity SNe II-P and emphasized what a uniform set they form in terms of V-band LC, color evolution, spectral evolution, or expansion rates (Chapter 3). It is hard to understand how a wide range of ejecta/progenitor properties can arise from such a uniform set of events.

In our work, we favor low-mass massive stars as progenitors of SNe II-P, which is in agreement with Pastorello et al. (2004); Spiro et al. (2014); Pumo et al. (2017), or Fraser et al. (2011). In some studies, the progenitor radius is claimed to be as low as 85–130 $R_\odot$ (Chugai & Utrobin 2000; Zampieri et al. 2003; Pastorello et al. 2009; Roy et al. 2011), which is more typical of BSG progenitors. Low-luminosity SNe II-P do not have a Type II-pec evolution like SN 1987A, and such small radii are also in strong disagreement with the constraints from pre-explosion images. Stellar evolution also predicts that the majority of low/moderate mass massive stars die as RSG stars, not BSG stars.

Our results are in conflict with the results of Turatto et al. (1998), who propose a 24 $M_\odot$ ejecta for SN 1997D.

5.5 Conclusions

In this work, we have studied the properties of observed low-luminosity SNe II-P and confronted them to the radiation properties obtained numerically from the explosion of low- and high-mass RSG stars (12, 25 and 27 $M_\odot$ on the main sequence).

Observations of low-luminosity SNe II-P reveal a very uniform class of objects, both photometrically and spectroscopically. All events show a plateau LC in the V-band during the photospheric phase — there are no fast decliners (II-L like) in this set. The plateau duration is tightly centered around 110 ± 10 d. Their color evolution is also analogous for all objects, showing a progressive and monotonic reddening during the photospheric phase. A larger scatter in color appears at nebular times, driven from differences in ^{56}Ni mass and perhaps from chemical mixing in the He core (L17). All low-luminosity SN II-P ejecta contain some ^{56}Ni, with a minimum inferred mass of 0.001 $M_\odot$. Spectroscopically, low-luminosity SNe II-P systematically exhibit narrower lines than standard-luminosity SNe II-P, which implies lower ejecta expansion rate. It thus appears that low-luminosity SNe II-P are low energy explosions of RSG stars.

Using stellar evolution and explosion models for stars of initial mass of 12, 25, and 27 $M_\odot$, we study the radiation properties of SNe arising from the explosion of low- and high-mass RSG stars. We find systematic differences between these two mass domains, which arise from their distinct pre-SN structure.

RSG stars of greater initial mass produce bigger He cores and greater surface luminosities, giving rise to a greater mass loss. Consequently, the RSG radius increases with the main-sequence mass while the ratio of the H-rich envelope mass to the He-core mass decreases. For large enough mass loss, the envelope may shrink, as in our model m27. For models m12, m25, and m27, the surface radius is 502, 872, and 643 $R_\odot$. As reported in Dessart & Hillier (2011); Dessart et al. (2013b), we find that the larger the progenitor radius, the bluer is the SN at early times, i.e., prior to the recombination phase. Only the explosion of more compact, i.e., lower mass RSG stars, matches the color evolution of low-luminosity SNe II-P.

Because the ratio of the H-rich envelope mass to the He-core mass decreases with increasing main-sequence mass, low- and high-mass RSG stars have a very different chemical stratification in mass space. This stratification is visible in velocity space after explosion, with the H-rich ejecta layers being confined to higher velocity regions in SNe II models from higher mass RSG stars. The smaller H-rich envelope mass in higher mass RSG stars tends to produce a shorter plateau (models m25 and m27). As the H-rich envelope drops to just a few solar masses, the V-band light curve shows a faster decline rate, in contradiction to observations of low-luminosity SNe II-P. Furthermore, only in model m12 do Hα and Fe II 5169 Å follow their observed counterparts. In model m25 and m27, Hα remains much too broad at late times, reflecting the large velocity of the H-rich layers (or the large velocity of the former He-core material).

Third, some difficulties with high-mass progenitors arise concerning the amount of ^{56}Ni ejected in the explosions. This parameter is very well constrained from the observed LCs at nebular times (in the sense that it does not require radiative transfer modelling), and found to be at least 0.001 $M_\odot$. SN 1999eu may have ejected even less ^{56}Ni but the nebular phase photometric data is too sparse to say confidently. Admittedly, for very low ^{56}Ni extract the SN brightness from the image photometry, especially for SNe lying in relatively dense star clusters.

In our models m25 and m27, no ^{56}Ni is ejected due to the highly bound He-core and the strength of the reverse shock. These models experience strong fallback, the entire CO core falling into the compact remnant and forming a $\sim 6\,M_\odot$ BH. The ejecta kinetic energy of 4.2×10^{50} erg in models m25 and m27, small enough to prevent ^{56}Ni ejection in these ejecta, is likely overestimated as the line profiles are broader than observed during the photospheric phase. Reducing the

discrepancy in line widths at early time would require reducing the explosion energy, which would enhance the amount of fallback, this time perhaps of the entire He core. In this context, observing narrow O I or Ca II lines at nebular times in a low-luminosity SN II-P is unambiguous evidence that some ^{56}Ni is ejected. If the power at nebular times comes instead from interaction with the progenitor wind, only a broad Hα line should be seen. This may help to refine the interpretation for the origin of the faint brightness at nebular times.

According to the results of our modelling and the confrontation to observed LCs and multi-epoch spectra, we conclude that low-mass RSG stars are the preferred progenitor population for the observed low-luminosity SNe II-P. It is however unclear whether all low-mass RSG stars produce low energy explosions. For a standard initial mass function with exponent 2.3, 42% of massive stars are born in the range $8-12\,M_\odot$, and 15% in the range $8-9\,M_\odot$. In contrast, only 5% of all Type II SNe are low energy explosions. So, either the mass range for these low-energy SNe II-P is very narrow (e.g., narrower than 8 to $9\,M_\odot$), or $8-12\,M_\odot$ exhibit some diversity in explosion energy, or we are missing numerous low-energy Type II-SNe because of an observational bias. A combination of all three might hold in Nature. From the point of view of the explosion mechanism, low-energy explosions seem to naturally occur in massive star progenitors characterized by a steeply declining density profile above the degenerate core, which is a generic feature of the lowest mass massive stars (Kitaura et al., 2006). The low-energy SNe II-P may then arise from the collapse of the ONeMg core leading to electron-capture SNe (Poelarends et al., 2008).

Chapter 6

Kinetic energy variation

In this chapter, we explore the impact of the variation in ejecta kinetic energy and ^{56}Ni mass on the resulting SN radiation (see also Section 9 of Dessart et al. 2013b). We are trying to answer the question whether the diversity of H-rich core-collapse SNe could be explained by the different explosion energy or if it requires a variation in ejecta mass.

We limit the parameter space by selecting one progenitor only, model Y. It corresponds to a 12 $M_\odot$ star, evolved from main sequence until core-collapse at a metallicity of 0.0162. The model at the onset of core collapse has a total mass of 11.01 $M_\odot$ and a surface radius of 405 $R_\odot$ (see Table 4.1 and Figure 4.1). From this progenitor model Y, we produce three models YE1, YE2, and YE3 with an ejecta kinetic energy at infinity of 3.3, 6.4, and 12.3×10^{50} erg and a ^{56}Ni mass of 0.003, 0.008, and 0.036 $M_\odot$ (Table 4.2) — the total ejecta mass covers the range 9.36–9.50 $M_\odot$. Using the observational data (described in Appendix A), we compare each of these models to the multi-band light curves and multi-epoch spectra of SNe 2005cs, 2012ec, and 1999em (Figures 6.2, 6.3, 6.4). Figure 6.1 illustrates how these three models of increasing $E_{\rm kin}/M_{\rm e}$ follow the trend of increasing spectral line widths in these SNe. We focus on the photospheric phase since mixing can strongly affect the properties at nebular times and this requires a separate study (Section 4.5.3).

Models YE1, YE2, and YE3 were not produced to match these specific observations so the comparison to observations is done here to check the overall adequacy of these ejecta models. For example, the ^{56}Ni mass of each model is not tuned to match the nebular luminosity of these SNe.

6.1 Model YE1 and comparison to SN 2005cs

Model YE1 is a close equivalent to the model X, which matches the properties of SN 2008bk satisfactorily (Section 4.4). Model YE1 has a somewhat more energetic and more massive ejecta, and stems from a more compact progenitor star than model X. Model YE1 is computed for post-explosion times > 10 d and follows satisfactorily the $UBVRI$ light curves, the color evolution and the duration of the high-brightness phase of SN 2005cs (Figure 6.2). One discrepancy is that model YE1 is $\sim 30\%$ more luminous than SN 2005cs (which corresponds to a magnitude offset of 0.3 mag in all bands). The spectral evolution is also well matched during the photospheric phase. The poor fit to Hα at 62 d is due to the neglect of Ba II in the YE1 model (see Section 4.4.3 and Figure 4.13 in the context of SN 2008bk).

Model YE1 has a similar progenitor radius and explosion as the model of Utrobin & Chugai, 2008 (600 $R_\odot$ and 4.1×10^{50} erg), but model YE1 has an ejecta mass of 9.36 $M_\odot$, while Utrobin & Chugai find an ejecta mass of 15.9 $M_\odot$. Interestingly, the model of Utrobin & Chugai has an

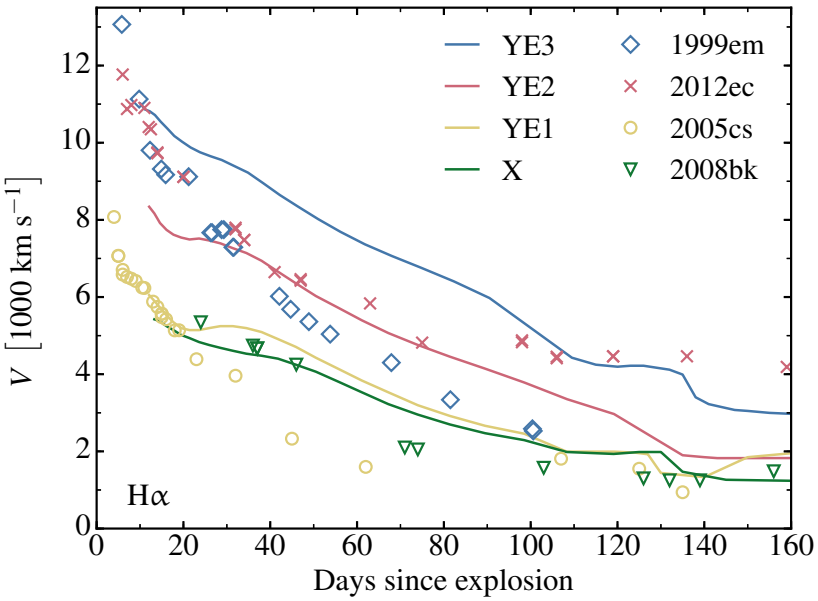

Figure 6.1 – Comparison of the velocity at maximum absorption in Hα for the models X, YE1, YE2, and YE3, with the values measured from the observations of SNe 2008bk, 2005cs, 2012ec, and 1999em.

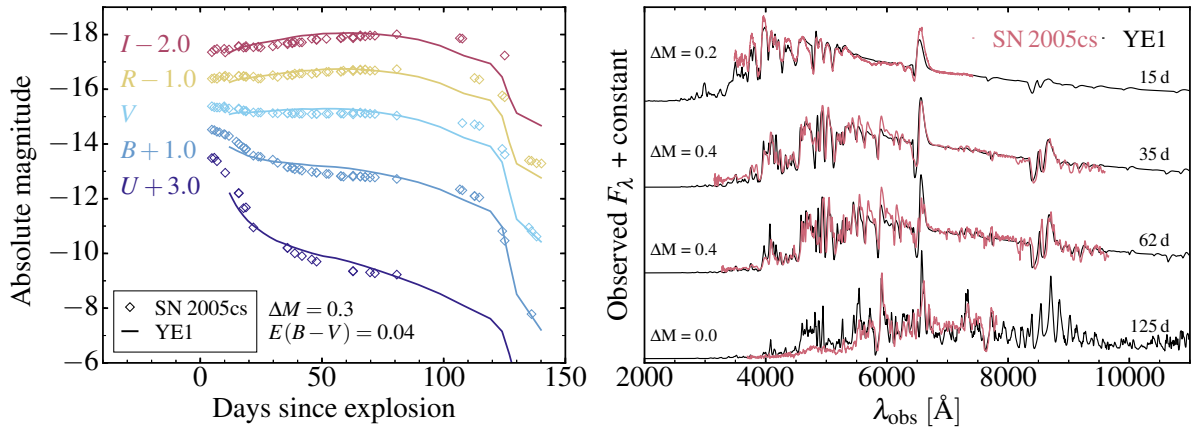

Figure 6.2 – Comparison of multi-band light curves (left) and multi-epoch spectra (right; shown versus observed wavelength) for model/observation pair YE1/SN 2005cs (a magnitude offset of 0.3 mag is applied). See Appendix A for details on the observational data and the adopted explosion dates, distance, reddening, and redshift.

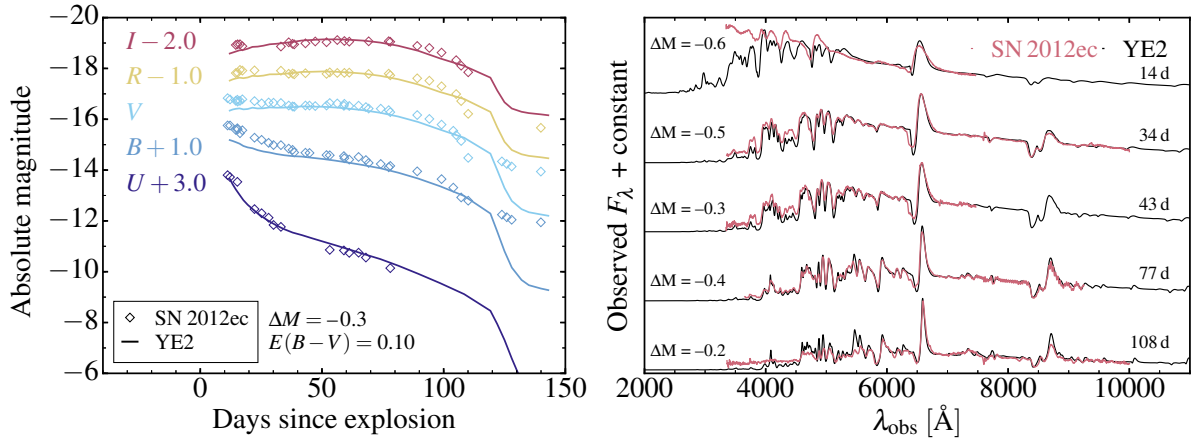

Figure 6.3 – Same as Figure 6.2, but for model YE2 and SN 2012ec (a magnitude offset of −0.3 mag is applied). See Appendix A for details on the observational data and the adopted explosion dates, distance, reddening, and redshift.

8 $M_\odot$ H-rich envelope mass, which is the same as our model YE1. As discussed in Dessart et al. (2013b), the discrepancy stems from the mass of the He-core material in the model of Utrobin & Chugai, which is large but in fact poorly (if at all) constrained from the light curve modelling. The density structure proposed by Utrobin & Chugai is quantitatively and, more importantly, qualitatively in contradiction with models of massive stars, which predict that the He core lies within 1 $R_\odot$ and is at large density, few orders of magnitude larger than the H-rich envelope material (see, e.g., Woosley et al. 2002; Dessart et al. 2010b). The implications of this feature are manifold and hard to predict. The simulations of Utrobin & Chugai will not produce a reverse shock as the SN shock enters the H-rich envelope (this reverse shock inevitably forms as the SN shock enters the flat density profile in the RSG H-rich envelope). The reverse shock leads to a deceleration and significant heating of the He-core material (see, e.g., Paxton et al. 2015). Furthermore, the He-core material does not have the right binding energy initially, being located at too large distances. This implies that it does not cool as much as it should from expansion, and there is too little work done to propel it out of the gravitation potential. Much mass can reside in the He core of a SN II without affecting the light curve.

6.2 Model YE2 and comparison to SN 2012ec

Model YE2 has the same ejecta mass and the same progenitor properties as model YE1, but its kinetic energy at infinity is 6.4×10^{50} erg. The middle row of Figure 6.3 shows a comparison of model YE2 with the multi-band light curves and multi-epoch spectra of SN 2012ec. Model YE2 is somewhat under-luminous for SN 2012ec but it follows the same color evolution. It overestimates the duration of the photospheric phase by about 20 d. To remedy these deficiencies would require a high ejecta kinetic energy and lower H-rich envelope mass, especially because we underestimate the ^{56}Ni mass — model YE2 has 0.008 $M_\odot$ of ^{56}Ni while Barbarino et al. (2015) infer a mass of 0.04 $M_\odot$ for SN 2012ec.

Barbarino et al. propose an ejecta mass of 12.6 $M_\odot$ (35% larger than model YE2) and a kinetic energy of 1.2×10^{51} erg (twice the value for model YE2) and a progenitor radius of 230 $R_\odot$ (half the value for model YE2). These model parameters are significantly different from ours. Our lower ejecta mass is compensated by a lower ejecta kinetic energy and offers an alternate solution at low mass — a solution is probably not unique. Furthermore, we match the color evolution with

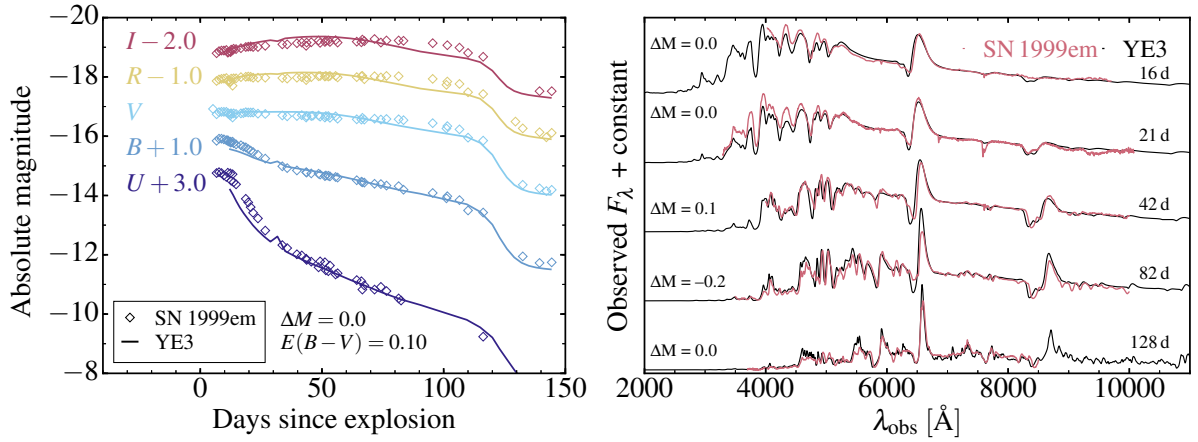

Figure 6.4 – Same as Figure 6.2, but for model YE3 and SN 1999em. See Appendix A for details on the observational data and the adopted explosion dates, distance, reddening, and redshift.

a radius of 405 $R_\odot$. A lower radius, incompatible with a RSG star progenitor, would bring the onset of recombination at the photosphere even earlier and lead to a more rapid color evolution, bringing a disagreement with the observations of SN 2012ec. The predictions of Barbarino et al. (2015) are based on gray radiation hydrodynamics which constrain the bolometric luminosity light curve, not the color evolution, and are therefore less suitable for constraining the progenitor radius (see discussion in Dessart et al. 2013b). Little information on the progenitor model is provided by Barbarino et al., so it is not possible to comment further on the disagreement.

6.3 Model YE3 and comparison to SN 1999em

Model YE3 has the same ejecta mass and the same progenitor properties as model YE1, but its kinetic energy at infinity is 1.23×10^{51} erg. Figure 6.4 shows a comparison of model YE3 with the multi-band light curves and multi-epoch spectra of SN 1999em. The model matches closely the length of the photospheric phase (or high brightness phase), the color evolution, and the spectral evolution, including the width/strength of the line profiles. Model YE3 is a close counterpart of the model MLT3 (Dessart et al., 2013b). The main difference is that model YE3 has a smaller ejecta mass (9.5 compared to 12.52 $M_\odot$ for model MLT3) and does not overestimate the plateau duration of SN 1999em like model MLT3 does.

SN 1999em has been studied in the past. Gray radiation hydrodynamics simulations have been used to constrain the progenitor and explosion properties based on the bolometric light curve and the evolution of the photospheric velocity. Utrobin (2007) proposes a progenitor radius of 500 $R_\odot$, an ejecta mass of 19.0 $M_\odot$, and an ejecta kinetic energy of 1.3×10^{51} erg. The main difference with our model YE3 is the ejecta mass, which is twice as large as for our model, even though our model matches well the observations of SN 1999em (our work is not limited to the modelling of the bolometric luminosity and the Hα line; our model also matches the multi-band light curves and spectral evolution). Bersten et al. (2011) propose a progenitor radius of 800 $R_\odot$, an ejecta mass of 17.6 $M_\odot$, and an ejecta kinetic energy of 1.25×10^{51} erg. As discussed in Dessart et al. (2013b), a progenitor radius of 800 $R_\odot$ is inadequate because it leads to a SN with blue colors for too long. Our model YE3 has a 9.5 $M_\odot$ ejecta mass, much lower than the 17.6 $M_\odot$ of Bersten et al. (2011), although our model matches the length of the photospheric phase.

Compared to both Utrobin (2007) and Bersten et al. (2011), our modelling predicts a much smaller ejecta mass than their predictions, which are based on gray radiation hydrodynamics.

As discussed in Dessart et al. (2013b), the likely origin of this difference is their use of a RSG density structure that does not have the He-core structure predicted by (single) massive star evolution. For example, as can be seen in Figures 3–4 of Bersten et al. (2011), the density is $< 10^{-5}$ g cm^{-3} outside of a 3 M$_\odot$ Lagrangian mass (their Figure 3), while the edge of the helium core is located at a 9 M$_\odot$ Lagrangian mass (the same feature applies to the model of Utrobin, 2007). A stellar evolution model would put that density drop at the edge of the He core (as can be seen, for example, in our models shown in Figure 4.1), which in the model of Bersten et al. would be at 9 M$_\odot$ — this He-core mass is typical of a non-rotating 25 M$_\odot$ main-sequence star (see, e.g., Figure 2 of Dessart et al., 2010b for the models of Woosley et al. 2002). As discussed above in Section 4.5.1, this very important because with such a density structure, the shock dynamics is significantly different.

More importantly, when considering the mass of the H-rich regions of the ejecta, the models of Bersten et al. (2011) and Utrobin (2007) predict a mass of about 10 M$_\odot$, which is close to our model YE3. So, the large ejecta masses predicted by Utrobin and Bersten et al. arise from their prediction of a large mass for the He-rich layers. However, these layers are only visible at nebular times and their mass cannot be estimated from the light curve modelling of the high-brightness phase (see, e.g., Dessart & Hillier, 2011). There is admittedly large uncertainties with stellar evolution, but these uncertainties are unlikely to concern the structure of the He core. The properties that its mass is an increasing function of the main sequence mass in single 10–30 M$_\odot$ stars (Woosley et al., 2002) and that it is highly bound (Dessart et al., 2010b) seem robust. Crafting models that depart dramatically from these results seems unwise, and as we show here, largely unwarranted.

What we have shown is that using the same progenitor star to produce three ejecta of increasing kinetic energy, we obtain a fair agreement with the observations of SNe 2005cs, 2012ec, and 1999em. All three models have an ejecta mass of ~ 9.5 M$_\odot$, which is systematically lower than the predictions based on gray radiation hydrodynamics simulations, which use polytropic or crafted progenitor models. The larger ejecta masses from these studies stem from the large mass of He-rich shells. The light curve modelling constrains the H-rich ejecta mass (i.e., the H-envelope mass of the progenitor), and that mass is comparable in our models. Overall, our results suggest there is no discrepancy from inferences based on pre-explosion images (see discussion in Smartt 2009).

6.4 Conclusions

We have explored variants of model X, all with the same ejecta mass of ~ 9.5 M$_\odot$, but with increasing explosion energies of 3.3, 6.4, and 12.3 $\times 10^{50}$ erg (models YE1, YE2, and YE3). We find that these three models, despite having the same ejecta mass, yield a fair match to the multi-band light curves and multi-epoch spectra of SNe 2005cs, 2012ec, and 1999em. This suggests that the origin of the diversity in brightness of these Type II SNe may be the explosion energy rather than the ejecta mass. Because of differences in wind mass loss rates and final density structures, a given ejecta mass (strictly speaking, we should say H-rich envelope mass) may nonetheless correspond to a range of stellar masses on the zero-age main-sequence. In any case, our ejecta masses are much lower that those typically inferred by alternate studies based on gray radiation hydrodynamics modelling. As discussed in Dessart et al. (2013b) and in this work, the likely origin of this difference is the treatment of the He core in these other studies: while they include He-rich layers (mixed with H), they position those layers at low density, as if the He-core material (which, in reality, is highly bound in the progenitor) was part of the H envelope (which, instead, is loosely bound in the RSG progenitor). This He core mass cannot

be constrained through light curve modelling but requires instead nebular-phase spectroscopy. However, when considering the mass of the H-rich layers in the pre-SN progenitor star (i.e., $\sim 9.5\,M_{\odot}$), our inferred values are in fact in rough agreement. If, as in the models we propose in this work, the He core mass is relatively small, our progenitor masses are in agreement with estimates from pre-explosion imaging. There is no discrepancy.

Conclusions

When comparing our results to previous work, one should recall that one CMFGEN simulation takes typically 2–3 months to deliver a full time sequence. The alternate approach of gray radiation hydrodynamics delivers a full (but only bolometric) light curve in one day. Hence, it is not possible to run large grids of models, varying stellar parameters across a huge parameter space. Consequently, with CMFGEN, we focus on quality rather than quantity. In practice, we limit the parameter space by using physical models of the progenitors. Despite the uncertainties in our understanding of stellar evolution, this approach captures fundamental dependencies that exist between main sequence mass and He core mass at death, between He core mass and RSG surface radius at death, the tight connection between density structure and composition profile in a RSG star (e.g., the distinction between He core and H-rich envelope). Discrepancies between our results and other studies stem primarily in the use of polytropes or crafted models in the latter, as we explain below. Let us also stress that the progenitor and ejecta properties one infers from light curve and spectra do not all suffer the same level of uncertainty. The four main quantities of interest are $R_\star$, $M_{\rm ej}$ (see Section 4.5), $E_{\rm kin}$, and ^{56}Ni mass (see Chapter 6). Estimating any of these quantities is subject to the uncertainty in the adopted distance and reddening.

Of all four quantities, the most certain inference is the ^{56}Ni mass because it is the most direct. In fact, one can estimate the ^{56}Ni mass without any modelling at all. In numerous radiation hydrodynamics simulations (see, e.g., Utrobin 2007; Bersten et al. 2011), explosive nucleosynthesis is ignored and the ^{56}Ni mass is prescribed to match the observed nebular flux. In V1D, explosive nucleosynthesis is treated and the ^{56}Ni mass is then dependent on the density structure, the mass cut, the explosion power — many of these are not known from first principles. Consequently, the ^{56}Ni mass is not a result from a model, although it can impact the results from a model (e.g., by lengthening the length of the photospheric phase or modulating the composition/ionization).

The three other parameters ($R_\star$, $M_{\rm ej}$, $E_{\rm kin}$) are not independently constrained and there are probably multiple combinations that provide a satisfactory match to the observations. As discussed in Dessart et al. (2013b) and vividly illustrated by the different color evolution of a Type II-peculiar SN (like SN 1987A) and a Type II-P SN (like SN 1999em), the progenitor radius has a huge impact on the color evolution and the time at which hydrogen recombination starts at the photosphere. Frequency/energy-dependent radiative transfer is therefore more suitable than gray radiation hydrodynamics to constrain the progenitor radius. The photospheric phase duration, the associated brightness, and the expansion rate as inferred from line profiles are then used to constrain $M_{\rm ej}$ and $E_{\rm kin}$. As we have stressed repeatedly in this manuscript, the $M_{\rm ej}$ constrained from light curve modelling is in fact the H-rich envelope mass of the progenitor — the light curve is very weakly sensitive to the He core mass. Furthermore, because of the unknown pre-SN mass loss history, SN modelling can only provide speculations on the main sequence mass of the progenitor. In Chapter 6, we showed that SN II-P of any luminosity may arise from 12 $M_\odot$ progenitor by varying only the kinetic energy of explosion.

Present work studies the most complete sample of low-luminosity SNe II to date. Due to

low expansion rates, lines in the spectra of these objects are narrow. This, combined with our modelling technique, allowed to find out a possible reason of the structure seen in Hα — it can be a Ba II 6496.6Å line.

In Chapters 4 and 5, we showed that the subclass of low-luminosity Type II SNe cannot stem from very massive progenitors as it is proposed in number of works (see Table 5.4). Our modelling, that includes stellar evolution and thus follows progenitor from early stages of its life, allows to point to the markers which cannot miss from the observational data of SN explosions resulting from the initially very massive progenitors. Since these markers are not observed in the real data, we conclude that no initially massive progenitors produced low-luminosity explosions of Type II SNe.

Acknowledgements

Author acknowledges financial support from the Erasmus Mundus Joint Doctorate Program by Grants Number 2013-1471 from the agency EACEA of the European Commission.

Author thanks the developers of Open Supernova Catalog[15] (Guillochon et al., 2017), where we retrieved the data for most of SNe used in the dissertation. Author thanks for the provided data Guliano Pignata (SN 2008bk), Claudia Patricia Gutiérrez Avendaño (SN 1992ba), Andrea Pastorello (SN 2003Z data published in Knop et al., 2007).

Author thanks the thesis director Thierry Lanz for his continuous support and readiness to help with any question.

Author thanks the thesis co-director Luc Dessart for the great amount of time he spent giving personal lectures, for interesting discussions, and for being an example of a conscientious and enthusiastic scientist. Author also is very grateful to Luc and Thierry for their immense patience.

Author thanks all staff of Observatoire de la Côte d'Azur for their professionalism and benevolence, which made all the time of author's stay in Nice pleasant and useful.

Author thanks Hunan Abrahamyan for proofreading of the manuscript and his valuable comments.

Author thanks Konstantin Malanchev[16] for significant help with the `Python` programming language, which was used to plot every single figure in this manuscript.

Author thanks his parents Natalya and Mikhail Lisakov for their love and support. Author is grateful to his brother Mikhail — he is the person who introduced author to astronomy.

Maria Pruzhinskaya[17] played the most important role: author would never have decided to start a PhD without her convincing motivation, which manifested not only in a form of words, but mainly in her passion for doing science.

[15] https://sne.space
[16] https://homb.it
[17] https://pruzhinskaya.com

Appendix A

Observational data

A.1 A sample of low-luminosity Type II SNe

The sample of low-luminosity SNe II-P consists of 17 objects: 1994N, 1997D, 1999br, 1999eu, 1999gn, 2001dc, 2002gd, 2003Z, 2004eg, 2005cs, 2006ov, 2008bk, 2008in, 2009N, 2009md, 2010id, 2013am. Some of the objects from the sample, such as 2005cs and 2008bk, were followed spectroscopically and photometrically with a high cadence. Others have been observed just few times, but all these SNe are confirmed as subluminous Type II-P supernovae.

In the Table A.1 we summarize the main information for our sample. Presented A_V corresponds to the Galactic extinction (Schlafly & Finkbeiner, 2011). However, A_V for some SNe also includes host galaxy extinction. Such cases are marked in the Table A.1 and discussed explicitly in sections below. We adopt visual extinction to reddening ratio $R_V = A_V/E(B-V) = 3.1$. An additional information, which is not included in the Table A.1, is presented below for each object.

Host galaxies for all SNe from our sample are shown in Fig. A.1. Most of the objects are located in the arms of big spiral galaxies, i.e. in the regions of active star formation. It is expected since the progenitors of core-collapse SNe are relatively young massive stars.

A.1.1 SN 1994N

SN 1994N was discovered in UGC 5695 on 10 May 1994 during an observation of Type IIn SN 1993N with ESO 3.6m telescope (Turatto et al., 1994). For SN 1994N we use the photometric and spectroscopic data from Pastorello et al. (2004).

A.1.2 SN 1997D

Supernova 1997D was discovered in NGC 1536 on 14 January 1997 about 100 days after maximum (de Mello et al., 1997), so the explosion epoch is not very well constrained (MJD 50361 ± 15; Spiro et al. 2014). The red spectra and narrow lines together with the light curve indicate that this object was captured at the end of the plateau phase. In some works a short plateau of 40–50 days is proposed (Chugai & Utrobin, 2000). Given the high homogeneity of all the low-luminosity SNe II-P known to date, we adopt in this work a more conventional plateau length of ~120 days, following Zampieri et al. (2003); Pastorello et al. (2004) and (Spiro et al., 2014). For SN 1997D we use the photometric and spectroscopic data from Benetti et al. (2001).

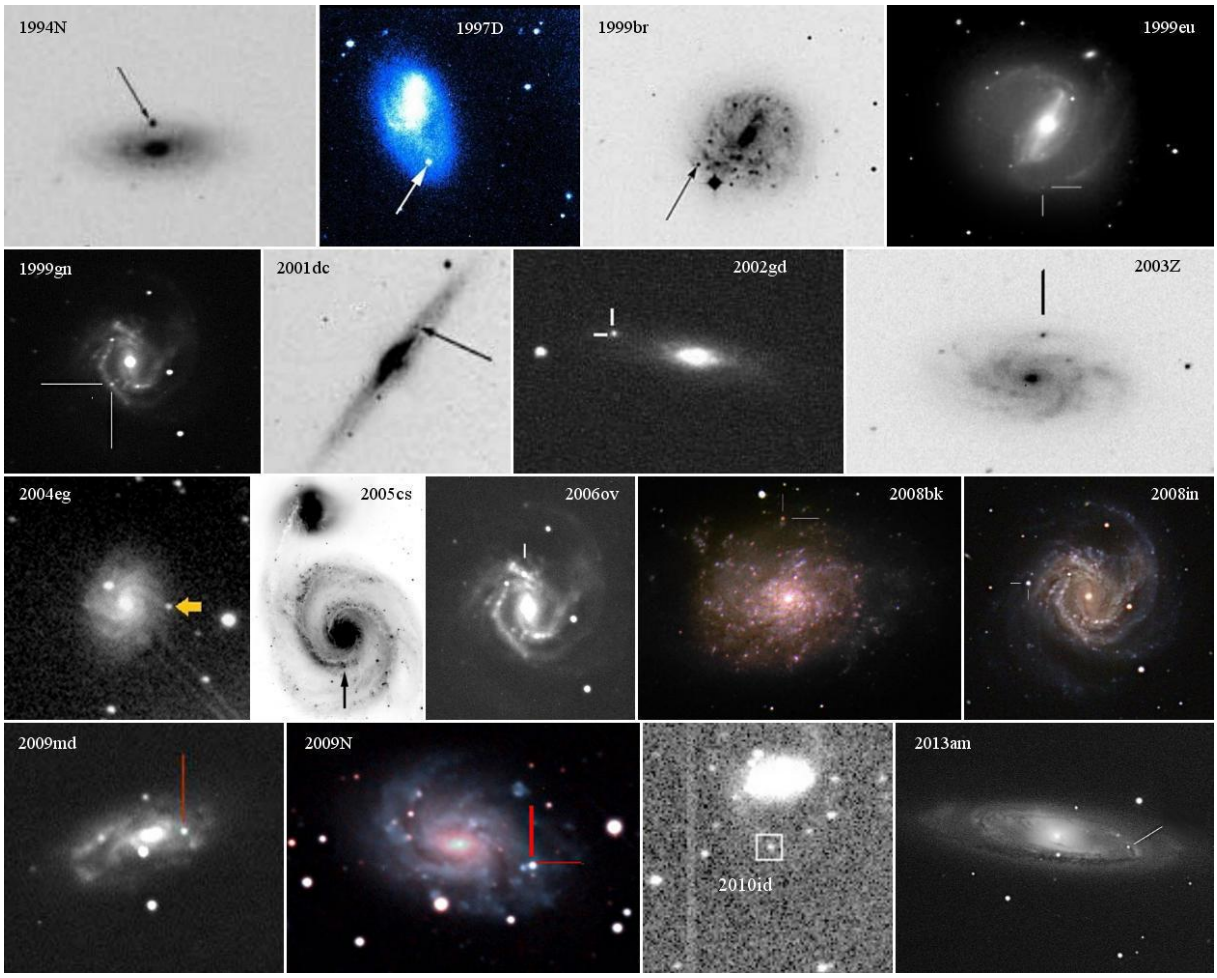

Figure A.1 – Host galaxies and SNe locations for all objects from our low-luminosity sample. Images of SNe 1994N, 1999br, 2001dc are taken from Pastorello et al. 2004; 2003Z from Spiro et al. 2014; 1997D from `imagine.gsfc.nasa.gov` (corresponding ATel is de Mello et al. 1997), 2004eg from `youngsphotogallery.com` (James W. Young), 2005cs from Li et al. (2006), 2010id from Catalina Sky Survey (Drake et al., 2009). Images of the following SNe are taken from `rochesterastronomy.com`: 1999eu (Dean Easton), 1999gn (Rafael Ferrando) , 2002gd (Campo Catino), 2003Z (KAIT), 2006ov (Koichi Itagaki), 2008bk (Patrice Poyet), 2008in (Rick Johnson), 2009md (Joel Nicolas), 2009N (Joseph Brimacombe), 2013am (Bill Williams).

Table A.1 – Observational data for our sample of low-luminosity Type II-P SNe. $V_{\rm rec}$ is recessional velocity.

SN	Host galaxy	Explosion date MJD	A_V^1 [mag]	μ [mag]	$V_{\rm rec}$ [km s^{-1}]	References[2]
1994N	UGC 5695	49451.0±10	0.103	33.09±0.31	2940	P04
1997D	NGC 1536	50361.0±15	0.058	31.29	1461	P04, S14
1999br	NGC 4900	51278.0±3	0.065	31.90**	968	P04, S14
1999eu	NGC 1097	51394.0±15	0.073	31.08	1273	P04, S14
1999gn	M 61	51520.0±10	0.061	30.50±0.20	1616	S14
2001dc	NGC 5777	52047.0±5	1.250*	33.19±0.43	2140	P04, S14, So14
2002gd	NGC 7537	52552.0±2	0.184	32.87±0.35	2678	S14, W10
2003Z	NGC 2742	52665.0±4	0.106	31.70±0.60	1280	S14, H12
2004eg	UGC 3053	53170.0±30	1.237*	32.64±0.38	2434	S14, C11
2005cs	M 51	53547.6±0.5	0.124*	29.75±0.16	466	D08
2006ov	M 61	53974.0±6	0.061	30.50±0.20	1616	S14
2008bk	NGC 7793	54548.0±2	0.062*	27.68±0.05	283	L17, P10, P
2008in	M 61	54825.0±1	0.305*	30.50±0.20	1616	R11
2009N	NGC 4487	54848.1±1.2	0.403*	31.67±0.11	1050	T14
2009md	NGC 3389	55162.0±8	0.380*	31.64±0.21	1298	F11, H12
2010id	NGC 7483	55452.0±2	0.167	33.15±0.45	4940	G10, T07
2013am	M 65	56372.0±1	1.767*	30.54±0.40	775	Z14, N11

[1] In most cases visual extinction A_V corresponds to the Galactic extinction (Schlafly & Finkbeiner, 2011), but for some SNe A_V also includes additional extinction (see Section Appendix A for details). In this case A_V value is followed by an asterisk. In some cases A_V is calculated from A_B or $E(B-V)$, provided in the corresponding papers.

[2] P04: Pastorello et al. (2004); S14: Spiro et al. (2014); D08: Dessart et al. (2008); L17: in L17 we adopted an explosion date of 54546.0 MJD for SN 2008bk basing on the explosion date estimation of 54548.0±2 MJD from Pignata (2013) and spectral evolution of model m12; P10: Pietrzyński et al. (2010); P: Pignata, private communication; R11: Roy et al. (2011); T14: Takáts et al. (2014); F11: Fraser et al. (2011); G10: Gal-Yam et al. (2011); Z14: Zhang & Wang (2014); So14: Sorce et al. (2014); W10: Wei et al. (2010); H12: Hakobyan et al. (2012); C11: Cappellari et al. (2011); T07: Theureau et al. (2007); N11: Nasonova et al. (2011).

** The distance to SN 1999br in Pastorello et al. (2004) is 17.3 Mpc (distance modulus $\mu = 31.19$). Pignata (2013) supposes that the distance for the 1999br may be underestimated, basing on the similarities between SN 1999br and SN 2008bk. We use the mean result from the NED catalogue, derived from 7 distance estimations to the host galaxy NGC 4900.

A.1.3 SN 1999br

Supernova 1999br was discovered in NGC 4900 on 12 April 1999 (King, 1999) and there was no evidence of the SN on frames taken on 4.4 April 1999 with limiting magnitude 17 (Yoshida et al., 1999).

This SN could be the faintest in our sample if one adopts the distance of 17.3 Mpc (Pastorello et al., 2004). However, Pignata (2013) assumes that the distance for the 1999br is probably underestimated, basing on the similarities between SN 1999br and SN 2008bk. In this paper, we use the distance of 24.0 Mpc — the mean result from the NED catalogue, derived from seven distance estimations to the host galaxy NGC 4900.

Explosion took place on the periphery of NGC 4900 and the spectra does not show any evidence of internal extinction (Pastorello et al., 2004). For SN 1999br we use the photometric and spectroscopic data from Pastorello et al. (2004).

A.1.4 SN 1999eu

This supernova was discovered in NGC 1097 on 5 November 1999 (Nakano & Aoki, 1999). It is located in an arm of the host galaxy. For SN 1999eu we use the photometric and spectroscopic data from Pastorello et al. (2004).

A.1.5 SNe 1999gn, 2006ov and 2008in

The galaxy M61 (NGC 4303) hosts 3 SNe from our sample.

SN 1999gn was discovered on 17 December 1999 (Dimai & Li, 1999), approximately 10 days after explosion. For SN 1999gn we use the spectroscopic data from Spiro et al. (2014). No photometric follow-up of this SN has been performed, we use two individual measurements in V-band reported in Dimai & Li (1999) and Kiss et al. (2000).

SN 2006ov was discovered on 24 November 2006 (Nakano et al., 2006). For SN 2006ov we use the photometric and spectroscopic data from Spiro et al. (2014).

SN 2008in was discovered on 26 December 2008 (Nakano et al., 2008). We use the photometric and spectroscopic data from Roy et al. (2011). For SN 2008in we adopt A_V (estimated as a sum of Galactic and host galaxy extinction) of 0.305 (Roy et al., 2011).

A.1.6 SN 2001dc

This supernova was discovered in the edge-on Type Sbc galaxy NGC 5777 not far from the nucleus on 30 May 2001 (Hurst et al., 2001). For SN 2001dc we use the photometric and spectroscopic data from Spiro et al. (2014).

The position of SN in the host galaxy and its color indicate significant reddening. We adopt the total extinction $A_V = 1.250$ (Spiro et al., 2014).

A.1.7 SN 2002gd

This supernova was discovered in the NGC 7537 on 5 October 2002 (Klotz et al., 2002) at a very early phase (Spiro et al., 2014). For SN 2002gd we use the photometric and spectroscopic data from Spiro et al. (2014).

A.1.8 SN 2003Z

Supernova 2003Z was discovered in NGC 2742 on 29 January 2003 by Qiu & Hu (Boles et al., 2003). For SN 2003Z we use the photometric and spectroscopic data from Spiro et al. (2014).

A.1.9 SN 2004eg

Supernova 2004eg was discovered in UGC 3053 on 1 September 2004 (Young et al., 2004). Only two spectra are available for this SN with phases 93 and 171 days. For SN 2004eg we use the photometric and spectroscopic data from Spiro et al. (2014). The total extinction $A_V = 1.237$ mag (Spiro et al., 2014).

A.1.10 SN 2005cs

Supernova 2005cs was discovered in NGC 2742 on 30 June 2005 (Modjaz et al., 2005). For SN 2005cs we use the photometric and spectroscopic data from Pastorello et al. (2009). We adopt the total extinction $A_V = 0.124$ mag as inferred from the multi-epoch photometric and spectroscopic modelling of Dessart et al. (2008).

A.1.11 SN 2008bk

Supernova 2008bk was discovered in the NGC 7793 on 26 March 2008 (Monard, 2008), and it was the second-brightest SN of the year. A low-mass RSG was identified in archival images (Mattila et al., 2008; Van Dyk et al., 2012a). The detailed study of SN 2008bk, including the simulations of the progenitor star and radiative-transfer modelling of the ejecta, demonstrated a suitability of low-mass progenitor with the initial mass of 12 $M_\odot$ (L17).

For SN 2008bk we use the photometric and spectroscopic data from Pignata (2013) and spectropolarimetric observations from Leonard et al. (2012a). Following L17, we adopted an $A_V = 0.062$ mag. This is within 0.01 mag of the value reported by Schlafly & Finkbeiner (2011) for the line-of-sight towards NGC 7793, the galaxy host of SN 2008bk.

A.1.12 SN 2009N

Supernova 2009N was discovered in NGC 4487 on 24 January 2009 (Nakano et al., 2009a). For SN 2009N we use the photometric and spectroscopic data from Takáts et al. (2014). The total extinction $A_V = 0.403$ mag as it estimated from the equivalent width of the Na I D line by Takáts et al. (2014).

A.1.13 SN 2009md

Supernova 2009md was discovered in NGC 3389 on 4.81 December 2009 (Nakano et al., 2009b). For SN 2009md we use the photometric and spectroscopic data from Fraser et al. (2011). The adopted total extinction $A_V = 0.380$ mag (Fraser et al., 2011).

A.1.14 SN 2010id

Supernova 2010id was discovered in NGC 7483 on 16.33 September 2010 (Lin et al., 2010). For SN 2010id we use the photometric and spectroscopic data from Gal-Yam et al. (2011).

A.1.15 SN 2013am

Supernova 2013am was discovered in M65 on 21 March 2013 (Yaron et al., 2013). For SN 2013am we use the photometric and spectroscopic data from Zhang & Wang (2014). The adopted sum of the Galactic and host galaxy extinction $A_V = 1.767$ (Zhang & Wang, 2014).

A.1.16 Other candidates in low-luminosity SNe II-P

In this section we list other possible low-luminosity Type II-P supernovae that we did not include in our sample.

A.1.16.1 SN 1991G

Adopting the distance to and the reddening for SN 1991G from Blanton et al. (1995), $D = 15.5$ Mpc and $A_V = 0.025$ (which is even lower than for the reddening due to the Milky Way according to the more recent works of Schlegel et al. 1998; Schlafly & Finkbeiner 2011), one would obtain a luminosity, similar to that of SN 2002gd (brightest from our sample). It seems to be incompatible with the expansion rate of 6450 km s^{-1} as derived from the minima position of Fe II (5169Å) line at ~21 days since explosion, which is a typical value for standard SNe Type II-P, not the low-luminosity ones. With such a low value of the reddening, the first available spectrum observed on 14 February 1991 (~21 days since explosion) would be extremely red in comparison to the SNe from our sample. On the contrary, if one adopts high reddening for the SN 1991G, e.g. $A_V = 2.0$ mag, the spectrum has reasonable color and the 1991G becomes brighter than standard Type II-P SN 1999em. It may be also that the spectrum has not been calibrated correctly. Due to these uncertainties with the reddening and/or with the calibration of the spectra, we do not include SN 1991G in the current study.

A.1.16.2 SN 2003ie

SN 2003ie was classified by Arcavi et al. (2013) as a faint Type II-P event. However, its luminosity at the discovery is higher than the luminosity of any supernovae from our sample. Moreover, the poor cadence of photometric observations and the availability of only one spectrum do not allow to estimate the explosion date. The spectrum is quite different from the spectra from our sample (e.g., the strength of Hα line is lower).

A.1.16.3 SN 2014bi

SN 2014bi has been classified as a faint SN II-P (Zhang & Wang, 2014). The observational data are very scarce, only one low-quality spectrum and few photometric points are available (Zheng & Filippenko, 2014; Zhang & Wang, 2014).

Since the absolute magnitude in R band is > -12 mag, the reddening should be very high (Khazov et al., 2016). The exact value of the reddening is unknown, therefore we cannot determine the supernova luminosity.

A.1.17 Archetypical Type II-P SN 1999em

Supernova 1999em was discovered in NGC 1637 on 30 October 1999 by Li (1999). SN 1999em is a standard Type II-P supernova with $M_V \sim -17$ mag during the plateau phase. It has a dense set of spectroscopic and photometric observational data and we use it to compare to our low-luminosity sample.

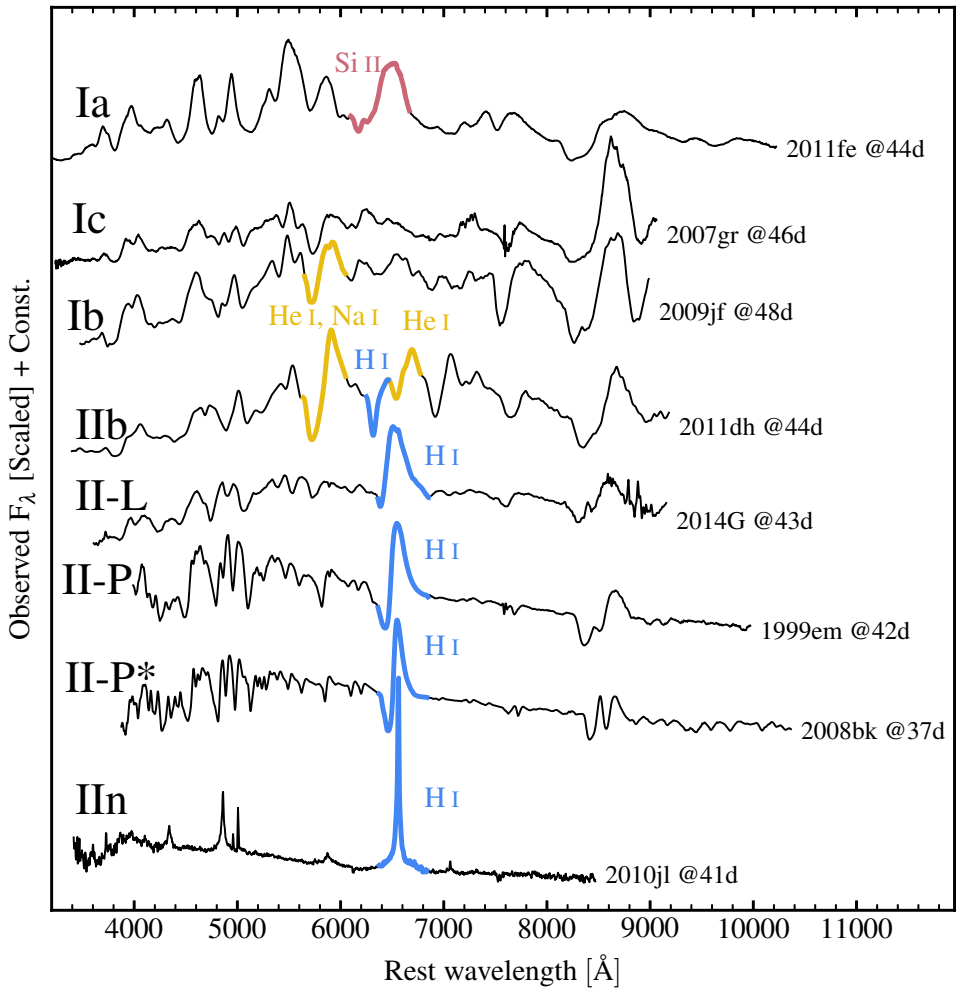

Figure A.2 – Spectral montage of different SNe types at around 40 d since explosion. See Figure 1.4 for early time spectra (1–2 weeks since explosion).

The photometric and spectroscopic data are taken from Hamuy (2001) and Leonard et al. (2003). We adopt a total extinction $A_V = 0.310$ mag (Dessart & Hillier, 2006).

A.2 A sample of core-collapse SNe

Core-collapse supernovae of different types, used in the dissertation, are listed with the data sources in Table A.2.

Table A.2 – Observational data for core-collapse SNe, used in the dissertation.

SN	Type	Host galaxy	Expl. date [MJD]	A_V^a [mag]	μ [mag]	V_{rec} [km s^{-1}]	References[b]
1969L	II-P	NGC 1058	40549±5	0.163	30.00±0.22	518	C71, A76, L12, T88
1979C	II-L	M 100	43795±3	0.07	31.52	1587	V81
1986L	II-L	NGC 1559	46703±3	0.08	31.64±0.46	1304	E86, T15, K04
1992ba	II-P	NGC 2082	48888.5±8	0.156	31.34±0.53	1246	H01, A14, O10, F96
1999bg	II-P	IC7 58	51251±14	0.052	32.41±0.18	1290	F14, P09, V91
1999gi	II-P	NGC 3184	51518±4	0.651*	30.34±0.14	592	F14, J09, S92
1999em	II-P	NGC 1637	51474.3±2	0.31*	30.30±0.17	800	DH06, L03
2000eo	IIn	PGC 11782	51864±5	0.212	33.01	3246	H17
2001X	II-P	NGC 5921	51963±5	0.106	31.85±0.22	1470	F14, R14
2001hg	II-P	NGC 4162	52260±20	0.1	33.07±0.50	2580	S09, F14
2002ca	II-P	UGC 8521	52353±15	0.063	33.03±0.45	3264	F14, T07
2003T	II-P	UGC 4864	52645[c]	0.084	35.21±0.42	8373	G16, A14, O10
2003bn	II-P	PGC831618	52694.5±3	0.174	33.67±0.42	3831	A14, O10
2003gd	II-P	M 74	52720±30[d]	0.187	29.76±0.29	657	F14, G16, R14, L93
2003hl	II-P	NGC 0772	52868.5±5	1.55*	32.39±0.30	2475	A14, F14
2003hn	II-P	NGC 1448	52866.5±10	0.408*	31.14±0.40	1170	A14, H08, O10
2004A	II-P	NGC 6207	53010±10	0.180*	31.44±0.40	852	T08a, H06, G08, S09, H98
2004dj	II-pec	NGC 2403	53170±8	0.107	27.54±0.24	133	Z06, T08b, V06, C05, F01, S10
2004et	II-P	NGC 6946	53271±1	1.3*	28.67±0.40	40	S06, F14, B14, E08
2005ay	II-P	NGC 3938	53456±10[e]	0.34*	31.27±0.30	809	GY08, F14, P09
2007gr	Ic	NGC 1058	54327	0.165	29.38	492	M14, V08
2009ib	II-P	NGC 1559	55041.3±3.1	0.5*	31.48±0.30	1304	T15, K04
2009jf	Ib	NGC 7479	55100	0.037	32.67	2443	M14
2009kr	II-L	NGC 1832	55141	0.195	32.31	1994	H17
2011dh	IIb	M 51	55712	0.095	29.75±0.60	466	H17
2011fe	Ia	M 101	55796.5	0.024	28.86	240	T13
2012aw	II-P	M 95	56003	0.23	30.00±0.22	778	D14, M13, B13, V91
2012ec	II-P	NGC 1084	56143±2	0.31*	31.33±0.43	1407	S15, B15, MCa13, So14, K04
2013ej	II-P/L	M 74	56500	0.19	29.93±0.12	657	Y16, V14, L93
2014cx	II-P	NGC 337	56901±1.5	0.297	31.33±0.43	1698	V16, C16, So14, V91

[a] In most cases, the visual extinction A_V corresponds to the Galactic extinction (Schlafly & Finkbeiner, 2011). When the quoted A_V has a superscript *, its value corresponds to the total extinction, taken from the cited literature.

[b] A14: Anderson et al. (2014a), A76: Arnett & Falk (1976), B13: Bose et al. (2013), B14: Bose & Kumar (2014), B15: Barbarino et al. (2015), C05: Chugai et al. (2005), C16: Childress et al. (2016). C71: Ciatti et al. (1971), DH06: Dessart & Hillier (2006); D14: Dall'Ora et al. (2014), E08: Epinat et al. (2008), E86: Lloyd Evans et al. (1986), F01: Freedman et al. (2001), F14: Faran et al. (2014b), F96: Fixsen et al. (1996), G08: Gurugubelli et al. (2008), G16: Galbany et al. (2016), GY08: Gal-Yam et al. (2008), H01: Hamuy (2001), H06: Hendry et al. (2006b), H08: Harutyunyan et al. (2008), H17: Hicken et al. (2017), H98: Haynes et al. (1998), J09: Jones et al. (2009), K04: Koribalski et al. (2004), L03: Leonard et al. (2003); L12: Lennarz et al. (2012), L93: Lu et al. (1993), M13: Munari et al. (2013), M14: Modjaz et al. (2014), Ma13: Maund et al. (2013), O10: Olivares E. et al. (2010), P09: Poznanski et al. (2009), R14: Rodríguez et al. (2014), S06: Sahu et al. (2006), S09: Springob et al. (2009), S10: Sellwood & Sánchez (2010), S15: Smartt et al. (2015), S92: Strauss et al. (1992), So14: Sorce et al. (2014), T07: Theureau et al. (2007), T08a: Tsvetkov (2008), T08b: Tsvetkov et al. (2008), T13: Tsvetkov et al. (2013), T15: Takáts et al. (2015), T88: Tifft & Cocke (1988), V06: Vinkó et al. (2006), V08: Valenti et al. (2008), V14: Valenti et al. (2014), V16: Valenti et al. (2016), V81: de Vaucouleurs et al. (1981),V91: de Vaucouleurs et al. (1991),Y16: Yuan et al. (2016), Z06: Zhang et al. (2006),

[c] For 2003T, we adopt explosion epoch of MJD 52645 in contrast to MJD 52654.5 (A14), basing on the plateau length (around 100 days in our case) and colors of spectra.

[d] For 2003gd, we adopt explosion epoch of MJD 52720±30, basing on the plateau length. The SN was discovered on MJD 52802, so the explosion epoch is highly uncertain.

[e] For 2005ay, we adopt explosion epoch of MJD 52645, basing on the plateau length and spectra colors.

Appendix B

Contributions of indiviudal ions to model spectra

In this appendix, plots show the quantity $F_{\lambda,\mathrm{All}}/F_{\lambda,\mathrm{less}}$, where $F_{\lambda,\mathrm{All}}$ is the total synthetic spectrum and $F_{\lambda,\mathrm{less}}$ is the spectrum computed with the bound-bound transitions of one atom/ion omitted.

B.1 Models m12, m25 and m27

Below we present plots indicating contributions of the individual ions to the model spectra of model m12 (discussed in Chapter 4 and Chapter 5), m25 and m27 (discussed in Chapter 5).

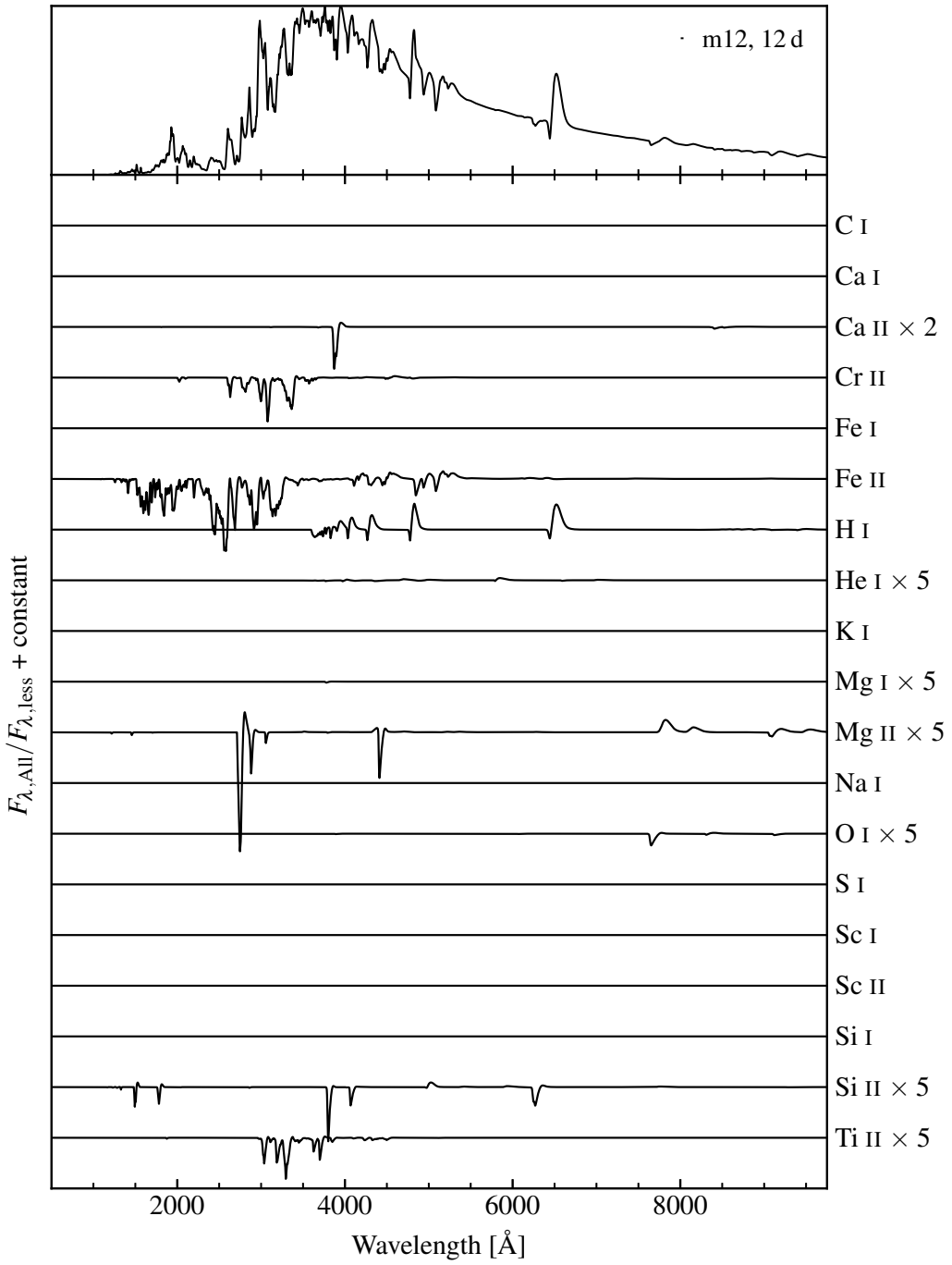

Figure B.1 – The top panel shows spectrum for model m12 at 12 d. The bottom panel stacks the quantity $F_{\lambda,\mathrm{All}}/F_{\lambda,\mathrm{less}}$, where $F_{\lambda,\mathrm{All}}$ is the total synthetic spectrum and $F_{\lambda,\mathrm{less}}$ is the spectrum computed with the bound-bound transitions of one atom/ion omitted (see label). For marked species, we apply some scaling factor (2 to 5, see label) to reveal the weak line features.

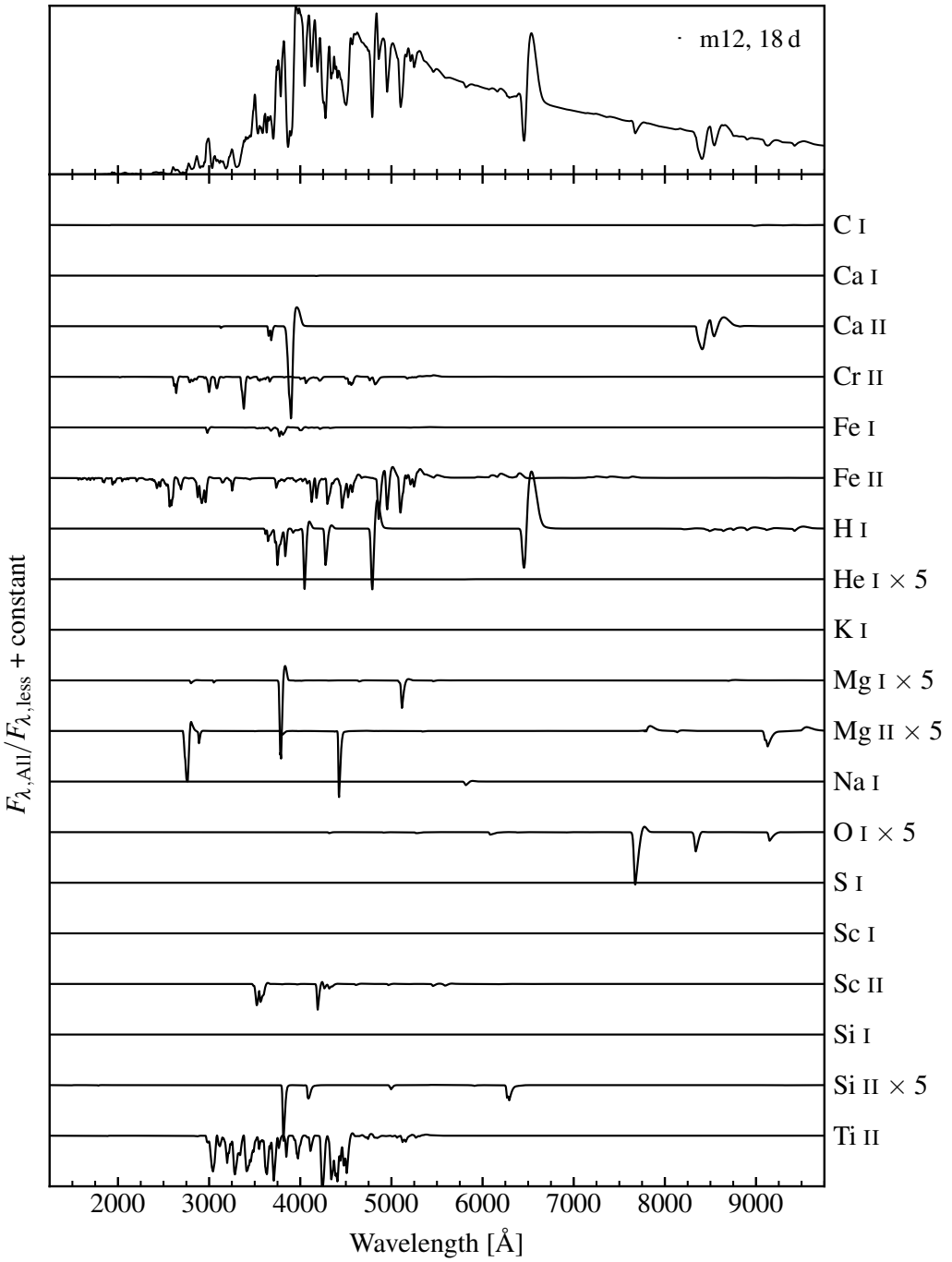

Figure B.2 – Same as Figure B.1, but for model m12 at 18 d.

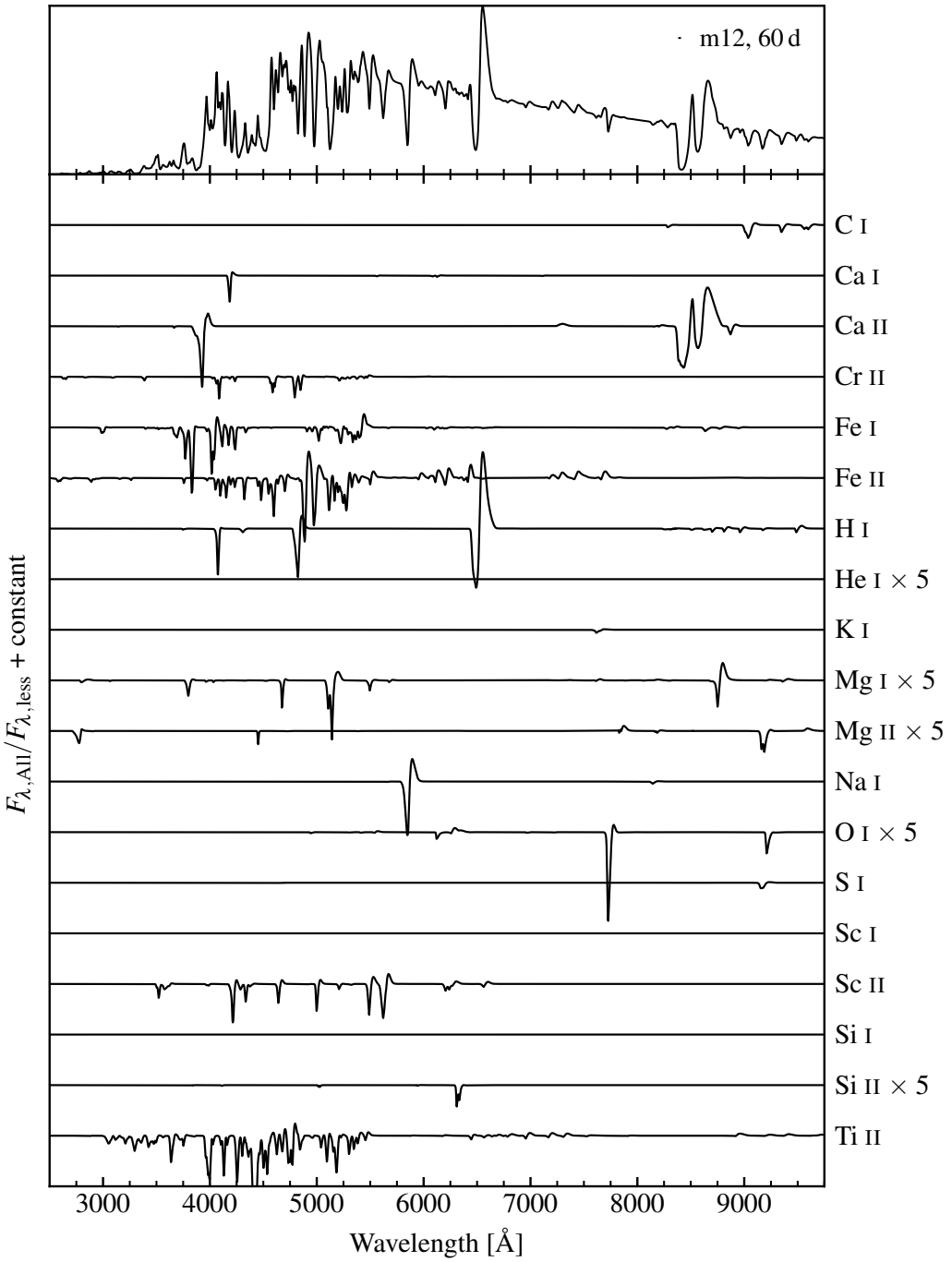

Figure B.3 – Same as Figure B.1, but for model m12 at 60 d.

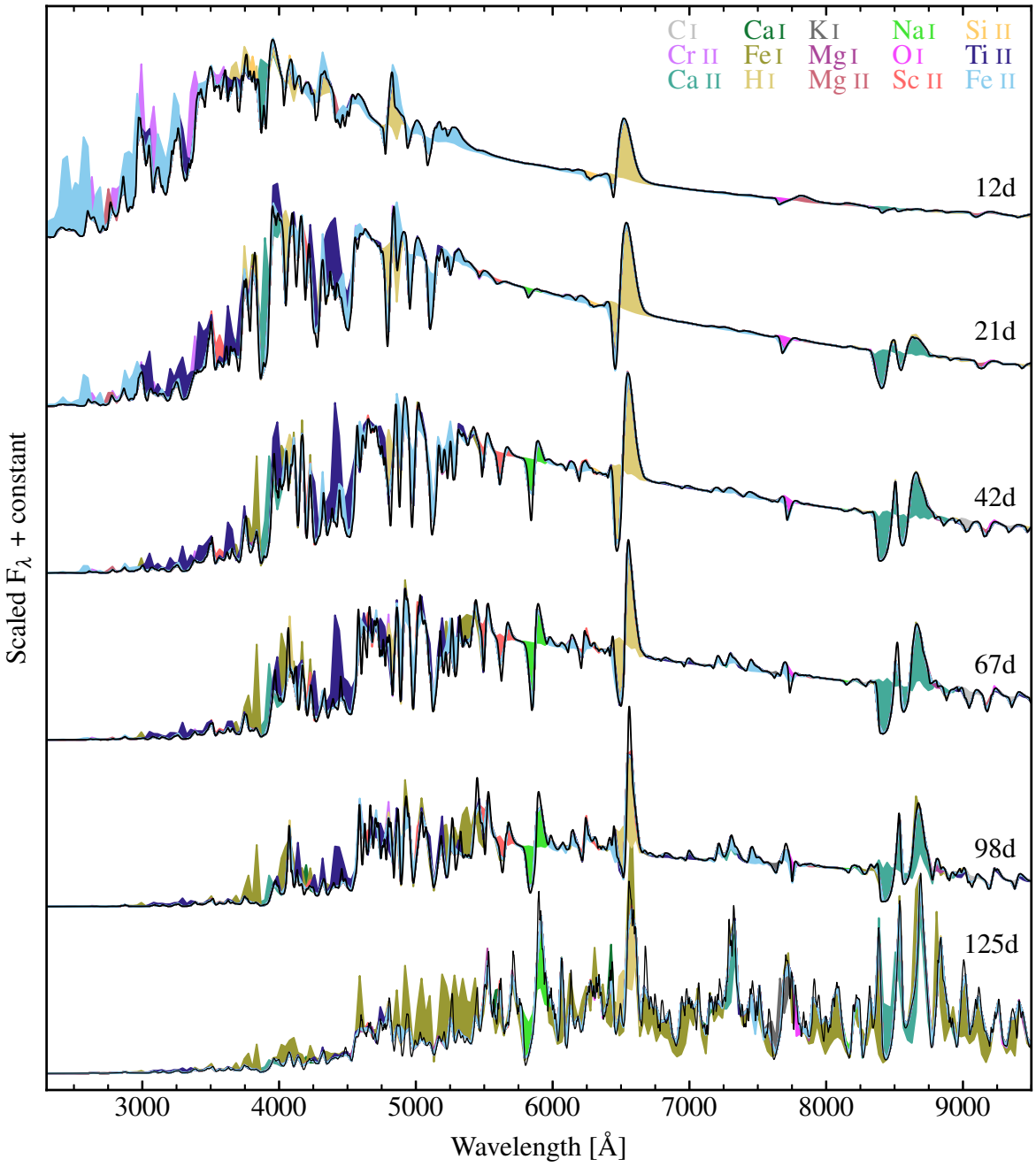

Figure B.4 – Another way of indicating ion contributions to the final spectra. Montage is shown for the model m12 at five different epochs.

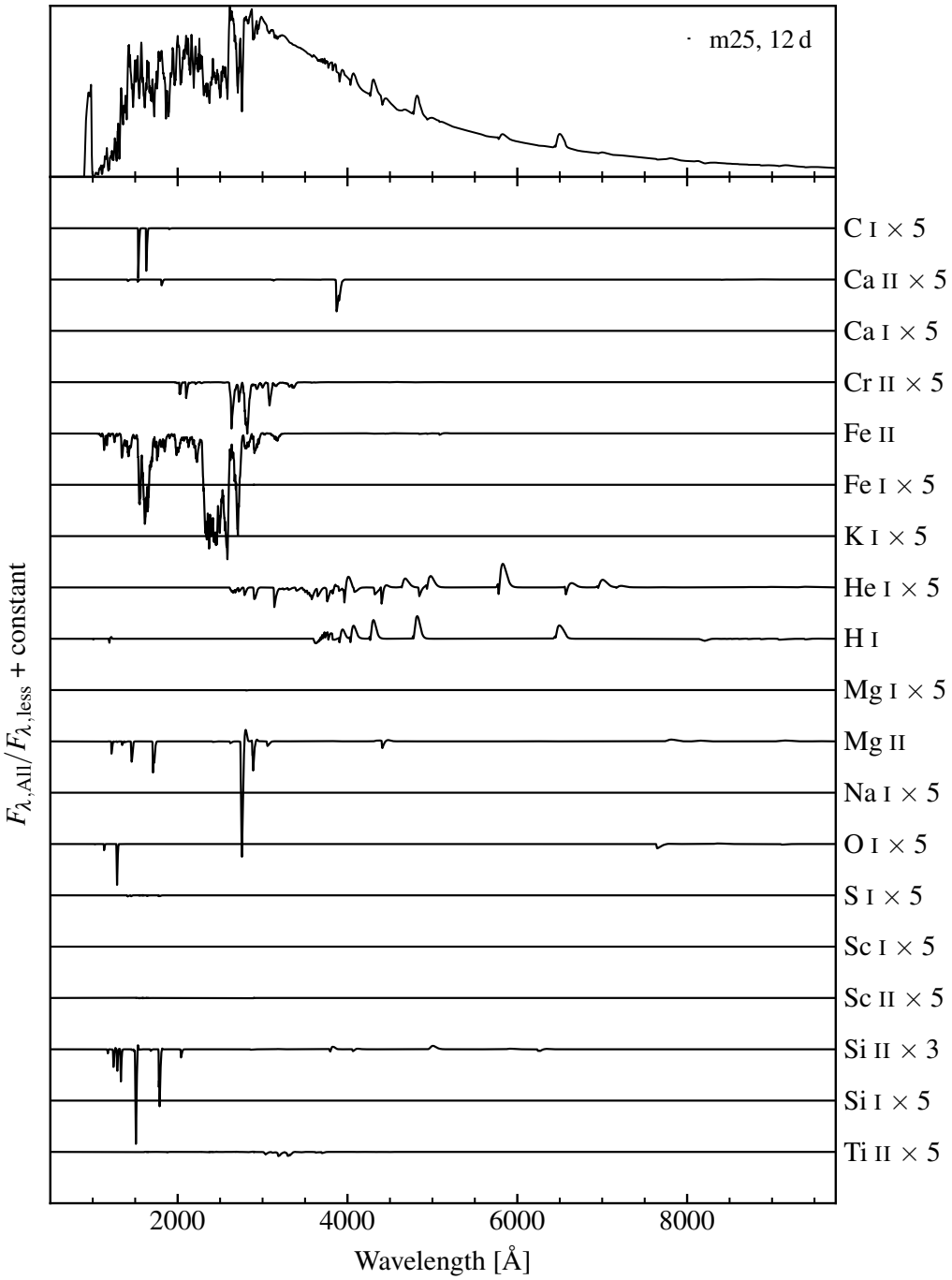

Figure B.5 – Same as Figure B.1, but for model m25 at 12 d.

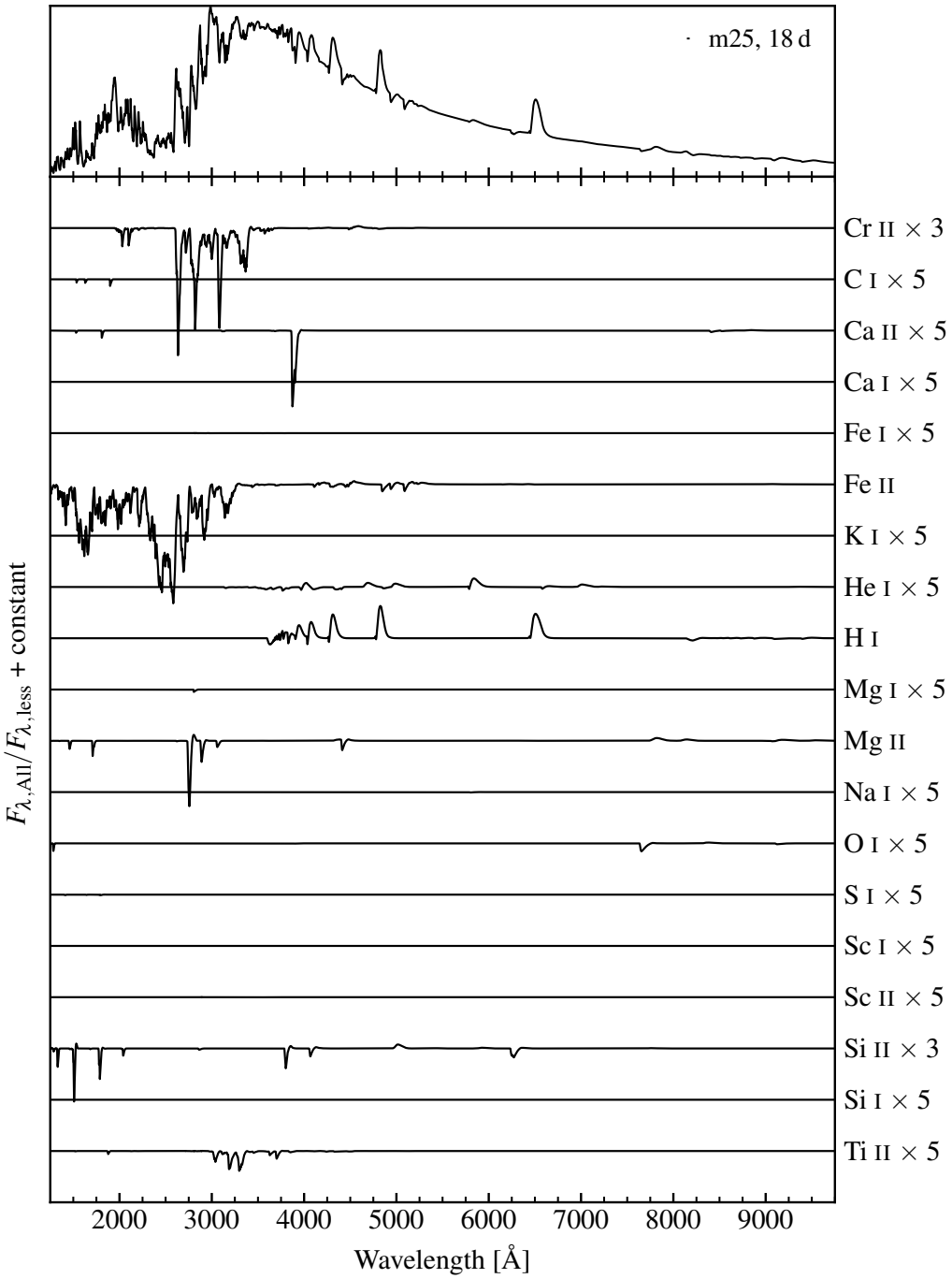

Figure B.6 – Same as Figure B.1, but for model m25 at 18 d.

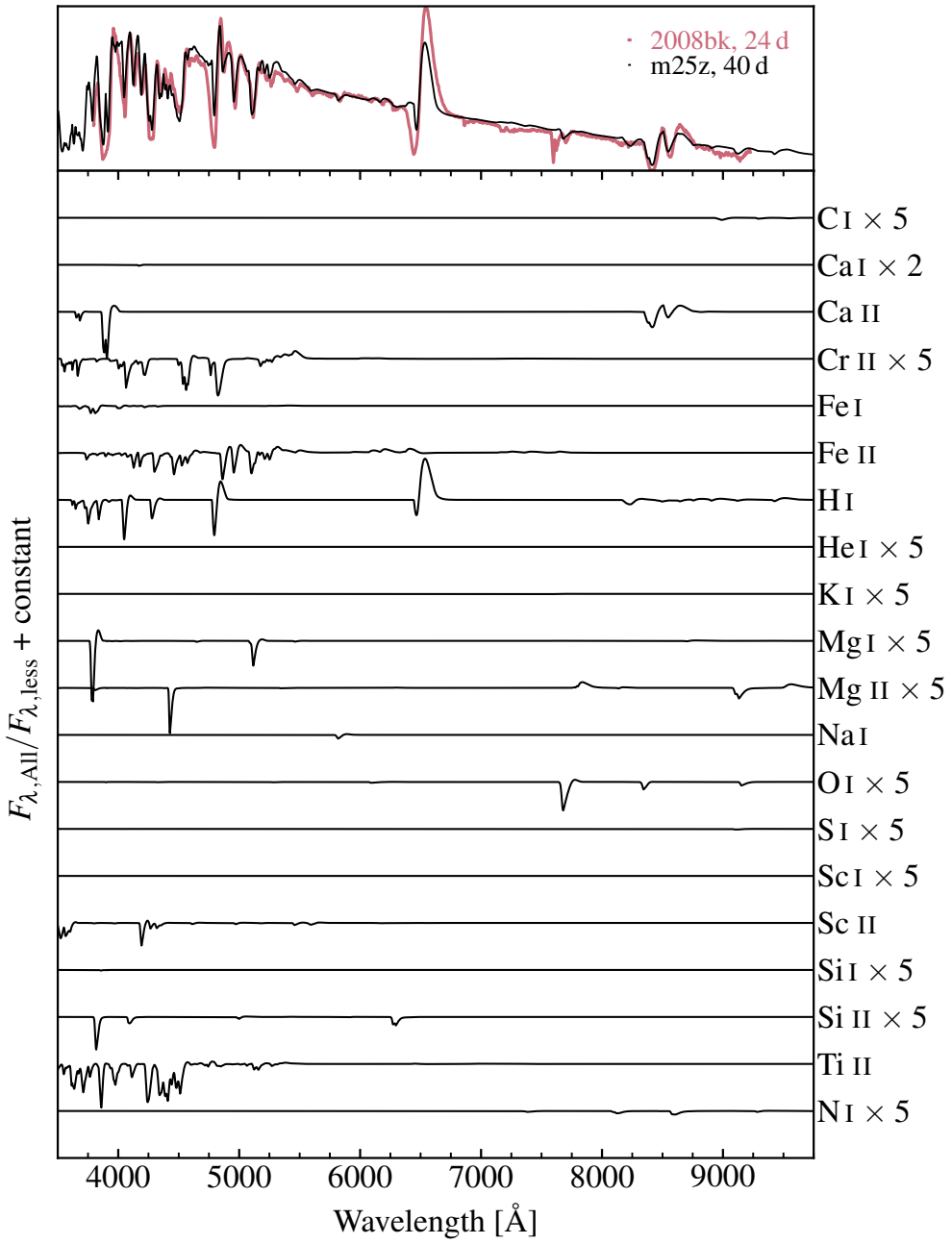

Figure B.7 – The top panel compares model m25 at 40 d with the observations (dereddened, deredshifted and normalized at 7100 Å) of SN 2008bk on 13th of April 2008 (which is about 24 d after our adopted time of explosion of MJD 54546.0). The bottom panel stacks the quantity $F_{\lambda,\mathrm{All}}/F_{\lambda,\mathrm{less}}$, where $F_{\lambda,\mathrm{All}}$ is the total synthetic spectrum and $F_{\lambda,\mathrm{less}}$ is the spectrum computed with the bound-bound transitions of one atom/ion omitted (see label). For marked species, we apply some scaling factor (2 to 5, see label) to reveal the weak line features.

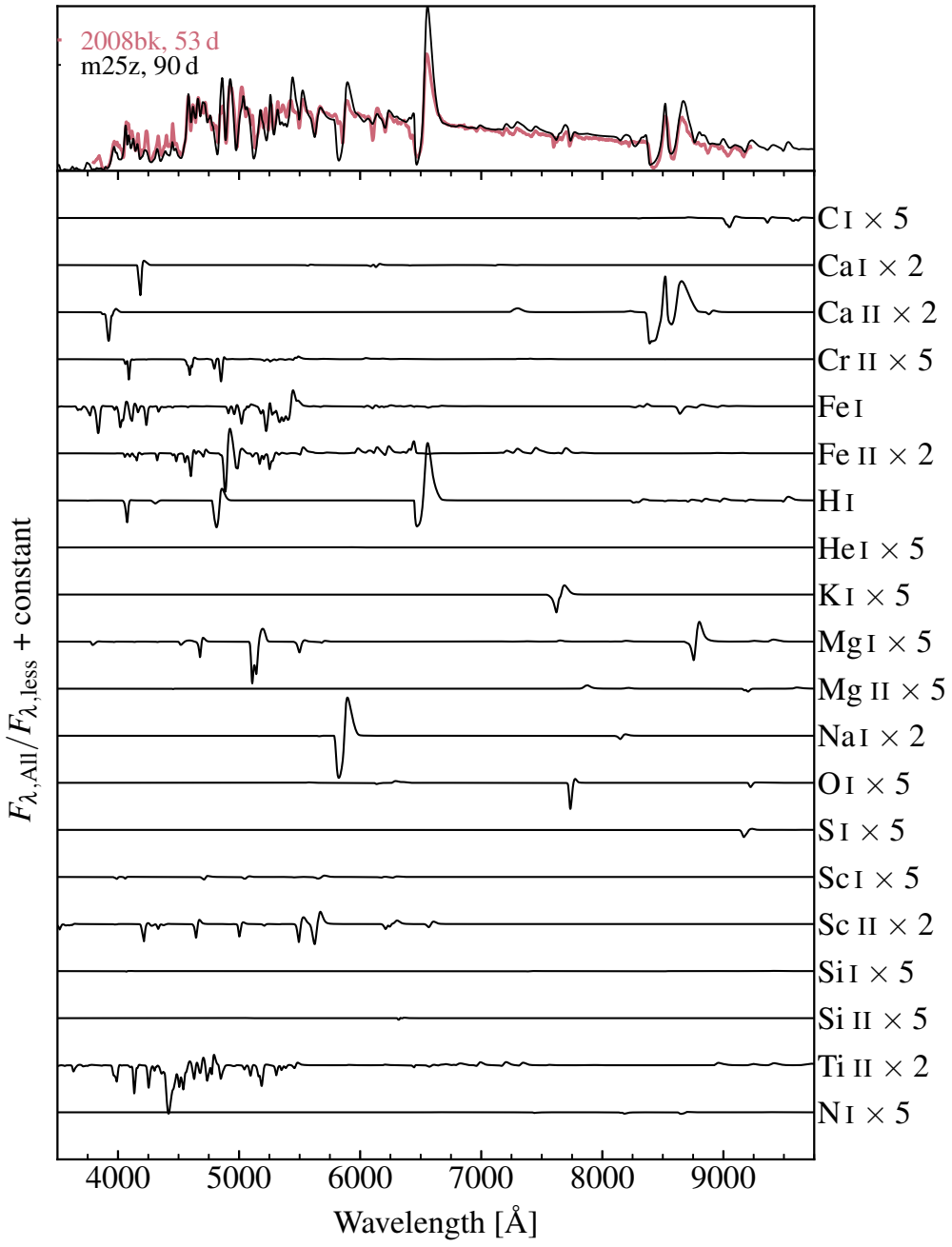

Figure B.8 – Same as Figure B.1, but SN 2008bk is shown at 53 d since explosion and model m25 at 90 d since explosion.

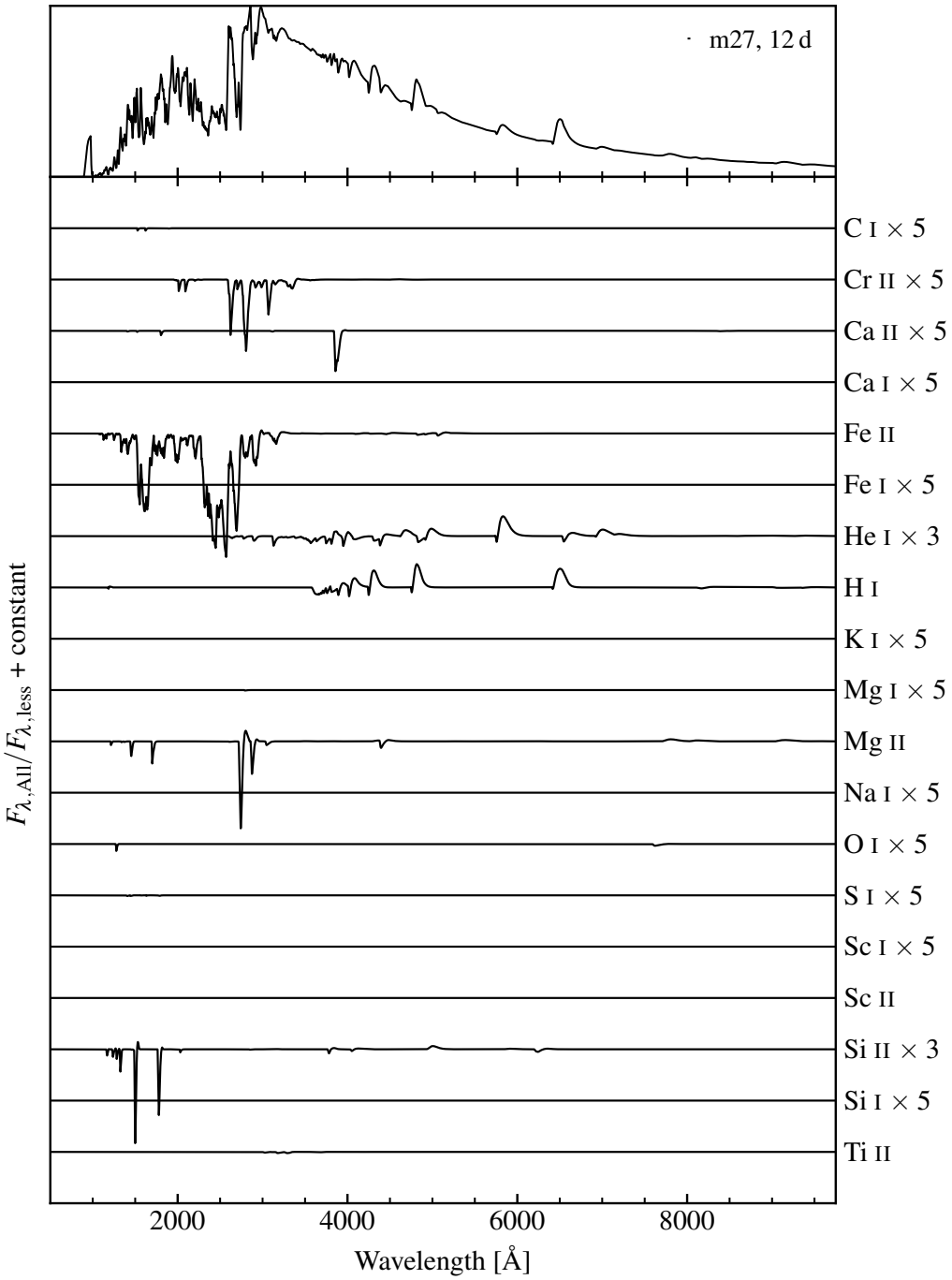

Figure B.9 – Same as Figure B.1, but for model m27 at 12 d.

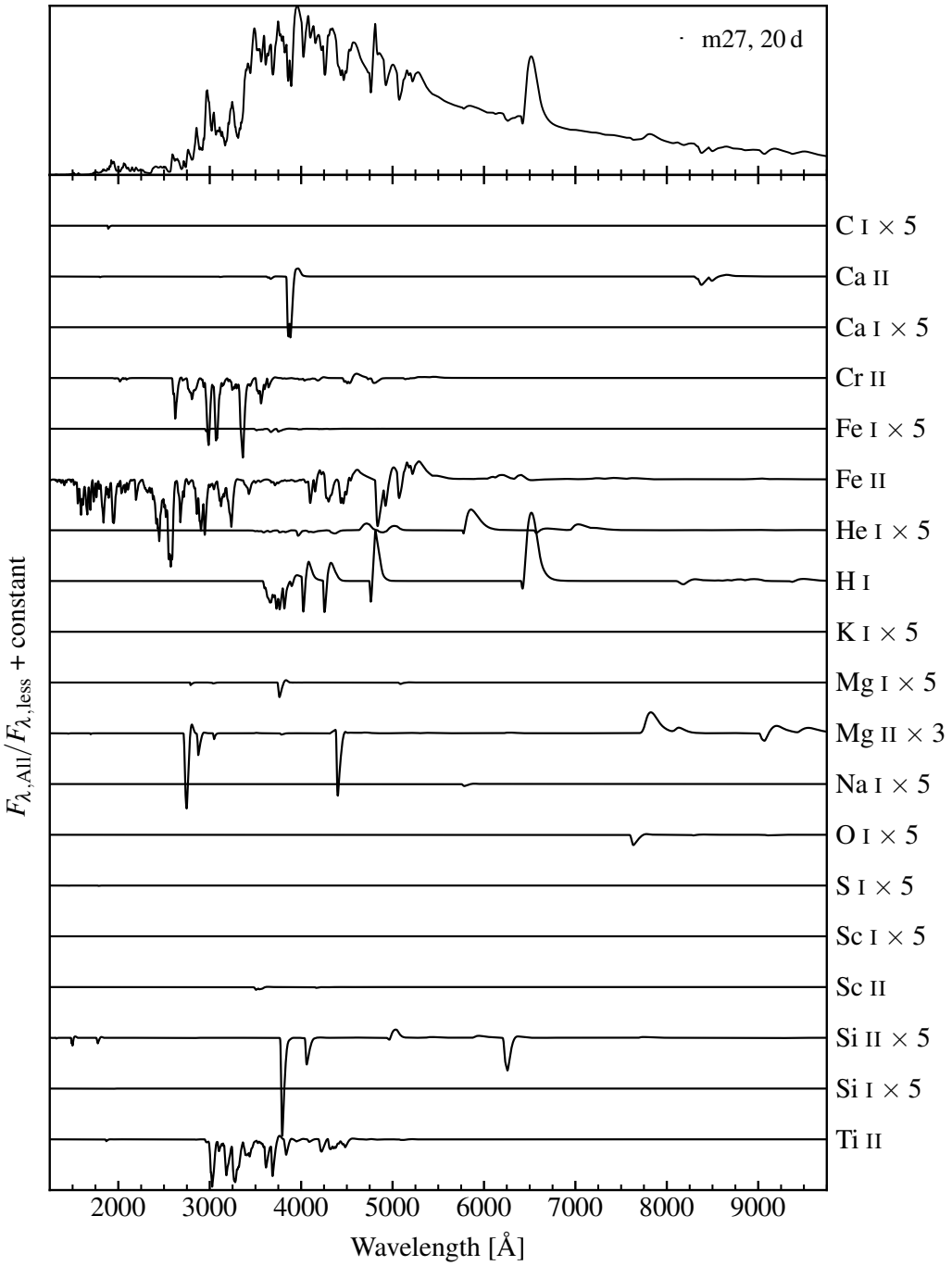

Figure B.10 – Same as Figure B.1, but for model m27 at 20 d.

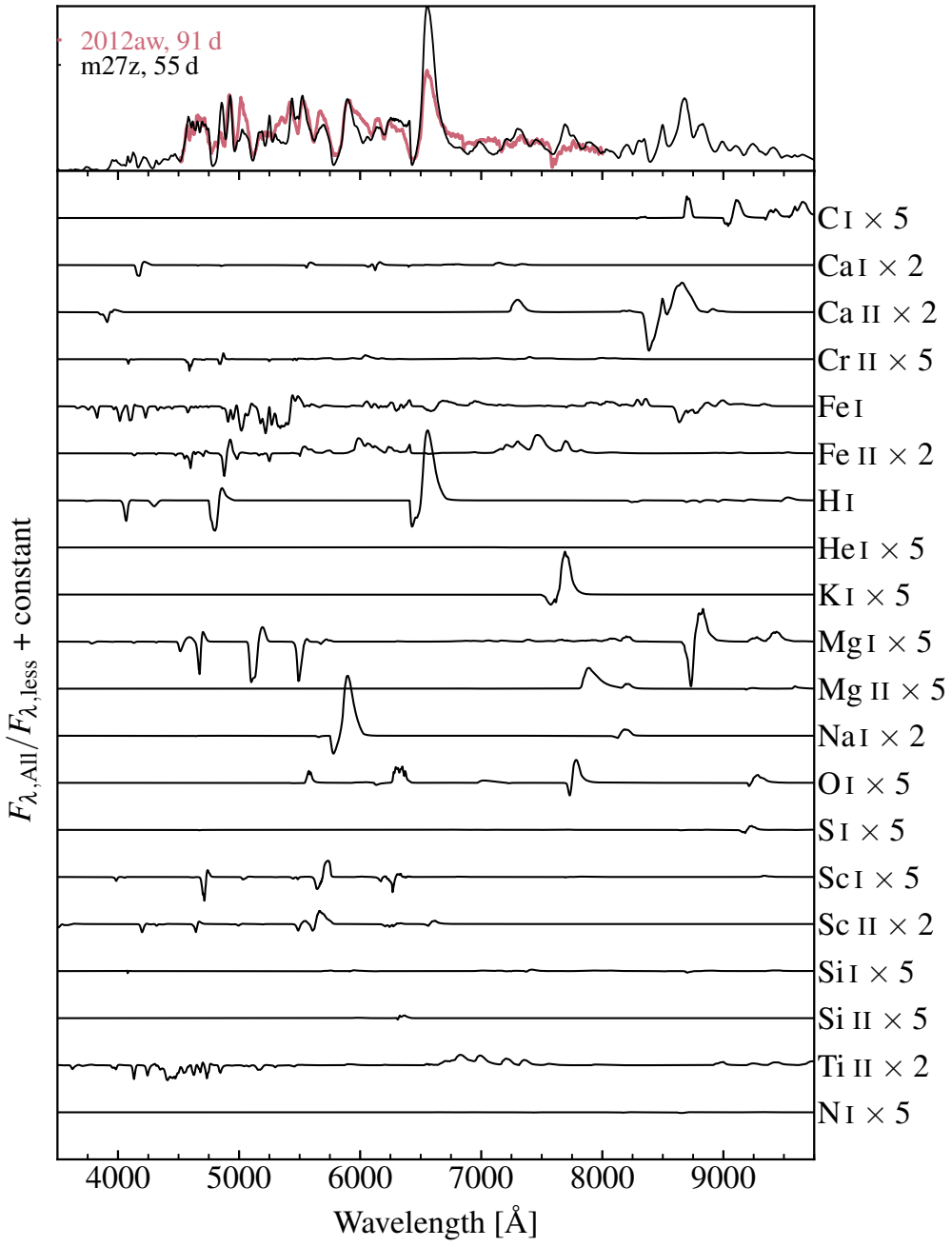

Figure B.11 – Same as Figure B.1, but model is compared to SN 2012aw at 91 d since explosion and model m27 at 55 d since explosion.

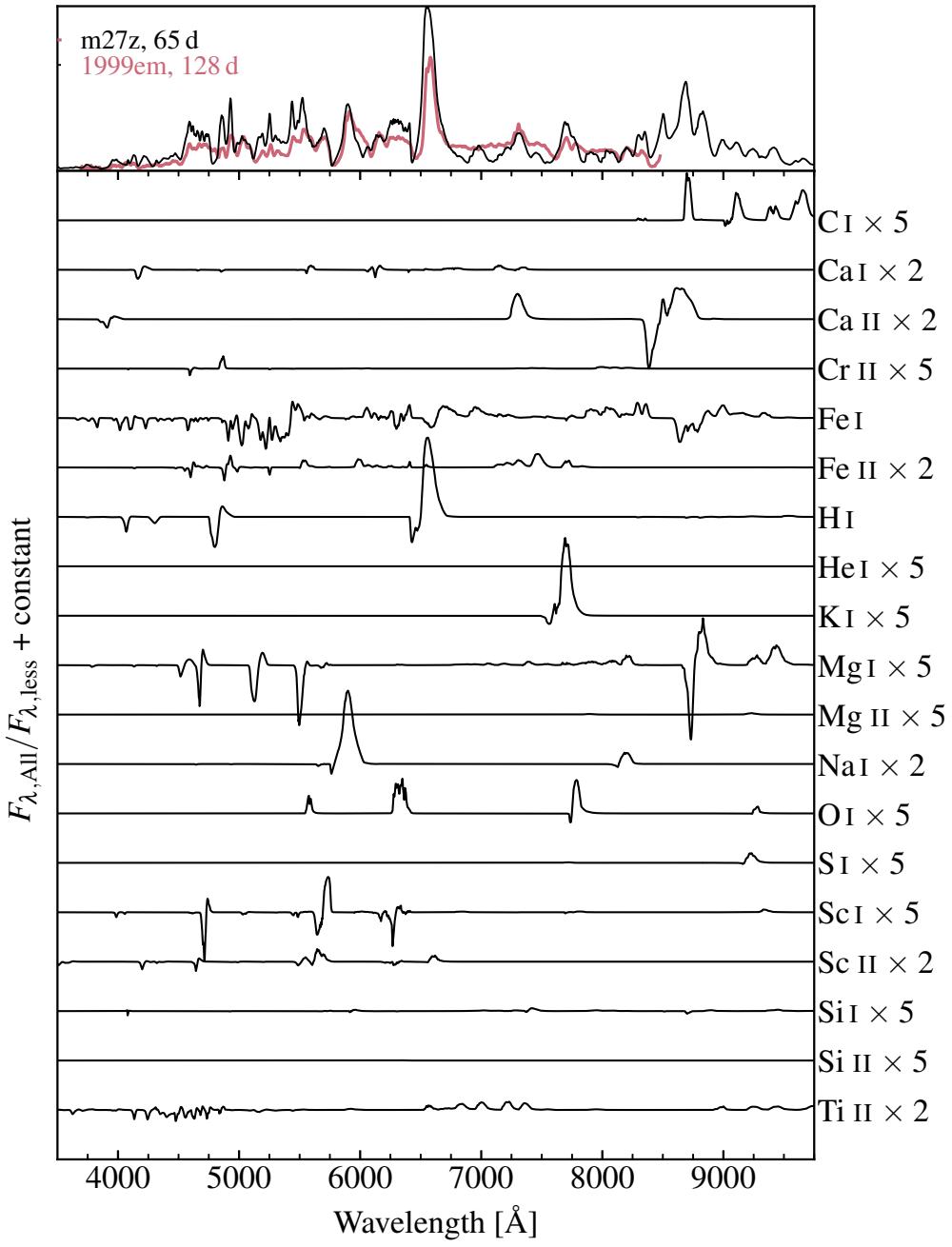

Figure B.12 – Same as Figure B.1, but model m27 at 65 d since explosion is compared to SN 1999em at 128 d since explosion.

Bibliography

Aldering G., Humphreys R. M., and Richmond M. (1994). SN 1993J: The optical properties of its progenitor. *Astronomical Journal*, 107:662–672. In the dissertation: 23

Anderson J. P., González-Gaitán S., Hamuy M., Gutiérrez C. P., Stritzinger M. D., Olivares E. F., et al. (2014a). Characterizing the V-band Light-curves of Hydrogen-rich Type II Supernovae. *ApJ*, 786:67. In the dissertation: 24, 27, 45, 46, 58, 91, 118

Anderson J. P., Dessart L., Gutierrez C. P., Hamuy M., Morrell N. I., Phillips M., Folatelli G., Stritzinger M. D., Freedman W. L., González-Gaitán S., McCarthy P., Suntzeff N., and Thomas-Osip J. (2014b). Analysis of blueshifted emission peaks in Type II supernovae. *MNRAS*, 441:671–680. In the dissertation: 49

Anderson W. (1929). Über die Grenzdichte der Materie und der Energie. *Zeitschrift fur Physik*, 56:851–856. In the dissertation: 20

Arcavi I., Gal-Yam A., and Sergeev S. G. (2013). Supernova 2003ie Was Likely a Faint Type IIP Event. *Astronomical Journal*, 145:99. In the dissertation: 116

Arnett D. (1996). Supernovae and Nucleosynthesis: An Investigation of the History of Matter from the Big Bang to the Present. In the dissertation: 12, 13, 15

Arnett W. D. (1980). Analytic solutions for light curves of supernovae of Type II. *ApJ*, 237:541–549. In the dissertation: 85

Arnett W. D. & Falk S. W. (1976). Some comparisons of theoretical supernova light curves with supernova 1969L (type II) in NGC 1058. *ApJ*, 210:733–740. In the dissertation: 118

Baade W. (1938). The Absolute Photographic Magnitude of Supernovae. *ApJ*, 88:285. In the dissertation: 10

Baade W. (1952). *Trans. IAU*, 8:397. In the dissertation: 10

Baklanov P. V., Blinnikov S. I., and Pavlyuk N. N. (2005). Parameters of the classical type-IIP supernova SN 1999em. *Astronomy Letters*, 31:429–441. In the dissertation: 37

Baltay C., Rabinowitz D., Hadjiyska E., Walker E. S., Nugent P., Coppi P., Ellman N., Feindt U., McKinnon R., Horowitz B., and Effron A. (2013). The La Silla-QUEST Low Redshift Supernova Survey. *Publications of the ASP*, 125:683. In the dissertation: 17

Barbarino C., Dall'Ora M., Botticella M. T., Della Valle M., Zampieri L., Maund J. R., et al. (2015). SN 2012ec: mass of the progenitor from PESSTO follow-up of the photospheric phase. *MNRAS*, 448:2312–2331. In the dissertation: 103, 104, 118

Barbon R., Ciatti F., and Rosino L. (1979). Photometric properties of type II supernovae. *A&A*, 72:287–292. In the dissertation: 17, 24

Barkat Z., Rakavy G., and Sack N. (1967). Dynamics of Supernova Explosion Resulting from Pair Formation. *Physical Review Letters*, 18:379–381. In the dissertation: 26

Baron E. & Hauschildt P. H. (1998). Parallel Implementation of the PHOENIX Generalized Stellar Atmosphere Program. II. Wavelength Parallelization. *ApJ*, 495:370–376. In the dissertation: 38

Bartunov O. S. & Blinnikov S. I. (1992). A model of supernova 1979C with radiative transfer in the envelope. *Soviet Astronomy Letters*, 18:43. In the dissertation: 21, 53, 91

Bartunov O. S., Blinnikov S. I., Pavlyuk N. N., and Tsvetkov D. Y. (1994). A model for Supernova 1993J. *A&A*, 281:L53–L55. In the dissertation: 24

Benetti S., Chugai N. N., Utrobin V. P., Cappellaro E., Patat F., Pastorello A., Turatto M., Cupani G., Neuhäuser R., Caldwell N., Pignata G., and Tomasella L. (2016). The spectacular evolution of Supernova 1996al over 15 yr: a low-energy explosion of a stripped massive star in a highly structured environment. *MNRAS*, 456:3296–3317. In the dissertation: 23

Benetti S., Turatto M., Balberg S., Zampieri L., Shapiro S. L., Cappellaro E., Nomoto K., Nakamura T., Mazzali P. A., and Patat F. (2001). The fading of supernova 1997D. *MNRAS*, 322:361–368. In the dissertation: 58, 111

van den Bergh S. (1988). Novae, Supernovae, and the Island Universe Hypothesis. *Publications of the ASP*, 100:8–17. In the dissertation: 9

Bersten M. C., Benvenuto O., and Hamuy M. (2011). Hydrodynamical Models of Type II Plateau Supernovae. *ApJ*, 729:61. In the dissertation: 45, 71, 104, 105, 107

Bertola F. (1964). The Supernovae in NGC 1073 and NGC 1058. *Annales d'Astrophysique*, 27:319. In the dissertation: 23

Bethe H. A. (1939). Energy Production in Stars. *Physical Review*, 55:434–456. In the dissertation: 13

Bethe H. A. & Wilson J. R. (1985). Revival of a stalled supernova shock by neutrino heating. *ApJ*, 295:14–23. In the dissertation: 15

Blanton E. L., Schmidt B. P., Kirshner R. P., Ford C. H., Chromey F. R., and Herbst W. (1995). Observations of the Type II-P SN 1991G in NGC 4088. *Astronomical Journal*, 110:2868. In the dissertation: 116

Blinnikov S. I., Eastman R., Bartunov O. S., Popolitov V. A., and Woosley S. E. (1998). A Comparative Modeling of Supernova 1993J. *ApJ*, 496:454–472. In the dissertation: 34, 37

Blinnikov S. I., Lundqvist P., Bartunov O. S., Nomoto K., and Iwamoto K. (2000). Radiation Hydrodynamics of SN 1987A. I. Global Analysis of the Light Curve for the First 4 Months. *ApJ*, 532:1132–1149. In the dissertation: 16

Blinnikov S. I., Röpke F. K., Sorokina E. I., Gieseler M., Reinecke M., Travaglio C., Hillebrandt W., and Stritzinger M. (2006). Theoretical light curves for deflagration models of type Ia supernova. *A&A*, 453:229–240. In the dissertation: 34, 37

Blondin S., Prieto J. L., Patat F., Challis P., Hicken M., Kirshner R. P., Matheson T., and Modjaz M. (2009). A Second Case of Variable Na I D Lines in a Highly Reddened Type Ia Supernova. *ApJ*, 693:207–215. In the dissertation: 20

Boles T., Beutler B., Li W., Qiu Y. L., Hu J. Y., and Schwartz M. (2003). Supernovae 2003X, 2003Y, and 2003Z. *IAU Cirulars*, 8062. In the dissertation: 115

Bose S. & Kumar B. (2014). Distance Determination to Eight Galaxies Using Expanding Photosphere Method. *ApJ*, 782:98. In the dissertation: 118

Bose S., Kumar B., Sutaria F., Kumar B., Roy R., Bhatt V. K., Pandey S. B., Chandola H. C., Sagar R., Misra K., and Chakraborti S. (2013). Supernova 2012aw — a high-energy clone of archetypal Type IIP SN 1999em. *MNRAS*, 433:1871–1891. In the dissertation: 118

Branch D., Jeffery D. J., Young T. R., and Baron E. (2006). Hydrogen in Type Ic Supernovae? *Publications of the ASP*, 118:791–796. In the dissertation: 25

Burrows A. (1988). Supernova neutrinos. *ApJ*, 334:891–908. In the dissertation: 15

Burrows A. (1990). Neutrinos from supernova explosions. *Annual Review of Nuclear and Particle Science*, 40:181–212. In the dissertation: 15

Burrows A., Hayes J., and Fryxell B. A. (1995). On the Nature of Core-Collapse Supernova Explosions. *ApJ*, 450:830. In the dissertation: 15

Burrows A. & Lattimer J. M. (1986). The birth of neutron stars. *ApJ*, 307:178–196. In the dissertation: 15

Cano Z., Wang S. Q., Dai Z. G., and Wu X. F. (2017). The Observer's Guide to the Gamma-Ray Burst Supernova Connection. *Advances in Astronomy*, 2017:8929054. In the dissertation: 26

Cao Y., Kasliwal M. M., Arcavi I., Horesh A., Hancock P., Valenti S., et al. (2013). Discovery, Progenitor and Early Evolution of a Stripped Envelope Supernova iPTF13bvn. *ApJ Letters*, 775:L7. In the dissertation: 23

Cappellari M., Emsellem E., Krajnović D., McDermid R. M., Scott N., Verdoes Kleijn G. A., et al. (2011). The ATLAS^{3D} project — I. A volume-limited sample of 260 nearby early-type galaxies: science goals and selection criteria. *MNRAS*, 413:813–836. In the dissertation: 113

Catchpole R. M., Menzies J. W., Monk A. S., Wargau W. F., Pollaco D., Carter B. S., Whitelock P. A., Marang F., Laney C. D., Balona L. A., Feast M. W., Lloyd Evans T. H. H., Sekiguchi K., Laing J. D., Kilkenny D. M., Spencer Jones J., Roberts G., Cousins A. W. J., van Vuuren G., and Winkler H. (1987). Spectroscopic and photometric observations of SN 1987a. II — Days 51 to 134. *MNRAS*, 229:15P–25P. In the dissertation: 25

Chakraborti S., Childs F., and Soderberg A. (2016). Young Remnants of Type Ia Supernovae and Their Progenitors: A Study of SNR G1.9+0.3. *ApJ*, 819:37. In the dissertation: 16

Chandrasekhar S. (1931). The Maximum Mass of Ideal White Dwarfs. *ApJ*, 74:81. In the dissertation: 20

Chevalier R. A. & Irwin C. M. (2011). Shock Breakout in Dense Mass Loss: Luminous Supernovae. *ApJ Letters*, 729:L6. In the dissertation: 26

Childress M. J., Tucker B. E., Yuan F., Scalzo R., Ruiter A., Seitenzahl I., et al. (2016). The ANU WiFeS SuperNovA Programme (AWSNAP). *Publ. Astron. Soc. Australia*, 33:e055. In the dissertation: 118

Chomiuk L., Chornock R., Soderberg A. M., Berger E., Chevalier R. A., Foley R. J., et al. (2011). Pan-STARRS1 Discovery of Two Ultraluminous Supernovae at $z \approx 0.9$. *ApJ*, 743:114. In the dissertation: 26

Chugai N. N., Blinnikov S. I., Cumming R. J., Lundqvist P., Bragaglia A., Filippenko A. V., Leonard D. C., Matheson T., and Sollerman J. (2004). The Type IIn supernova 1994W: evidence for the explosive ejection of a circumstellar envelope. *MNRAS*, 352:1213–1231. In the dissertation: 37

Chugai N. N., Chevalier R. A., and Utrobin V. P. (2007). Optical Signatures of Circumstellar Interaction in Type IIP Supernovae. *ApJ*, 662:1136–1147. In the dissertation: 74

Chugai N. N., Fabrika S. N., Sholukhova O. N., Goranskij V. P., Abolmasov P. K., and Vlasyuk V. V. (2005). Optical Observations of Type IIP Supernova 2004dj: Evidence for Asymmetry of the ^{56}Ni Ejecta. *Astronomy Letters*, 31:792–805. In the dissertation: 118

Chugai N. N. & Utrobin V. P. (2000). The nature of SN 1997D: low-mass progenitor and weak explosion. *A&A*, 354:557–566. In the dissertation: 97, 111

Ciatti F., Rosino L., and Bertola F. (1971). The type II supernova 1969 l in NGC 1058. *Mem. Soc. Astron. Italiana*, 42:163. In the dissertation: 118

Clayton D. D. (1968). Principles of stellar evolution and nucleosynthesis. In the dissertation: 13

Clocchiatti A. & Wheeler J. C. (1997). On the Light Curves of Stripped-Envelope Supernovae. *ApJ*, 491:375–380. In the dissertation: 55

Cohen J. G., Darling J., and Porter A. (1995). The Nonvariability of the Progenitor of Supernova 1993J in M81. *Astronomical Journal*, 110:308. In the dissertation: 23

Colgate S. A. (1989). Hot bubbles drive explosions. *Nature*, 341:489–490. In the dissertation: 15

Conselice C. J., Wilkinson A., Duncan K., and Mortlock A. (2016). The Evolution of Galaxy Number Density at $z < 8$ and Its Implications. *ApJ*, 830:83. In the dissertation: 16

Crockett R. M., Eldridge J. J., Smartt S. J., Pastorello A., Gal-Yam A., Fox D. B., Leonard D. C., Kasliwal M. M., Mattila S., Maund J. R., Stephens A. W., and Danziger I. J. (2008). The type IIb SN 2008ax: the nature of the progenitor. *MNRAS*, 391:L5–L9. In the dissertation: 23

Crockett R. M., Smartt S. J., Pastorello A., Eldridge J. J., Stephens A. W., Maund J. R., and Mattila S. (2011). On the nature of the progenitors of three Type II-P supernovae: 2004et, 2006my and 2006ov. *MNRAS*, 410:2767–2786. In the dissertation: 23

Curtis H. D. (1917). Novae in the Spiral Nebulae and the Island Universe Theory. *Publications of the ASP*, 29:206–207. In the dissertation: 9

Dall'Ora M., Botticella M. T., Pumo M. L., Zampieri L., Tomasella L., Pignata G., et al. (2014). The Type IIP Supernova 2012aw in M95: Hydrodynamical Modeling of the Photospheric Phase from Accurate Spectrophotometric Monitoring. *ApJ*, 787:139. In the dissertation: 118

Davies B., Crowther P. A., and Beasor E. R. (2018). The luminosities of cool supergiants in the Magellanic Clouds, and the Humphreys-Davidson limit revisited. *MNRAS*, 478:3138–3148. In the dissertation: 21

Dessart L., Waldman R., Livne E., Hillier D. J., and Blondin S. (2013a). Radiative properties of pair-instability supernova explosions. *MNRAS*, 428:3227–3251. In the dissertation: 26

Dessart L., Blondin S., Brown P. J., Hicken M., Hillier D. J., Holland S. T., Immler S., Kirshner R. P., Milne P., Modjaz M., and Roming P. W. A. (2008). Using Quantitative Spectroscopic Analysis to Determine the Properties and Distances of Type II Plateau Supernovae: SN 2005cs and SN 2006bp. *ApJ*, 675:644–669. In the dissertation: 113, 115

Dessart L. & Hillier D. J. (2005a). Quantitative spectroscopy of photospheric-phase type II supernovae. *A&A*, 437:667–685. In the dissertation: 39, 49, 59, 85

Dessart L. & Hillier D. J. (2005b). Distance determinations using type II supernovae and the expanding photosphere method. *A&A*, 439:671–685. In the dissertation: 71

Dessart L. & Hillier D. J. (2006). Quantitative spectroscopic analysis of and distance to SN1999em. *A&A*, 447:691–707. In the dissertation: 71, 117, 118

Dessart L. & Hillier D. J. (2008). Time-dependent effects in photospheric-phase Type II supernova spectra. *MNRAS*, 383:57–74. In the dissertation: 39, 59, 85

Dessart L. & Hillier D. J. (2010). Supernova radiative-transfer modelling: a new approach using non-local thermodynamic equilibrium and full time dependence. *MNRAS*, 405:2141–2160. In the dissertation: 39

Dessart L. & Hillier D. J. (2011). Non-LTE time-dependent spectroscopic modelling of Type II-plateau supernovae from the photospheric to the nebular phase: case study for 15 and 25 $M_{\odot}$ progenitor stars. *MNRAS*, 410:1739–1760. In the dissertation: 49, 58, 68, 74, 91, 92, 98, 105

Dessart L., Hillier D. J., Blondin S., and Khokhlov A. (2014). Critical ingredients of Type Ia supernova radiative-transfer modelling. *MNRAS*, 441:3249–3270. In the dissertation: 39

Dessart L., Hillier D. J., Li C., and Woosley S. (2012). On the nature of supernovae Ib and Ic. *MNRAS*, 424:2139–2159. In the dissertation: 24, 25, 35, 36

Dessart L., Hillier D. J., Livne E., Yoon S. C., Woosley S., Waldman R., and Langer N. (2011). Core-collapse explosions of Wolf-Rayet stars and the connection to Type IIb/Ib/Ic supernovae. *MNRAS*, 414:2985–3005. In the dissertation: 24, 25, 55

Dessart L., Hillier D. J., Waldman R., and Livne E. (2013b). Type II-Plateau supernova radiation: dependences on progenitor and explosion properties. *MNRAS*, 433:1745–1763. In the dissertation: 39, 58, 59, 61, 67, 68, 71, 76, 77, 85, 91, 98, 101, 103, 104, 105, 107

Dessart L., Livne E., and Waldman R. (2010a). Shock-heating of stellar envelopes: a possible common mechanism at the origin of explosions and eruptions in massive stars. *MNRAS*, 405:2113–2131. In the dissertation: 35, 59, 85, 87

Dessart L., Livne E., and Waldman R. (2010b). Determining the main-sequence mass of Type II supernova progenitors. *MNRAS*, 408:827–840. In the dissertation: 35, 58, 59, 85, 88, 94, 97, 103, 105

Dimai A. & Li W. (1999). Supernova 1999gn in M61. *IAU Cirulars*, 7335. In the dissertation: 114

Drake A. J., Djorgovski S. G., Mahabal A., Beshore E., Larson S., Graham M. J., Williams R., Christensen E., Catelan M., Boattini A., Gibbs A., Hill R., and Kowalski R. (2009). First Results from the Catalina Real-Time Transient Survey. *ApJ*, 696:870–884. In the dissertation: 17, 112

Drake A. J., Prieto J. L., Djorgovski S. G., Mahabal A. A., Graham M. J., Williams R., McNaught R. H., Catelan M., Christensen E., Beshore E. C., Larson S. M., and Howerton S. (2010). New Luminous Outbursts of Supernova Impostor SN 2009ip. *The Astronomer's Telegram*, 2897. In the dissertation: 25

Dubey A., Reid L. B., Weide K., Antypas K., Ganapathy M. K., Riley K., Sheeler D., and Siegal A. (2009). Extensible Component Based Architecture for FLASH, A Massively Parallel, Multiphysics Simulation Code. *ArXiv e-prints*. In the dissertation: 34

Eldridge J. J. & Tout C. A. (2004). The progenitors of core-collapse supernovae. *MNRAS*, 353:87–97. In the dissertation: 24

Elias-Rosa N., Pastorello A., Benetti S., Cappellaro E., Taubenberger S., Terreran G., et al. (2016). Dead or Alive? Long-term evolution of SN 2015bh (SNhunt275). *MNRAS*, 463:3894–3920. In the dissertation: 23

Elias-Rosa N., Van Dyk S. D., Li W., Miller A. A., Silverman J. M., Ganeshalingam M., Boden A. F., Kasliwal M. M., Vinkó J., Cuillandre J. C., Filippenko A. V., Steele T. N., Bloom J. S., Griffith C. V., Kleiser I. K. W., and Foley R. J. (2010). The Massive Progenitor of the Type II-linear Supernova 2009kr. *ApJ Letters*, 714:L254–L259. In the dissertation: 23

Elias-Rosa N., Van Dyk S. D., Li W., Morrell N., Gonzalez S., Hamuy M., Filippenko A. V., Cuillandre J. C., Foley R. J., and Smith N. (2009). On the Progenitor of the Type II-Plateau SN 2008cn in NGC 4603. *ApJ*, 706:1174–1183. In the dissertation: 23

Elias-Rosa N., Van Dyk S. D., Li W., Silverman J. M., Foley R. J., Ganeshalingam M., Mauerhan J. C., Kankare E., Jha S., Filippenko A. V., Beckman J. E., Berger E., Cuillandre J. C., and Smith N. (2011). The Massive Progenitor of the Possible Type II-Linear Supernova 2009hd in Messier 66. *ApJ*, 742:6. In the dissertation: 23

Epinat B., Amram P., Marcelin M., Balkowski C., Daigle O., Hernandez O., Chemin L., Carignan C., Gach J. L., and Balard P. (2008). GHASP: an Hα kinematic survey of spiral and irregular galaxies — VI. New Hα data cubes for 108 galaxies. *MNRAS*, 388:500–550. In the dissertation: 118

Ertl T., Janka H. T., Woosley S. E., Sukhbold T., and Ugliano M. (2016). A Two-parameter Criterion for Classifying the Explodability of Massive Stars by the Neutrino-driven Mechanism. *ApJ*, 818:124. In the dissertation: 35

Falk S. W. & Arnett W. D. (1977). Radiation Dynamics, Envelope Ejection, and Supernova Light Curves. *ApJ, Supplement*, 33:515. In the dissertation: 24, 57, 68

Faran T., Poznanski D., Filippenko A. V., Chornock R., Foley R. J., Ganeshalingam M., Leonard D. C., Li W., Modjaz M., Nakar E., Serduke F. J. D., and Silverman J. M. (2014a). Photometric and spectroscopic properties of Type II-P supernovae. *MNRAS*, 442:844–861. In the dissertation: 58

Faran T., Poznanski D., Filippenko A. V., Chornock R., Foley R. J., Ganeshalingam M., Leonard D. C., Li W., Modjaz M., Nakar E., Serduke F. J. D., and Silverman J. M. (2014b). Photometric and spectroscopic properties of Type II-P supernovae. *MNRAS*, 442:844–861. In the dissertation: 118

Faran T., Poznanski D., Filippenko A. V., Chornock R., Foley R. J., Ganeshalingam M., Leonard D. C., Li W., Modjaz M., Serduke F. J. D., and Silverman J. M. (2014c). A sample of Type II-L supernovae. *MNRAS*, 445:554–569. In the dissertation: 58

Filippenko A. V. (1997). Optical Spectra of Supernovae. *Annual Review of Astronomy and Astrophysics*, 35:309–355. In the dissertation: 18, 24, 46, 55

Fixsen D. J., Cheng E. S., Gales J. M., Mather J. C., Shafer R. A., and Wright E. L. (1996). The Cosmic Microwave Background Spectrum from the Full COBE FIRAS Data Set. *ApJ*, 473:576. In the dissertation: 118

Folatelli G., Contreras C., Phillips M. M., Woosley S. E., Blinnikov S., Morrell N., et al. (2006). SN 2005bf: A Possible Transition Event between Type Ib/c Supernovae and Gamma-Ray Bursts. *ApJ*, 641:1039–1050. In the dissertation: 37

Foley R. J., Berger E., Fox O., Levesque E. M., Challis P. J., Ivans I. I., Rhoads J. E., and Soderberg A. M. (2011). The Diversity of Massive Star Outbursts. I. Observations of SN 2009ip, UGC 2773 OT2009-1, and Their Progenitors. *ApJ*, 732:32. In the dissertation: 23

Foley R. J., Simon J. D., Burns C. R., Gal-Yam A., Hamuy M., Kirshner R. P., Morrell N. I., Phillips M. M., Shields G. A., and Sternberg A. (2012). Linking Type Ia Supernova Progenitors and Their Resulting Explosions. *ApJ*, 752:101. In the dissertation: 20

Fraser M., Ergon M., Eldridge J. J., Valenti S., Pastorello A., Sollerman J., et al. (2011). SN 2009md: another faint supernova from a low-mass progenitor. *MNRAS*, 417:1417–1433. In the dissertation: 23, 45, 97, 113, 115

Fraser M., Maund J. R., Smartt S. J., Botticella M. T., Dall'Ora M., Inserra C., Tomasella L., Benetti S., Ciroi S., Eldridge J. J., Ergon M., Kotak R., Mattila S., Ochner P., Pastorello A., Reilly E., Sollerman J., Stephens A., Taddia F., and Valenti S. (2012). Red and Dead: The Progenitor of SN 2012aw in M95. *ApJ Letters*, 759:L13. In the dissertation: 23

Fraser M., Maund J. R., Smartt S. J., Kotak R., Lawrence A., Bruce A., Valenti S., Yuan F., Benetti S., Chen T. W., Gal-Yam A., Inserra C., and Young D. R. (2014). On the progenitor of the Type IIP SN 2013ej in M74. *MNRAS*, 439:L56–L60. In the dissertation: 23

Fraser M., Takáts K., Pastorello A., Smartt S. J., Mattila S., Botticella M. T., Valenti S., Ergon M., Sollerman J., Arcavi I., Benetti S., Bufano F., Crockett R. M., Danziger I. J., Gal-Yam A., Maund J. R., Taubenberger S., and Turatto M. (2010). On the Progenitor and Early Evolution of the Type II Supernova 2009kr. *ApJ Letters*, 714:L280–L284. In the dissertation: 23

Freedman W. L., Madore B. F., Gibson B. K., Ferrarese L., Kelson D. D., Sakai S., Mould J. R., Kennicutt, Jr. R. C., Ford H. C., Graham J. A., Huchra J. P., Hughes S. M. G., Illingworth G. D., Macri L. M., and Stetson P. B. (2001). Final Results from the Hubble Space Telescope Key Project to Measure the Hubble Constant. *ApJ*, 553:47–72. In the dissertation: 118

Frieman J. A., Bassett B., Becker A., Choi C., Cinabro D., DeJongh F., et al. (2008). The Sloan Digital Sky Survey-II Supernova Survey: Technical Summary. *Astronomical Journal*, 135:338–347. In the dissertation: 17

Fryxell B., Arnett D., and Mueller E. (1991). Instabilities and clumping in SN 1987A. I — Early evolution in two dimensions. *ApJ*, 367:619–634. In the dissertation: 36, 80

Fryxell B., Olson K., Ricker P., Timmes F. X., Zingale M., Lamb D. Q., MacNeice P., Rosner R., Truran J. W., and Tufo H. (2000). FLASH: An Adaptive Mesh Hydrodynamics Code for Modeling Astrophysical Thermonuclear Flashes. *ApJ, Supplement*, 131:273–334. In the dissertation: 34

Gal-Yam A. (2012). Luminous Supernovae. *Science*, 337:927. In the dissertation: 25

Gal-Yam A., Bufano F., Barlow T. A., Baron E., Benetti S., Cappellaro E., et al. (2008). GALEX Spectroscopy of SN 2005ay Suggests Ultraviolet Spectral Uniformity among Type II-P Supernovae. *ApJ Letters*, 685:L117. In the dissertation: 118

Gal-Yam A., Kasliwal M. M., Arcavi I., Green Y., Yaron O., Ben-Ami S., et al. (2011). Real-time Detection and Rapid Multiwavelength Follow-up Observations of a Highly Subluminous Type II-P Supernova from the Palomar Transient Factory Survey. *ApJ*, 736:159. In the dissertation: 113, 115

Gal-Yam A. & Leonard D. C. (2009). A massive hypergiant star as the progenitor of the supernova SN 2005gl. *Nature*, 458:865–867. In the dissertation: 23

Gal-Yam A., Leonard D. C., Fox D. B., Cenko S. B., Soderberg A. M., Moon D. S., Sand D. J., Caltech Core Collapse Program, Li W., Filippenko A. V., Aldering G., and Copin Y. (2007). On the Progenitor of SN 2005gl and the Nature of Type IIn Supernovae. *ApJ*, 656:372–381. In the dissertation: 23

Gal-Yam A., Mazzali P., Ofek E. O., Nugent P. E., Kulkarni S. R., Kasliwal M. M., et al. (2009). Supernova 2007bi as a pair-instability explosion. *Nature*, 462:624–627. In the dissertation: 26

Galbany L., Hamuy M., Phillips M. M., Suntzeff N. B., Maza J., de Jaeger T., et al. (2016). UBVRIz Light Curves of 51 Type II Supernovae. *Astronomical Journal*, 151:33. In the dissertation: 58, 118

Gilmer M. S., Kozyreva A., Hirschi R., Fröhlich C., and Yusof N. (2017). Pair-instability Supernova Simulations: Progenitor Evolution, Explosion, and Light Curves. *ApJ*, 846:100. In the dissertation: 22

Gilmozzi R., Cassatella A., Clavel J., Fransson C., Gonzalez R., Gry C., Panagia N., Talavera A., and Wamsteker W. (1987). The progenitor of SN1987A. *Nature*, 328:318–320. In the dissertation: 23

González M., Audit E., and Huynh P. (2007). HERACLES: a three-dimensional radiation hydrodynamics code. *A&A*, 464:429–435. In the dissertation: 34

González-Gaitán S., Tominaga N., Molina J., Galbany L., Bufano F., Anderson J. P., Gutierrez C., Förster F., Pignata G., Bersten M., Howell D. A., Sullivan M., Carlberg R., de Jaeger T., Hamuy M., Baklanov P. V., and Blinnikov S. I. (2015). The rise-time of Type II supernovae. *MNRAS*, 451:2212–2229. In the dissertation: 77

Gorbovskoy E. S., Lipunov V. M., Kornilov V. G., Belinski A. A., Kuvshinov D. A., Tyurina N. V., Sankovich A. V., Krylov A. V., Shatskiy N. I., Balanutsa P. V., Chazov V. V., Kuznetsov A. S., Zimnukhov A. S., Shumkov V. P., Shurpakov S. E., Senik V. A., Gareeva D. V., and Pruzhinskaya M. V. (2013). The MASTER-II network of robotic optical telescopes. First results. *Astronomy Reports*, 57:233–286. In the dissertation: 17

Grassberg E. K., Imshennik V. S., and Nadyozhin D. K. (1971). On the Theory of the Light Curves of Supernovate. *Astrophysics and Space Science*, 10:28–51. In the dissertation: 24, 57

Graur O., Bianco F. B., Modjaz M., Shivvers I., Filippenko A. V., Li W., and Smith N. (2017). LOSS Revisited. II. The Relative Rates of Different Types of Supernovae Vary between Low- and High-mass Galaxies. *ApJ*, 837:121. In the dissertation: 43

Grebenev S. A., Lutovinov A. A., Tsygankov S. S., and Winkler C. (2012). Hard-X-ray emission lines from the decay of ^{44}Ti in the remnant of supernova 1987A. *Nature*, 490:373–375. In the dissertation: 41

Guillochon J., Parrent J., Kelley L. Z., and Margutti R. (2017). An Open Catalog for Supernova Data. *ApJ*, 835:64. In the dissertation: 109

Gurugubelli U. K., Sahu D. K., and Anupama G. C. (2011). Photometric and spectroscopic evolution of the type IIp supernova SN 2008in. In *Astronomical Society of India Conference Series*, volume 3, page 128. In the dissertation: 97

Gurugubelli U. K., Sahu D. K., Anupama G. C., and Chakradhari N. K. (2008). Photometric and spectroscopic evolution of type II-P supernova SN 2004A. *Bulletin of the Astronomical Society of India*, 36:79–97. In the dissertation: 118

Hakobyan A. A., Adibekyan V. Z., Aramyan L. S., Petrosian A. R., Gomes J. M., Mamon G. A., Kunth D., and Turatto M. (2012). Supernovae and their host galaxies. I. The SDSS DR8 database and statistics. *A&A*, 544:A81. In the dissertation: 113

Hamuy M. (2001). Type II supernovae as distance indicators. PhD thesis, The University of Arizona. In the dissertation: 117, 118

Hamuy M. (2003). Observed and Physical Properties of Core-Collapse Supernovae. *ApJ*, 582:905–914. In the dissertation: 48, 49, 50, 57, 58

Hamuy M., Phillips M. M., Suntzeff N. B., Maza J., González L. E., Roth M., Krisciunas K., Morrell N., Green E. M., Persson S. E., and McCarthy P. J. (2003). An asymptotic-giant-branch star in the progenitor system of a type Ia supernova. *Nature*, 424:651–654. In the dissertation: 18

Hamuy M., Phillips M. M., Suntzeff N. B., Schommer R. A., Maza J., Smith R. C., Lira P., and Aviles R. (1996). The Morphology of Type IA Supernovae Light Curves. *Astronomical Journal*, 112:2438. In the dissertation: 20

Hamuy M. & Pinto P. A. (2002). Type II Supernovae as Standardized Candles. *ApJ Letters*, 566:L63–L65. In the dissertation: 48

Harutyunyan A. H., Pfahler P., Pastorello A., Taubenberger S., Turatto M., Cappellaro E., Benetti S., Elias-Rosa N., Navasardyan H., Valenti S., Stanishev V., Patat F., Riello M., Pignata G., and Hillebrandt W. (2008). ESC supernova spectroscopy of non-ESC targets. *A&A*, 488:383–399. In the dissertation: 118

Hauschildt P. H. & Baron E. (1999). Numerical solution of the expanding stellar atmosphere problem. *Journal of Computational and Applied Mathematics*, 109:41–63. In the dissertation: 38

Hauschildt P. H., Baron E., and Allard F. (1997). Parallel Implementation of the PHOENIX Generalized Stellar Atmosphere Program. *ApJ*, 483:390–398. In the dissertation: 38

Hauschildt P. H., Lowenthal D. K., and Baron E. (2001). Parallel Implementation of the PHOENIX Generalized Stellar Atmosphere Program. III. A Parallel Algorithm for Direct Opacity Sampling. *ApJ, Supplement*, 134:323–329. In the dissertation: 38

Haynes M. P., van Zee L., Hogg D. E., Roberts M. S., and Maddalena R. J. (1998). Asymmetry in high-precision global H I profiles of isolated spiral galaxies. *Astronomical Journal*, 115:62. In the dissertation: 118

Heger A., Fryer C. L., Woosley S. E., Langer N., and Hartmann D. H. (2003). How Massive Single Stars End Their Life. *ApJ*, 591:288–300. In the dissertation: 24

Hendry M. A., Smartt S. J., Crockett R. M., Maund J. R., Gal-Yam A., Moon D. S., Cenko S. B., Fox D. W., Kudritzki R. P., Benn C. R., and Østensen R. (2006a). SN 2004A: another Type II-P supernova with a red supergiant progenitor. *MNRAS*, 369:1303–1320. In the dissertation: 23

Hendry M. A., Smartt S. J., Crockett R. M., Maund J. R., Gal-Yam A., Moon D. S., Cenko S. B., Fox D. W., Kudritzki R. P., Benn C. R., and Østensen R. (2006b). SN 2004A: another Type II-P supernova with a red supergiant progenitor. *MNRAS*, 369:1303–1320. In the dissertation: 118

Hertzsprung E. (1905). Zur Stralung Der Strerne. *Zeitschrift Fur Wissenschaftliche Photographie, Vol 3, p. 442-449*, 3:442–449. In the dissertation: 12

Hicken M., Challis P., Jha S., Kirshner R. P., Matheson T., Modjaz M., et al. (2009). CfA3: 185 Type Ia Supernova Light Curves from the CfA. *ApJ*, 700:331–357. In the dissertation: 18

Hicken M., Friedman A. S., Blondin S., Challis P., Berlind P., Calkins M., Esquerdo G., Matheson T., Modjaz M., Rest A., and Kirshner R. P. (2017). Type II Supernova Light Curves and Spectra from the CfA. *ApJ, Supplement*, 233:6. In the dissertation: 118

Hillier D. J. & Dessart L. (2012). Time-dependent radiative transfer calculations for supernovae. *MNRAS*, 424:252–271. In the dissertation: 39, 59, 85

Hillier D. J. & Miller D. L. (1998). The Treatment of Non-LTE Line Blanketing in Spherically Expanding Outflows. *ApJ*, 496:407–427. In the dissertation: 39, 59, 85

Hirschi R., Meynet G., and Maeder A. (2004). Stellar evolution with rotation. XII. Pre-supernova models. *A&A*, 425:649–670. In the dissertation: 24

Hodgkin S. T., Wyrzykowski L., Blagorodnova N., and Koposov S. (2013). Transient astronomy with the Gaia satellite. *Philosophical Transactions of the Royal Society of London Series A*, 371:20120239–20120239. In the dissertation: 17

Howell D. A., Sullivan M., Nugent P. E., Ellis R. S., Conley A. J., Le Borgne D., Carlberg R. G., Guy J., Balam D., Basa S., Fouchez D., Hook I. M., Hsiao E. Y., Neill J. D., Pain R., Perrett K. M., and Pritchet C. J. (2006). The type Ia supernova SNLS-03D3bb from a super-Chandrasekhar-mass white dwarf star. *Nature*, 443:308–311. In the dissertation: 20

Hoyle F. & Fowler W. A. (1960). Nucleosynthesis in Supernovae. *ApJ*, 132:565. In the dissertation: 17, 20

Hubble E. P. (1926). Extragalactic nebulae. *ApJ*, 64. In the dissertation: 10

Hubble E. P. (1929). A Relation between Distance and Radial Velocity among Extra-Galactic Nebulae. *Proceedings of the National Academy of Science*, 15:168–173. In the dissertation: 10

Hurst G. M., Armstrong M., Meikle P., Bramich D., Corradi R., Erwin P., Boles T., Irwin M., and Fassia A. (2001). Supernova 2001dc in NGC 5777. *IAU Cirulars*, 7662. In the dissertation: 114

Iben, Jr. I. & Tutukov A. V. (1984). Supernovae of type I as end products of the evolution of binaries with components of moderate initial mass (M not greater than about 9 solar masses). *ApJ, Supplement*, 54:335–372. In the dissertation: 20

de Jager C., Nieuwenhuijzen H., and van der Hucht K. A. (1988). Mass loss rates in the Hertzsprung-Russell diagram. *A&A, Supplement*, 72:259–289. In the dissertation: 21

Janka H. T., Gabler M., and Wongwathanarat A. (2017). Spatial distribution of radionuclides in 3D models of SN 1987A and Cas A. *ArXiv e-prints*. In the dissertation: 35

Janka H. T., Langanke K., Marek A., Martínez-Pinedo G., and Müller B. (2007). Theory of core-collapse supernovae. *Physics Reports*, 442:38–74. In the dissertation: 16

Janka H. T. & Mueller E. (1996). Neutrino heating, convection, and the mechanism of Type-II supernova explosions. *A&A*, 306:167. In the dissertation: 15, 34

Jerkstrand A., Ergon M., Smartt S. J., Fransson C., Sollerman J., Taubenberger S., Bersten M., and Spyromilio J. (2015). Late-time spectral line formation in Type IIb supernovae, with application to SN 1993J, SN 2008ax, and SN 2011dh. *A&A*, 573:A12. In the dissertation: 88

Jerkstrand A., Fransson C., and Kozma C. (2011). The ^{44}Ti-powered spectrum of SN 1987A. *A&A*, 530:A45. In the dissertation: 41

Jerkstrand A., Fransson C., Maguire K., Smartt S., Ergon M., and Spyromilio J. (2012). The progenitor mass of the Type IIP supernova SN 2004et from late-time spectral modeling. *A&A*, 546:A28. In the dissertation: 58, 80

Jerkstrand A., Smartt S. J., Inserra C., Nicholl M., Chen T. W., Krühler T., Sollerman J., Taubenberger S., Gal-Yam A., Kankare E., Maguire K., Fraser M., Valenti S., Sullivan M., Cartier R., and Young D. R. (2017). Long-duration Superluminous Supernovae at Late Times. *ApJ*, 835:13. In the dissertation: 26

Jones M. I., Hamuy M., Lira P., Maza J., Clocchiatti A., Phillips M., Morrell N., Roth M., Suntzeff N. B., Matheson T., Filippenko A. V., Foley R. J., and Leonard D. C. (2009). Distance Determination to 12 Type II Supernovae Using the Expanding Photosphere Method. *ApJ*, 696:1176–1194. In the dissertation: 118

Kaiser N., Aussel H., Burke B. E., Boesgaard H., Chambers K., Chun M. R., et al. (2002). Pan-STARRS: A Large Synoptic Survey Telescope Array. In Tyson J. A. & Wolff S., editors, *Survey and Other Telescope Technologies and Discoveries*, volume 4836 of *Proc. SPIE*, pages 154–164. In the dissertation: 17

Kasen D. & Bildsten L. (2010). Supernova Light Curves Powered by Young Magnetars. *ApJ*, 717:245–249. In the dissertation: 26

Kasen D., Thomas R. C., and Nugent P. (2006). Time-dependent Monte Carlo Radiative Transfer Calculations for Three-dimensional Supernova Spectra, Light Curves, and Polarization. *ApJ*, 651:366–380. In the dissertation: 38

Kasen D. & Woosley S. E. (2009). Type II Supernovae: Model Light Curves and Standard Candle Relationships. *ApJ*, 703:2205–2216. In the dissertation: 35, 68, 85, 96, 97

Khazov D., Yaron O., Gal-Yam A., Manulis I., Rubin A., Kulkarni S. R., et al. (2016). Flash Spectroscopy: Emission Lines from the Ionized Circumstellar Material around <10-day-old Type II Supernovae. *ApJ*, 818:3. In the dissertation: 116

Kifonidis K., Plewa T., Janka H. T., and Müller E. (2000). Nucleosynthesis and Clump Formation in a Core-Collapse Supernova. *ApJ Letters*, 531:L123–L126. In the dissertation: 36

Kifonidis K., Plewa T., Janka H. T., and Müller E. (2003). Non-spherical core collapse supernovae. I. Neutrino-driven convection, Rayleigh-Taylor instabilities, and the formation and propagation of metal clumps. *A&A*, 408:621–649. In the dissertation: 34, 36

Kifonidis K., Plewa T., Scheck L., Janka H. T., and Müller E. (2006). Non-spherical core collapse supernovae. II. The late-time evolution of globally anisotropic neutrino-driven explosions and their implications for SN 1987 A. *A&A*, 453:661–678. In the dissertation: 36

Kilpatrick C. D., Foley R. J., Abramson L. E., Pan Y. C., Lu C. X., Williams P., Treu T., Siebert M. R., Fassnacht C. D., and Max C. E. (2017). On the progenitor of the Type IIb supernova 2016gkg. *MNRAS*, 465:4650–4657. In the dissertation: 23

King J. Y. (1999). Supernova 1999br in NGC 4900. *IAU Cirulars*, 7141. In the dissertation: 114

Kiss L., Sarneczky K., and Sziladi K. (2000). Supernovae 1999gh, 1999gk, 1999gm, 1999gn, 1999gq. *IAU Cirulars*, 7347. In the dissertation: 114

Kitaura F. S., Janka H. T., and Hillebrandt W. (2006). Explosions of O-Ne-Mg cores, the Crab supernova, and subluminous type II-P supernovae. *A&A*, 450:345–350. In the dissertation: 93, 99

Klotz A., Puckett T., Langoussis A., Wood-Vasey W. M., Aldering G., Nugent P., and Stephens R. (2002). Supernova 2002gd in NGC 7537. *IAU Cirulars*, 7986. In the dissertation: 114

Knop S., Hauschildt P. H., Baron E., and Dreizler S. (2007). Analyzing SN 2003Z with PHOENIX. *A&A*, 469:1077–1081. In the dissertation: 38, 109

Koribalski B. S., Staveley-Smith L., Kilborn V. A., Ryder S. D., Kraan-Korteweg R. C., Ryan-Weber E. V., et al. (2004). The 1000 Brightest HIPASS Galaxies: H I Properties. *Astronomical Journal*, 128:16–46. In the dissertation: 118

Kozyreva A., Gilmer M., Hirschi R., Fröhlich C., Blinnikov S., Wollaeger R. T., Noebauer U. M., van Rossum D. R., Heger A., Even W. P., Waldman R., Tolstov A., Chatzopoulos E., and Sorokina E. (2017). Fast evolving pair-instability supernova models: evolution, explosion, light curves. *MNRAS*, 464:2854–2865. In the dissertation: 22, 35, 38

Kromer M. & Sim S. A. (2009). Time-dependent three-dimensional spectrum synthesis for Type Ia supernovae. *MNRAS*, 398:1809–1826. In the dissertation: 38

Kroupa P. (2001). On the variation of the initial mass function. *MNRAS*, 322:231–246. In the dissertation: 16, 22

Langer N. (1991). Supernova 1987 A — Prototype of low metallicity type II supernovae or peculiar exception? *A&A*, 243:155–159. In the dissertation: 25

Law N. M., Kulkarni S. R., Dekany R. G., Ofek E. O., Quimby R. M., Nugent P. E., et al. (2009). The Palomar Transient Factory: System Overview, Performance, and First Results. *Publications of the ASP*, 121:1395. In the dissertation: 17

Leloudas G., Chatzopoulos E., Dilday B., Gorosabel J., Vinko J., Gallazzi A., et al. (2012). SN 2006oz: rise of a super-luminous supernova observed by the SDSS-II SN Survey. *A&A*, 541:A129. In the dissertation: 26

Lemaître G. (1927). Un Univers homogène de masse constante et de rayon croissant rendant compte de la vitesse radiale des nébuleuses extra-galactiques. *Annales de la Société Scientifique de Bruxelles*, 47:49–59. In the dissertation: 10

Lennarz D., Altmann D., and Wiebusch C. (2012). A unified supernova catalogue. *A&A*, 538:A120. In the dissertation: 118

Leonard D. C., Dessart L., Hillier D. J., and Pignata G. (2012a). A spectropolarimetric comparison of the type II-Plateau supernovae SN 2008bk and SN 2004dj. In Hoffman J. L., Bjorkman J., and Whitney B., editors, *American Institute of Physics Conference Series*, volume 1429 of *American Institute of Physics Conference Series*, pages 204–207. In the dissertation: 59, 115

Leonard D. C., Filippenko A. V., Gates E. L., Li W., Eastman R. G., Barth A. J., Bus S. J., Chornock R., Coil A. L., Frink S., Grady C. A., Harris A. W., Malkan M. A., Matheson T., Quirrenbach A., and Treffers R. R. (2002a). The Distance to SN 1999em in NGC 1637 from the Expanding Photosphere Method. *Publications of the ASP*, 114:35–64. In the dissertation: 58

Leonard D. C., Filippenko A. V., Li W., Matheson T., Kirshner R. P., Chornock R., Van Dyk S. D., Berlind P., Calkins M. L., Challis P. M., Garnavich P. M., Jha S., and Mahdavi A. (2002b). A Study of the Type II-Plateau Supernova 1999gi and the Distance to its Host Galaxy, NGC 3184. *Astronomical Journal*, 124:2490–2505. In the dissertation: 49

Leonard D. C., Gal-Yam A., Fox D. B., Cameron P. B., Johansson E. M., Kraus A. L., Le Mignant D., and van Dam M. A. (2008). An Upper Mass Limit on a Red Supergiant Progenitor for the Type II-Plateau Supernova SN 2006my. *Publications of the ASP*, 120:1259. In the dissertation: 23

Leonard D. C., Kanbur S. M., Ngeow C. C., and Tanvir N. R. (2003). The Cepheid Distance to NGC 1637: A Direct Test of the Expanding Photosphere Method Distance to SN 1999em. *ApJ*, 594:247–278. In the dissertation: 117, 118

Leonard D. C., Pignata G., Dessart L., Hillier D., Horst C., Fedrow J. M., and Brewer L. (2012b). Early-Time Polarization of the Type II-Plateau Supernova SN 2012aw. *The Astronomer's Telegram*, 4033. In the dissertation: 68

Li W., Van Dyk S. D., Filippenko A. V., and Cuillandre J. C. (2005). On the Progenitor of the Type II Supernova 2004et in NGC 6946. *Publications of the ASP*, 117:121–131. In the dissertation: 23

Li W., Van Dyk S. D., Filippenko A. V., Cuillandre J. C., Jha S., Bloom J. S., Riess A. G., and Livio M. (2006). Identification of the Red Supergiant Progenitor of Supernova 2005cs: Do the Progenitors of Type II-P Supernovae Have Low Mass? *ApJ*, 641:1060–1070. In the dissertation: 23, 43, 45, 58, 112

Li W., Wang X., Van Dyk S. D., Cuillandre J. C., Foley R. J., and Filippenko A. V. (2007). On the Progenitors of Two Type II-P Supernovae in the Virgo Cluster. *ApJ*, 661:1013–1024. In the dissertation: 23

Li W. D. (1999). Supernova 1999em in NGC 1637. *IAU Cirulars*, 7294. In the dissertation: 116

Li W. D., Filippenko A. V., Treffers R. R., Friedman A., Halderson E., Johnson R. A., King J. Y., Modjaz M., Papenkova M., Sato Y., and Shefler T. (2000). The Lick Observatory Supernova Search. In Holt S. S. & Zhang W. W., editors, *American Institute of Physics Conference Series*, volume 522 of *American Institute of Physics Conference Series*, pages 103–106. In the dissertation: 17

Limongi M. & Chieffi A. (2003). Evolution, Explosion, and Nucleosynthesis of Core-Collapse Supernovae. *ApJ*, 592:404–433. In the dissertation: 24

Lin K., Cenko S. B., Li W., and Filippenko A. V. (2010). Supernova 2010id in NGC 7483. *Central Bureau Electronic Telegrams*, 2467. In the dissertation: 115

Lipunov V., Kornilov V., Gorbovskoy E., Shatskij N., Kuvshinov D., Tyurina N., et al. (2010). Master Robotic Net. *Advances in Astronomy*, 2010:349171. In the dissertation: 17

Lisakov S., Dessart L., Hillier D. J., Waldman R., and Livne E. (2017). A study of the low-luminosity Type II-Plateau supernova 2008bk. *MNRAS*, 466:34–48. In the dissertation: 86, 87, 88, 89, 93, 94, 95, 96, 97, 98, 113, 115

Lisakov S., Dessart L., Hillier D. J., Waldman R., and Livne E. (2018). Progenitors of low-luminosity Type II-Plateau supernovae. *MNRAS*, 473:3863–3881. In the dissertation: 85

Litvinova I. I. & Nadezhin D. K. (1983). Hydrodynamical models of type II supernovae. *Astrophysics and Space Science*, 89:89–113. In the dissertation: 24, 85

Litvinova I. Y. & Nadezhin D. K. (1985). Determination of Integrated Parameters for Type-II Supernovae. *Soviet Astronomy Letters*, 11:145–147. In the dissertation: 85

Livne E. (1993). An implicit method for two-dimensional hydrodynamics. *ApJ*, 412:634–647. In the dissertation: 35, 59, 85

Lloyd Evans T., Evans R., and McNaught R. H. (1986). Supernova 1986L in NGC 1559. *IAU Cirulars*, 4262. In the dissertation: 118

Lu N. Y., Hoffman G. L., Groff T., Roos T., and Lamphier C. (1993). H I 21 centimeter observations and I-band CCD surface photometry of spiral galaxies behind the Virgo Cluster and toward its antipode. *ApJ, Supplement*, 88:383–413. In the dissertation: 118

Lucy L. B. (2002). Monte Carlo transition probabilities. *A&A*, 384:725–735. In the dissertation: 38

Lucy L. B. (2003). Monte Carlo transition probabilities. II. *A&A*, 403:261–275. In the dissertation: 38

Lucy L. B. (2005). Monte Carlo techniques for time-dependent radiative transfer in 3-D supernovae. *A&A*, 429:19–30. In the dissertation: 38

Lyutikov M. & Blackman E. G. (2001). Gamma-ray bursts from unstable Poynting-dominated outflows. *MNRAS*, 321:177–186. In the dissertation: 26

MacFadyen A. I. & Woosley S. E. (1999). Collapsars: Gamma-Ray Bursts and Explosions in "Failed Supernovae". *ApJ*, 524:262–289. In the dissertation: 26

Maguire K., Jerkstrand A., Smartt S. J., Fransson C., Pastorello A., Benetti S., Valenti S., Bufano F., and Leloudas G. (2012). Constraining the physical properties of Type II-Plateau supernovae using nebular phase spectra. *MNRAS*, 420:3451–3468. In the dissertation: 58, 59

Maoz D., Mannucci F., and Nelemans G. (2014). Observational Clues to the Progenitors of Type Ia Supernovae. *Annual Review of Astronomy and Astrophysics*, 52:107–170. In the dissertation: 16

Matheson T., Filippenko A. V., Ho L. C., Barth A. J., and Leonard D. C. (2000). Detailed Analysis of Early to Late-Time Spectra of Supernova 1993J. *Astronomical Journal*, 120:1499–1515. In the dissertation: 54

Mattila S., Smartt S. J., Eldridge J. J., Maund J. R., Crockett R. M., and Danziger I. J. (2008). VLT Detection of a Red Supergiant Progenitor of the Type II-P Supernova 2008bk. *ApJ Letters*, 688:L91–L94. In the dissertation: 23, 43, 58, 59, 61, 115

Maund J. R., Fraser M., Ergon M., Pastorello A., Smartt S. J., Sollerman J., Benetti S., Botticella M. T., Bufano F., Danziger I. J., Kotak R., Magill L., Stephens A. W., and Valenti S. (2011). The Yellow Supergiant Progenitor of the Type II Supernova 2011dh in M51. *ApJ Letters*, 739:L37. In the dissertation: 22, 23

Maund J. R., Fraser M., Reilly E., Ergon M., and Mattila S. (2015). Whatever happened to the progenitors of supernovae 2008cn, 2009kr and 2009md? *MNRAS*, 447:3207–3217. In the dissertation: 22, 23, 45

Maund J. R., Fraser M., Smartt S. J., Botticella M. T., Barbarino C., Childress M., Gal-Yam A., Inserra C., Pignata G., Reichart D., Schmidt B., Sollerman J., Taddia F., Tomasella L., Valenti S., and Yaron O. (2013). Supernova 2012ec: identification of the progenitor and early monitoring with PESSTO. *MNRAS*, 431:L102–L106. In the dissertation: 23, 118

Maund J. R., Mattila S., Ramirez-Ruiz E., and Eldridge J. J. (2014a). A new precise mass for the progenitor of the Type IIP SN 2008bk. *MNRAS*, 438:1577–1592. In the dissertation: 23, 43, 45, 58, 59

Maund J. R., Reilly E., and Mattila S. (2014b). A late-time view of the progenitors of five Type IIP supernovae. *MNRAS*, 438:938–958. In the dissertation: 23

Maund J. R. & Smartt S. J. (2005). Hubble Space Telescope imaging of the progenitor sites of six nearby core-collapse supernovae. *MNRAS*, 360:288–304. In the dissertation: 23

Maund J. R., Smartt S. J., and Danziger I. J. (2005). The progenitor of SN 2005cs in the Whirlpool Galaxy. *MNRAS*, 364:L33–L37. In the dissertation: 23, 43, 45, 58

Mauron N. & Josselin E. (2011). The mass-loss rates of red supergiants and the de Jager prescription. *A&A*, 526:A156. In the dissertation: 21

Meija J., Coplen T. B., Berglund M., Brand W. A., de Bièvre P., Gröning M., Holden N. E., Irrgeher J., Loss R. D., Walczyk T., and Prohaska T. (2016). Atomic weights of the elements 2013 (IUPAC Technical Report). *Pure Appl. Chem.*, 77:265–291. In the dissertation: 11

de Mello D., Benetti S., and Massone G. (1997). Supernova 1997D in NGC 1536. *IAU Cirulars*, 6537. In the dissertation: 111, 112

Menon A. & Heger A. (2017). The quest for blue supergiants: binary merger models for the evolution of the progenitor of SN 1987A. *MNRAS*, 469:4649–4664. In the dissertation: 25

Menzies J. W., Catchpole R. M., van Vuuren G., Winkler H., Laney C. D., Whitelock P. A., Cousins A. W. J., Carter B. S., Marang F., Lloyd Evans T. H. H., Roberts G., Kilkenny D., Spencer Jones J., Sekiguchi K., Fairall A. P., and Wolstencroft R. D. (1987). Spectroscopic and photometric observations of SN 1987a — The first 50 days. *MNRAS*, 227:39P–49P. In the dissertation: 25

Meynet G., Chomienne V., Ekström S., Georgy C., Granada A., Groh J., Maeder A., Eggenberger P., Levesque E., and Massey P. (2015). Impact of mass-loss on the evolution and pre-supernova properties of red supergiants. *A&A*, 575:A60. In the dissertation: 21

Milisavljevic D., Margutti R., Kamble A., Patnaude D. J., Raymond J. C., Eldridge J. J., et al. (2015). Metamorphosis of SN 2014C: Delayed Interaction between a Hydrogen Poor Core-collapse Supernova and a Nearby Circumstellar Shell. *ApJ*, 815:120. In the dissertation: 23

Minkowski R. (1941). Spectra of Supernovae. *Publications of the ASP*, 53:224. In the dissertation: 17

Modjaz M., Blondin S., Kirshner R. P., Matheson T., Berlind P., Bianco F. B., Calkins M. L., Challis P., Garnavich P., Hicken M., Jha S., Liu Y. Q., and Marion G. H. (2014). Optical Spectra of 73 Stripped-envelope Core-collapse Supernovae. *Astronomical Journal*, 147:99. In the dissertation: 55, 118

Modjaz M., Kirshner R., Challis P., and Hutchins R. (2005). Supernovae 2005cp and 2005cs. *Central Bureau Electronic Telegrams*, 174. In the dissertation: 115

Monard L. A. G. (2008). Supernova 2008bk in NGC 7793. *Central Bureau Electronic Telegrams*, 1315. In the dissertation: 115

Moriya T., Tominaga N., Tanaka M., Maeda K., and Nomoto K. (2010). A Core-collapse Supernova Model for the Extremely Luminous Type Ic Supernova 2007bi: An Alternative to the Pair-instability Supernova Model. *ApJ Letters*, 717:L83–L86. In the dissertation: 25

Moriya T. J., Pruzhinskaya M. V., Ergon M., and Blinnikov S. I. (2016). On the nature of rapidly fading Type II supernovae. *MNRAS*, 455:423–430. In the dissertation: 21, 37, 53

Morozova V., Piro A. L., Renzo M., Ott C. D., Clausen D., Couch S. M., Ellis J., and Roberts L. F. (2015). Light Curves of Core-collapse Supernovae with Substantial Mass Loss Using the New Open-source SuperNova Explosion Code (SNEC). *ApJ*, 814:63. In the dissertation: 34

Müller T., Prieto J. L., Pejcha O., and Clocchiatti A. (2017). The Nickel Mass Distribution of Normal Type II Supernovae. *ApJ*, 841:127. In the dissertation: 48

Munari U., Henden A., Belligoli R., Castellani F., Cherini G., Righetti G. L., and Vagnozzi A. (2013). BVRI lightcurves of supernovae SN 2011fe in M101, SN 2012aw in M95, and SN 2012cg in NGC 4424. *New Astronomy*, 20:30–37. In the dissertation: 118

Nadyozhin D. K. (1994). The properties of Ni → Co → Fe decay. *ApJ, Supplement*, 92:527–531. In the dissertation: 41

Nakano S. & Aoki M. (1999). Supernova 1999eu in NGC 1097. *IAU Cirulars*, 7304. In the dissertation: 114

Nakano S., Itagaki K., and Kadota K. (2006). Supernova 2006ov in M61. *Central Bureau Electronic Telegrams*, 756. In the dissertation: 114

Nakano S., Kadota K., and Buzzi L. (2009a). Supernova 2009N in NGC 4487. *Central Bureau Electronic Telegrams*, 1670. In the dissertation: 115

Nakano S., Kadota K., and Wells W. (2008). Supernova 2008in in M61. *Central Bureau Electronic Telegrams*, 1636. In the dissertation: 114

Nakano S., Yusa T., and Kadota K. (2009b). Supernova 2009md in NGC 3389. *Central Bureau Electronic Telegrams*, 2065. In the dissertation: 115

Nasonova O. G., de Freitas Pacheco J. A., and Karachentsev I. D. (2011). Hubble flow around Fornax cluster of galaxies. *A&A*, 532:A104. In the dissertation: 113

Noebauer U. M. & Sim S. A. (2015). Self-consistent modelling of line-driven hot-star winds with Monte Carlo radiation hydrodynamics. *MNRAS*, 453:3120–3134. In the dissertation: 34

Noebauer U. M., Sim S. A., Kromer M., Röpke F. K., and Hillebrandt W. (2012). Monte Carlo radiation hydrodynamics: methods, tests and application to Type Ia supernova ejecta. *MNRAS*, 425:1430–1444. In the dissertation: 34

Nomoto K., Suzuki T., Shigeyama T., Kumagai S., Yamaoka H., and Saio H. (1993). A Type IIb model for supernova 1993J. *Nature*, 364:507–509. In the dissertation: 24

Nomoto K. I., Iwamoto K., and Suzuki T. (1995). The evolution and explosion of massive binary stars and Type Ib-Ic-IIb-IIL supernovae. *Physics Reports*, 256:173–191. In the dissertation: 24, 55

Nugis T. & Lamers H. J. G. L. M. (2000). Mass-loss rates of Wolf-Rayet stars as a function of stellar parameters. *A&A*, 360:227–244. In the dissertation: 21

Olivares E. F., Hamuy M., Pignata G., Maza J., Bersten M., Phillips M. M., Suntzeff N. B., Filippenko A. V., Morrel N. I., Kirshner R. P., and Matheson T. (2010). The Standardized Candle Method for Type II Plateau Supernovae. *ApJ*, 715:833–853. In the dissertation: 118

Osterbrock D. E. (2001). Who Really Coined the Word Supernova? Who First Predicted Neutron Stars? In *American Astronomical Society Meeting Abstracts*, volume 33 of *Bulletin of the American Astronomical Society*, page 1330. In the dissertation: 10

Pastorello A., Mattila S., Zampieri L., Della Valle M., Smartt S. J., Valenti S., et al. (2008). Massive stars exploding in a He-rich circumstellar medium — I. Type Ibn (SN 2006jc-like) events. *MNRAS*, 389:113–130. In the dissertation: 24

Pastorello A., Smartt S. J., Botticella M. T., Maguire K., Fraser M., Smith K., et al. (2010). Ultra-bright Optical Transients are Linked with Type Ic Supernovae. *ApJ Letters*, 724:L16–L21. In the dissertation: 26

Pastorello A., Valenti S., Zampieri L., Navasardyan H., Taubenberger S., Smartt S. J., et al. (2009). SN 2005cs in M51 — II. Complete evolution in the optical and the near-infrared. *MNRAS*, 394:2266–2282. In the dissertation: 97, 115

Pastorello A., Zampieri L., Turatto M., Cappellaro E., Meikle W. P. S., Benetti S., Branch D., Baron E., Patat F., Armstrong M., Altavilla G., Salvo M., and Riello M. (2004). Low-luminosity Type II supernovae: spectroscopic and photometric evolution. *MNRAS*, 347:74–94. In the dissertation: 43, 45, 53, 58, 93, 97, 111, 112, 113, 114

Patat F., Chandra P., Chevalier R., Justham S., Podsiadlowski P., Wolf C., et al. (2007). Detection of Circumstellar Material in a Normal Type Ia Supernova. *Science*, 317:924. In the dissertation: 20

Paxton B., Bildsten L., Dotter A., Herwig F., Lesaffre P., and Timmes F. (2011). Modules for Experiments in Stellar Astrophysics (MESA). *ApJ, Supplement*, 192:3. In the dissertation: 14, 29, 59, 60, 85

Paxton B., Cantiello M., Arras P., Bildsten L., Brown E. F., Dotter A., Mankovich C., Montgomery M. H., Stello D., Timmes F. X., and Townsend R. (2013). Modules for Experiments in Stellar Astrophysics (MESA): Planets, Oscillations, Rotation, and Massive Stars. *ApJ, Supplement*, 208:4. In the dissertation: 29, 59, 60, 85

Paxton B., Marchant P., Schwab J., Bauer E. B., Bildsten L., Cantiello M., Dessart L., Farmer R., Hu H., Langer N., Townsend R. H. D., Townsley D. M., and Timmes F. X. (2015). Modules for Experiments in Stellar Astrophysics (MESA): Binaries, Pulsations, and Explosions. *ApJ, Supplement*, 220:15. In the dissertation: 29, 34, 59, 60, 85, 103

Paxton B., Schwab J., Bauer E. B., Bildsten L., Blinnikov S., Duffell P., Farmer R., Goldberg J. A., Marchant P., Sorokina E., Thoul A., Townsend R. H. D., and Timmes F. X. (2018). Modules for Experiments in Stellar Astrophysics (MESA): Convective Boundaries, Element Diffusion, and Massive Star Explosions. *ApJ, Supplement*, 234:34. In the dissertation: 29, 38

Perlmutter S., Aldering G., Goldhaber G., Knop R. A., Nugent P., Castro P. G., et al. (1999). Measurements of Ω and Λ from 42 High-Redshift Supernovae. *ApJ*, 517:565–586. In the dissertation: 10

Pietrzyński G., Gieren W., Hamuy M., Pignata G., Soszyński I., Udalski A., Walker A., Fouqué P., Bresolin F., Kudritzki R. P., Garcia-Varela A., Szewczyk O., Szymański M., Kubiak M., and Wyrzykowski Ł. (2010). The Araucaria Project: First Cepheid Distance to the Sculptor Group Galaxy NGC 7793 from Variables Discovered in a Wide-field Imaging Survey. *Astronomical Journal*, 140:1475–1485. In the dissertation: 59, 113

Pignata G. (2013). Four years of observations of SN 2008bk. In *Massive Stars: From alpha to Omega*, page 176. In the dissertation: 58, 59, 71, 87, 113, 114, 115

Pignata G., Maza J., Antezana R., Cartier R., Folatelli G., Forster F., Gonzalez L., Gonzalez P., Hamuy M., Iturra D., Lopez P., Silva S., Conuel B., Crain A., Foster D., Ivarsen K., Lacluyze A., Nysewander M., and Reichart D. (2009). The CHilean Automatic Supernova sEarch (CHASE). In Giobbi G., Tornambe A., Raimondo G., Limongi M., Antonelli L. A., Menci N., and

Brocato E., editors, *American Institute of Physics Conference Series*, volume 1111 of *American Institute of Physics Conference Series*, pages 551–554. In the dissertation: 17

Pinto P. A., Woosley S. E., and Ensman L. M. (1988). SN 1987A — Out on the tail. *ApJ Letters*, 331:L101–L104. In the dissertation: 41

Piran T. (2004). The physics of gamma-ray bursts. *Reviews of Modern Physics*, 76:1143–1210. In the dissertation: 26

Piro A. L. & Nakar E. (2013). What can we Learn from the Rising Light Curves of Radioactively Powered Supernovae? *ApJ*, 769:67. In the dissertation: 22

Planck Collaboration (2014). Planck 2013 results. I. Overview of products and scientific results. *A&A*, 571:A1. In the dissertation: 10

Podsiadlowski P. (1992). The progenitor of SN 1987 A. *Publications of the ASP*, 104:717–729. In the dissertation: 12, 25

Podsiadlowski P., Hsu J. J. L., Joss P. C., and Ross R. R. (1993). The progenitor of supernova 1993J – A stripped supergiant in a binary system? *Nature*, 364:509–511. In the dissertation: 24

Poelarends A. J. T., Herwig F., Langer N., and Heger A. (2008). The Supernova Channel of Super-AGB Stars. *ApJ*, 675:614–625. In the dissertation: 11, 99

Popov D. V. (1993). An analytical model for the plateau stage of Type II supernovae. *ApJ*, 414:712–716. In the dissertation: 24, 85

Poznanski D., Butler N., Filippenko A. V., Ganeshalingam M., Li W., Bloom J. S., Chornock R., Foley R. J., Nugent P. E., Silverman J. M., Cenko S. B., Gates E. L., Leonard D. C., Miller A. A., Modjaz M., Serduke F. J. D., Smith N., Swift B. J., and Wong D. S. (2009). Improved Standardization of Type II-P Supernovae: Application to an Expanded Sample. *ApJ*, 694:1067–1079. In the dissertation: 118

Prieto J. L., Osip D., and Palunas P. (2012). Candidate Progenitor of the Type II SN 2012A in the Near-IR. *The Astronomer's Telegram*, 3863. In the dissertation: 23

Pruzhinskaya M. V. & Lisakov S. (2016). How supernovae became the basis of observational cosmology. *Journal of Astronomical History and Heritage*, 19:203–215. In the dissertation: 20

Pskovskii I. P. (1977). Light curves, color curves, and expansion velocity of type I supernovae as functions of the rate of brightness decline. *Soviet Astronomy*, 21:675–682. In the dissertation: 20

Pskovskii Y. P. (1984). Photometric classification and basic parameters of type I supernovae. *Soviet Astronomy*, 28:658–664. In the dissertation: 20

Pskovskii Y. P. (1969). Identification of the Absorption Spectrum of the Type I Supernova. *Soviet Astronomy*, 12:750. In the dissertation: 17

Pumo M. L., Zampieri L., Spiro S., Pastorello A., Benetti S., Cappellaro E., Manicò G., and Turatto M. (2017). Radiation-hydrodynamical modelling of underluminous Type II plateau supernovae. *MNRAS*, 464:3013–3020. In the dissertation: 97

Quimby R. M. (2006). The Texas Supernova Search. PhD thesis, The University of Texas at Austin. In the dissertation: 17

Quimby R. M., Aldering G., Wheeler J. C., Höflich P., Akerlof C. W., and Rykoff E. S. (2007). SN 2005ap: A Most Brilliant Explosion. *ApJ Letters*, 668:L99–L102. In the dissertation: 26

Quimby R. M., Kulkarni S. R., Kasliwal M. M., Gal-Yam A., Arcavi I., Sullivan M., et al. (2011). Hydrogen-poor superluminous stellar explosions. *Nature*, 474:487–489. In the dissertation: 26

Rakavy G. & Shaviv G. (1967). Instabilities in Highly Evolved Stellar Models. *ApJ*, 148:803. In the dissertation: 26

Rauscher T., Heger A., Hoffman R. D., and Woosley S. E. (2002). Nucleosynthesis in Massive Stars with Improved Nuclear and Stellar Physics. *ApJ*, 576:323–348. In the dissertation: 34

Riess A. G., Filippenko A. V., Challis P., Clocchiatti A., Diercks A., Garnavich P. M., Gilliland R. L., Hogan C. J., Jha S., Kirshner R. P., Leibundgut B., Phillips M. M., Reiss D., Schmidt B. P., Schommer R. A., Smith R. C., Spyromilio J., Stubbs C., Suntzeff N. B., and Tonry J. (1998). Observational Evidence from Supernovae for an Accelerating Universe and a Cosmological Constant. *Astronomical Journal*, 116:1009–1038. In the dissertation: 10

Ritchey G. W. (1917). Novae in Spiral Nebulae. *Publications of the ASP*, 29:210. In the dissertation: 9

Rodríguez Ó., Clocchiatti A., and Hamuy M. (2014). Photospheric Magnitude Diagrams for Type II Supernovae: A Promising Tool to Compute Distances. *Astronomical Journal*, 148:107. In the dissertation: 118

Roy R., Kumar B., Benetti S., Pastorello A., Yuan F., Brown P. J., et al. (2011). SN 2008in — Bridging the Gap between Normal and Faint Supernovae of Type IIP. *ApJ*, 736:76. In the dissertation: 53, 97, 113, 114

Rust B. W. (1974). Use of supernovae light curves for testing the expansion hypothesis and other cosmological relations. PhD thesis, Oak Ridge National Lab., TN. In the dissertation: 20

Ryder S., Staveley-Smith L., Dopita M., Petre R., Colbert E., Malin D., and Schlegel E. (1993). SN 1978K: an Extraordinary Supernova in the Nearby Galaxy NGC 1313. *ApJ*, 416:167. In the dissertation: 23

Sahu D. K., Anupama G. C., Srividya S., and Muneer S. (2006). Photometric and spectroscopic evolution of the Type IIP supernova SN 2004et. *MNRAS*, 372:1315–1324. In the dissertation: 118

Sana H., de Mink S. E., de Koter A., Langer N., Evans C. J., Gieles M., Gosset E., Izzard R. G., Le Bouquin J. B., and Schneider F. R. N. (2012). Binary Interaction Dominates the Evolution of Massive Stars. *Science*, 337:444. In the dissertation: 25

Sandage A. (1958). Current Problems in the Extragalactic Distance Scale. *ApJ*, 127:513. In the dissertation: 10

Sanders N. E., Soderberg A. M., Gezari S., Betancourt M., Chornock R., Berger E., et al. (2015). Toward Characterization of the Type IIP Supernova Progenitor Population: A Statistical Sample of Light Curves from Pan-STARRS1. *ApJ*, 799:208. In the dissertation: 24, 27, 58

Scalzo R. A., Aldering G., Antilogus P., Aragon C., Bailey S., Baltay C., et al. (2010). Nearby Supernova Factory Observations of SN 2007if: First Total Mass Measurement of a Super-Chandrasekhar-Mass Progenitor. *ApJ*, 713:1073–1094. In the dissertation: 20

Schlafly E. F. & Finkbeiner D. P. (2011). Measuring Reddening with Sloan Digital Sky Survey Stellar Spectra and Recalibrating SFD. *ApJ*, 737:103. In the dissertation: 111, 113, 115, 116, 118

Schlegel D. J., Finkbeiner D. P., and Davis M. (1998). Maps of Dust Infrared Emission for Use in Estimation of Reddening and Cosmic Microwave Background Radiation Foregrounds. *ApJ*, 500:525–553. In the dissertation: 59, 116

Sellwood J. A. & Sánchez R. Z. (2010). Quantifying non-circular streaming motions in disc galaxies. *MNRAS*, 404:1733–1744. In the dissertation: 118

Shapley H. (1917). Note on the Magnitudes of Novae in Spiral Nebulae. *Publications of the ASP*, 29:213. In the dissertation: 9

Shapley H. & Curtis H. D. (1921). The Scale of the Universe. *Bulletin of the National Research Council, Vol. 2, Part 3, No. 11, p. 171-217*, 2:171–217. In the dissertation: 9

Shappee B. J., Prieto J. L., Grupe D., Kochanek C. S., Stanek K. Z., De Rosa G., et al. (2014). The Man behind the Curtain: X-Rays Drive the UV through NIR Variability in the 2013 Active Galactic Nucleus Outburst in NGC 2617. *ApJ*, 788:48. In the dissertation: 17

Silverman J. M., Ganeshalingam M., Li W., Filippenko A. V., Miller A. A., and Poznanski D. (2011). Fourteen months of observations of the possible super-Chandrasekhar mass Type Ia Supernova 2009dc. *MNRAS*, 410:585–611. In the dissertation: 20

Sim S. A., Kromer M., Röpke F. K., Sorokina E. I., Blinnikov S. I., Kasen D., and Hillebrandt W. (2010). Monte Carlo Radiative Transfer Simulations: Applications to Astrophysical Outflows and Explosions. In Pogorelov N. V., Audit E., and Zank G. P., editors, *Numerical Modeling of Space Plasma Flows, Astronum-2009*, volume 429 of *Astronomical Society of the Pacific Conference Series*, page 148. In the dissertation: 38

Simon J. D., Gal-Yam A., Gnat O., Quimby R. M., Ganeshalingam M., Silverman J. M., et al. (2009). Variable Sodium Absorption in a Low-extinction Type Ia Supernova. *ApJ*, 702:1157–1170. In the dissertation: 20

Smartt S. J. (2009). Progenitors of Core-Collapse Supernovae. *Annual Review of Astronomy and Astrophysics*, 47:63–106. In the dissertation: 57, 105

Smartt S. J., Eldridge J. J., Crockett R. M., and Maund J. R. (2009). The death of massive stars — I. Observational constraints on the progenitors of Type II-P supernovae. *MNRAS*, 395:1409–1437. In the dissertation: 21, 22

Smartt S. J., Maund J. R., Hendry M. A., Tout C. A., Gilmore G. F., Mattila S., and Benn C. R. (2004). Detection of a Red Supergiant Progenitor Star of a Type II-Plateau Supernova. *Science*, 303:499–503. In the dissertation: 23

Smartt S. J., Valenti S., Fraser M., Inserra C., Young D. R., Sullivan M., et al. (2015). PESSTO: survey description and products from the first data release by the Public ESO Spectroscopic Survey of Transient Objects. *A&A*, 579:A40. In the dissertation: 118

Smith N. (2014). Mass Loss: Its Effect on the Evolution and Fate of High-Mass Stars. *Annual Review of Astronomy and Astrophysics*, 52:487–528. In the dissertation: 22

Smith N., Li W., Filippenko A. V., and Chornock R. (2011). Observed fractions of core-collapse supernova types and initial masses of their single and binary progenitor stars. *MNRAS*, 412:1522–1538. In the dissertation: 57

Smith N., Li W., Foley R. J., Wheeler J. C., Pooley D., Chornock R., Filippenko A. V., Silverman J. M., Quimby R., Bloom J. S., and Hansen C. (2007). SN 2006gy: Discovery of the Most Luminous Supernova Ever Recorded, Powered by the Death of an Extremely Massive Star like η Carinae. *ApJ*, 666:1116–1128. In the dissertation: 26

Smith N., Miller A., Li W., Filippenko A. V., Silverman J. M., Howard A. W., Nugent P., Marcy G. W., Bloom J. S., Ghez A. M., Lu J., Yelda S., Bernstein R. A., and Colucci J. E. (2010). Discovery of Precursor Luminous Blue Variable Outbursts in Two Recent Optical Transients: The Fitfully Variable Missing Links UGC 2773-OT and SN 2009ip. *Astronomical Journal*, 139:1451–1467. In the dissertation: 23

Sonneborn G., Altner B., and Kirshner R. P. (1987). The progenitor of SN 1987A — Spatially resolved ultraviolet spectroscopy of the supernova field. *ApJ Letters*, 323:L35–L39. In the dissertation: 23

Sorce J. G., Tully R. B., Courtois H. M., Jarrett T. H., Neill J. D., and Shaya E. J. (2014). From Spitzer Galaxy photometry to Tully-Fisher distances. *MNRAS*, 444:527–541. In the dissertation: 113, 118

Spiro S., Pastorello A., Pumo M. L., Zampieri L., Turatto M., Smartt S. J., et al. (2014). Low luminosity Type II supernovae — II. Pointing towards moderate mass precursors. *MNRAS*, 439:2873–2892. In the dissertation: 43, 45, 46, 53, 58, 93, 97, 111, 112, 113, 114, 115

Springob C. M., Masters K. L., Haynes M. P., Giovanelli R., and Marinoni C. (2009). Erratum: "SFI++ II: A New I-Band Tully-Fisher Catalog, Derivation of Peculiar Velocities and Data Set Properties". *ApJ, Supplement*, 182:474–475. In the dissertation: 118

Sternberg A., Gal-Yam A., Simon J. D., Leonard D. C., Quimby R. M., Phillips M. M., Morrell N., Thompson I. B., Ivans I., Marshall J. L., Filippenko A. V., Marcy G. W., Bloom J. S., Patat F., Foley R. J., Yong D., Penprase B. E., Beeler D. J., Allende Prieto C., and Stringfellow G. S. (2011). Circumstellar Material in Type Ia Supernovae via Sodium Absorption Features. *Science*, 333:856. In the dissertation: 20

Stoner E. (1930). The Equilibrium of Dense Stars. *The London, Edinburgh, and Dublin Philosophical Magazine and Journal of Science: Series 7, Issue 60*, 9:944–963. In the dissertation: 20

Strauss M. A., Huchra J. P., Davis M., Yahil A., Fisher K. B., and Tonry J. (1992). A redshift survey of IRAS galaxies. VII — The infrared and redshift data for the 1.936 Jansky sample. *ApJ, Supplement*, 83:29–63. In the dissertation: 118

Stromberg G. (1925). Analysis of radial velocities of globular clusters and non-galactic nebulae. *ApJ*, 61. In the dissertation: 10

Sukhbold T., Ertl T., Woosley S. E., Brown J. M., and Janka H. T. (2016). Core-collapse Supernovae from 9 to 120 Solar Masses Based on Neutrino-powered Explosions. *ApJ*, 821:38. In the dissertation: 34, 35, 88

Swartz D. A., Wheeler J. C., and Harkness R. P. (1991). Model light curves of linear Type II supernovae. *ApJ*, 374:266–280. In the dissertation: 24

Takáts K., Pignata G., Pumo M. L., Paillas E., Zampieri L., Elias-Rosa N., et al. (2015). SN 2009ib: a Type II-P supernova with an unusually long plateau. *MNRAS*, 450:3137–3154. In the dissertation: 23, 48, 118

Takáts K., Pumo M. L., Elias-Rosa N., Pastorello A., Pignata G., Paillas E., et al. (2014). SN 2009N: linking normal and subluminous Type II-P SNe. *MNRAS*, 438:368–387. In the dissertation: 97, 113, 115

Tartaglia L., Fraser M., Sand D. J., Valenti S., Smartt S. J., McCully C., et al. (2017). The Progenitor and Early Evolution of the Type IIb SN 2016gkg. *ApJ Letters*, 836:L12. In the dissertation: 23

Taubenberger S., Benetti S., Childress M., Pakmor R., Hachinger S., Mazzali P. A., et al. (2011). High luminosity, slow ejecta and persistent carbon lines: SN 2009dc challenges thermonuclear explosion scenarios. *MNRAS*, 412:2735–2762. In the dissertation: 20

Tauris T. M., Langer N., Moriya T. J., Podsiadlowski P., Yoon S. C., and Blinnikov S. I. (2013). Ultra-stripped Type Ic Supernovae from Close Binary Evolution. *ApJ Letters*, 778:L23. In the dissertation: 37

The L. S., Diehl R., Hartmann D. H., Iyudin A. F., Leising M. D., and Oberlack U. (2000). The galactic supernova rate from COMPTEL ^{44}Ti γ-line observations. In McConnell M. L. & Ryan J. M., editors, *American Institute of Physics Conference Series*, volume 510 of *American Institute of Physics Conference Series*, pages 64–68. In the dissertation: 17

Theureau G., Hanski M. O., Coudreau N., Hallet N., and Martin J. M. (2007). Kinematics of the Local Universe. XIII. 21-cm line measurements of 452 galaxies with the Nançay radiotelescope, JHK Tully-Fisher relation, and preliminary maps of the peculiar velocity field. *A&A*, 465:71–85. In the dissertation: 113, 118

Thöne C. C., de Ugarte Postigo A., Leloudas G., Gall C., Cano Z., Maeda K., Schulze S., Campana S., Wiersema K., Groh J., de la Rosa J., Bauer F. E., Malesani D., Maund J., Morrell N., and Beletsky Y. (2017). SN 2015bh: NGC 2770's 4th supernova or a luminous blue variable on its way to a Wolf-Rayet star? *A&A*, 599:A129. In the dissertation: 23

Tifft W. G. & Cocke W. J. (1988). Uncertainties in 21 centimeter redshifts. I — Data. *ApJ, Supplement*, 67:1–75. In the dissertation: 118

Timmes F. X., Woosley S. E., Hartmann D. H., and Hoffman R. D. (1996). The Production of ^{44}Ti and ^{60}Co in Supernovae. *ApJ*, 464:332. In the dissertation: 41

Tomasella L., Cappellaro E., Fraser M., Pumo M. L., Pastorello A., Pignata G., et al. (2013). Comparison of progenitor mass estimates for the Type IIP SN 2012A. *MNRAS*, 434:1636–1657. In the dissertation: 23

Tominaga N., Blinnikov S., Baklanov P., Morokuma T., Nomoto K., and Suzuki T. (2009). Properties of Type II Plateau Supernova SNLS-04D2dc: Multicolor Light Curves of Shock Breakout and Plateau. *ApJ Letters*, 705:L10–L14. In the dissertation: 37

Tripp R. (1998). A two-parameter luminosity correction for Type IA supernovae. *A&A*, 331:815–820. In the dissertation: 20

Tsvetkov D. Y. (2008). Photometric Observations of Two Type II-P Supernovae: Normal SN II-P 2004A and Unusual SN 2004ek. *Peremennye Zvezdy*, 28. In the dissertation: 118

Tsvetkov D. Y., Goranskij V., and Pavlyuk N. (2008). Photometric Investigation of Bright Type II-P Supernova 2004dj. *Peremennye Zvezdy*, 28. In the dissertation: 118

Tsvetkov D. Y., Shugarov S. Y., Volkov I. M., Goranskij V. P., Pavlyuk N. N., Katysheva N. A., Barsukova E. A., and Valeev A. F. (2013). Optical observations of SN 2011fe. *Contributions of the Astronomical Observatory Skalnate Pleso*, 43:94–108. In the dissertation: 118

Turatto M., Gouiffes C., and Leibundgut B. (1994). Supernova 1994N in UGC 5695. *IAU Cirulars*, 5987:1. In the dissertation: 111

Turatto M., Mazzali P. A., Young T. R., Nomoto K., Iwamoto K., Benetti S., Cappellaro E., Danziger I. J., de Mello D. F., Phillips M. M., Suntzeff N. B., Clocchiatti A., Piemonte A., Leibundgut B., Covarrubias R., Maza J., and Sollerman J. (1998). The Peculiar Type II Supernova 1997D: A Case for a Very Low ^{56}Ni Mass. *ApJ Letters*, 498:L129–L133. In the dissertation: 45, 58, 97

Ugliano M., Janka H. T., Marek A., and Arcones A. (2012). Progenitor-explosion Connection and Remnant Birth Masses for Neutrino-driven Supernovae of Iron-core Progenitors. *ApJ*, 757:69. In the dissertation: 35, 87

Utrobin V. (1994). Type IIb supernova 1993J in M81: The explosion of a approximately 4 solar mass star in a close binary system. *A&A*, 281:L89–L92. In the dissertation: 24

Utrobin V. P. (2007). An optimal hydrodynamic model for the normal type IIP supernova 1999em. *A&A*, 461:233–251. In the dissertation: 57, 71, 78, 104, 105, 107

Utrobin V. P. & Chugai N. N. (2008). Progenitor mass of the type IIP supernova 2005cs. *A&A*, 491:507–513. In the dissertation: 97, 101, 103

Utrobin V. P. & Chugai N. N. (2013). Type IIP supernova 2008in: the explosion of a normal red supergiant. *A&A*, 555:A145. In the dissertation: 97

Utrobin V. P., Chugai N. N., and Pastorello A. (2007). Ejecta and progenitor of the low-luminosity type IIP supernova 2003Z. *A&A*, 475:973–979. In the dissertation: 45, 58, 97

Valenti S., Elias-Rosa N., Taubenberger S., Stanishev V., Agnoletto I., Sauer D., et al. (2008). The Carbon-rich Type Ic SN 2007gr: The Photospheric Phase. *ApJ Letters*, 673:L155. In the dissertation: 118

Valenti S., Howell D. A., Stritzinger M. D., Graham M. L., Hosseinzadeh G., Arcavi I., et al. (2016). The diversity of Type II supernova versus the similarity in their progenitors. *MNRAS*, 459:3939–3962. In the dissertation: 118

Valenti S., Sand D., Pastorello A., Graham M. L., Howell D. A., Parrent J. T., Tomasella L., Ochner P., Fraser M., Benetti S., Yuan F., Smartt S. J., Maund J. R., Arcavi I., Gal-Yam A., Inserra C., and Young D. (2014). The first month of evolution of the slow-rising Type IIP SN 2013ej in M74★. *MNRAS*, 438:L101–L105. In the dissertation: 118

Van Dyk S. D. (2013). An Echo of Supernova 2008bk. *Astronomical Journal*, 146:24. In the dissertation: 59

Van Dyk S. D. (2017). The direct identification of core-collapse supernova progenitors. *Philosophical Transactions of the Royal Society of London Series A*, 375:20160277. In the dissertation: 23

Van Dyk S. D., Davidge T. J., Elias-Rosa N., Taubenberger S., Li W., Levesque E. M., Howerton S., Pignata G., Morrell N., Hamuy M., and Filippenko A. V. (2012a). Supernova 2008bk and Its Red Supergiant Progenitor. *Astronomical Journal*, 143:19. In the dissertation: 23, 43, 45, 58, 59, 61, 115

Van Dyk S. D., Cenko S. B., Poznanski D., Arcavi I., Gal-Yam A., Filippenko A. V., Silverio K., Stockton A., Cuillandre J. C., Marcy G. W., Howard A. W., and Isaacson H. (2012b). The Red Supergiant Progenitor of Supernova 2012aw (PTF12bvh) in Messier 95. *ApJ*, 756:131. In the dissertation: 23

Van Dyk S. D., Li W., Cenko S. B., Kasliwal M. M., Horesh A., Ofek E. O., Kraus A. L., Silverman J. M., Arcavi I., Filippenko A. V., Gal-Yam A., Quimby R. M., Kulkarni S. R., Yaron O., and Polishook D. (2011). The Progenitor of Supernova 2011dh/PTF11eon in Messier 51. *ApJ Letters*, 741:L28. In the dissertation: 23

Van Dyk S. D., Li W., and Filippenko A. V. (2003a). A Search for Core-Collapse Supernova Progenitors in Hubble Space Telescope Images. *Publications of the ASP*, 115:1–20. In the dissertation: 23

Van Dyk S. D., Li W., and Filippenko A. V. (2003b). On the Progenitor of the Type II-Plateau Supernova 2003gd in M74. *Publications of the ASP*, 115:1289–1295. In the dissertation: 23

Van Dyk S. D., Peng C. Y., King J. Y., Filippenko A. V., Treffers R. R., Li W., and Richmond M. W. (2000). SN 1997bs in M66: Another Extragalactic η Carinae Analog? *Publications of the ASP*, 112:1532–1541. In the dissertation: 23

Van Dyk S. D., Zheng W., Fox O. D., Cenko S. B., Clubb K. I., Filippenko A. V., Foley R. J., Miller A. A., Smith N., Kelly P. L., Lee W. H., Ben-Ami S., and Gal-Yam A. (2014). The Type IIb Supernova 2013df and its Cool Supergiant Progenitor. *Astronomical Journal*, 147:37. In the dissertation: 23

de Vaucouleurs G., de Vaucouleurs A., Buta R., Ables H. D., and Hewitt A. V. (1981). The bright supernova 1979c in M100. *Publications of the ASP*, 93:36–44. In the dissertation: 92, 118

de Vaucouleurs G., de Vaucouleurs A., Corwin, Jr. H. G., Buta R. J., Paturel G., and Fouqué P. (1991). Third Reference Catalogue of Bright Galaxies. Volume I: Explanations and references. Volume II: Data for galaxies between 0^h and 12^h. Volume III: Data for galaxies between 12^h and 24^h. In the dissertation: 118

Vink J. S., de Koter A., and Lamers H. J. G. L. M. (2000). New theoretical mass-loss rates of O and B stars. *A&A*, 362:295–309. In the dissertation: 20

Vinkó J., Takáts K., Sárneczky K., Szabó G. M., Mészáros S., Csorvási R., Szalai T., Gáspár A., Pál A., Csizmadia S., Kóspál A., Rácz M., Kun M., Csák B., Fürész G., DeBond H., Grunhut J., Thomson J., Mochnacki S., and Koktay T. (2006). The first year of SN 2004dj in NGC 2403. *MNRAS*, 369:1780–1796. In the dissertation: 118

Volnova A. A., Pruzhinskaya M. V., Pozanenko A. S., Blinnikov S. I., Minaev P. Y., Burkhonov O. A., Chernenko A. M., Ehgamberdiev S. A., Inasaridze R., Jelinek M., Khorunzhev G. A., Klunko E. V., Krugly Y. N., Mazaeva E. D., Rumyantsev V. V., and Volvach A. E. (2017). Multicolour modelling of SN 2013dx associated with GRB 130702A★. *MNRAS*, 467:3500–3512. In the dissertation: 37

Weaver T. A., Zimmerman G. B., and Woosley S. E. (1978). Presupernova evolution of massive stars. *ApJ*, 225:1021–1029. In the dissertation: 34

Wei L. H., Kannappan S. J., Vogel S. N., and Baker A. J. (2010). Gas Mass Fractions and Star Formation in Blue-Sequence E/S0 Galaxies. *ApJ*, 708:841–861. In the dissertation: 113

Wheeler J. C., Yi I., Höflich P., and Wang L. (2000). Asymmetric Supernovae, Pulsars, Magnetars, and Gamma-Ray Bursts. *ApJ*, 537:810–823. In the dissertation: 26

Whelan J. & Iben, Jr. I. (1973). Binaries and Supernovae of Type I. *ApJ*, 186:1007–1014. In the dissertation: 20

White G. L. & Malin D. F. (1987). Possible binary star progenitor for SN1987A. *Nature*, 327:36–38. In the dissertation: 23

Wollaeger R. T. & van Rossum D. R. (2014). Radiation Transport for Explosive Outflows: Opacity Regrouping. *ApJ, Supplement*, 214:28. In the dissertation: 34

Wollaeger R. T., van Rossum D. R., Graziani C., Couch S. M., Jordan, IV G. C., Lamb D. Q., and Moses G. A. (2013). Radiation Transport for Explosive Outflows: A Multigroup Hybrid Monte Carlo Method. *ApJ, Supplement*, 209:36. In the dissertation: 34

Wongwathanarat A., Müller E., and Janka H. T. (2015). Three-dimensional simulations of core-collapse supernovae: from shock revival to shock breakout. *A&A*, 577:A48. In the dissertation: 36, 46, 80, 88

Woosley S. E. (1993). Gamma-ray bursts from stellar mass accretion disks around black holes. *ApJ*, 405:273–277. In the dissertation: 26

Woosley S. E. (2010). Bright Supernovae from Magnetar Birth. *ApJ Letters*, 719:L204–L207. In the dissertation: 26

Woosley S. E., Blinnikov S., and Heger A. (2007a). Pulsational pair instability as an explanation for the most luminous supernovae. *Nature*, 450:390–392. In the dissertation: 22

Woosley S. E. & Bloom J. S. (2006). The Supernova Gamma-Ray Burst Connection. *Annual Review of Astronomy and Astrophysics*, 44:507–556. In the dissertation: 26

Woosley S. E., Eastman R. G., Weaver T. A., and Pinto P. A. (1994). SN 1993J: A Type IIb supernova. *ApJ*, 429:300–318. In the dissertation: 24

Woosley S. E., Hartmann D., and Pinto P. A. (1989). Hard emission at late times from SN 1987A. *ApJ*, 346:395–404. In the dissertation: 41

Woosley S. E. & Heger A. (2007). Nucleosynthesis and remnants in massive stars of solar metallicity. *Physics Reports*, 442:269–283. In the dissertation: 34

Woosley S. E., Heger A., and Weaver T. A. (2002). The evolution and explosion of massive stars. *Reviews of Modern Physics*, 74:1015–1071. In the dissertation: 11, 12, 13, 14, 15, 31, 85, 86, 103, 105

Woosley S. E. & Janka T. (2005). The physics of core-collapse supernovae. *Nature Physics*, 1:147–154. In the dissertation: 34

Woosley S. E., Kasen D., Blinnikov S., and Sorokina E. (2007b). Type Ia Supernova Light Curves. *ApJ*, 662:487–503. In the dissertation: 38

Woosley S. E. & Weaver T. A. (1995). The Evolution and Explosion of Massive Stars. II. Explosive Hydrodynamics and Nucleosynthesis. *ApJ, Supplement*, 101:181. In the dissertation: 24

Wyrzykowski Ł., Kostrzewa-Rutkowska Z., Kozłowski S., Udalski A., Poleski R., Skowron J., Blagorodnova N., Kubiak M., Szymański M. K., Pietrzyński G., Soszyński I., Ulaczyk K., Pietrukowicz P., and Mróz P. (2014). OGLE-IV Real-Time Transient Search. *Acta Astronomica*, 64:197–232. In the dissertation: 17

Yamanaka M., Kawabata K. S., Kinugasa K., Tanaka M., Imada A., Maeda K., et al. (2009). Early Phase Observations of Extremely Luminous Type Ia Supernova 2009dc. *ApJ Letters*, 707:L118–L122. In the dissertation: 20

Yaron O., Gal-Yam A., Fox O. D., Kelly P., Zheng W., Cenko S. B., Filippenko A. V., Silverman J. M., Walker E. S., Mazzali P. A., Pian E., Nugent P. E., Cao Y., Horesh A., and Kasliwal M. M. (2013). Independent iPTF detection and spectroscopic follow-up observations of the Type II SN 2013am = iPTF13aaz in M65. *The Astronomer's Telegram*, 4910. In the dissertation: 116

Yoon S. C. (2017). Towards a better understanding of the evolution of Wolf-Rayet stars and Type Ib/Ic supernova progenitors. *MNRAS*, 470:3970–3980. In the dissertation: 21

Yoshida S., Kadota K., and Hanzl D. (1999). Supernova 1999br in NGC 4900. *IAU Cirulars*, 7143. In the dissertation: 114

Young J., Boles T., and Li W. (2004). Supernovae 2004eg, 2004eh, and 2004ei. *IAU Cirulars*, 8401. In the dissertation: 85, 115

Yu Y. W., Zhu J. P., Li S. Z., Lü H. J., and Zou Y. C. (2017). A Statistical Study of Superluminous Supernovae Using the Magnetar Engine Model and Implications for Their Connection with Gamma-Ray Bursts and Hypernovae. *ApJ*, 840:12. In the dissertation: 25

Yuan F., Jerkstrand A., Valenti S., Sollerman J., Seitenzahl I. R., Pastorello A., et al. (2016). 450 d of Type II SN 2013ej in optical and near-infrared. *MNRAS*, 461:2003–2018. In the dissertation: 118

Zampieri L. (2007). Exploring the Physics of Type II Supernovae. In di Salvo T., Israel G. L., Piersant L., Burderi L., Matt G., Tornambe A., and Menna M. T., editors, *The Multicolored Landscape of Compact Objects and Their Explosive Origins*, volume 924 of *American Institute of Physics Conference Series*, pages 358–365. In the dissertation: 58

Zampieri L., Pastorello A., Turatto M., Cappellaro E., Benetti S., Altavilla G., Mazzali P., and Hamuy M. (2003). Peculiar, low-luminosity Type II supernovae: low-energy explosions in massive progenitors? *MNRAS*, 338:711–716. In the dissertation: 45, 58, 97, 111

Zhang J. & Wang X. (2014). Spectroscopic Classification of PSN J12060299+4729335 as A Low-Luminosity Type II-P Supernova. *The Astronomer's Telegram*, 6192. In the dissertation: 113, 116

Zhang T., Wang X., Li W., Zhou X., Ma J., Jiang Z., and Chen J. (2006). Optical Photometry of the Type II-P Supernova 2004dj in NGC 2403. *Astronomical Journal*, 131:2245–2255. In the dissertation: 118

Zheng W. & Filippenko A. V. (2014). KAIT Discovery and Robotic Follow-up Observations of a Possible SN Candidate in NGC 4096: PSN J12060299+4729335. *The Astronomer's Telegram*, 6190. In the dissertation: 116

Zwicky F. (1940). Types of Novae. *Reviews of Modern Physics*, 12:66–85. In the dissertation: 10

Zwicky F. (1964). NGC 1058 and its Supernova 1961. *ApJ*, 139:514. In the dissertation: 23

List of Figures

List of Tables